UNIVERSITY OF MALTA
L-Università ta' Malta

Fast Automatic Beam-Based Alignment of the LHC Collimator Jaws

by

Gianluca Valentino

under the supervision of
Dr. Ing. Nicholas Sammut (UoM)
Dr. Ralph W. Assmann (CERN)

A dissertation submitted to the University of Malta for the degree of
Doctor of Philosophy

June 2013

UNIVERSITY OF MALTA
L-Università ta' Malta

No portion of the work referred to in the thesis has been submitted in support of an application for another degree or qualification of this or any other university or other institute of learning.

_____   _____
Student Name   Signature

FACULTY OF INFORMATION AND COMMUNICATION TECHNOLOGY

Declaration

Plagiarism is defined as "the unacknowledged use, as one's own, of work of another person, whether or not such work has been published, and as may be further elaborated in Faculty or University guidelines" (University Assessment Regulations, 2009, Regulation 39 (b)(i), University of Malta).

I, the undersigned, declare that the dissertation submitted is my work, except where acknowledged and referenced.

I understand that the penalties for committing a breach of the regulations include loss of marks; cancellation of examination results; enforced suspension of studies; or expulsion from the degree programme.

Work submitted without this signed declaration will not be corrected, and will be given zero marks.

_____   _____
Student Name   Signature

_____
                              Title of work submitted

_____
Date

Nothing has such power to broaden the mind as the ability to investigate systematically and truly all that comes under thy observation in life.

- Marcus Aurelius Antoninus Augustus

Abstract

The CERN Large Hadron Collider (LHC) in Geneva, Switzerland is the largest and most powerful particle accelerator ever built. With a circumference of 27 km, it is designed to collide particles in two counter-rotating beams at a centre-of-mass energy of 14 TeV to explore the fundamental forces and constituents of matter.

Due to its potentially destructive high energy particle beams, the LHC is equipped with several machine protection systems. The LHC collimation system is tasked with scattering and absorbing beam halo particles before they can quench the superconducting magnets. The 108 collimators also protect the machine from damage in the event of very fast beam losses, and shields sensitive devices in the tunnel from radiation over years of operation. Each collimator is made up of two blocks or 'jaws' of carbon, tungsten or copper material. The collimator jaws need be placed symmetrically on either side of the beam trajectory, to clean halo particles with maximum efficiency. The beam orbit and beam size need to be determined for each collimator, to be able to position the jaws within a certain number of standard deviations (beam σ) from the beam centre.

Beam-based alignment is used to determine these values at every collimator location. In the alignment procedure, each jaw is moved separately towards the beam trajectory, in 5 μm steps, until a spike appears in the signal of a Beam Loss Monitoring (BLM) detector positioned a couple of metres downstream of the collimator. A balance is required between scraping enough beam to obtain a signal, avoiding automatically triggered beam extractions (or dumps) in the event of high beam losses, and completing the alignment in the shortest time possible to allow the LHC to produce maximum luminosity.

In the 2010 LHC run, almost 30 hours were required for an alignment of all collimators, and 8 beam dumps were caused due to operator mistakes. A phased development, commissioning and usage of various algorithms in the 2011-2012 LHC runs allowed the alignment time to decrease to just over 4 hours, with no more beam dumps. The algorithms range from automatic selection of BLM thresholds during the alignment, to BLM-based feedback loops and pattern recognition of the BLM signal spikes. The BLM-based feedback loop was also successfully used

by the ALFA and TOTEM particle physics experiments in Roman Pot alignment campaigns. A Roman Pot is a detector that intercepts slightly deflected particles from head-on collisions to measure the total collision rate (cross-section).

An alignment simulator was developed in MATLAB based on an empirical model of the BLM detector signal steady-state and crosstalk, as well as a beam diffusion model which allows the prediction of the characteristic BLM detector signal spike and decay. The simulator is targeted at validating possible future alignment algorithms which would otherwise require dedicated beam tests.

A new collimator design for future LHC operation envisages Beam Position Monitor (BPM) pick-up buttons embedded inside the jaws. The BPMs will provide an accurate and continuous measurement of the beam centres without requiring BLM-based alignment. One quarter of the LHC collimators (tertiary collimators and IR6 secondary collimators) will be replaced with the new design, as foreseen since several years. Hence, an algorithm to automatically position the jaws around the beam centre at a large jaw gap was developed and tested with a prototype mock-up collimator installed in the Super Proton Synchrotron (SPS). Alignment times of approximately 20 s were reached.

The work described in this dissertation was adopted by CERN for the first LHC running period (2008 - 2013). It will continue to be used in future operation post-2015 after a two-year shutdown, in which the machine will be upgraded to be able to operate at the design parameters.

Sommarju

Il-"Large Hadron Collider" (LHC) li jinsab CERN f' Ġinevra, fl-Isvizzera huwa l-ikbar u l-iktar aċċelleratur ta' partiċelli b' saħħtu li qatt inbena'. B' ċirkonferenza ta' 27 km, huwa ddisinjat sabiex iħabbat partiċelli f' żewġ faxex iduru kontra xulxin b' ċentru ta' massa enerġetika nominali ta' 14 TeV. B' hekk jistgħu jsiru esperimenti li jesploraw il-forzi fundamentali tan-Natura u jiskopru minn xiex hija magħmula l-materja.

Minħabba li l-faxex tal-partiċelli jistgħu jikkawżaw il-ħsara lill-magna, l-LHC huwa mgħammar b' numru ta' sistemi ta' protezzjoni. Is-sistema tal-kollimazzjoni tal-LHC għandha r-rwol li tferrex u tassorbi il-partiċelli li jinsabu fuq il-partijiet ta' barra tal-faxxa, qabel dawn jaħbtu mal-kalamiti superkonduttivi u jsaħħnuhom. Il-108 kollimatur installati fl-LHC jipproteġu l-magna wkoll minn telf veloċi tal-faxxa, kif ukoll strumenti vulnerabbli mir-radjazzjoni fuq medda ta' snin ta' operazzjoni. Kull kollimatur huwa magħmul minn żewġ blokok jew 'xedaq' magħmulin mill-karbonju, tungstenu jew ram. Dawn ix-xedaq iridu jitpoġġu b'mod simmettriku fuq kull naħa tad-direzzjoni tal-faxxa. B' dan il-mod, il-kollimaturi jistgħu jneħħu il-partiċelli tat-trufijiet tal-faxxa bl-ikbar effiċjenza. Iċ-ċentru u l-wisa' tal-faxxa fil-posizzjoni ta' kull kollimatur iridu jkunu magħrufin sabiex ix-xedaq jitpoġġu ċertu distanza miċ-ċentru tal-faxxa.

Proċedura ta' allinjament tintuża biex jinsabu il-valuri għaċ-ċentru u l-wisa' tal-faxxa. L-allinjament isir billi kull xedaq jitmexxa lejn il-faxxa b' distanza ta' 5 μm ma' kull moviment, sakemm tidher żieda qawwija fit-telf ta' partiċelli rrikordjat minn "Beam Loss Monitoring (BLM) detector", li hu installat madwar 2 metri wara kull kollimatur. Bilanċ irid jinstab bejn l-ammont ta' faxxa li titneħħa li jiżgura żieda ċara fis-sinjal tal-"BLM detector", evitar li l-faxex jitneħħew awtomatikament mill-LHC minħabba telfiet kbar ta' partiċelli, u tlestija tal-allinjament f' ħin qasir sabiex l-LHC tista' tiffoka fuq il-produzzjoni tal-luminożita'.

Fl-2010, inħtieġu kwazi 30 siegħa għal allinjament tal-kollimaturi kollha, u l-faxex tneħħew mill-LHC tmien darbiet minħabba żbalji ta' l-operaturi. Żvilupp u testijiet ta' algoritmi li saru f' fażijiet fuq medda ta' sentejn bejn l-2011 u l-2012

għenu sabiex il-ħin għall-allinjament naqas għal kważi 4 siegħat, u qatt ma reġgħu ntilfu l-faxex waqt l-allinjament. Dawn l-algoritmi jinkludu selezzjoni awtomatika ta' limiti għall-"BLM detectors" u "feedback loop" li twaqqaf il-moviment tax-xedaq meta t-telfiet huma ogħla mill-limitu, fost oħrajn. Il-"feedback loop" intuża wkoll mill-esperimenti ta' ALFA u TOTEM għal-allinjament tal-apparat tagħhom ("Roman Pots").

Inbena' ukoll "simulator" bil-MATLAB, ibbażat fuq mudell empiriku tas-sinjal tal-"BLM detector" meta dan ikun f' "steady-state" u meta jikkawża "crosstalk", u mudell tad-diffużjoni tal-faxxa li kapaċi jbassar il-forma taż-żieda u tnaqqis fis-sinjal tal-"BLM detector". Dan is-"simulator" jista' jintuża għal testijiet ta' algoritmi ġodda li kieku jeħtieġu testijiet dedikati bil-faxxa fl-LHC.

Disinn ġdid għall-kollimaturi se jkollu "Beam Position Monitors" (BPMs) imwaħħlin ġox-xedaq. Dawn il-BPMs se jipprovdu kejl preċiż taċ-ċentru tal-faxxa mingħajr il-bżonn tal-allinjament bil-"BLM detectors". Kwart tal-kollimaturi kollha fl-LHC (ċioè l-kollimaturi terzjarji u dawk sekondarji f' IR6) se jkollhom dan id-disinn, bħal ma kien imbassar għal diversi snin. Għalhekk, sar żvilupp ta' algoritmu li jpoġġi x-xedaq awtomatikament madwar iċ-ċentru tal-faxxa. Testijiet ta' dan l-algoritmu saru fis-"Super Proton Synchrotron" (SPS), fejn l-allinjament sar f' ħin ta' madwar 20 sekonda.

Ix-xogħol li sar f' din it-teżi ġie addottat minn CERN għall-ewwel perjodu ta' operazzjoni (2008 - 2013), u se jkompli jintuża wara sentejn ta' waqfien ta' operazzjoni, fejn l-komponenti tal-LHC ser jiġu aġġornati sabiex l-LHC tkun tista' topera bil-parametri nominali.

Acknowledgements

Contents

List of Figures

List of Tables

Nomenclature

Symbols

β_i amplitude of the β function at element i

β^* amplitude of the β function in the experimental insertion point

D_i dispersion function at element i

ϵ beam emittance

J_c collimator jaw centre

J_L left collimator jaw position

J_R right collimator jaw position

N_i half gap opening in units of beam σ specific to a collimator family

σ_i one standard deviation of the beam size at element i

S_i^{Thres} BLM stop threshold

$T_{average}$ average alignment time per collimator

T_{beam} beam time required for collimator alignment

T_{setup} total time required for collimator alignment

V_j BPM electrode signal for the jth jaw corner

$x_i^{L,m}$ left jaw setup position determined from BLM-based alignment

$x_i^{R,m}$ right jaw setup position determined from BLM-based alignment

X_{abs} beam offset with respect to an ideal orbit trajectory, measured from BPM-based alignment

Δx_i beam offset at collimator i with respect to an ideal orbit trajectory, measured from BLM-based alignment

Δx_i^{int} BPM-interpolated beam offset with respect to an ideal orbit trajectory at collimator i

X_{beam} actual beam position with respect to an ideal orbit trajectory

X_{bpm} beam offset with respect to an ideal orbit trajectory, measured from BPM-based alignment, relative to J_c

X_{raw} difference over sum of the measured BPM electrode signals

Acronyms

ADC Analogue-to-Digital Converter

$ALFA$ Absolute Luminosity For ATLAS

$ALICE$ A Large Ion Collider Experiment

$ATLAS$ A Toroidal LHC ApparatuS

$B1$ LHC Beam 1

$B2$ LHC Beam 2

BLM Beam Loss Monitoring

BPM Beam Position Monitor

CCC CERN Control Centre

CFC Carbon Fibre Composite

CMW Common Middleware

$CERN$ European Organization for Nuclear Research

CMS Compact Muon Solenoid

DIM Distributed Information Management

$FBCT$ Fast Beam Current Transformer

$FESA$ Front-End Software Architecture

$FPGA$ Field Programmable Gate Array

GUI Graphical User Interface

IC Ionization Chamber

IP Interaction Point

IR Insertion Region

LD Left Downstream Jaw Corner

$LEIR$	Low Energy Ion Ring
LHC	Large Hadron Collider
$LHCb$	LHC beauty
LSA	LHC Software Architecture
LU	Left Upstream Jaw Corner
$LVDT$	Linear Variable Differential Transformer
MD	Machine Development
MDC	Motor Drive Control
PRS	Position Readout Survey
PS	Proton Synchrotron
PSB	Proton Synchrotron Booster
QPS	Quench Protection System
RD	Right Downstream Jaw Corner
RF	Radio Frequency
RU	Right Upstream Jaw Corner
SPS	Super Proton Synchrotron
SVM	Support Vector Machine
$TCDQ$	Target Collimator Dump Quadrupole
TCP	Target Collimator Primary
$TCLA$	Target Collimator Long
$TCLA$	Target Collimator Long Absorber
$TCLI$	Target Collimator Long Injection Protection
$TCSG$	Target Collimator Secondary Graphite
TCT	Target Collimator Tertiary
TDI	Target Dump Injection
$TOTEM$	TOTal Elastic and diffractive cross-section Measurement
UDP	User Datagram Protocol

List of Publications

The following publications are the result of the work of this thesis.

Journals

1. G. Valentino, R. W. Assmann, R. Bruce, S. Redaelli, A. Rossi, N. Sammut, D. Wollmann, "Semiautomatic beam-based LHC collimator alignment", Phys. Rev. ST Accel. Beams 15, 015002 (2012).

2. G. Valentino, R. W. Assmann, R. Bruce, F. Burkart, V. Previtali, S. Redaelli, B. Salvachua, A. Valishev, "Beam diffusion measurements using collimator scans in the LHC", Phys. Rev. ST Accel. Beams 16, 021003 (2013).

3. G. Valentino, R. W. Assmann, R. Bruce, S. Redaelli, B. Salvachua, N. Sammut, D. Wollmann, "Operational results with fast automatic beam-based LHC collimator alignment", accepted for publication in Xjenza (2013).

4. G. Valentino, R. Bruce, M. Gasior, D. Mirarchi, A. Nosych, S. Redaelli, B. Salvachua, D. Wollmann, "Automatic BPM-based LHC collimator alignment", submitted to Phys. Rev. ST Accel. Beams (2013).

5. G. Valentino, R. W. Assmann, N. Sammut, "A simulator for LHC beam-based collimator alignment", submitted to Phys. Rev. ST Accel. Beams (2013).

Conferences

1. G. Valentino, R. W. Assmann, S. Redaelli, N. Sammut, D. Wollmann, "Semi-automatic beam-based alignment algorithm for the LHC collimation system". In Proceedings of IPAC'11, San Sebastian, Spain, pp. 3768-3770, 2011.

2. G.Valentino, R. W. Assmann, R. Bruce, F. Burkart, M. Cauchi, D. Deboy, S. Redaelli, A. Rossi, N. Sammut, D. Wollmann, "Comparison of LHC collimation setups with manual and semi-automatic collimator alignment". In Proceedings of IPAC'11, San Sebastian, Spain, pp. 3771-3773, 2011.

3. G. Valentino, R. W. Assmann, R. Bruce, N. Sammut, "Classification of LHC beam loss spikes using Support Vector Machines". In Proceedings of the IEEE 10th Jubilee International Symposium on Applied Machine Intelligence and Informatics, Herl'any, Slovakia, pp. 355-358, 2012.

4. G. Valentino, R. W. Assmann, R. Bruce, G. J. Müller, S. Redaelli, A. Rossi, N. Sammut, "Comparison of LHC collimator beam-based alignment centers to the BPM-interpolated orbit". In Proceedings of IPAC'12, New Orleans, USA, pp. 2062-2064, 2012.

5. G. Valentino, R. W. Assmann, F. Burkart, S. Redaelli, A. Rossi, N. Sammut, D. Wollmann, "Modeling and simulation of LHC beam-based collimator setup". In Proceedings of IPAC'12, New Orleans, USA, pp. 2059-2061, 2012.

6. G. Valentino, R. W. Assmann, R. Bruce, S. Redaelli, N. Sammut, D. Wollmann, "Automatic computer algorithms for beam-based setup of the LHC collimators". In Proceedings of ICAP'12, Rostock-Warnemunde, Germany, pp. 15-19, 2012 (invited talk).

7. G. Valentino, R. W. Assmann, R. Bruce, G. J. Müller, S. Redaelli, B. Salvachua, N. Sammut, "A tool based on the BPM-interpolated orbit for speeding up LHC collimator alignment". In Proceedings of HB2012, Beijing, China, pp. 162-165, 2012.

8. G. Valentino, R. W. Assmann, R. Bruce, S. Redaelli, N. Sammut, "Automatic threshold selection for BLM signals during LHC collimator alignment". In Proceedings of the Sixth UKSim/AMSS European Symposium on Computer Modeling and Simulation (EMS), Valletta, Malta, pp. 210-213, 2012.

9. G. Valentino, R. W. Assmann, M. Gasior, S. Redaelli, N. Sammut, D. Wollmann, "Development and beam tests of an automatic algorithm for alignment of LHC collimators with embedded BPMs". In Proceedings of IPAC'13, Shanghai, China, pp. 3349-3341, 2013.

10. G. Valentino, R. W. Assmann, D. Jacquet, S. Redaelli, E. Veyrunes, "Online status and settings monitoring for the LHC collimators". Accepted for publication at ICALEPCS'13, 2013.

11. G. Valentino, R. W. Assmann, S. Redaelli, N. Sammut, "LHC collimator alignment operational tool". Accepted for publication at ICALEPCS'13, 2013.

12. G. Valentino, R. W. Assmann, R. Bruce, S. Jackson, S. Redaelli, B. Salvachua, N. Sammut, D. Wollmann, C. Zamantzas, "Fast automatic beam-based alignment of the LHC collimation system". Accepted for publication at ICALEPCS'13, 2013.

Workshops

1. G. Valentino, R. W. Assmann, G. Bellodi, R. Bruce, F. Burkart, M. Cauchi, D. Deboy, J. M. Jowett, S. Redaelli, A. Rossi, B. Salvachua, D. Wollmann, "Multi-turn losses and cleaning in 2011 and 2012". In Proceedings of the 3rd Evian Workshop on LHC Beam Operation, Evian, France, pp. 111-116, 2011.

2. G. Valentino, R. Bruce, S. Redaelli, "Collimator settings generation, management and verification". In Proceedings of the 2nd LHC Machine Protection Workshop, Annecy, France, 2013.

Chapter 1

Introduction

1.1   CERN and the Large Hadron Collider

CERN is the largest particle physics laboratory in the world, straddling the Franco-Swiss border near Geneva in Switzerland. It gathers together physicists, engineers and computer scientists from around the globe to focus their efforts on non-military fundamental research. CERN was launched as a provisional body in 1952, and the original acronym in French stood for *Conseil Européen pour la Recherche Nucléaire*. At the official founding in 1954, the Council was dissolved, and the new organization was given the title European Organization for Nuclear Research.

The Large Hadron Collider (LHC) is CERN's flagship particle accelerator. It is a synchrotron capable of accelerating and colliding proton beams, each at a nominal energy of 7 TeV per beam, with a design luminosity of $10^{34} \text{cm}^{-2}\text{s}^{-1}$ at a bunch collision rate of 40 MHz [1]. The LHC has a circumference of 27 km, and is housed in a tunnel approximately 100 m underground. It is fed by a series of linear and circular accelerators depending on the particle type (protons or heavy ions). An overview of the CERN accelerator complex is depicted in Fig. 1.1.

Protons are generated by a Duoplasmatron Proton Source, which ionizes hydrogen atoms and directs them into Linac2, a linear accelerator. Linac2 accelerates the protons to an energy of 50 MeV, before transferring them to the Proton Synchrotron Booster (PSB). If heavy-ion beams are required, lead ions from a source of vaporized lead are placed in Linac3. These are then accelerated and directed to the Low Energy Ion Ring (LEIR) [2]. Particles from both the proton and heavy-ion pre-injectors are then separately inserted into the Proton Synchrotron (PS). In the PS, particles are accelerated further to 25 GeV, and are then fed into the Super Proton Synchrotron (SPS). Two particle beams, beam 1 (B1) and beam 2 (B2) are injected into the LHC from the SPS at an energy of 450 GeV via the transfer lines TI2 and TI8 respectively.

The LHC consists of eight arcs, each made up of 23 focusing and defocusing quadrupole magnets separated by dipole magnets (FODO cells), and eight straight
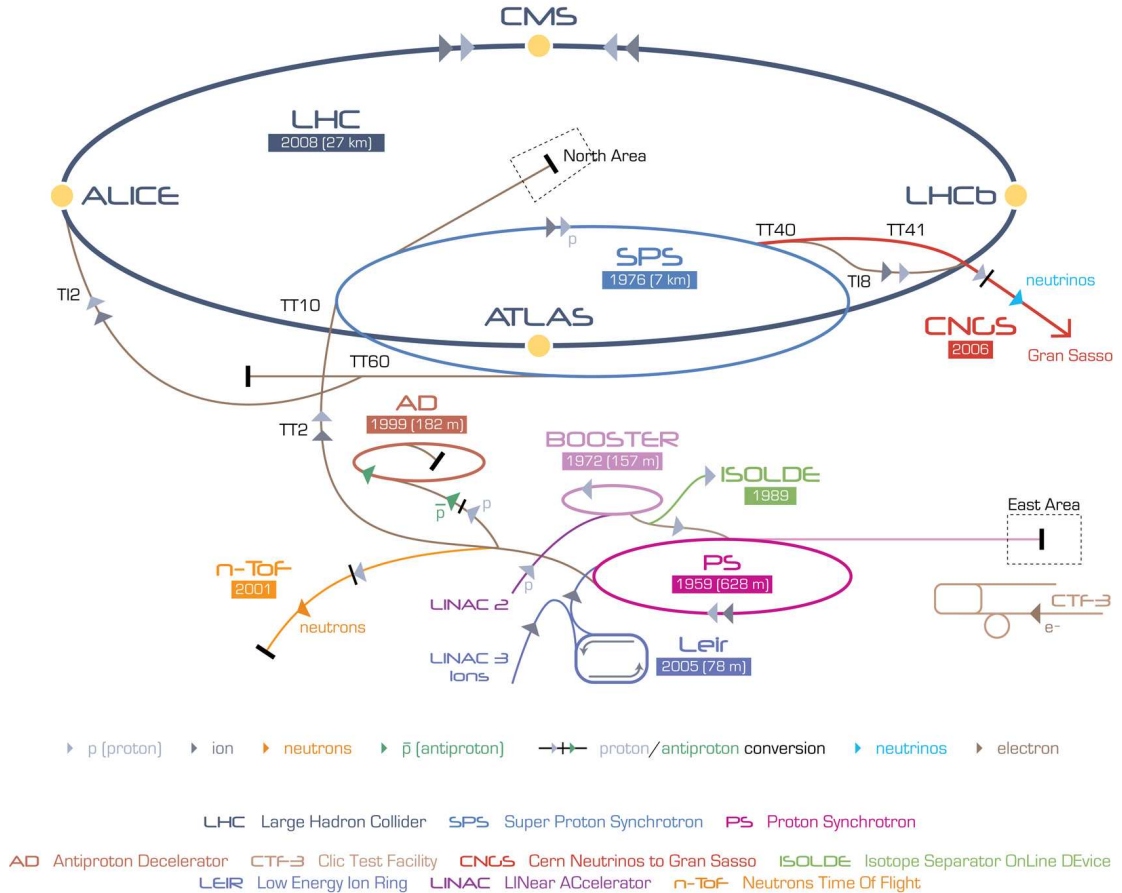
Figure 1.1: The CERN accelerator complex, showing in particular the chain of accelerators from the injector Linac up to the LHC (not to scale).

sections (insertion regions). Each insertion region (IR) houses an experimental region or a utility insertion (see Fig. 1.2). The four main experiments (ATLAS, ALICE, CMS and LHCb) are located at Interaction Points (IPs) 1, 2, 5 and 8 respectively, where the beams are brought into collisions [3]. The ATLAS [4] (A Toroidal LHC ApparatuS) and CMS [5] (Compact Muon Solenoid) detectors are designed for high-luminosity experiments related to the Higgs boson [6] discovery[1] and supersymmetry [8]. ALICE [9] (A Large Ion Collider Experiment) is used to investigate the physics of strongly interacting matter and quark-gluon plasma in heavy ion collisions, while the LHCb [10] (LHC beauty) experiment studies CP-violation and hadron decays with rare flavours, such as B-mesons [8]. Other experiments include ALFA [11] (Absolute Luminosity For ATLAS), which measures elastic proton-proton scattering and small angles in the Coulomb-Nuclear Interference region, and TOTEM [12] (TOTal Elastic and diffractive cross-section Measurement), an experiment which measures total cross-section, elastic scattering and diffractive processes. These experiments rely on Roman Pots [13] to conduct measurements, and are installed in IP1 and IP5 respectively.

---

[1]The ATLAS and CMS experiments announced the discovery of a new, Higgs-like particle on 4th July 2012 [7].
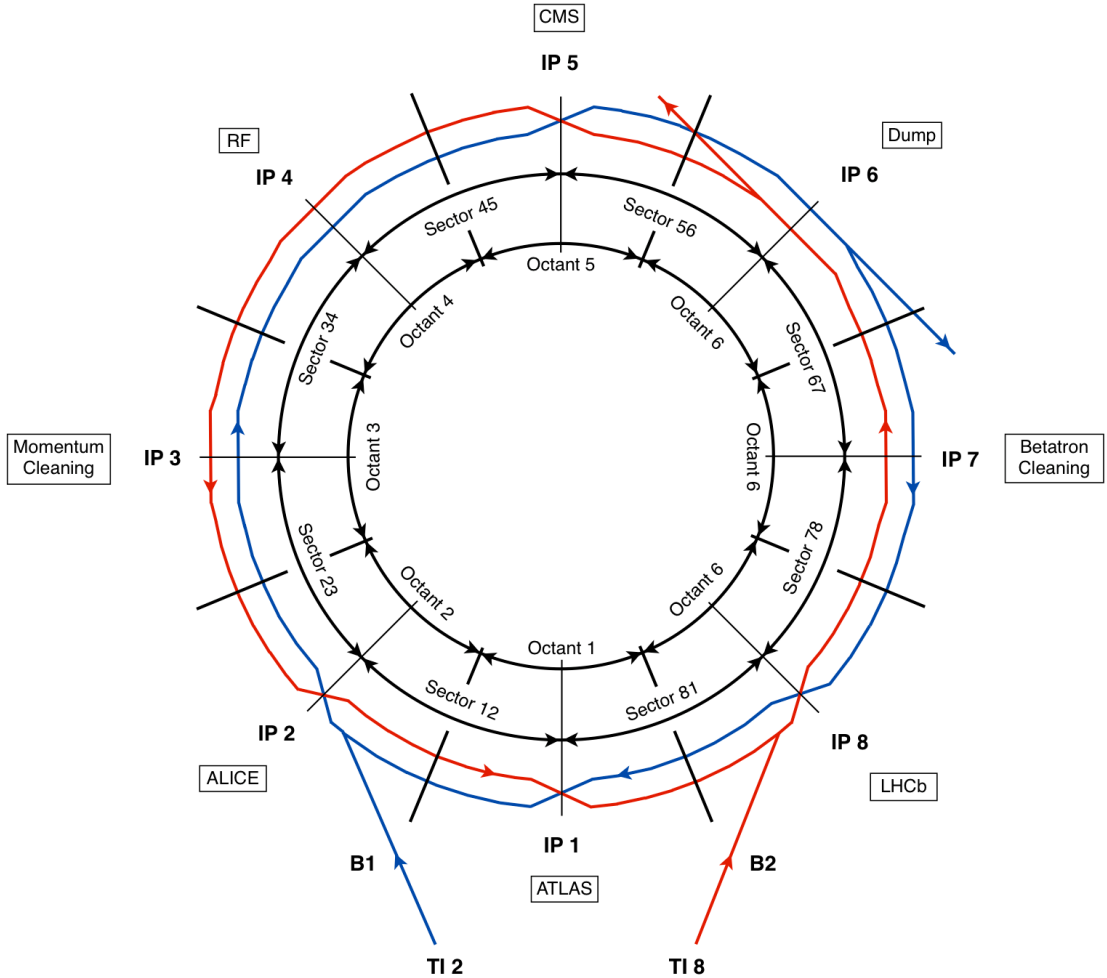
Figure 1.2: The layout of the Large Hadron Collider. Beam 1 circulates in a clockwise direction, while Beam 2 circulates counterclockwise. The beams can be brought into collisions at four interaction points: ATLAS (IP1), ALICE (IP2), CMS (IP5) and LHCb (IP8).

The radio frequency (RF) cavities placed in IR4 are used to accelerate the beams in bunches of $\sim 1.15 \times 10^{11}$ particles each. The electric field of the RF cavities, which provides the accelerating force to the particles, is synchronized with the ramp in the magnetic field of the superconducting magnets so that the particles maintain their orbit around the LHC ring. Hence, the LHC is known as a synchrotron. Photographs of the RF cavities and the superconducting magnets are shown in Fig. 1.3 and Fig. 1.4 respectively.

At the end of a physics fill or in the event of operational problems the beams can be extracted in IR6, where a septum magnet can be triggered to deviate the beams and deposit them on a solid carbon block outside the LHC main ring. This occurs automatically as software interlocks are triggered by the operator or by the components which cause the failure. Collimators are mainly located in

two cleaning insertions, IR3 and IR7, and provide cleaning of particles with large momentum and betatron offsets respectively. They also protect the beam dump, injection and transfer line regions of the LHC.
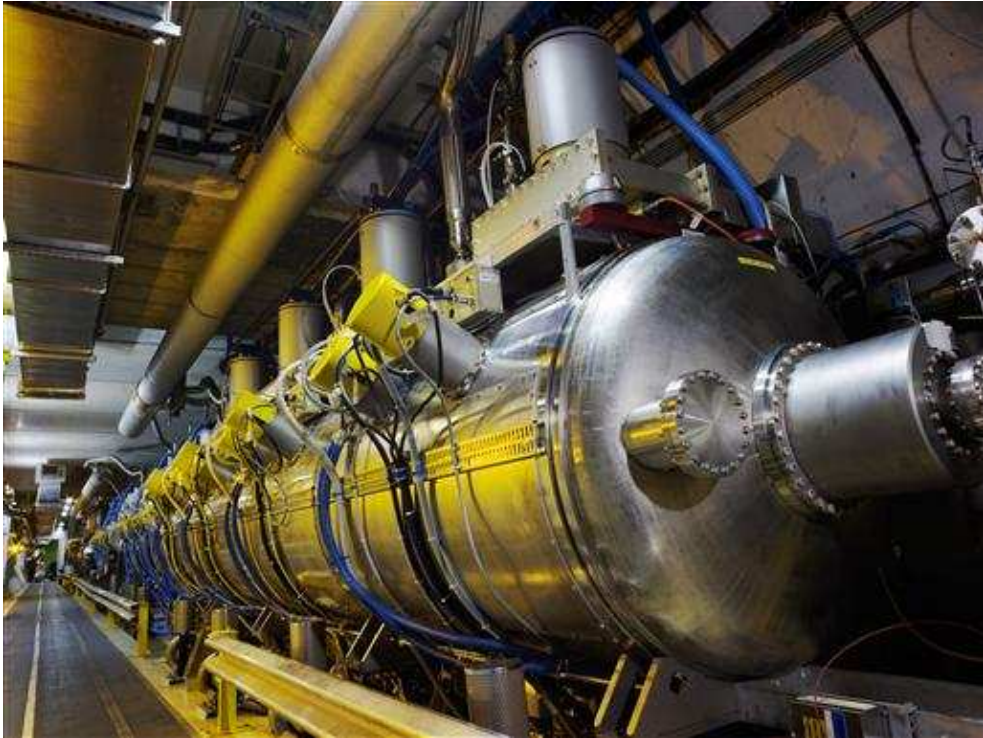
Figure 1.3: RF cavities in IP4, from [14].
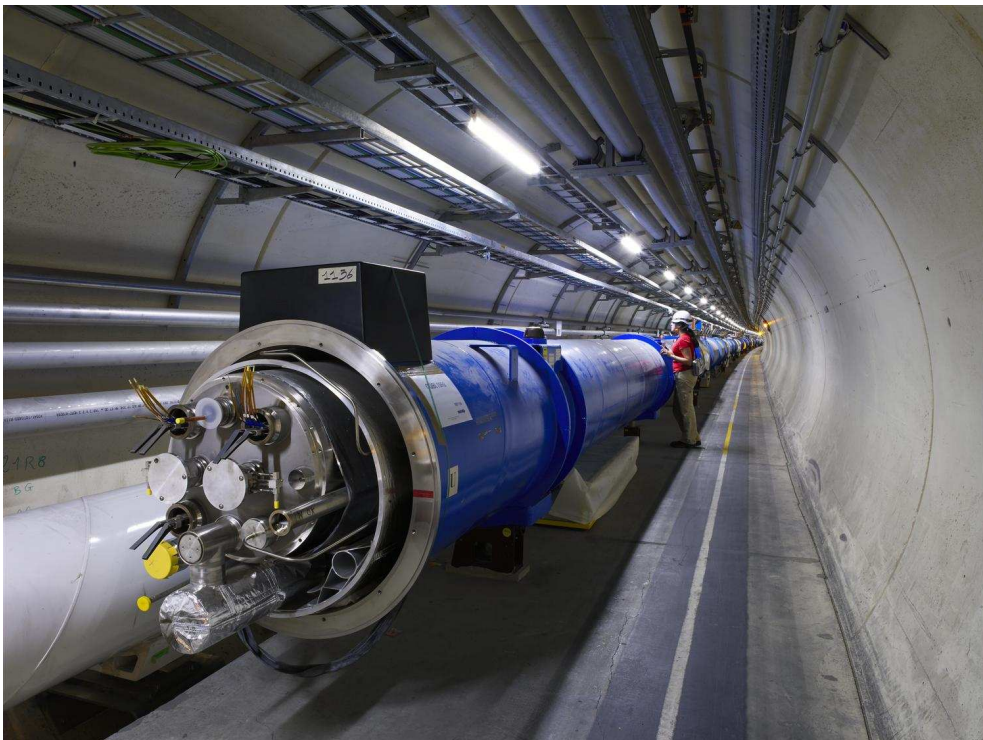
Figure 1.4: Superconducting magnets near the ATLAS experiment, from [15].

Proton beams were first injected into the LHC on the 10th September 2008. This was followed by a commissioning phase, which involves ensuring the correct operation of all the machine sub-systems and fine-tuning accelerator devices to allow the LHC to achieve nominal operation [16]. Table 1.1 and Table 1.2 show the nominal LHC parameters for proton and heavy ion beams respectively.

Table 1.1: Nominal LHC parameters for proton beams [17].

Beam Parameters	Nominal Values	
	Injection	Collisions
Energy [GeV]	450	7000
Relativistic γ	479.6	7461
Number of particles per bunch	1.15×10^{11}	
Number of bunches per beam	2808	
Stored energy per beam [MJ]	23.2	362
Bunch spacing [ns]	25	
Transverse normalized emittance [μm]	3.75	
Longitudinal emittance ($4\ \sigma$) [eV s]	1	2.5
Revolution frequency [kHz]	11.245	
β_z^* at IP1 and IP5 [m]	11	0.55
β_z^* at IP2 [m]	10	
β_z^* at IP8 [m]	10	1-50
Peak Luminosity in IP1 and IP5 [cm^{-2}s^{-1}]	-	10^{34}

Table 1.2: Nominal LHC parameters for heavy ion beams [17].

Beam Parameters	Nominal Values	
	Injection	Collisions
Energy [GeV]	36900	7000
Energy per nucleon [GeV]	177.4	2759
Relativistic γ	190.5	2963.5
Number of particles per bunch	7×10^7	
Number of bunches per beam	592	
Stored energy per beam [MJ]	0.245	3.81
Bunch spacing [ns]	100	
Transverse normalized emittance [μm]	1.5	
Longitudinal emittance ($4\ \sigma$) [eV s]	0.7	2.5
Revolution frequency [kHz]	11.245	
β_z^* at IP1 and IP5 [m]	11	0.55
β_z^* at IP2 [m]	10	0.5
β_z^* at IP8 [m]	10	1-50
Peak Luminosity in IP2 [cm^{-2}s^{-1}]	-	10^{27}

The LHC and its injector chain are operated remotely from the CERN Control Centre (CCC). Four 'islands', each equipped with monitors and switches allow the operators on shift to access and control many of the accelerator sub-systems. The LHC island is shown in Fig. 1.5.

Figure 1.5: The LHC island in the CERN Control Centre.

1.2 Linear beam dynamics

A single particle with charge q travelling in a static electromagnetic field is subject to the Lorentz force:

$$\vec{F} = q(\vec{E} + \vec{v} \times \vec{B}) \tag{1.1}$$

where $\vec{E}$ is the electric field component (which acts along the direction of motion), $\vec{B}$ is the magnetic field component (which acts perpendicular to the direction of motion) and $\vec{v}$ is the particle velocity. This gives rise to longitudinal and transverse motion, which are collectively known as linear beam dynamics.

1.2.1 Longitudinal motion

In the presence of a sinusoidally varying electric field of an RF cavity, a charged particle gains an energy ΔE and is accelerated each turn [18]:

$$\Delta E = q\hat{V}_{RF} \sin \omega_{RF} t \tag{1.2}$$

where $\hat{V}_{RF}$ is the peak accelerating potential and ω_{RF} is the angular frequency of the RF cavity. Hence, $\phi_0 = \omega_{RF}t$ is the phase of the particle with respect to that of the RF cavity. For the special case of $\phi_0 = 0$, the particle maintains constant energy turn after turn. In the case of $\phi_0 > 0$, the particle is accelerated, while if $\phi_0 < 0$, the particle is decelerated. The particle which circulates with a constant phase ϕ_s turn after turn is known as the synchronous particle. In practice, there exists a phase distribution centred around ϕ_s, and particles oscillate around the phase of the synchronous particle turn after turn. An illustration is provided in Fig. 1.6.
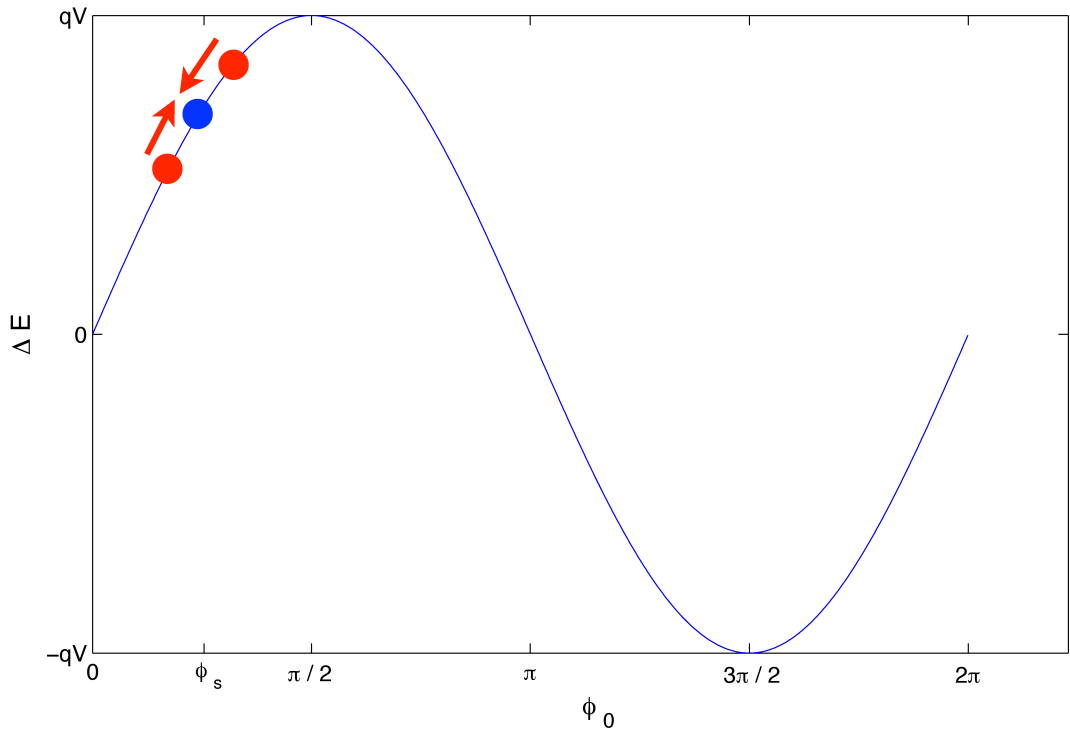
Figure 1.6: The sinusoidally varying electric field, showing the location of the synchronous particle (blue) and other particles (red) oscillating around the synchronous particle.

To ensure that the particles always see an accelerating voltage when they transit the RF cavity, the alternation frequency of the electric field has to be an integer multiple of the LHC revolution frequency:

$$h = \frac{f_{RF}}{f_{rev}} \tag{1.3}$$

Each period of the electric field is known as an RF bucket. For a selected frequency of 400 MHz, and a revolution frequency of 11.245 kHz, a maximum number of 35,571 RF buckets are available. However, a number of consecutive RF buckets (known as the abort gap) must be left empty to allow enough time for kicker magnets in IR6 to fire and remove the beam from the LHC in the event of a beam dump. This, together with other constraints, such as long range beam-beam interactions, minimum bunch spacing induced by electron-cloud, total beam power and the collimation cleaning efficiency, leaves a total of 2808 occupied bunches [19].

1.2.2 Transverse motion

Dipole magnets are used to bend particles, while focusing and defocusing quadrupole magnets keep the beam focused along the desired trajectory. The quadrupole magnet fields cause the particles to perform betatron oscillations in a simple harmonic motion fashion. Hence, the motion can be expressed using the Hill's equation, assuming no momentum spread (i.e. $\Delta p/p = 0$):

$$z''(s) + K(s)z(s) = 0 \tag{1.4}$$

where z represents the x or y plane, s is the longitudinal coordinate and K is the quadrupole focusing strength. The general solution of the Hill's equation is:

$$z(s) = \sqrt{\epsilon_z \beta_z(s)} \cos(\phi_z(s) + \phi_{z0}) \tag{1.5}$$

where $\beta_z(s)$ is the amplitude modulation of the betatron oscillation, ϵ_z is the emittance, ϕ_z and ϕ_{z0} are the phase advance and the initial phase of the betatron oscillation respectively. Differentiating Eq. (1.5) with respect to s yields:

$$z'(s) = -\sqrt{\frac{\epsilon_z}{\beta_z(s)}} \sin(\phi_z(s) + \phi_{z0}) \tag{1.6}$$

By obtaining the so-called Twiss parameters from Eq. (1.5):

$$\alpha_z(s) = -\frac{1}{2}\beta'_z(s) \tag{1.7}$$

$$\beta_z(s)$$

$$\gamma_z(s) = \frac{1 + \alpha_z^2(s)}{\beta_z(s)}$$

one can obtain an expression for the occupied phase space volume (beam emittance):

$$\epsilon_z = \gamma_z(s)z^2(s) + 2\alpha_z(s)z(s)z'(s) + \beta_z(s)z'^2(s) \tag{1.8}$$

The number of betatron oscillations per revolution, or machine tune Q_z, is calculated by dividing the phase advance over one turn by 2π. In practice, a momentum spread exists, which means that the particles do not transit the quadrupoles at a fixed radial position. If $\Delta p/p \neq 0$, then Eq. (1.5) becomes:

$$z(s) = \sqrt{\epsilon_z \beta_z(s)}\cos(\phi_z(s) + \phi_{z0}) + D_z(s)\delta_p \tag{1.9}$$

where $\delta_p = \Delta p/p$ is the momentum offset and D_z is the dispersion. The momentum spread also introduces a tune spread, which can be calculated in terms of the chromaticity ξ_z:

$$\Delta Q_z = \xi_z \frac{\Delta p}{p} \tag{1.10}$$

High-energy particle beams are generally considered as having a Gaussian distribution of particles in the transverse plane. One standard deviation of the Gaussian beam, comprising $\sim$68% of all particles, is known as 1 σ. The beam core is usually defined as 0 - 3 σ (99.7% of all particles), while the region $> 3\,\sigma$ is known as the beam halo, as illustrated in Fig. 1.7. Including the dispersion contribution, the betatronic 1 σ beam size can be expressed in terms of the r.m.s. emittance as:

$$\sigma_z(s) = \sqrt{\epsilon_{rms,z}\beta_z(s) + (D_z(s)\sigma_p)^2} \tag{1.11}$$
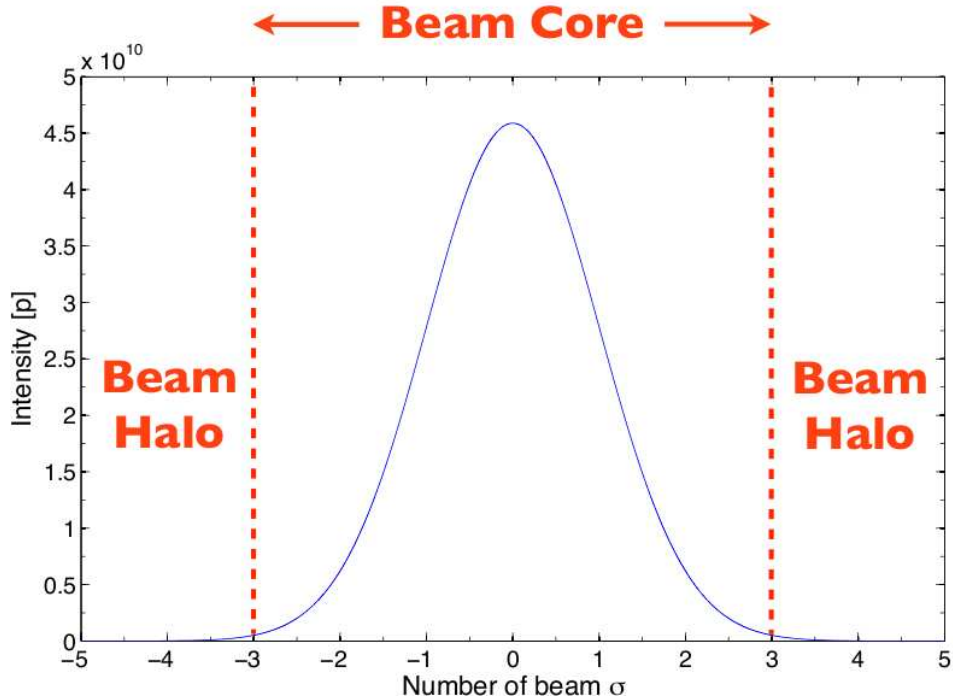
Figure 1.7: The Gaussian distribution of a particle beam made up of 1 nominal bunch (1.15×10^{11} p), showing the core and halo regions.

The geometric emittance is proportional to the Lorentz factor γ, which is the ratio of the current and rest particle energy ($\gamma = E/E_0$):

$$\epsilon_{geom} = \frac{\epsilon_{norm}}{\gamma} \tag{1.12}$$

Hence, for conserved normalized emittance, the 1 σ beam size decreases with the square root of the energy. This effect is known as adiabatic damping.

1.3 LHC machine operation

The operation of the LHC follows well-established stages, which together form a machine cycle. A typical LHC machine cycle is shown in Fig. 1.8. At the *injection* stage (1), the LHC receives two beams from the SPS at an energy of 450 GeV per beam. The beams arrive in bunch trains, which may consist of 1 - 144 bunches, depending on whether the machine is to be filled for beam tests or physics. When the filling procedure is completed, both beams are *ramped up* (2) until the desired energy (3.5 TeV in 2010-2011; 4 TeV in 2012-2013; 7 TeV for nominal operation). At *flat top* (3), the machine operators initiate the *beam squeeze* procedure (4), in
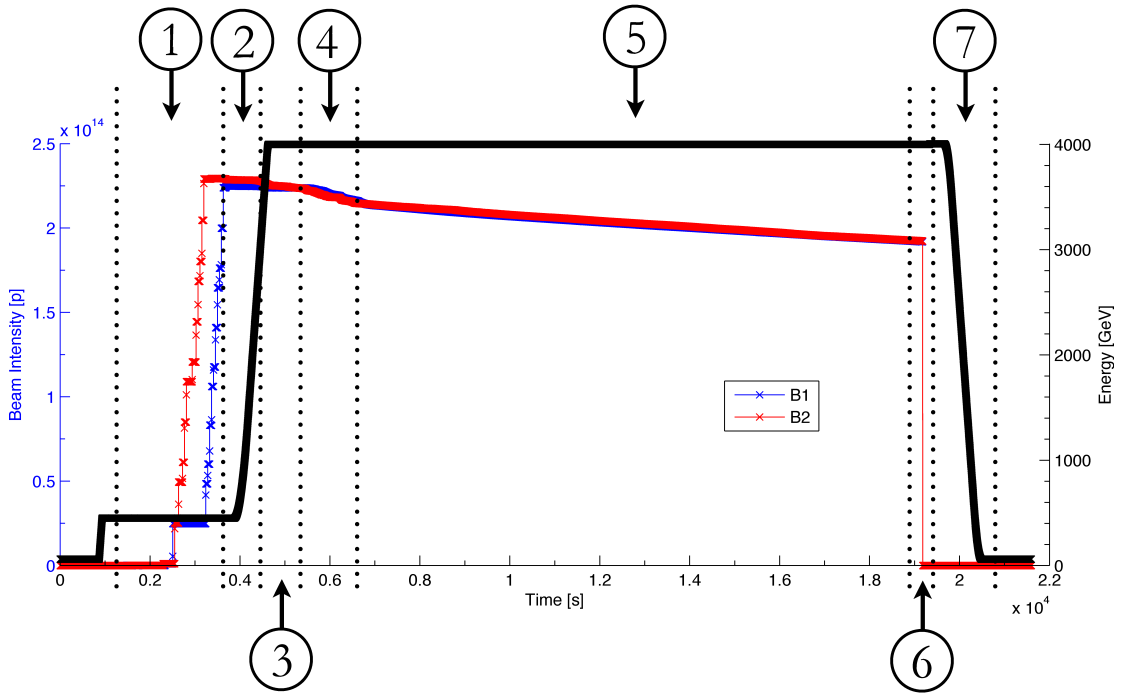
Figure 1.8: The LHC machine cycle, illustrated by the beam energy and beam intensities taken from fill number 3131 (t[0] = 05.10.2012 01:00:00). There are seven stages: 1) injection; 2) ramp; 3) flat top; 4) squeeze; 5) stable beams; 6) beam dump; 7) ramp down.

which corrector magnets are used to shrink the beam size at the experimental IPs to achieve the desired β^* (the β-function at the experimental IPs).

Up to this point, the beams are separated by several σ in all IPs. Hence, the final step is to collapse the separation orbit bumps and bring the beams into collisions. The operational state known as *stable beams* (5) is declared, and the experiments begin taking data. An illustration of the squeezed beams colliding in IP1 is shown in Fig. 1.9.
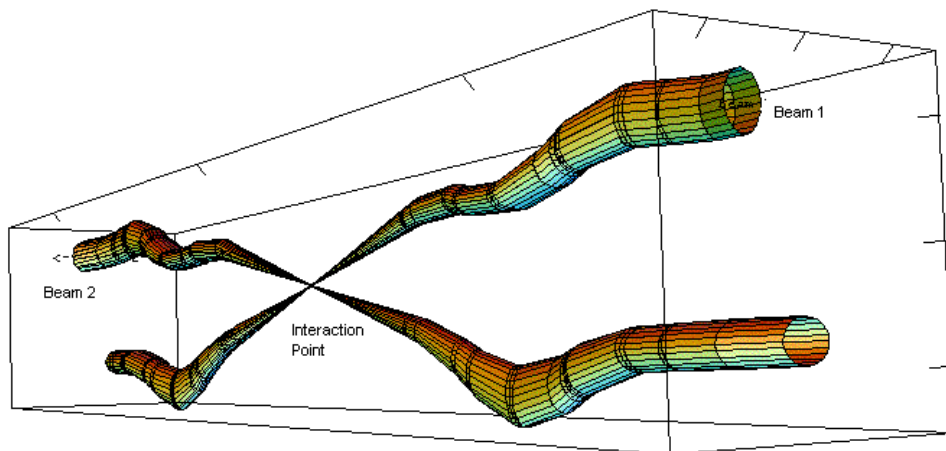
Figure 1.9: Illustration of squeezed beams in the LHC, colliding in IP1, from [20].

The beams may be extracted or *dumped* (6) at any point during the fill due to operational requirements, equipment failures, beam instabilities or operator mistakes. When this happens, the machine is *ramped down* (7) to injection energy in preparation for the next fill. The data presented in Fig. 1.8 are taken from fill number 3131, in which a total of 1374 bunches were present in the machine, and $130 \times 10^3 \, \mu\text{b}^{-1}$ of luminosity was delivered to the ATLAS and CMS experiments in 3.5 hours of stable beams. The average time spent in stable beams in the 2012 run was 6 hours [21]. The objective of the LHC is to achieve the maximum luminosity $\mathcal{L}$ possible, which is a measure of the count rate at the experiments, and is inversely proportional to the β^*:

$$\mathcal{L} = \frac{N_b^2 n_b f_{rev} \gamma}{4\pi \varepsilon_n \beta_z *} F \tag{1.13}$$

where N_b is the number of particles per bunch, n_b is the number of bunches in each ring, f_{rev} is the revolution frequency, ϵ_n is the normalized emittance and F is the geometric luminosity reduction factor which varies inversely with the beam crossing angle in the experimental IPs [1].

1.4 Thesis organization

This dissertation is structured as follows. An introduction to CERN and the LHC, including its design parameters, was provided in Chapter 1. An overview of basic linear beam dynamics in the longitudinal and transverse planes was given, including an explanation of the beam structure. This was followed by the LHC machine cycle and the different stages that need to be completed until the collider can start producing physics data.

The collimation system is expanded upon in detail in Chapter 2. The design of the collimation system as a multi-stage, multi-turn beam cleaning system is described, together with the software architecture that allows for operation of individual collimators. The generation of collimator settings for LHC operation is discussed.

An overview of two beam monitoring systems, which provide measurements of beam losses and beam positions at defined locations around the ring, is given in Chapter 3. The measurements from both systems are used by the alignment algorithms to perform the beam-based collimator setup.

The domain of the problem, namely beam-based collimator alignment, is presented in Chapter 4. The series of requirements that need to be met before commencing an alignment, as well as the alignment procedure itself, are described. The beam loss map technique for qualifying the beam-based values determined during an alignment is explained. Finally, the motivation for having fast and automatic alignment, as well as collimator alignment techniques used at other colliders are presented.

Chapter 5 starts off with a formal description of the problem, which is followed by a description of the design of several algorithms used to achieve the goals of this thesis. These include a BLM-based feedback loop, pattern recognition of BLM signal spikes, automatic selection of BLM thresholds, a coarse BPM-interpolation based algorithm and an alignment task sequencer. Finally, a validated algorithm for aligning a new collimator design based on feedback from BPMs is described.

The software development methodology and tools used to design, implement and commission the algorithms are explained in Chapter 6. This is followed by implementation details related to the two software applications and a collimator system fixed display.

A model and simulator of the beam loss signals during collimator alignment is presented in Chapter 7. The objective of the simulator is to be able to test future alignment algorithms without requiring dedicated and expensive beam time. The model is based on an empirical model of the BLM signal steady-state and crosstalk, and a diffusion model of the beam, which accurately predicts the signal spike and temporal decay when a jaw touches the beam.

Results from both simulations and operations are given in Chapter 8. Simulations are performed for various beam energies and collimator settings. The alignment performance over 4 years of operation is presented, for both proton and heavy ion beams.

Finally, Chapter 9 summarizes the achievements of the work, and provides some concluding remarks and suggestions for possible future work.

Chapter 2

The LHC Collimation System

2.1 Scope and layout of the collimation system

With a nominal stored energy of 362 MJ and a beam momentum of 7 TeV/c, the LHC is two orders of magnitude beyond other proton-proton colliders such as the Tevatron (Fermilab, USA) and HERA (DESY, Germany), as shown in Fig. 2.1. Uncontrolled beam losses of only 7.6×10^6 $ps^{-1}m^{-1}$ in a superconducting magnet can induce enough heating to cause a quench[1] [22]. This amounts to $\sim 2.5 \times 10^{-6}\%$ of the total circulating intensity of 3×10^{14} protons.
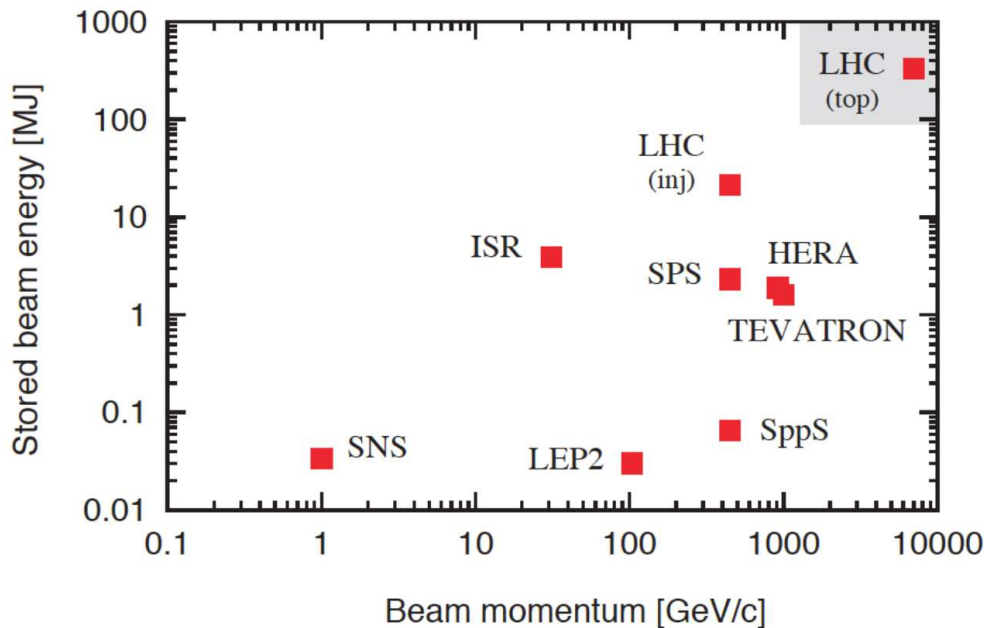
Figure 2.1: Stored beam energy in circular colliders as a function of the momentum [23].

As in any other synchrotron, the LHC is susceptible to beam losses deriving from normal or abnormal conditions [24, 25]. Normal losses are the unavoidable product of beam dynamics processes. Dynamic processes such as intrabeam scattering

---

[1]A magnet quench induced by beam losses is due to the deposition of energy in the superconducting coils, causing a temperature rise. The coils enter a resistive state, and the energy in the high magnetic field is converted into additional heat, which can damage the magnet and surrounding devices.

(IBS), scattering with residual gas molecules, beam-beam and synchrotron radiation all contribute to a slow, multi-turn drift of particles from the beam core to the beam halo regions. On the other hand, abnormal losses arise from equipment failures or operational errors. Abnormal scenarios include single-turn processes, such as injection errors (e.g. transverse mismatch of the beam) and beam dump errors (e.g. mis-firing of the extraction kicker magnets). Failures of equipment, such as the RF system, vacuum system and inadvertent insertion of movable components may also occur, but produce slower losses in the range of a few turns up to a few seconds.

For these reasons, the LHC needs to be protected from damage in case of beam losses. The collimation system serves this purpose by scattering and absorbing the beam halo, which consists of particles furthest away from the beam core [24]. It is designed to operate with both proton-proton and nucleus-nucleus beams, providing a cleaning efficiency of 99.998% of all halo particles. The machine aperture is also protected from single-turn abnormal losses, such as mis-kicked beams during injection and dump. The collimation system provides the following functionality [17]:

- Efficient cleaning of the beam halo throughout the LHC beam cycle, so that quenches of the superconducting magnets are avoided.

- Passive protection of the machine aperture against radiation effects which might damage other hardware such as electronics.

- Reduction of the halo-induced backgrounds in the experiments.

- Scraping of beam tails and diagnostics of halo population.

- Abort gap cleaning to avoid spurious quenches after normal beam dumps.

The LHC collimation system advances the state of the art found at the Tevatron [26] and RHIC [27]. It consists of 108 collimators, of which 86 are located in the LHC ring. Dedicated collimation insertions in IR3 and IR7 are required due to space, orbit configuration and radiation constraints, with the remaining IRs being taken up the experimental detectors, RF cavities and beam dump system. The collimation system is designed as a hierarchical system spread over four levels. Figure 2.2 gives a graphical overview of the collimator layout.
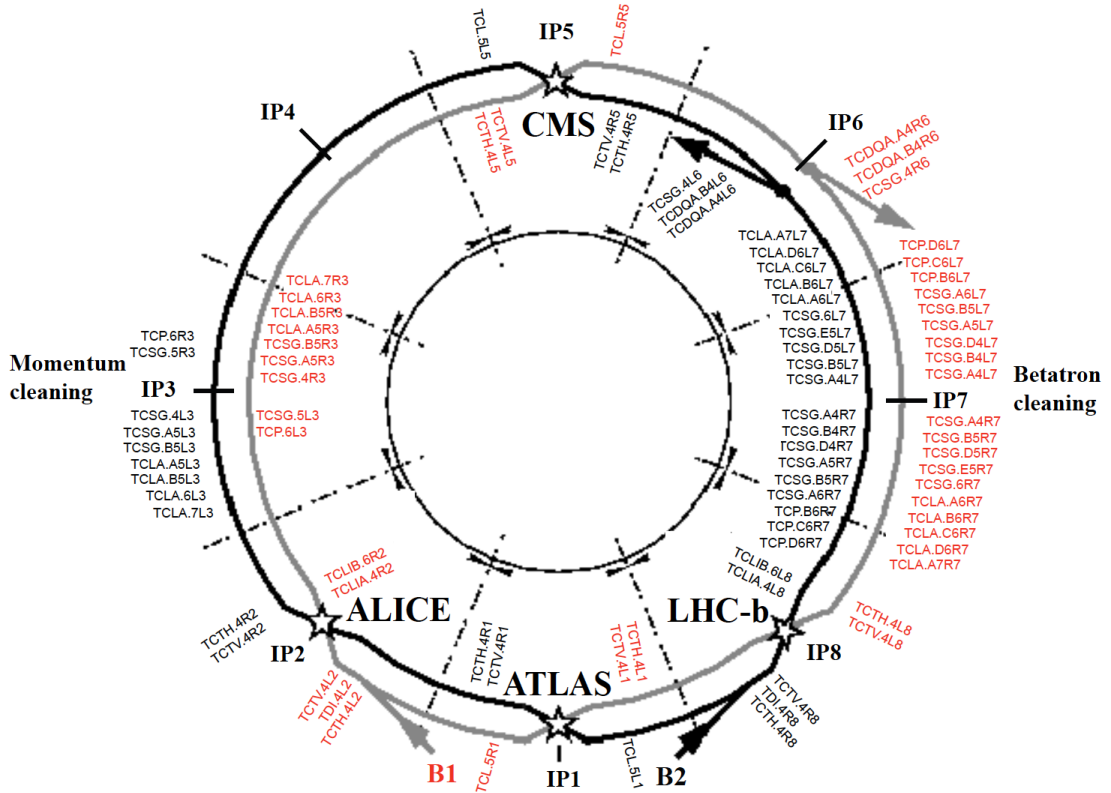
Figure 2.2: The LHC collimation system layout [25]. The majority of the collimators are located in the momentum and betatron cleaning regions (IR3 and IR7). Collimators are also positioned to protect the triplet magnets in the experimental IPs and in the dump and transfer regions.

For maximal cleaning efficiency, it is important to maintain the hierarchy at all times during the LHC beam cycle. The hierarchy can be established if the beam centres and beam sizes at the collimators are known. In the four-stage hierarchy, the primary collimator (TCP) is positioned closest to the beam in units of σ (see Fig. 2.3). The secondary collimators (TCSG) are retracted further, followed by the tertiary collimators (TCT) and the absorbers (TCLA), which are positioned furthest from the beam. The TCDQ is a single-jaw collimator which protects the beam dump region by absorbing the beam swept over the mechanical aperture in the event of an asynchronous beam dump [28].

An LHC collimator consists of two parallel blocks of carbon fibre composite (CFC), tungsten (W) or copper (Cu) material placed between the beam and the geometric aperture of the machine (see Fig. 2.4a and Fig. 2.4b). Described as *jaws*, they scatter and absorb halo particles that can damage the LHC. A collimator can clean in either of the horizontal, vertical or skew planes, depending on the rotation angle of the jaws. The jaws, identified conventionally as *left* and *right*, are housed in a tank, which is kept under vacuum.
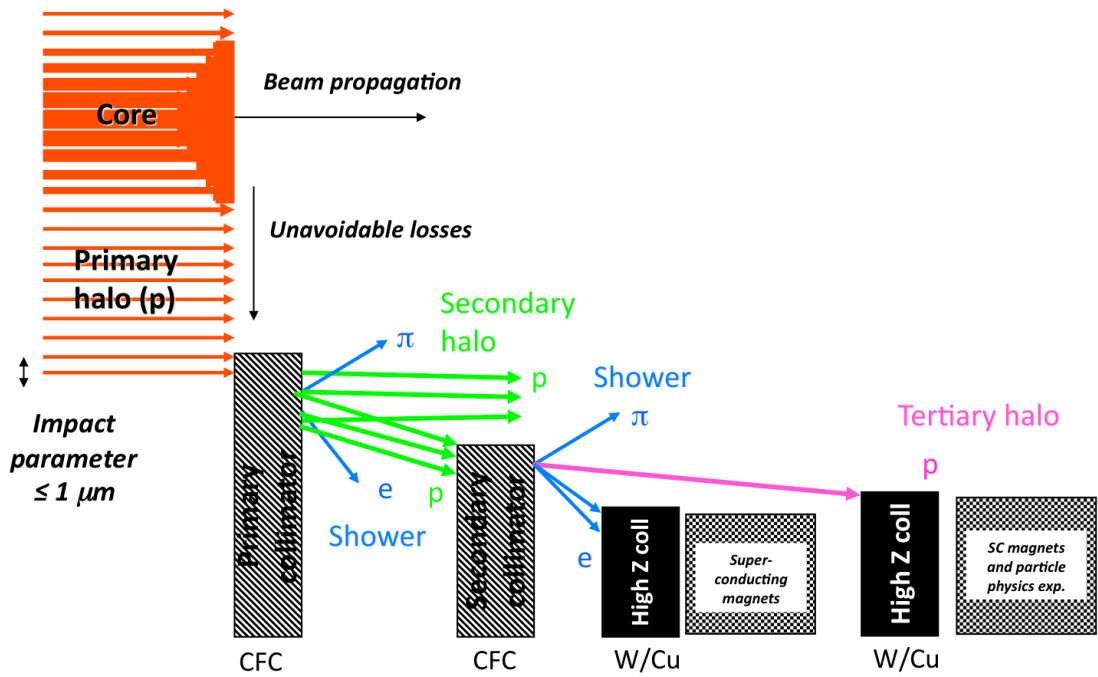
Figure 2.3: LHC multi-stage beam cleaning [29]. The primary halo is scattered by the TCPs. The secondary shower leaving the primary collimators is then scattered further by secondary TCSG and tertiary TCT collimators, until it is absorbed by TCLAs.
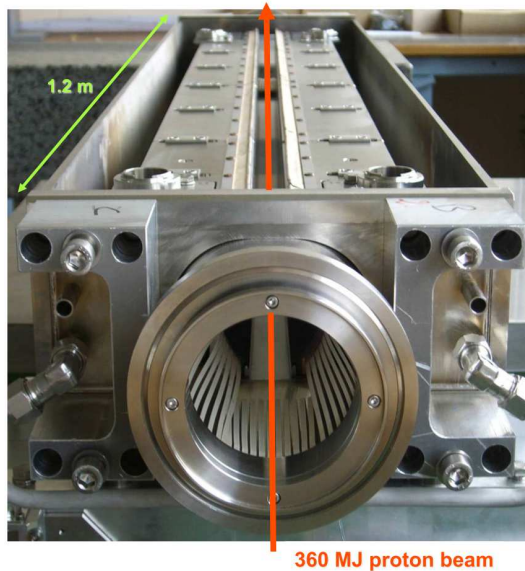
(a) LHC collimator viewed from one end [30]

(b) A single collimator jaw

Figure 2.4: Collimator jaws housed within the tank prior to installation (a) and a single collimator jaw (b). The red arrow denotes the beam trajectory in both cases.

The transverse rotation of the collimators follows the LHC clockwise coordinate system (see Fig. 2.5), where the zero angle lies along the negative x-axis. Hence, for a vertical collimator, the left jaw would be positioned above the beam, and the right jaw would lie below the beam. The jaws must be positioned symmetrically around the beam with one jaw on each side. Schematics showing the collimator coordinate system and angular tilt convention are shown in Fig. 2.6a and Fig. 2.6b respectively.
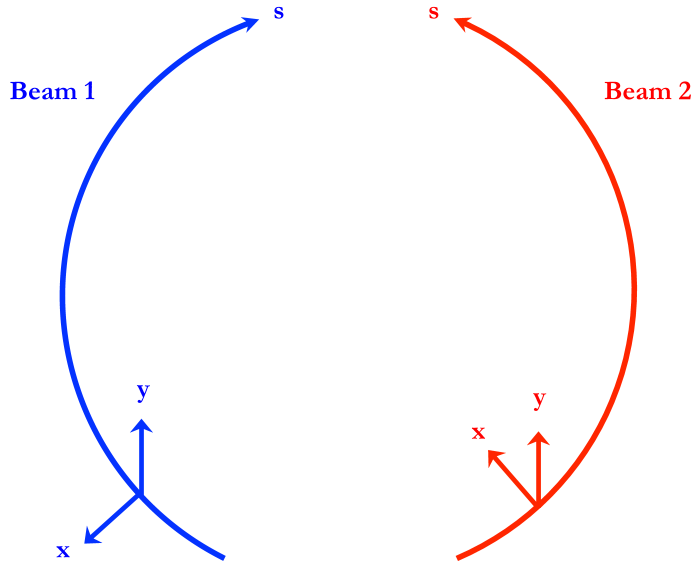
Figure 2.5: The LHC coordinate system for B1 and B2. The positive x-axis points outwards with respect to the ring for B1 and inwards for B2.

(a) Jaw coordinate system (b) Jaw angular tilt convention
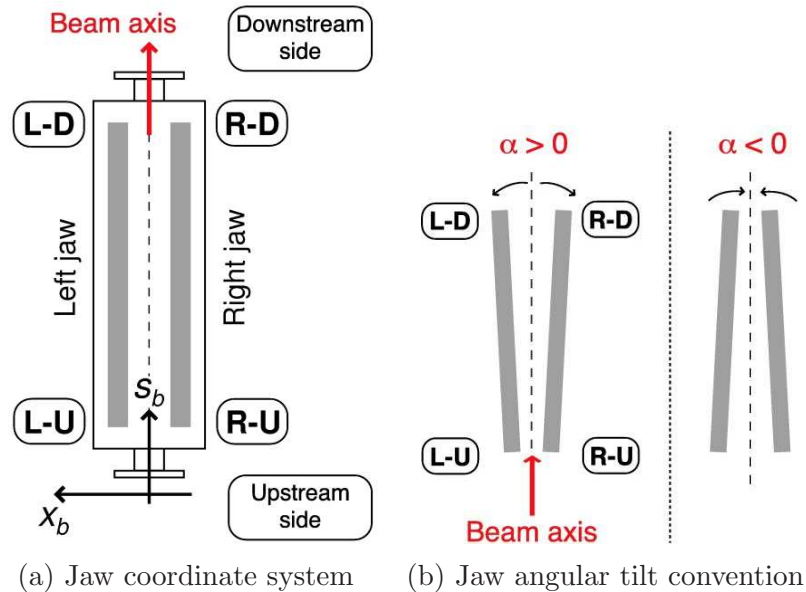
Figure 2.6: The collimator coordinate system (a) and the jaw tilt angular convention (b) as viewed from above, from [31]. The four motors positions at the edges of each jaw allow 4 degrees of freedom.

Each of the four jaw corners can be moved individually by a dedicated stepping motor. The jaw corners are known as left-up (LU), right-up (RU), left-down (LD) and right-down (RD), depending on whether they are located at the entrance or the exit of the beam to or from the collimator. A fifth axis is also available, allowing the tank housing the jaws to be moved in the vertical plane in case a region of the jaw surface is damaged due to beam impacts. Linear Variable Differential Transformers (LVDTs) provide an independent measurement of these five settings, as well as the upstream and downstream jaw gap. Four resolvers count the steps of each motor, and ten switches are in place to prevent the jaws from moving full-in, full-out or hitting one another. A schematic of the arrangement of the sensors and controllers is provided in Fig. 2.7.
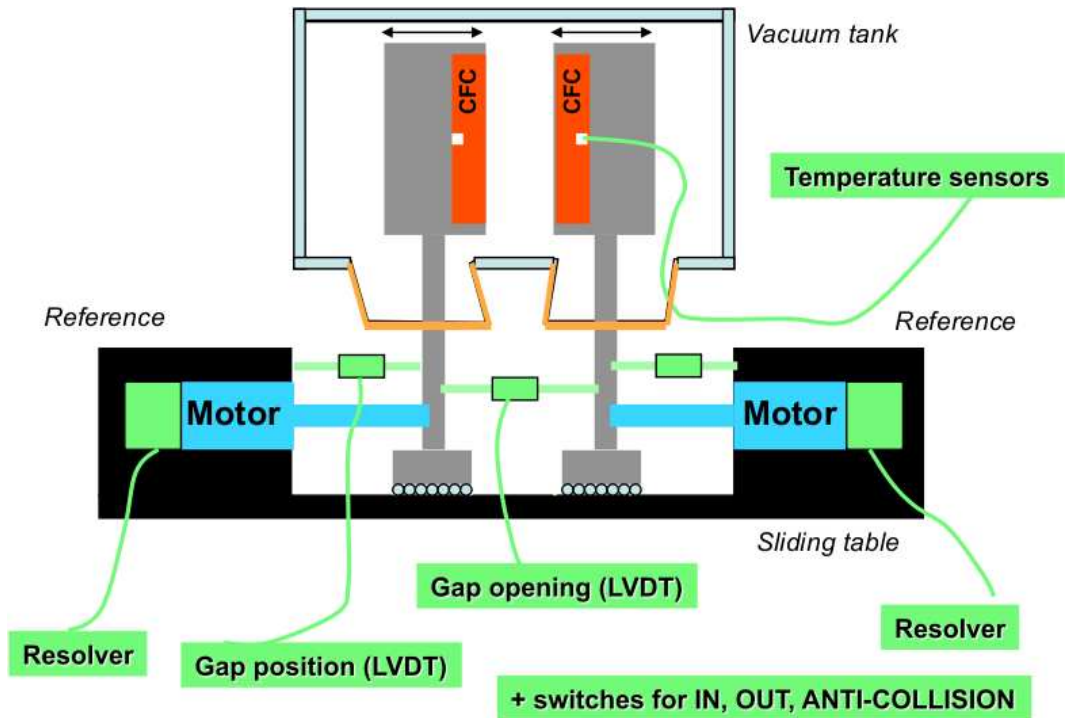
Figure 2.7: Schematic showing the arrangement of the collimator sensors and controllers, from [32].

The TCP collimator intercepts the primary beam halo. Particles impacting the jaw are either absorbed or scattered to larger betatron amplitudes, forming a secondary halo. A relative retraction $d_\sigma \geq 1\ \sigma$ is used to ensure that a secondary collimator does not become the primary bottleneck. The required longitudinal distance between primary and secondary collimators for a two-stage system is expressed in terms of the phase advance $\Delta\mu$ [33, 34]:

$$cos(\Delta\mu) = \frac{n_1}{n_2} \tag{2.1}$$

where n_1 is the distance between the beam axis and the TCP jaw in units of beam σ and $n_2 = n_1 + d_\sigma$. As the maximum amplitude of the scattered particles can be reached at two different values of the phase advance $\Delta\mu_1$ and $\Delta\mu_2$, at least two secondary collimators are required per primary collimator to intercept the secondary halo. This is illustrated in Fig. 2.8.
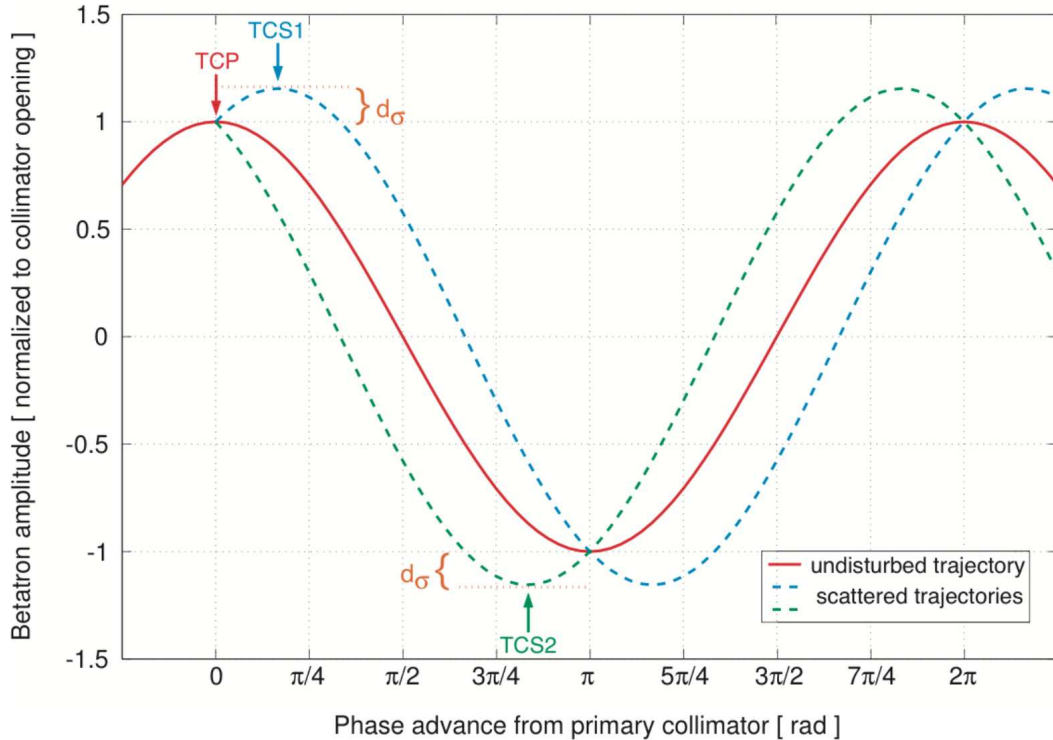
Figure 2.8: Location of two secondary collimators TCS1 and TCS2 designed to clean particles scattered at a given primary collimator as a function of the phase advance from the TCP, from [34].

The TCTs act as a third stage, protecting the critical triplet magnets in the experimental insertions. Finally, particle showers occurring when particles impact a collimator jaw are absorbed by the TCLA collimators. The number of collimators and their relative phase advance and azimuthal positions were optimized using simulations to achieve the best coverage in the two transverse phase-spaces [35]. The collimators are positioned at large β-function amplitudes to ensure larger opening gaps in mm and hence a reduced transverse resistive impedance. Impedance enhances beam instabilities, and decreases exponentially with the jaw gap [36]. Skew collimators are installed to intercept particles with large horizontal and vertical offsets simultaneously.

A schematic of the relative positions according to the collimator type is provided in Figure 2.9, with the collimator naming conventions in Table 2.1. A full list of the jaw materials, jaw lengths and azimuthal angles are provided in Appendix A.
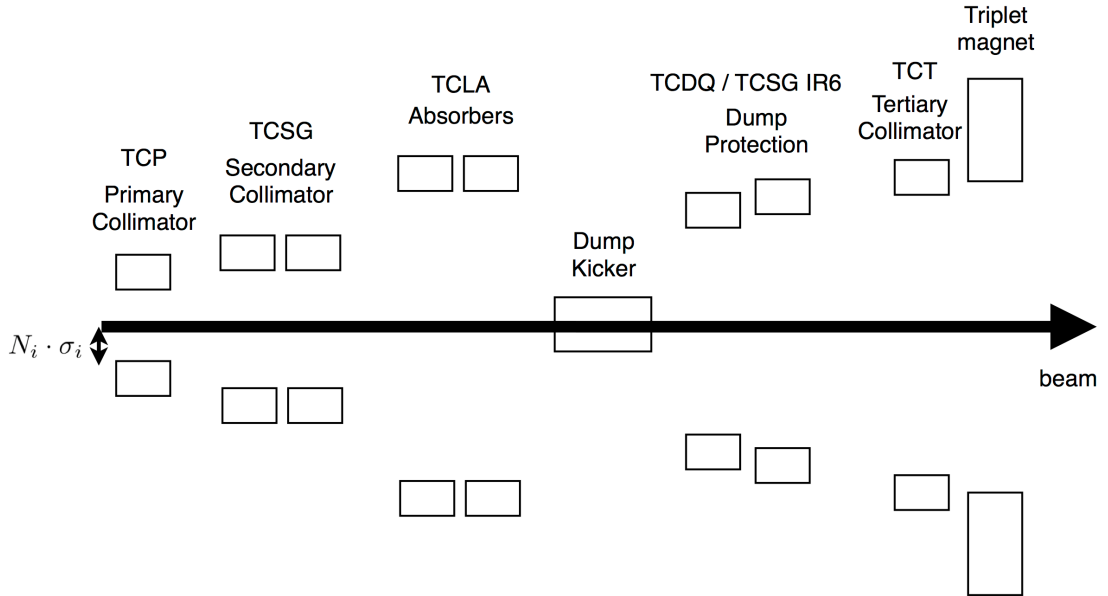
Figure 2.9: LHC multi-stage collimation hierarchy.

Table 2.1: LHC collimator types, naming conventions, jaw materials and lengths.

Collimator Type	Definition	Jaw Material	Jaw Length [m]
TCP	Target Collimator Primary	CFC	0.6
TCSG	Target Collimator Secondary Graphite	CFC	1.0
TCT	Target Collimator Tertiary	W	1.0
TCLA	Target Collimator Long Absorber	W	1.0
TCDQ	Target Collimator Dump Quadrupole	CFC	6.6
TCL	Target Collimator Long	Cu	1.0
TCLI	Target Collimator Long Injection Protection	CFC	1.0
TDI	Target Dump Injection	CFC	4.2

The number of collimators per family and the distribution in the IRs is provided in Table 2.2. The two collimator naming conventions, i.e. the *layout name* and the *display name* are shown in Fig. 2.10. The layout name is used in the official LHC layout, while the display name is conceived to provide quick information (e.g. the plane) which would otherwise require a database search.

Table 2.2: The number of collimators per family and in each IR.

Collimator Type	Number of Collimators
TCL IR1	2
TCL IR5	2
TCT IR1	4
TCT IR5	4
TCT IR2	4
TCT IR8	4
TCLI IR2	2
TCLI IR8	2
TDI IR2	1
TDI IR8	1
TCP IR3	2
TCSG IR3	8
TCLA IR3	8
TCDQ IR6	2
TCSG IR6	2
TCP IR7	6
TCSG IR7	22
TCLA IR7	10

TCP . C6L7 . B1

TCP: Collimator Family
C6: Cell Number
L: Left or Right of IP
7: IP Number
B1: Beam

TCP . IP7 . B1 . 2 . H

TCP: Collimator Family
IP7: IP Number
B1: Beam
2: Index within IR
H: Plane

Figure 2.10: The two collimator naming conventions: layout name (a) and display name (b). The layout name is used in the official LHC layout, while the display name is conceived to provide quick information (e.g. the plane) which would otherwise require a database search.

2.2 LHC collimator software architecture

The software architecture that has been designed and implemented for the LHC collimator system is a subset of the entire LHC Software Architecture (LSA). The latter consists of a 3-tier structure. The bottom layer is composed of actuators, sensors and measurement devices. These allow the tweaking of a variety of parameters, including the collimator left and right jaw positions, as well as the jaw angles. The collimator jaw positions can be positioned with an accuracy of 5 μm, which is 1.82% of the 1 σ beam size at 7 TeV. The maximum jaw movement rate is 2 mm/s.

Powerful UNIX servers that host databases and operation files make up the middle layer, on top of which Graphical User Interface (GUI) console applications run in the presentation layer. The collimator positions can be set from a remote location (the CCC) and in synchronization with the operation of the LHC. As shown in Fig. 2.11 and Fig. 2.12, software programs written in Java and C interact with the hardware via the Common Middleware (CMW) [37] and Front-End Software Architecture (FESA) [38] infrastructures.
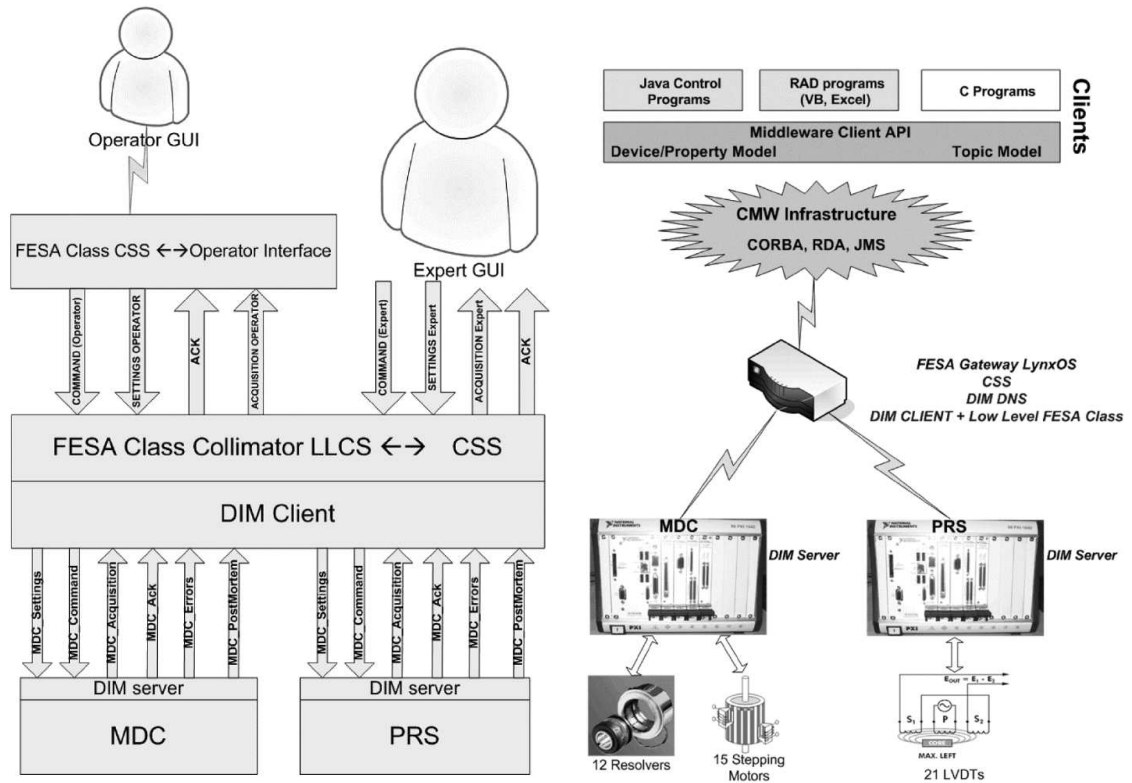
Figure 2.11: LHC collimator control system software (a) and hardware (b) architectures, from [39].

Requests are sent by the applications in the top layer to the Unix/LynxOS servers making up the CMW infrastructure, which then communicates with the low-level Motor Drive Control (MDC) and Position Readout Survey (PRS) through the Distributed Information Management (DIM) client and server. The LHC collimator software components are shown in Fig. 2.12. Components in blue represent the reference settings that the collimator software must make use of in order to appropriately position the collimator jaws.
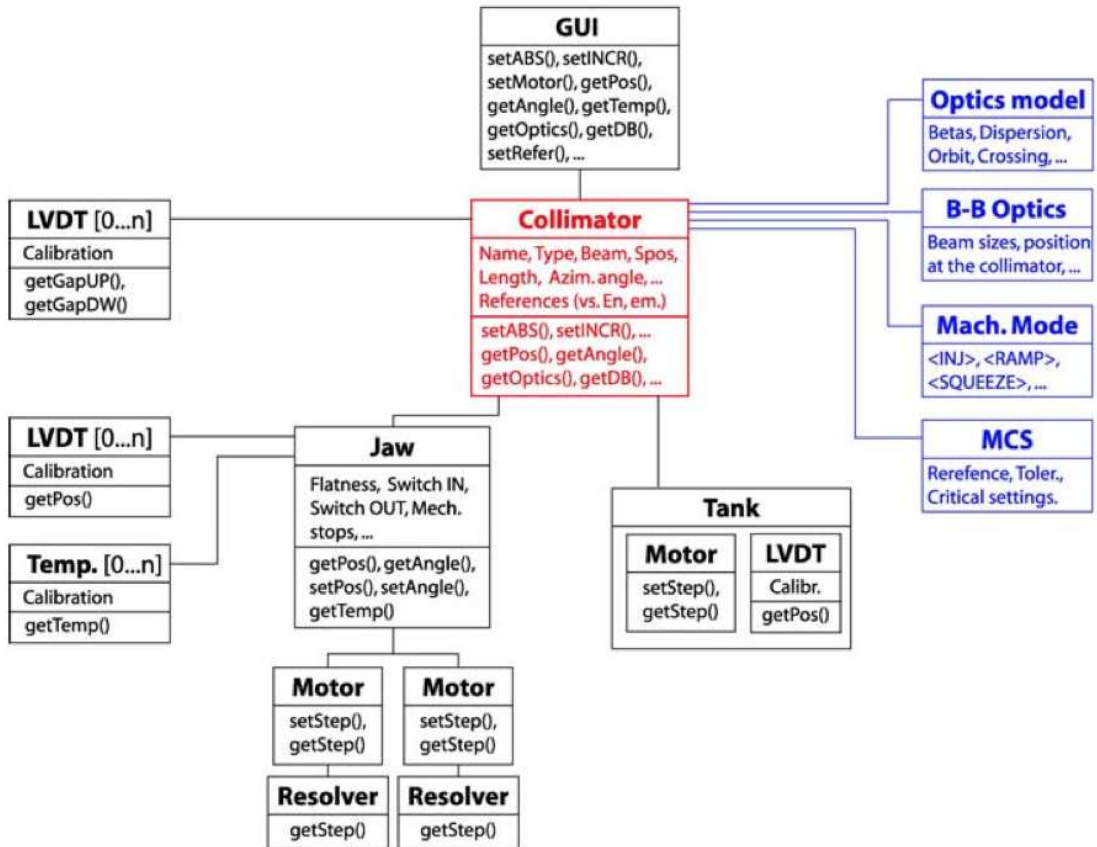
Figure 2.12: Main LHC collimator software components [40].

2.3 Collimator settings

In the LHC, collimation is required at all phases (injection, ramp, squeeze and physics) due to the high beam energies present in the machine. The motor position settings depend on key beam parameters, such as the energy, orbit and β-functions, which change as a function of time, energy and/or β^*. The result is unprecedented complexity, with approximately 400 axes of motion requiring function-based settings and a redundant interlocking strategy [41]. The settings must be continuously monitored and compared to the desired values. A schematic

of the collimator settings parameter space is shown in 2.13. The hardware only knows about the jaw corner positions.
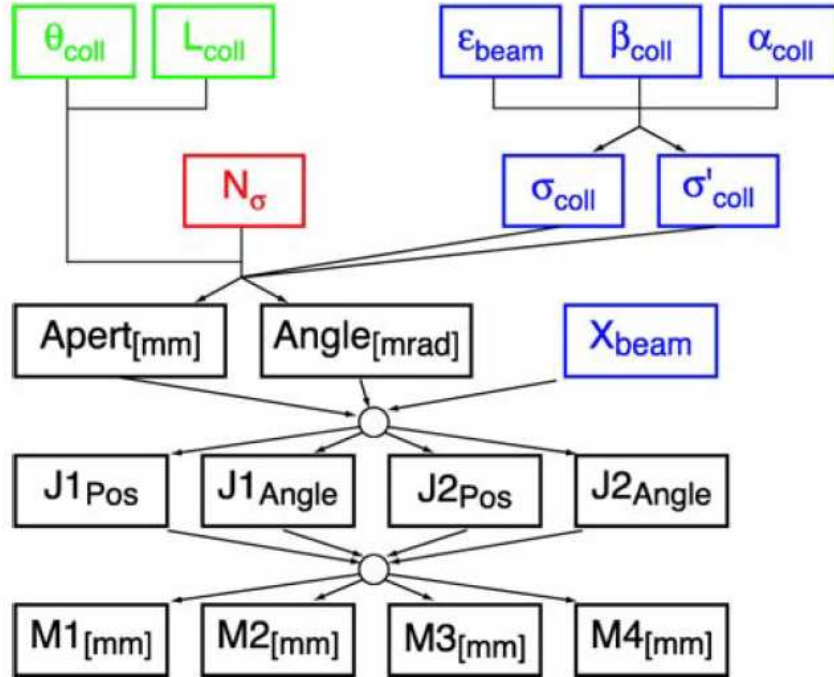
Figure 2.13: The collimator settings parameter space [40]. Mechanical parameters are shown in green, beam-based parameters in blue, the desired settings in units of σ in red, and the jaw corner positions in black.

The jaw corner positions in mm for any point in the operational cycle are determined from the local beam-based parameters and the desired half-gap opening in beam σ units at each collimator. Typically, the beam-based parameters are measured via collimator beam-based alignment at 4 points: injection, flat top, end of squeeze and in collisions. Functions are generated to ensure a smooth transition of the jaw positions from one point to another [42]. The positions for each point and function are stored in *beam processes*, which are played by the LHC Sequencer [43] as required during the fill. Table 2.3 lists the beam processes for the various beam modes, and the operations required to determine the settings for each case. Several instances of the same beam process can exist simultaneously, each containing different time-dependent settings and limits. However, each beam process belongs to a unique *hypercycle*, of which only one is active at any point in time. A hypercycle consists of a list of beam processes, which each contain the necessary settings for all the machine components for all stages, from injection to stable beams.

Table 2.3: The beam processes for various beam modes, and the operations required to determine the settings for each case. This set of beam processes, which contain the necessary settings for all machine components from the start to the end of fill, form a unique hypercycle.

Beam Mode	Beam Process	Operation
Injection	Ramp@start	Alignment
Ramp	Ramp function	$f(\gamma, t)$
Flat Top	Ramp@end/Squeeze@start	Alignment
Squeeze	Squeeze function	$f(\beta^*, t)$
Adjust	Squeeze@end/Collisions@start	Alignment
Adjust	Collisions function	$f(\theta, t)$
Stable Beams	Collisions@end	Alignment

The jaw positions are interlocked at all times. There are three interlock categories:

1. inner/outer limits for each jaw corner, stored in an actual or function beam process.

2. inner/outer β^* limits on the jaw gap, stored in a discrete beam process.

3. energy limits on the jaw gap, stored in a discrete beam process.

Typical values for the limits are ± 400 μm, or ~ 1 σ. If the limits are exceeded at any time, the beam is automatically dumped. Typical changes in the TCP and TCT settings as a function of time during a physics fill are shown in Fig. 2.14a and Fig. 2.14b respectively. Only the upstream jaw corner inner and outer dump limits (equivalent to the corresponding downstream jaw corner values) are shown for simplicity.
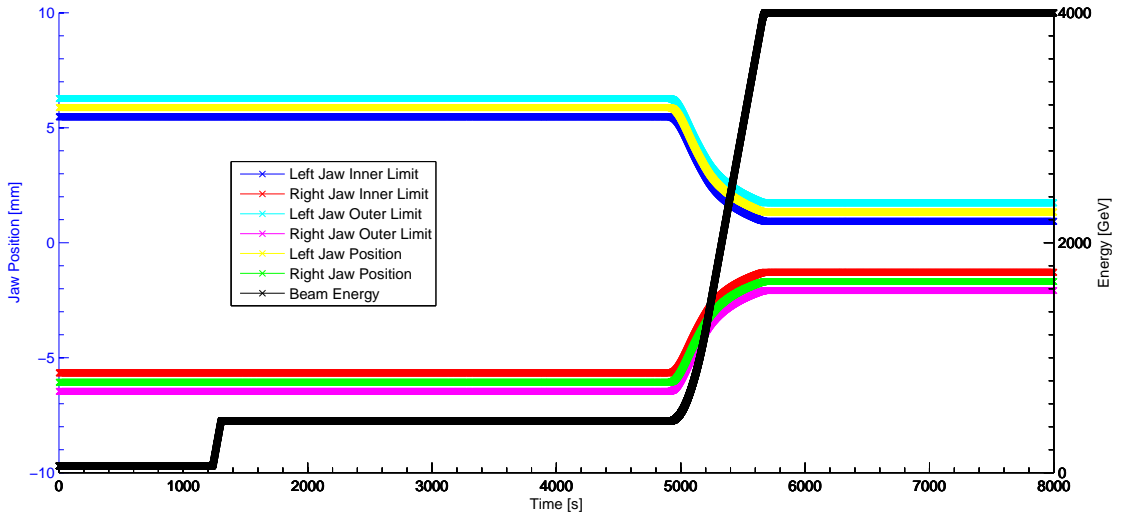
(a) TCP jaw positions and interlocks
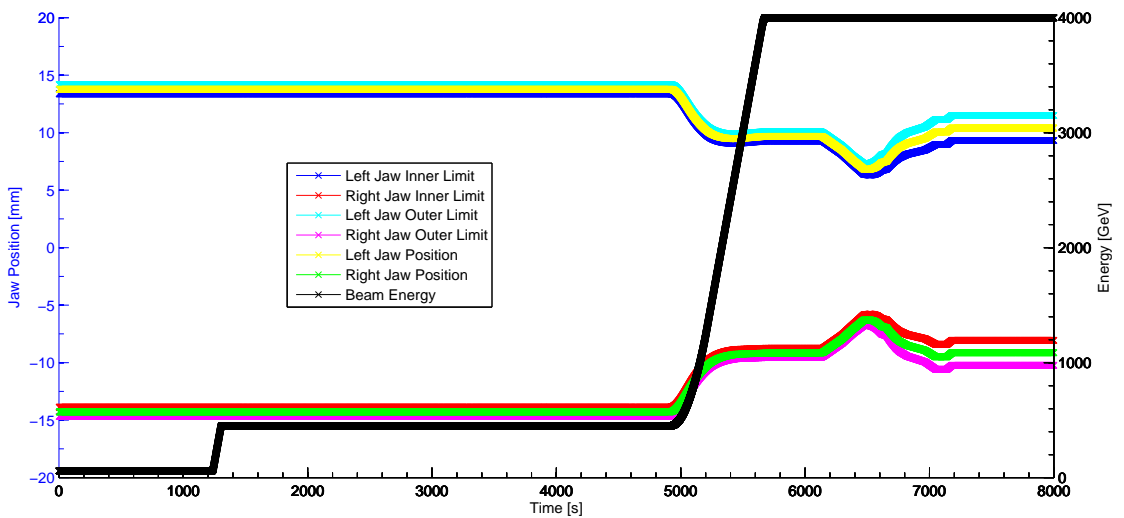
(b) TCT jaw positions and interlocks

Figure 2.14: The jaw positions and interlocks of the TCP.C6L7.B1 (a) and TCTH.4L1.B1 (b) during fill number 3016 (t[0] = 30.08.2012 22:30:00). The TCP jaws are moved in during the ramp, and stay at the same positions for the rest of the fill. The TCT jaws move in during the ramp, and follow the changes in beam size and beam offset during the squeeze and collisions beam processes respectively.

27

Chapter 3

Beam Monitoring Systems

3.1 Beam loss monitoring system

3.1.1 Standard system

Beam losses in the LHC are detected by two systems. There are several timescale categories: [44]:

- **Very fast losses** (0 - 3 turns, or 0 - 0.12 ms)

- **Fast losses** (3 - 250 turns, or 0.12 - 10 ms)

- **Slow losses** (250 turns and more, or 10 ms and longer)

The Quench Protection System (QPS) [45] detects slow losses which induce voltage changes in the superconducting cables in the magnets. The Beam Loss Monitoring (BLM) system consists of approximately 3600 ionization chambers (ICs) installed around the LHC ring to detect ionizing radiation deriving from particle losses [46, 47]. It is designed to detect losses on all three timescales. Both the QPS and the BLM system are able to trigger a beam extraction if the losses exceed pre-defined thresholds to prevent damage to the machine.

Figure 3.1a shows a BLM IC without its external casing. An IC consists of a cylinder filled with 1.1 bar of nitrogen, having a radius of 4.75 cm and a length of 49 cm. A typical example of a BLM IC installation in the LHC tunnel is shown in Fig. 3.1b. Several BLM ICs are specially placed within a few metres downstream of the collimators to detect beam losses resulting from halo particles impacting with the collimator jaws. The particle losses are proportional to the current induced in the BLM detector, which can be converted to units of Gy/s using a conversion factor. The losses are integrated over 12 periods of time, which are listed in Table 3.1. The integration time periods or running sums (RS) range from 40 μs, which represents a single turn, to 84 s, which is equivalent to ~2 million turns.

(a) A BLM ionization chamber without its casing

(b) BLM detectors attached to the walls of the LHC

Figure 3.1: BLM detector without its casing (a) and installed in the LHC (b), from [47].

Table 3.1: BLM running sums, from [48].

Signal Name	Integration Time [ms]	Refreshing Duration [ms]	Published Data Format
RS01	0.04	0.04	Maximum of sums normalized to window length
RS02	0.08	0.04	
RS03	0.32	0.04	
RS04	0.64	0.04	
RS05	2.56	0.08	
RS06	10.24	0.08	
RS07	81.92	2.56	
RS08	327.68	2.56	
RS09	1310.72	81.92	Last calculated sum normalized to window length
RS10	5242.88	81.92	
RS11	20971.5	655.36	
RS12	83886.1	655.36	

The basic timescale is 40 μs, and each nth running sum is a sliding window containing data from the previous 2^n windows. A threshold is allocated to each running sum, such that the beam is dumped if the losses exceed the threshold. The peak loss is published by RS01 to RS08, while the integrated loss is published by RS09 to RS12. As the collimators form part of a multi-turn and multi-stage cleaning system, the 1.3 s running sum is used to analyze its performance, as it contains information about steady-state losses over hundreds of turns. The BLM data for all running sums can be acquired at a rate of 1 Hz.

The software and hardware architectures of the LHC BLM system are shown in Fig. 3.2. Up to 8 ICs are connected to a Field Programmable Gate Array (FPGA) card in the LHC tunnel. Each card digitizes the signal from each IC every 40 μs using current-to-frequency converters and Analogue-to-Digital Converters (ADCs) with a dynamic range of 2.5 pA to 1 mA, or $\sim 1 \times 10^8$ Gy/s [49]. An offset level of $\sim 3 \times 10^{-7}$ Gy/s is introduced as a protection mechanism to avoid lockups resulting from noise and radiation deposited in the electronics, and is inversely proportional to the dynamic range achievable by the system [50]. The data are then transmitted to other FPGA devices at the surface via optical fibre, where operations such as data logging and BLM threshold checks are performed [51].

3.1.2 Improvements for collimator alignment

In January 2012, a new BLM data buffer was implemented to allow for automatic and faster collimator alignment [52]. The FPGA code in the surface cards was modified to include an additional CPU task, which reads a dedicated buffer holding the RS07 data and transmits them to the collimation client, in the form of User Datagram Protocol (UDP) packets at a rate of 12.5 Hz. Details about the software implementation of the BLM data acquisition are provided in Section 6.3.1.3.
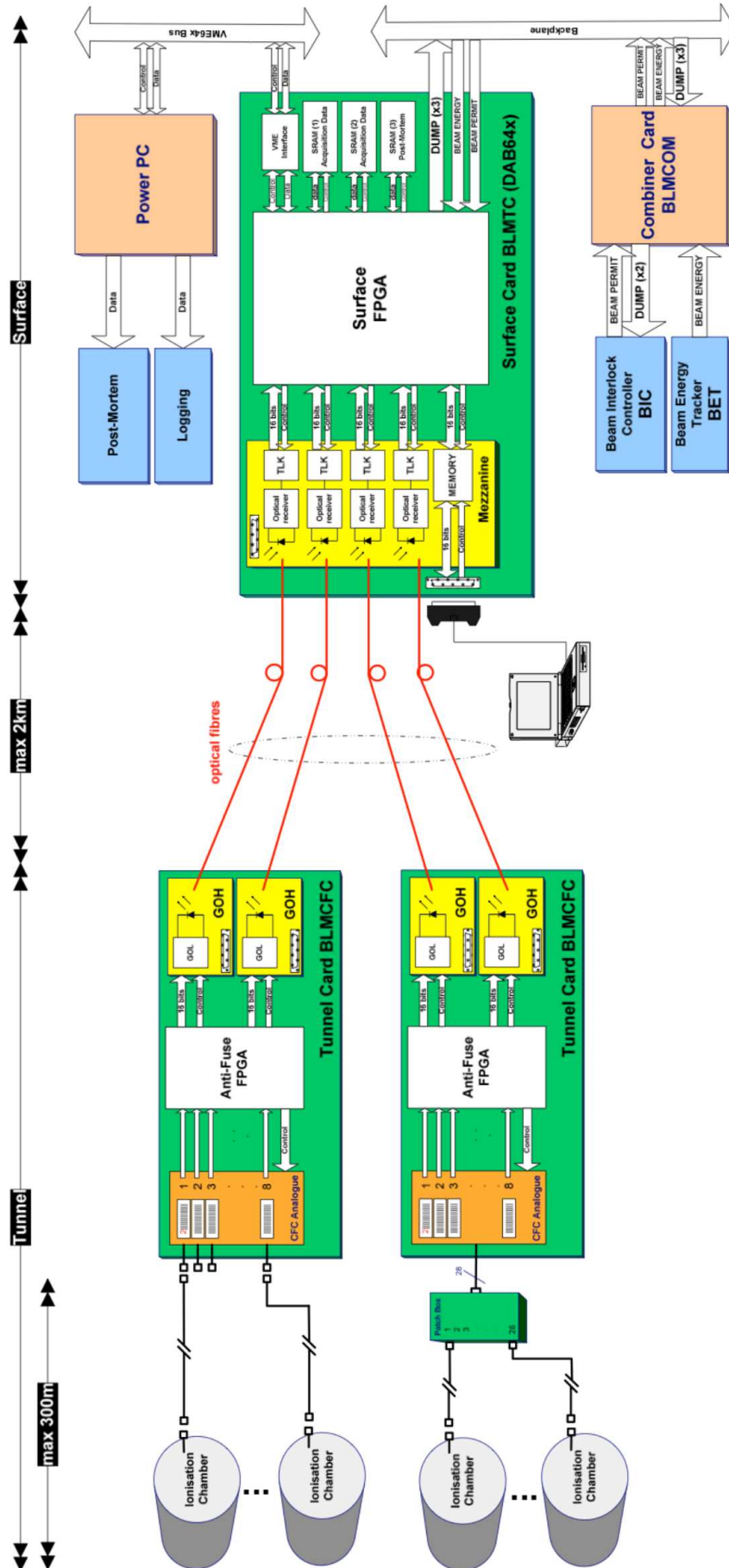
Figure 3.2: Hardware and software architecture of the LHC BLM system, from [51].

3.2   Beam position monitoring system

3.2.1   Beam Position Monitor

The beam position in the horizontal and vertical planes can be measured by a set of electromagnetic pickups, known as a Beam Position Monitor (BPM). A total of 1032 BPMs are installed in the LHC, 516 per beam, corresponding to almost one BPM per quadrupole magnet [53]. Figure 3.3a shows a schematic of an LHC button pick-up. An LHC BPM consists of four button electrodes mounted in an orthogonal fashion in the beam pipe, as illustrated in Fig. 3.3b. The BPM electronics allow for bunch-by-bunch position measurements through a wide-band-time-normalizer circuit.

(a) Button pick-up

(b) Cross-section of an LHC BPM, showing the four pickup electrodes
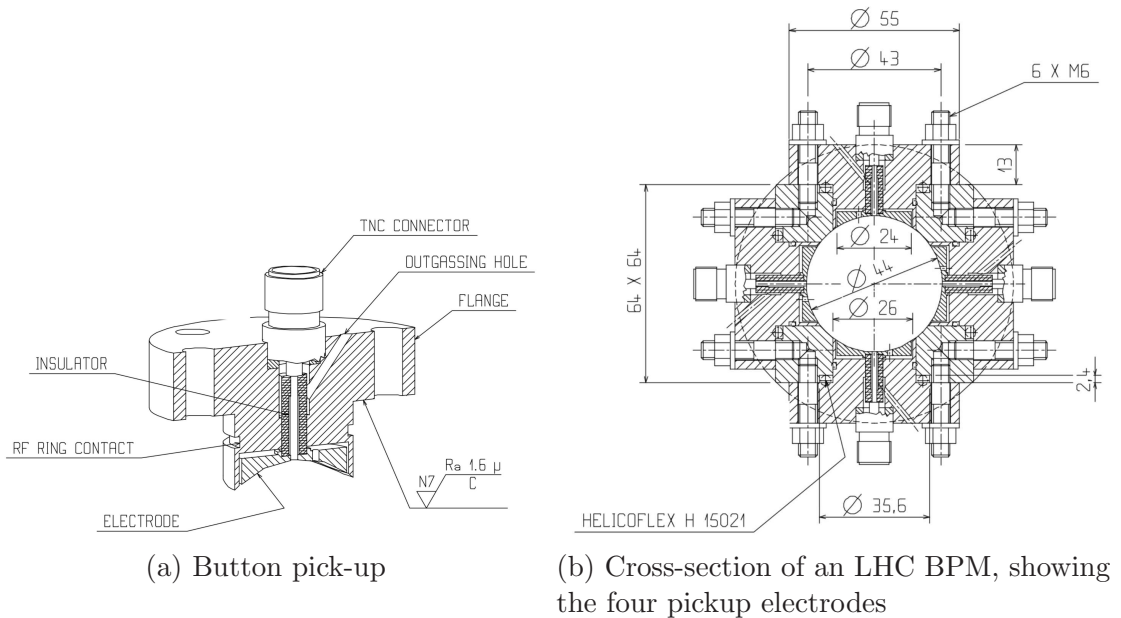
Figure 3.3: Drawings of the button pick-up (a) and a cross-section of an LHC BPM (b), from [54].

The BPM system is intended to measure three fundamental beam observables [55]:

- the single pass trajectory (beam positions versus machine azimuths)

- the beam oscillation sampled at one or several azimuths (beam positions versus time)

- the closed orbit (average beam positions versus machine azimuths)

In addition, it is also possible to measure the beam current intensity from the sum of the electrode signals from a single BPM.

3.2.2 LHC orbit correction system

The LHC orbit correction system relies on feedback BPMs to maintain the desired orbit in the rings. A total of 1060 dipole magnets, divided equally between the horizontal and vertical planes, are used to correct the orbit to the desired trajectory, or so-called *golden orbit* established in part by collimator alignment. The following are the orbit feedback control requirements [56, 57]:

- Global:

  - global r.m.s. (smooth operation, e.g. during the ramp): <0.5 mm

  - preserving 'scrubbing' performance (electron cloud reduction): <0.2 mm

- Local:

  - beam centring at the dampers: <200 μm

  - collimators in IR3 and IR7 (cleaning efficiency dependent on beam position): <70 μm

  - pre-alignment for luminosity feedback: <70 μm

  - TOTEM experiment: ideally <10 μm

3.2.3 Collimators with embedded BPMs

3.2.3.1 BPM pick-up buttons

After a long shutdown of the LHC foreseen for 2013-2015, newly-designed TCT and TCSG collimators with BPM pick-up buttons embedded in the jaws [58] will replace the existing TCTs and the TCSGs in IR6. This new design envisages the installation of two BPM pick-up buttons per jaw, with one positioned in each jaw corner (see Fig. 3.4). The pick-up buttons in the jaw corners are installed in a tapered region, with a retraction of 10.6 mm from the active surface of the jaw, and are hence protected from possible direct beam impacts.
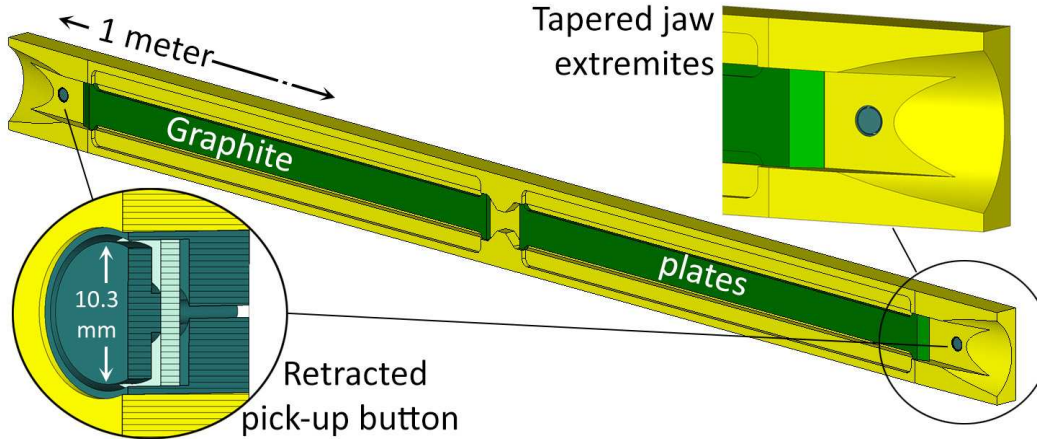
Figure 3.4: A model of one jaw of the collimator prototype with embedded BPM pick-up buttons.

3.2.3.2 BPM coordinate system

Figure 3.5 shows an adapted schematic of the collimator coordinate system presented in Fig. 2.6a and several further defined notations. The collimator prototype consists of two copper jaws and a 10 mm tapered graphite layer (resistivity 13 $\mu\Omega$m) on each jaw surface (Fig. 3.4). The four stainless steel pick-up buttons of diameter of 10.3 mm are placed at jaw extremities 0.6 mm below the copper level, i.e. 10.6 mm below the graphite surface [59]. With such a set-up, the total distance between BPM electrodes, referred to as *BPM aperture*, is:

$$B = J_L - J_R + 2 \times 10.6 = G + 21.2 \tag{3.1}$$

where J_L and J_R are the left and right jaw positions with respect to absolute axis, and G is the distance between the jaws, referred to as the *jaw gap*. Depending on the collimator type, the jaws may be positioned at gaps ranging from 2 mm (operational) to 60 mm (parked).

The *absolute axis* is defined as a geometrical axis of the beam-pipe, connected at both ends of the collimator. The beam traveling inside the beam-pipe may have an arbitrary offset from its absolute axis in the transverse plane. Since only the horizontal plane XS is considered, this offset is defined as the *beam axis* or X_{abs}. In this arrangement, a moving collimator defines another longitudinal axis, called the *jaw centre* or J_c, which describes the axis of the collimator, i.e. its mid-jaw position: $J_c = (J_L + J_R)/2$. Collimator BPMs measure the beam position X_{bpm} which is relative to the jaw centre. The beam axis is calculated generally as:
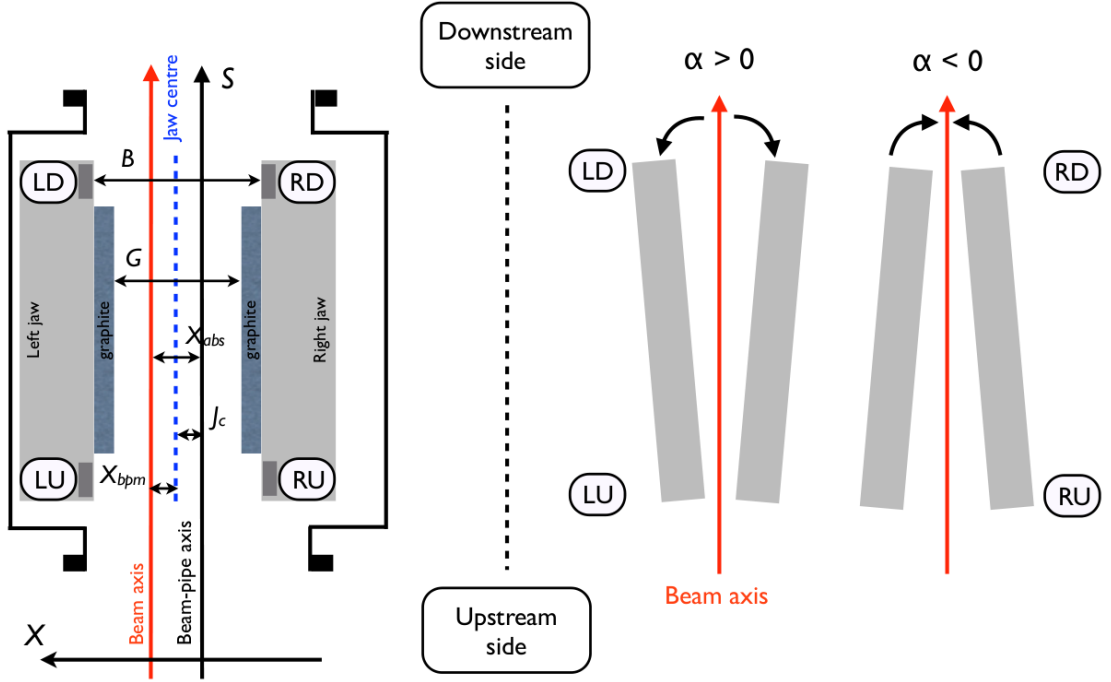
Figure 3.5: An adapted schematic of the collimator coordinate system, showing the electrode locations (a) and the jaw tilt angular convention (b) as viewed from above. The four motors positioned at the edges of each jaw allow four degrees of freedom.

$$X_{abs} = X_{bpm} + J_c \tag{3.2}$$

The jaws are considered centred around the beam when $X_{bpm} = 0$ and $J_c = X_{abs}$. The beam position between the two BPM electrodes can be measured directly using a well-known linear technique. Consider a simple 2D approximation of a collimator BPM arrangement, which consists of a circular beam-pipe and two point-like pick-ups located 180° apart as in Fig. 3.6.

Assuming that the BPMs are enclosed within a uniform cylinder with infinite conductivity, the potential angular distribution for an off-centred charge (x, y) is given by [61]:

$$\Phi(\rho, \theta) = \Phi_0 \frac{R^2 - \rho^2}{R^2 + \rho^2 - 2R\rho\cos(\theta - \theta_0)} \tag{3.3}$$

where Φ_0 is a constant, $\rho \equiv \sqrt{(x^2 + y^2)}$ is the radial position of the charge, R is the radius and the angles θ and θ_0 are defined in Fig. 3.6. The charge position with respect to the considered coordinate system is denoted as X_{bpm} and is calculated from the induced potential (voltage) V_L and V_R on the left and right BPM electrodes:

$$X_{bpm} = k_x \frac{V_L - V_R}{V_L + V_R} = k_x \times X_{raw} \tag{3.4}$$

Here k_x is a calibration constant which serves as a coefficient of linear conversion of relative raw readings X_{raw} to mm. It can be seen from this equation that X_{raw} lies in the range [-1, 1]. If only the horizontal electrodes are considered and are assumed to be point-like, then both offsets in the horizontal and vertical planes contribute to the charge position calculation:

$$\frac{x}{1 + \frac{x^2 + y^2}{R^2}} = -\frac{-R}{2} \frac{V_L - V_R}{V_L + V_R} \equiv X_{bpm} \tag{3.5}$$

From this it can be seen that in case of small offsets $(x, y \ll R)$ the linear equation (Eq. (3.4)) provides the approximate position of the charge between two opposite electrodes when $k_x = R/2$. This expression is often called a *difference-over-sum* linearization method, and provides a quick approximation when large beam drifts are not foreseen. If this is not the case, due to the non-linear contribution of the horizontal and vertical displacement in Eq. (3.5), the charge position must be expressed using a Taylor series:
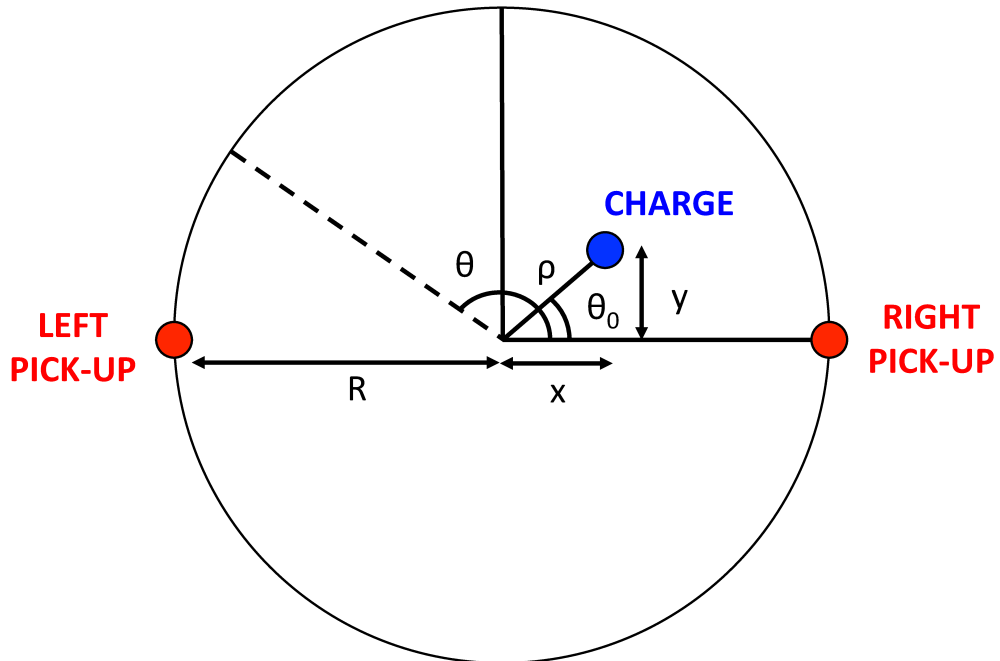
Figure 3.6: A schematic of a basic BPM arrangement consisting of two point-like pick-ups on opposite sides of an off-centred charge, adapted from [60].

$$X_{bpm} = \frac{R}{2} \frac{V_L - V_R}{V_L + V_R} \simeq \frac{2}{R} x \left(1 - \frac{x^2 + y^2}{R^2} + \ldots \right) \tag{3.6}$$

where the additional terms in the series are the non-linear contribution to BPM response. The *tilt* of a given jaw (for example, the left jaw) can be estimated to first order from:

$$\alpha_L^{tilt} = \frac{V_{LU} - V_{LD}}{V_{LU} + V_{LD}} \tag{3.7}$$

A sophisticated and accurate correction of non-linearities is essential for monitoring of the beam position at the collimators. In order to ensure accurate beam position measurement with the difference-over-sum method, k_x must be pre-calculated as a function of the jaw gap G and selected accordingly during operation. However, if the jaws are not centred around the beam, the BPM response will maintain a non-linear behavior as a function of the beam offset. This adds another dimension to the non-linearity and renders the difference-over-sum method inefficient for quick on-line orbit calculation. A single 2D correction polynomial derived from simulations is described in Appendix D, which covers correction of collimator's non-linear BPM readings for the whole jaw motion range and possible beam offsets within defined limits.

Chapter 4

Collimator Beam-Based Alignment

4.1 LHC collimator beam-based alignment

4.1.1 Pre-alignment procedure

Prior to commencing the beam-based alignment procedure, several requirements should be satisfied, as listed below:

- One to two nominal bunches (1.15×10^{11} p to 2.30×10^{11} p) are injected from the SPS into the LHC. Note that alternatively, several probe bunches can be injected, as long as the individual bunch intensity remains above the requirements of the BPM orbit feedback system. Multiple bunches are particularly useful if beam loss maps (introduced in Section 4.2) need to be performed after the alignment.

- The low beam intensity quoted above enables the safe beam flag to be set. However, the Engineer in Charge (EiC) must periodically ensure that the flag timeout does not elapse and trigger a beam dump.

- The EiC then opens all jaw position thresholds to allow the jaws to be moved freely, and masks all of the maskable BLM thresholds.

- The EiC performs wire-scans to determine the beam emittance, and switches off the orbit feedback.

4.1.2 Alignment procedure

Beam-based alignment of the LHC collimators is necessary to determine the beam centre (Δx_i) and the beam size (σ_i^m) at each collimator i, which are initially unknown. The actual beam orbit may deviate from the design orbit due to ground motion, thermal effects and machine sources such as multipole field errors [62]. The alignment procedure ensures that a correct collimator hierarchy is established

for normal operation. A schematic of the collimator jaws and the beam, showing Δx_i and σ_i^m is provided in Fig. 4.1, where J_L and J_R are respectively the left and right jaw positions with respect to the beam-pipe axis.
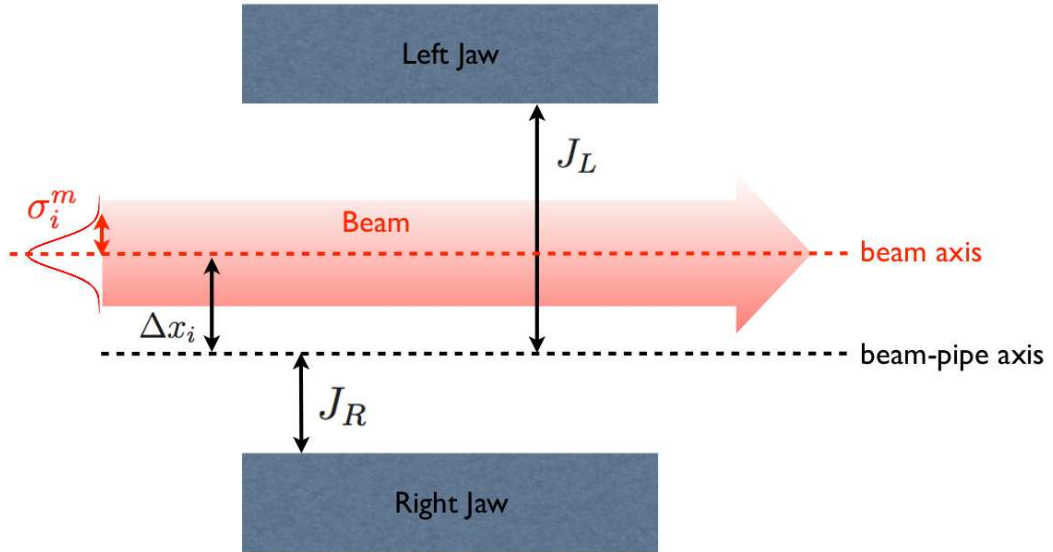
Figure 4.1: Schematic of the collimator jaws and the beam, showing Δx_i and σ_i^m. The parameters J_L and J_R are respectively the left and right jaw positions with respect to the beam-pipe axis.

The alignment is beam-based because a collimator jaw is aligned when a jaw movement towards the beam produces a clear loss spike in an assigned BLM detector located further downstream. An example of such a spike is provided in Fig. 4.2. The procedure is performed remotely from the CCC using a top-level application implemented in Java.
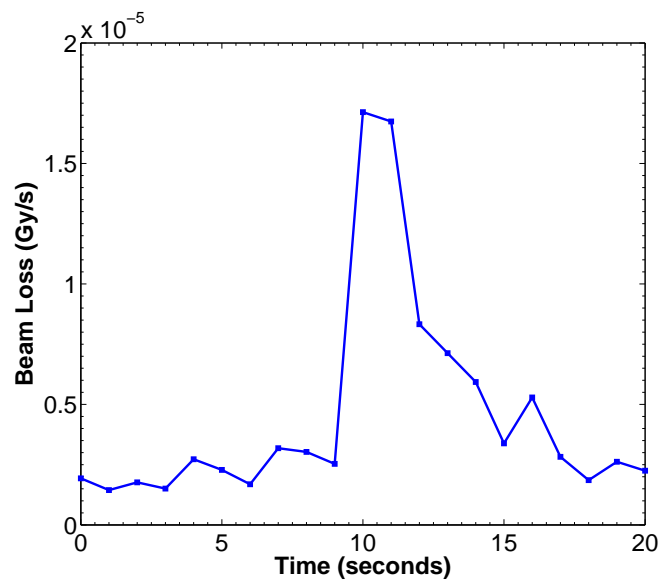
Figure 4.2: Typical example of a BLM signal resulting after an inward collimator jaw movement at $t = 9$ s.

Each collimator is aligned in a four-step procedure, which was established in [63]. The procedure was tested with a prototype collimator in the SPS [64, 34] and was first used in the 2010 LHC run [65]. The alignment sequence, involving the reference collimator and the collimator i to be aligned, is shown in Fig. 4.3. The collimator jaw of a reference collimator is moved in steps towards the beam to form a reference cut in the beam halo (step 1 in Fig. 4.3). The reference collimator is taken to be the primary collimator in the same plane (horizontal, vertical or skew) as the collimator i.
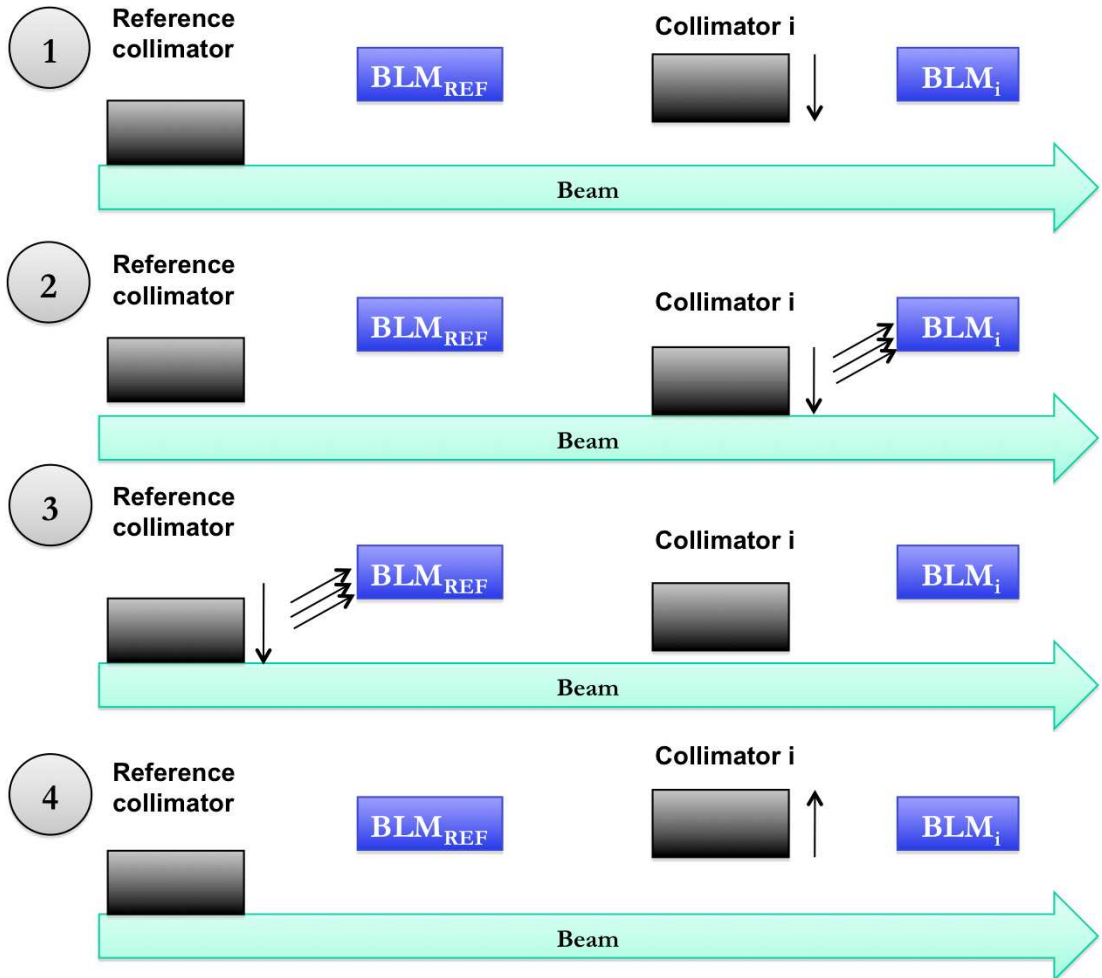
Figure 4.3: The four-stage beam-based alignment procedure for collimator i, using a primary collimator as a reference. Only one jaw is shown for simplicity.

A BLM signal spike can be attributed to a particular jaw movement if only that jaw was moving when the spike occurs. Therefore, the left and right jaws are aligned separately. After aligning both jaws of the reference collimator, the same procedure is performed for the collimator i (2), and the reference collimator is aligned once again (3). The beam centre can then be determined from the aligned jaw positions of collimator i:

$$\Delta x_i = \frac{x_i^{L,m} + x_i^{R,m}}{2} \tag{4.1}$$

where $x_i^{L,m}$ and $x_i^{R,m}$ are the measured left and right jaw setup positions. The jaw gap can also be calculated from these values:

$$G_i = x_i^{L,m} - x_i^{R,m} \tag{4.2}$$

The inferred beam size is expressed as a function of the half gap, with n_1 being the cut of the reference collimator in units of σ:

$$\sigma_i^{inf} = \frac{x_i^{L,m} - x_i^{R,m}}{2n_1} \tag{4.3}$$

The nominal 1 σ beam size at each collimator σ_i^n is determined from the nominal geometrical emittance, ϵ, the nominal beta functions $\beta_{x,i}$ and $\beta_{y,i}$ at the collimator i and the rotation angle of the collimator jaws ψ_i:

$$\sigma_i^{nom} = \sqrt{(\beta_{x,i}\epsilon_x + D_i\delta_p)\cos^2\psi_i + \beta_{y,i}\epsilon_y\sin^2\psi_i} \tag{4.4}$$

which is a more general form of the relation in Eq. (1.11). The dispersive beam size contribution $D_i\delta_p$ in the horizontal plane at collimator i is considered, assuming negligible dispersion in the vertical plane. Here D_i is the dispersion function and δ_p is the r.m.s. momentum spread of the beam particles. For a horizontal collimator with $\psi_i = 0$,

$$\sigma_i^{nom} = \sqrt{\beta_{x,i}\epsilon_x + (D_i\delta_p)^2}$$
$$(\sigma_i^{nom})^2 = \beta_{x,i}\epsilon_x + (D_i\delta_p)^2$$
$$(\sigma_i^{nom})^2 = \sigma_\beta^2 + \sigma_p^2 \tag{4.5}$$

with σ_β as the betatron beam size and σ_p as the momentum beam size. However, at the start of the horizontal collimator alignment, the momentum halo is cut using the primary collimator in the high-dispersion region in IR3. This ensures that the halo intercepted by the other collimators is dominated by the betatron

contribution. The contribution from σ_p^2 is rendered negligible, and can be omitted from the calculation of the nominal beam size.

The reference collimator is aligned both before and after the setup of collimator i, in order to account for the halo that is scraped away during the alignment when calculating the beam size. The half gap opening n_1 in units of σ for the two TCP alignments can be calculated as:

$$n_1^{k-1} = \frac{x_{k-1}^{L,m} - x_{k-1}^{R,m}}{2\sigma_{TCP}^{nom}} \tag{4.6}$$

$$n_1^k = \frac{x_k^{L,m} - x_k^{R,m}}{2\sigma_{TCP}^{nom}} \tag{4.7}$$

The nominal beam size at the primary collimator is used in each case and k is an index for the number of alignments of the reference collimator. The dispersive beam size contribution can be ignored for this calculation, as the reference collimator is located in a low-dispersion region (IR7). The beam size at all other collimators can then be inferred from the jaw positions of collimator i and the reference collimator, assuming nominal emittance and the real, imperfect β function. Substituting n_1 as the average of Eq. (4.6) and Eq. (4.7) in Eq. (4.3):

$$\sigma_i^{inf} = \frac{x_i^{L,m} - x_i^{R,m}}{n_1^{k-1} + n_1^k} \tag{4.8}$$

A schematic of the collimator jaws in the aligned positions, including Eq. (4.1) and Eq. (4.8) used to calculate the beam centre and the beam size respectively, is shown in Fig. 4.4.
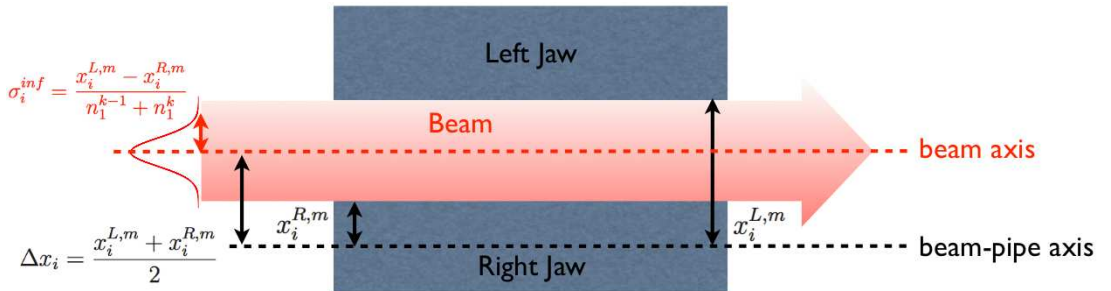
Figure 4.4: Schematic of the aligned collimator jaws and the beam, showing the equations for the beam centre Δx_i and the beam size σ_i^m.

The final step is to set the left and right jaws of collimator i using the values obtained for the beam centre and beam size to maintain the collimation hierarchy (4):

$$x_i^{L,set} = \Delta x_i + N_i \sigma_i^m \qquad (4.9)$$

$$x_i^{R,set} = \Delta x_i - N_i \sigma_i^m \qquad (4.10)$$

where N_i is the half gap opening specific to a collimator family. The nominal collimator settings were defined during the design of the LHC collimation system [33], however in practice these are relaxed for non-nominal beam parameters. A summary of the half gap openings is shown in Table 4.1. The so-called *relaxed* collimator settings were used in 2010 and 2011 at 3.5 TeV, while the *tight* collimator settings were used in 2012 at 4 TeV.

The number and types of collimators set up depend on the machine configuration for which the beam centres at the collimators must be known. At 450 GeV, all 86 ring collimators are set up. One nominal bunch containing $\sim 1.15 \times 10^{11}$ protons is used per beam. When the energy is ramped to flat top at 3.5 TeV or 4 TeV, a setup is performed for all collimators except for the 6 injection protection collimators (TCLI and TDI), which are placed in retracted or *parking* positions at this point in the machine cycle. Although the design machine optics at injection and flat top are identical, an alignment is required due to possible imperfections in the magnetic fields. After squeezing both beams to the operational β^* in the experimental interaction points, the 16 TCTs are aligned, since a large change occurs in the beam sizes for these collimators. When the orbit separation bumps are collapsed and the beams are brought into collisions, an alignment of the TCTs is required once again as their beam centres change in the crossing plane. This results in four setup operating points. The TCL collimators were only required for protection from luminosity debris as from the 2012 run, as the LHC beam intensity and energy was increased.

From experience during LHC operation, the determination of the beam size by beam-based alignment provides a consistent collimation hierarchy at injection, but not at top energy [31]. This is because the collimator gaps are smaller in mm at top energy, which makes the setup procedure more sensitive to gap measurement errors. The top energy collimator settings therefore rely on the nominal betatron beam size (Eq. (4.4) with $D_i \delta_p = 0$) instead of the inferred beam size (Eq. (4.8)).

Table 4.1: Operational half-gap openings N_i in units of the beam size σ for different energies and collimator families [66]. This establishes a multi-stage cleaning and protection hierarchy in betatron and momentum phase space. Different settings were used for the TCTs and TCDQs in 2010 and 2011 at 3.5 TeV.

Collimator Type	N_i at 450 GeV (σ)	N_i at 3.5 TeV in collisions (σ)	N_i at 4 TeV in collisions (σ)	N_i at 7 TeV in collisions (σ)
TCL IR1	parking	parking	10	10
TCL IR5	parking	parking	10	10
TCT IR1	13	15/11.8	9	8.3
TCT IR2	13	15/26	12	8.3
TCT IR5	13	15/11.8	9	8.3
TCT IR8	13	15/11.8	12	8.3
TCLI IR2	6.8	parking	parking	parking
TCLI IR8	6.8	parking	parking	parking
TDI IR2	7	parking	parking	parking
TDI IR8	7	parking	parking	parking
TCP IR3	8	12	12	15
TCSG IR3	9.3	15.6	15.6	18
TCLA IR3	10	17.6	17.6	20
TCDQ IR6	8	10.6/9.8	7.6	8
TCSG IR6	7	9.3	7.1	7.5
TCP IR7	5.7	5.7	4.3	5.7
TCSG IR7	6.7	8.5	6.3	6.7
TCLA IR7	10	17.7	8.3	10

On the other hand, the orbit determined from beam-based alignment is used at all stages.

The collimators are aligned in sequence depending on their longitudinal position in an anti-clockwise fashion, starting from IR6 for B1 and IR8 for B2. In this manner, BLM signal crosstalk within the same IR is minimized. The alignment sequence is given in Appendix A. Once all collimators in one plane (e.g. horizontal) have been aligned, any vertical and subsequently skew collimators are aligned.

4.2 Collimation hierarchy qualification

The collimation system hierarchy has to be qualified regularly to ensure that the collimators are at the right positions with respect to the beam. Qualification is performed by inducing slow (multi-turn) beam losses (betatron or momentum offsets) so that a large number of particles hit the collimators and the resulting showers are detected in the BLM detectors around the ring. Snapshots or beam loss maps can then be produced for the precise instant when the losses are maximal.

An example of a B1 vertical beam loss map at 3.5 TeV is shown in Fig. 4.5. The IR7 collimator hierarchy is observed when performing a betatron loss map, while the IR3 hierarchy is checked with a momentum loss map. The local cleaning inefficiency at any element is estimated by the ratio of its BLM signal to the BLM signal measured at the IR7 primary collimator.

Particles with a large betatron offset can be generated by crossing the third integer tune resonance for 1-2 s in the horizontal or vertical plane separately for both beams, thus creating horizontal or vertical beam losses. A disadvantage of this technique, in use in the 2010-2011 period, is that a large fraction (30 - 50%) of the beam is lost, often leading to beam dumps. As of 2012, the transverse damper (ADT) bunch-by-bunch blow-up technique [67] provides more control and flexibility over how many losses are generated, thus improving the operational efficiency. Off-momentum losses are created by varying the RF cavity frequency by ±500 Hz for negative and positive momentum offsets respectively. The off-momentum qualification is performed for both beams simultaneously to reduce the number of measurements required.
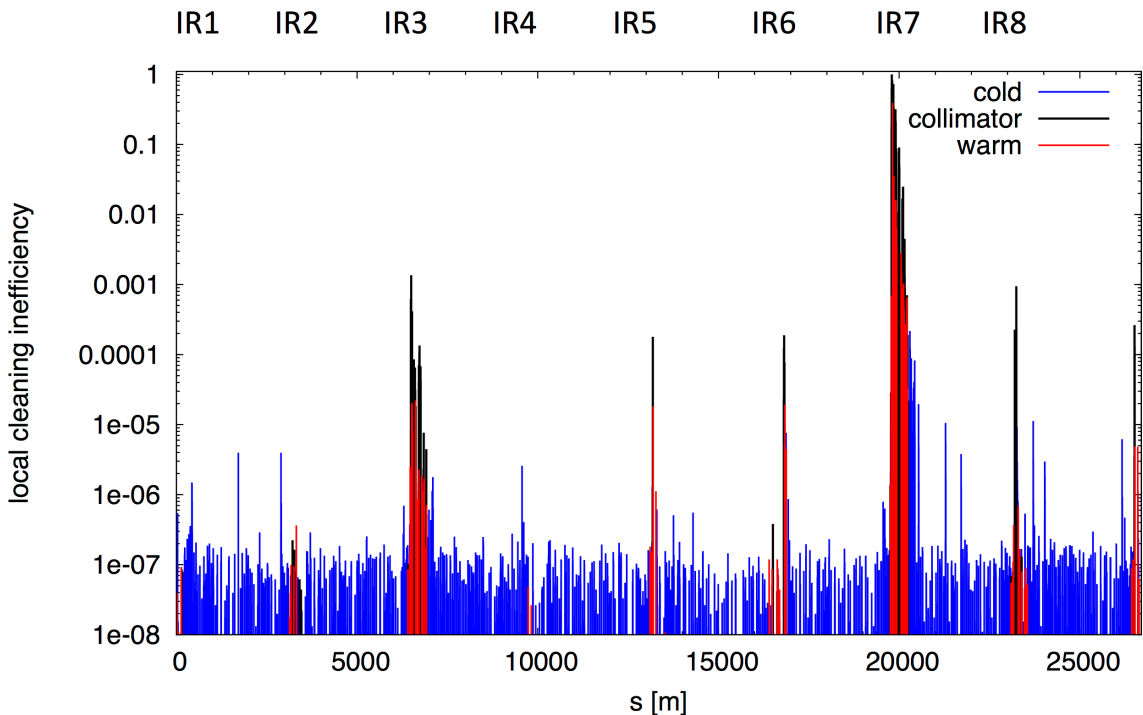
Figure 4.5: B1 betatron vertical beam loss map at 3.5 TeV. Each data point is a reading taken from a BLM detector. The loss monitors are located in the cold or warm regions, or may be associated with a collimator (colour-coded in blue, red and black respectively). The plot is normalized to the highest loss, which occurs at the primary collimator in IR7.

4.3 Collimator alignment in other colliders

At present, only three other operating or decommissioned circular colliders are equipped with beam collimation systems.

4.3.1 Tevatron

The Tevatron [68] was a high-energy proton-proton collider located in Illinois, USA. It is the closest machine to the LHC in terms of beam energy (1 TeV). The Tevatron has 12 single-jaw collimators (4 primary collimators and 8 secondary collimators), and operates using an active collimation procedure, known as *halo removal*. This procedure is done at the start of every fill, where the jaws are moved into the beam halo and stop based on feedback from BLM detectors. The jaws are then retracted for the rest of the store. The minimum jaw step size is 25 μm, a factor 5 more than the LHC collimator motors, and the halo removal process is completed in approximately 7 minutes [69].

4.3.2 RHIC

The Relativistic Heavy Ion Collider (RHIC) [70], located at the Brookhaven National Laboratory in New York, USA is equipped with 10 single-jaw L-shaped scrapers [27]. They are used only for experimental background reduction and abort gap cleaning. Alignment is performed by moving the jaw into the halo. Orbit drifts of a few hundred μm are tolerated [71].

4.3.3 HERA

The Hadron-Elektron-Ring-Anlage (HERA) [72] was an electron-proton collider located at the Deutsches Elektronen-SYnchrotron (DESY) laboratory in Hamburg, Germany. A total of 6 double-jaw collimators were installed to reduce the proton halo-induced background at the ZEUS and H1 detectors [73]. The collimator jaws were only moved in when the beams had been brought into collision. The alignment was carried out by either a file-based procedure, where the jaws are moved to pre-defined values regardless of beam loss rates, or by an automatic procedure which moves in the jaws until the losses exceed a pre-defined threshold. The alignment for the 6 collimators was completed in 20 minutes [73].

4.3.4 Comparison with LHC collimator alignment requirements

Due to higher beam energies and smaller beam sizes, a higher level of alignment precision is required for the LHC. The measured beam centres at the collimator locations in the LHC are fed into the orbit feedback correction system, and beam size measurements are incorporated into the collimator settings, both of which are not done at other colliders.

4.4 Motivation for fast automatic alignment

Regular collimator setups are required as the beam orbit may change over a few months due to ground motion, thermal effects and machine sources such as multipole field errors [62]. Setups of a subset of the collimators are also performed when machine parameters are changed, such as the β^* at the experimental IPs. In the 2010 run, the setups were performed 'manually', meaning that human feedback was required to determine when the jaw is aligned to the beam. This was achieved by observing the BLM signal on a screen following a jaw movement. Human error may produce incorrect jaw movements, causing high losses and beam dumps.

A disadvantage of the manual method is therefore the setup time required (up to 30 hours), which means that it cannot be performed frequently. This places constraints on the minimum β^* achievable, as a smaller β^* would require the jaws to be positioned more tightly around the beam, and hence the hierarchy is more sensitive to orbit drifts. Consequently the integrated and peak luminosity reach of the LHC [74] is limited (see Eq. (1.13) for the relationship between luminosity and β^*).

From the startup of the LHC in 2008 until now, the interim solution has been to perform the setups occasionally and keep monitoring the hierarchy by performing loss maps. However it is not known whether this will continue to be a viable solution once the LHC will operate at 7 TeV and with higher intensities. Additionally, beam time is costly (the LHC running costs are approximately €150,000 per hour), and therefore any saved time is of vital importance as it can be used for actual physics experiments and data-taking. Hence, to counteract all of this, it was concluded that an automated intelligent system would have to be developed.

Chapter 5

Alignment Algorithms

5.1 Introduction

A description of the alignment algorithms developed, and the specific beam tests carried out to validate each one are presented in this chapter. Beam tests were performed either during beam re-commissioning periods, which involve an alignment of all or a subset of the collimators, or during dedicated LHC Machine Development (MD) studies. Each MD study lasted typically 4-8 hours, and required a detailed proposal and eventual presentation of the results achieved. Specific results related to each algorithm are described here, while global results from beam-based collimator alignment are presented in Chapter 8.

5.2 Formal problem definition

This section provides a description of the problem that is solved in this thesis. The collimator setup problem involves the determination of the set of left and right aligned jaw position pairs for each collimator:

$$\mathcal{D} = ((x_1^{L,m}, x_1^{R,m}), (x_2^{L,m}, x_2^{R,m}), ..., (x_n^{L,m}, x_n^{R,m})). \tag{5.1}$$

The beam centres and beam sizes at each collimator i, given by equations (4.1) and (4.8) can then be calculated. The overall time required for setup, T_{setup}, must be minimized while each collimator jaw must be reliably aligned to the beam. The jaw positions $(x_i^{L,m}, x_i^{R,m})$ are determined sequentially, first by aligning one jaw to the beam, noting the final jaw position, and repeating the process for the other jaw.

There is no preferred alignment order: for example, the left jaw may be aligned first followed by the right, or vice-versa. Both jaws of multiple collimators may be moved simultaneously towards the beam, however if a beam loss spike is observed,

neither jaw can be declared as aligned to the beam with certainty. The accuracy of the setup must also be maximized, which means that the step size must be kept as small as possible.

No collimator setup induced beam dumps are tolerated, as this is the largest contribution to T_{setup}. A beam dump is triggered for machine protection reasons if any BLM signal S_i exceeds the dump threshold S_i^{dump} of that BLM detector.

5.3 BLM-based feedback loop

A BLM-based feedback system [75, 76] was developed as one of the first building blocks in order to create an automatic setup procedure. The BLM-based feedback loop algorithm was also successfully used for the alignment of Roman Pots for the TOTEM and ALFA physics experiments [77].

5.3.1 Single collimator movement

The feedback loop algorithm allows the user to specify four input parameters to move in one or both collimator jaws to the beam. The four inputs consist of the left and right jaw step sizes in μm, Δx_i^L and Δx_i^R, a BLM signal threshold S_i^{Thres} and the time interval between each step t_i^s. A set of pre-defined possible values exists for each input, based on experience with the collimation system in the 2010 LHC run. With every jaw step, the algorithm obtains the BLM data $S_i(t)$ associated with the collimator being moved, and stops the jaw movement if the loss threshold is exceeded. The BLM data were acquired at a rate of 1 Hz in 2010 and 2011, and at 12.5 Hz from 2012 onwards. The algorithm therefore automates two key parts of the setup process:

- Collimator jaw movement towards the beam with a user-defined step size and time interval.

- Collimator jaw stopping when the beam losses exceed a user-defined threshold.

When the jaw stops, human feedback is required to decide whether the jaw appears to be aligned from the BLM loss spike displayed. Hence, the algorithm provides

semi-automatic alignment. A flowchart of the alignment algorithm is shown in Fig. 5.1, and a description of the variable names used is given in Table 5.1. The left and right collimator jaw positions are logged automatically, so that the beam centre and beam size can be displayed. The algorithm was implemented into the top-level collimator control software [40], and was tested and commissioned during the collimator setup at 450 GeV held at the end of February 2011.
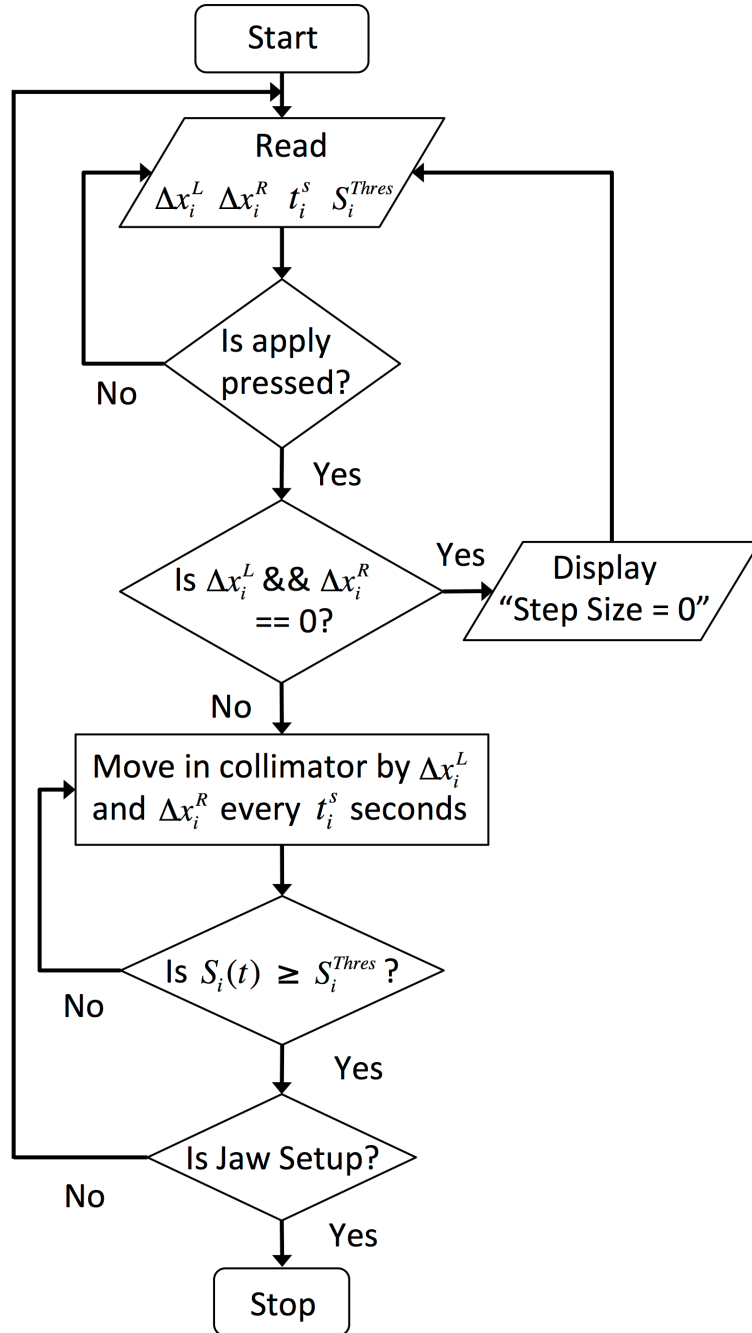
Figure 5.1: BLM-based feedback loop algorithm flowchart [76]. The decision made at the end whether to declare the jaw as setup is still made by the collimator expert, and hence the algorithm is semi-automatic.

Table 5.1: Overview of the variables used in the BLM-based feedback loop algorithm [76].

Variable Name	Description
Δx_i^L	Left jaw step size in μm
Δx_i^R	Right jaw step size in μm
S_i^{Thres}	Stop threshold in Gy/s
t_i^s	Time interval between each step in seconds
Apply	Button used to start the left and/or right jaw movement

5.3.2 Parallel collimator movement

Parallel collimator setup was developed to attempt to optimize the setup time, where any number of collimators can be aligned simultaneously to the beam. This means that the collimator jaw alignment algorithm discussed previously is executed for each selected collimator. Parallel collimator setup is used to provide a coarse but quick way of positioning a set of collimator jaws around the beam, after which each collimator is finely aligned in sequence. The algorithm was tested and commissioned during the collimator setup at 3.5 TeV flat top held in March 2011, as well as the 3.5 TeV setups after squeeze and during collisions on the 11th March 2011.

During the testing of this technique, an expected crosstalk effect was observed, in which the loss patterns registered on the BLM detector of a particular collimator were also being detected on other collimator BLM detectors around the LHC. An example is illustrated in Fig. 5.2, where the BLM threshold was set to 5×10^{-6} Gy/s for all collimators. Three have stopped moving as the losses on their BLM detectors have exceeded the threshold. Crosstalk prevented the parallel setup method from functioning efficiently, and therefore another algorithm was designed to identify which collimator jaw is at the beam.

The parallel setup algorithm uses a timer task (CheckColls) to check whether any collimators have stopped moving. As soon as a single collimator stops moving due to an exceeded BLM threshold, another timer task (CheckCollsT) is started to determine whether any other collimators also stop within a pre-defined time period T. This time period is set to 2 s to account for all possible software and network delays. If this is the case, then all the other collimators moving in parallel are stopped so that the algorithm can concentrate only on the first collimators. In case the BLM threshold set during the previous movement is now below the steady-state level (i.e. the collimator cannot be moved in again by a single step),
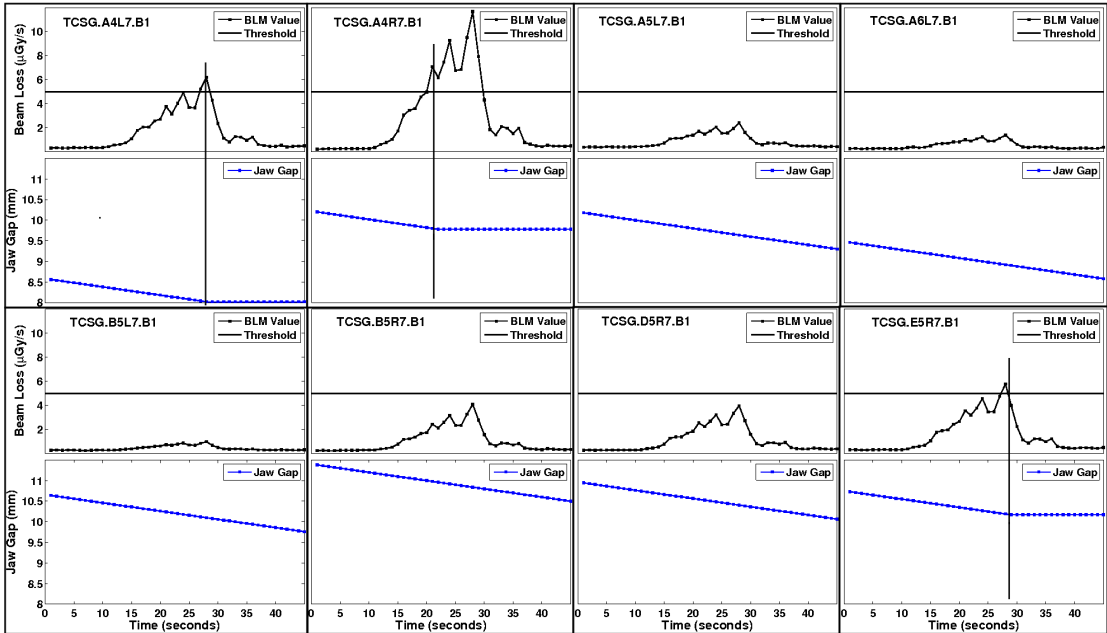
Figure 5.2: Both jaws of eight skew B1 collimators moving in parallel [76]. The similarity of the loss spike patterns detected on each BLM detector and the simultaneous stopping of three collimators highlights the need for being able to automatically identify which collimator jaw is actually aligned to the beam.

an option allows the user to instruct the program to automatically increase the BLM threshold in steps (S_{step}^{Thres}) up to a maximum amount S_{max}^{Thres}.

If the threshold is exceeded after the second step or thereafter, the collimator jaw is declared to be aligned to the beam, and the algorithm terminates to allow the operator to start the sequential alignment. For a flowchart of the parallel collimator setup algorithm, see Fig. 5.3. The variables employed are described in Table 5.2. A full description of the setup options is given in [78]. Beam tests were performed during the March 2011 alignment campaign for beam re-commissioning and in an MD study on the 2nd July 2011 [78].

5.3.3   Alignment algorithm input heuristics

The input parameters need to be adjusted as a function of the particle momentum, the stored beam intensity, and the depth of the jaw cut into the beam halo. Examples of values for the alignment inputs and the equivalent in beam σ for the step size are presented in Table 5.3. At injection energy, step sizes of 15 μm were required to be able to observe a significant loss spike, while at 3.5 TeV step sizes of 5 μm were sufficient. At higher energies, the beam distribution is narrower, and a large step size would make an unnecessarily large beam cut.
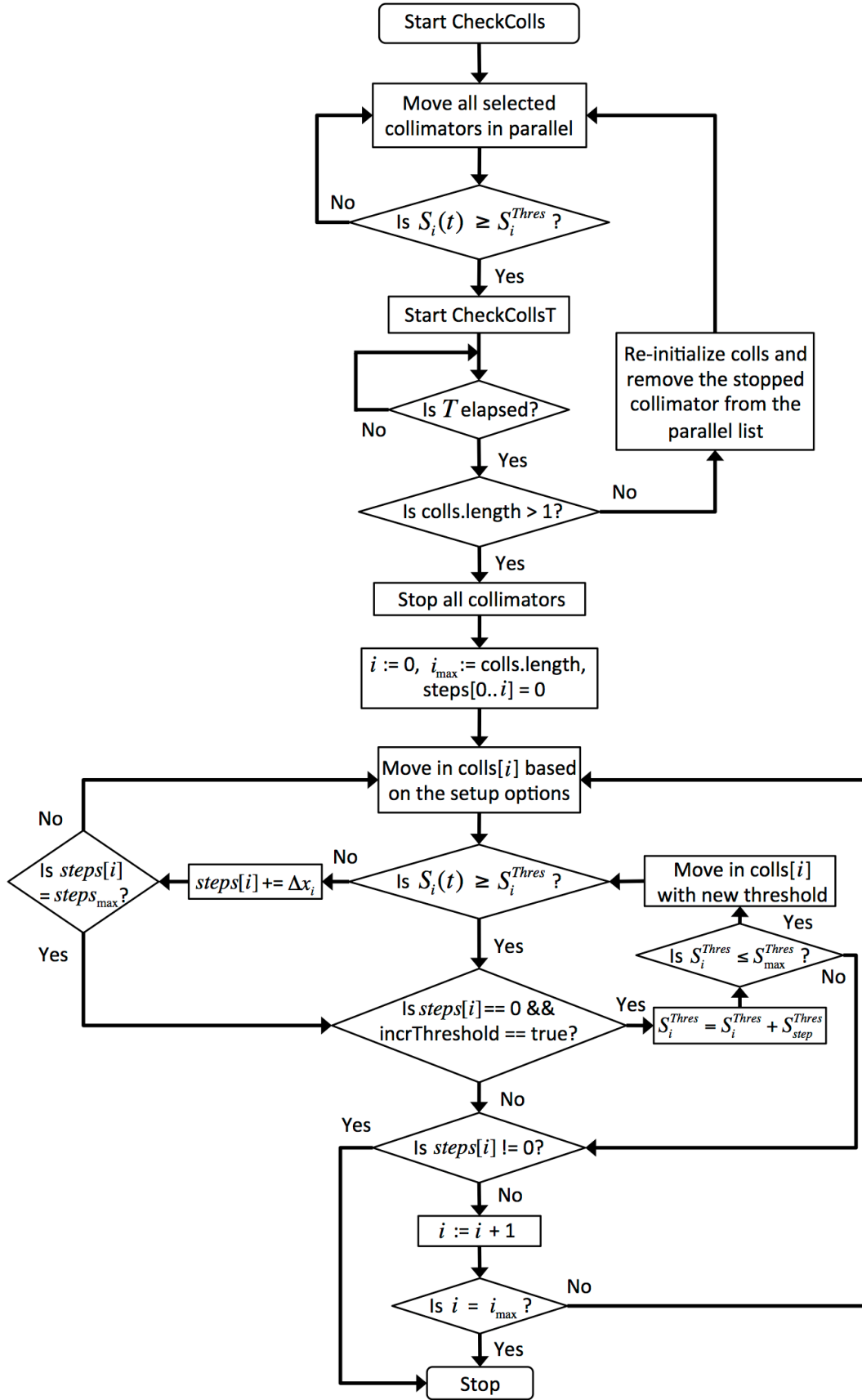
Figure 5.3: A flowchart of the software process that automatically identifies which collimator jaw is at the beam after multiple collimators stop moving due to crosstalk [76].

Table 5.2: Overview of the variables used in the parallel algorithm [76].

Variable Name	Description
CheckColls	Thread that polls the collimator status every second.
S_i^{Thres}	The user-specified loss threshold.
colls	An array of references to the stopped collimators.
CheckCollsT	Thread that checks whether any other collimators stop moving within a time interval T
T	If other collimators stop within the time interval T, they are added to colls.
Δx_i	The jaw step size in μm.
$steps$	The number of steps taken by a collimator.
$steps_{max}$	Maximum number of steps taken by a collimator until the BLM threshold is exceeded.
incrThreshold	If true, the threshold is increased if the losses are too high and the first jaw movement cannot be made.
S_{step}^{Thres}	The threshold increment value.
S_{max}^{Thres}	The maximum threshold that can be set.

At the start of the alignment, the steady-state loss rate is $\sim 4 \times 10^{-7}$ Gy/s. Hence, the loss threshold is set to 1×10^{-6} Gy/s, which corresponds to a loss of 1.25×10^{6} protons per second using an empirical calibration factor for converting between BLM signal and intensity loss [79]. As the collimator jaws cut further into the beam, the threshold is set manually according to the level steady-state loss signal observed after each loss spike, up to a maximum value of 1×10^{-4} Gy/s. This steady-state is a measure of the particle loss rate, and increases as the jaw cuts further into the beam and more secondary particles are scattered into the BLM detector. The time interval between each step is typically set to 0.125 to 1 s, as the maximum rate at which jaw movement requests can be sent to the low-level electronics is 8 Hz.

Table 5.3: Algorithm input heuristics and comparison to beam sigma [76].

Energy	Input Parameter	Typical Value
450 GeV	Step Size Δx_i (μm)	15
	Step Size $(\sigma)^2$	0.014
	Loss Threshold S_i^{Thres} (μGy/s)	1 - 100
	Step time interval t_i^s (s)	0.125 - 1
3.5 / 4 TeV	Step Size Δx_i (μm)	5
	Step Size $(\sigma)^2$	0.013
	Loss Threshold S_i^{Thres} (μGy/s)	1 - 100
	Step time interval (s) t_i^s	0.125 - 1

---

[2]Taken for the TCP.C6L7.B1 for which 1 σ corresponds to 1.05×10^{-3}m at 450 GeV and 3.76×10^{-4}m at 3.5 TeV

5.4 Loss spike recognition

5.4.1 Motivation for spike classification

Before the implementation of a loss spike classification algorithm, a collimator expert was required to visually judge if a loss pattern is a clear indication that the jaw has touched the beam during the setup process. This is carried out when the jaws stop moving after the pre-defined beam loss threshold is exceeded. An example of an optimal (clear) loss spike is illustrated in Fig. 5.4a , while a non-optimal loss spike is presented in Fig. 5.4b.

(a) Optimal Loss Spike

(b) Non-Optimal Loss Spike
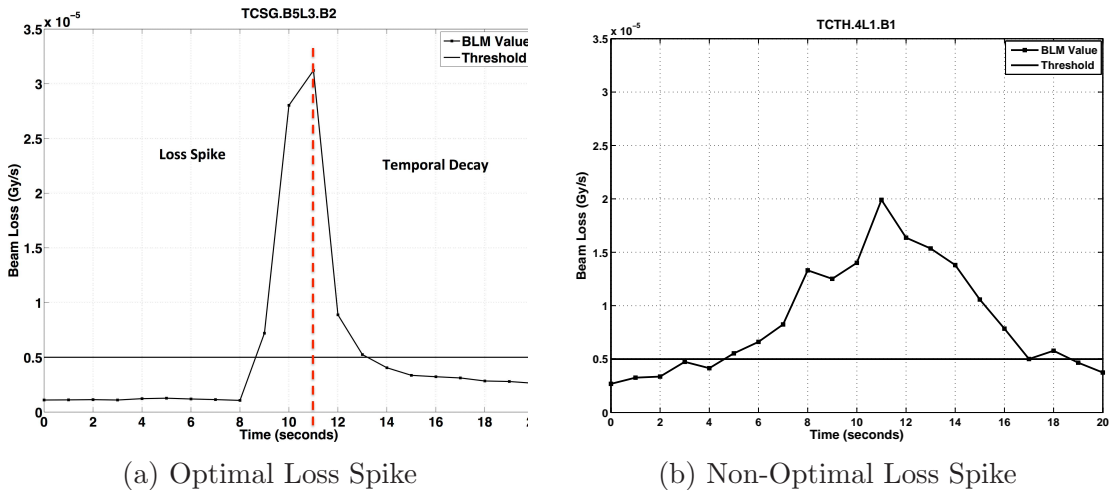
Figure 5.4: Optimal beam loss spike generated by the TCSG.B5L3.B2 collimator (a) and non-optimal beam loss spike generated by the TCTH.4L1.B1 collimator (b). A BLM threshold of 5×10^{-6} Gy/s was set in each case.

The beam loss signal (see Fig. 5.4) that is observed when a jaw touches the beam is the product of two physical processes. The first part of the signal is the loss spike. This sharp increase in the beam losses registered by the BLM detector is due to the scraping of particles from the beam halo, as illustrated in Fig. 5.5. The secondary particles formed as a result of the scraping are scattered into the BLM detector, and ionize the chamber to produce the spike. After the spike, the losses gradually decay to a steady-state signal. Any other pattern which does not have this structure is referred to as a non-optimal spike. This type of loss pattern can arise due to beam instabilities or mechanical vibrations of the opposite jaw which is close to the beam.

Collimator Jaw

Halo
Core
Halo

BLM

LHC Beam
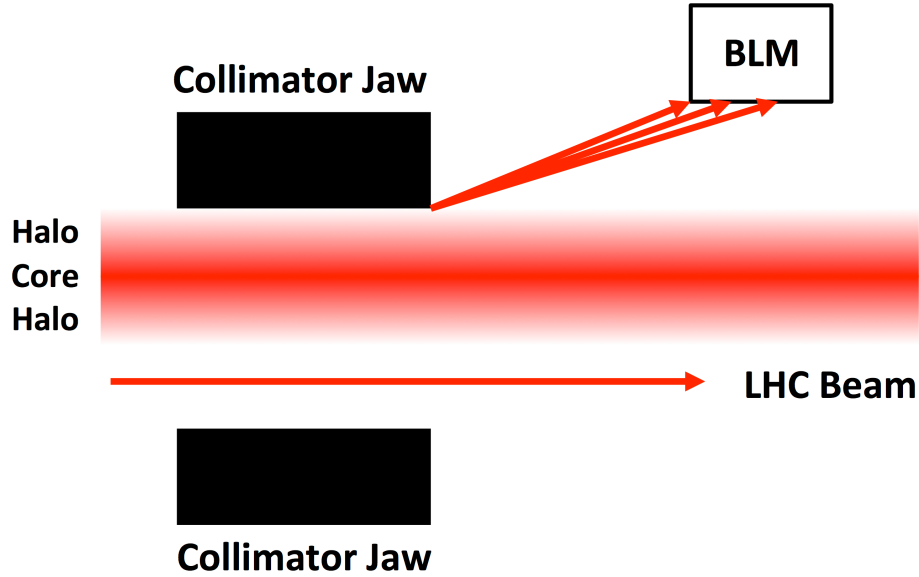
Collimator Jaw

Figure 5.5: Scraping of the beam halo when the collimator jaw is aligned to the beam. The scattered secondary particles are detected by a BLM detector downstream and result in a time-varying signal.

5.4.2 Support Vector Machines

The Support Vector Machine (SVM) algorithm is a supervised learning technique that can be used for classification of data. It operates by maximizing the margin between the training data points and the decision boundary [80]. SVMs perform well and have been employed in many applications, ranging from image recognition to bioinformatics. Kernel functions are particularly useful when the data are non-separable. They map data on to a higher dimensional space so that a linear classifier can then be used. Examples include the linear, polynomial and Radial Basis Function (RBF) kernels. The RBF kernel is the most popular of these, as it is perceived to classify data with the best performance for most applications [81]. It maps data to an infinite-dimensional Hilbert space through the following relation:

$$K(x, y) = e^{(-\gamma \|x-y\|^2)} \tag{5.2}$$

where x is the set of labelled training vectors, y is the set of classes and γ determines the width of the RBF. Another parameter is the penalty factor C, which if set too high results in a high penalty for non-separable data (overfitting), and if set too low leads to underfitting.

5.4.3 Feature selection

The performance of SVM is very dependent on the selection of the features. Fits can be applied separately to both components of the loss pattern in Fig. 5.4. The loss spike component was folded about the maximum value so that a Gaussian function could be fitted to it (see Fig. 5.6a), while a power function was used to fit the temporal decay component as shown in Fig. 5.6b. The fits were performed using the Ezyfit MATLAB tool [82], which uses MATLABs built-in fminsearch function based on the Nelder-Mead method.

A total of 6 input features were then considered, of which two pertain to the Gaussian fit and two to the power fit [83]:

- **Maximum Value:** determined by taking the maximum of the ten BLM values observed after the jaws have stopped moving. The losses may continue to increase after the threshold is exceeded, as shown in Fig. 5.4a.

- **Minimum Average:** the average of the three smallest loss points of the seven loss points immediately preceding the maximum value. The smallest values are considered to eliminate any spikes due to a previous movement. An optimal spike generally has a high maximum value relative to the minimum average.

- **Variance:** the width of the Gaussian fit. Generally, a spike with a smaller width is more optimal, as it reflects a sharp increase and a quick decrease of the losses. This value is equivalent to σ for the example shown in Fig. 5.6a.

- **Gaussian Correlation Coefficient:** indicates the proximity of the loss pattern to the Gaussian fit. The closer this value is to unity, the sharper the loss spike. This value corresponds to R in Fig. 5.6a.

- **Power Coefficient:** a steep temporal decay is indicative of an optimal spike, equivalent to n in the example in Fig. 5.6b.

- **Power Correlation Coefficient:** indicates the proximity of the loss pattern to the power fit. The temporal decay becomes smoother as this value approaches unity. This value corresponds to R in Fig. 5.6b.

(a) Gaussian Fit

(b) Power Fit
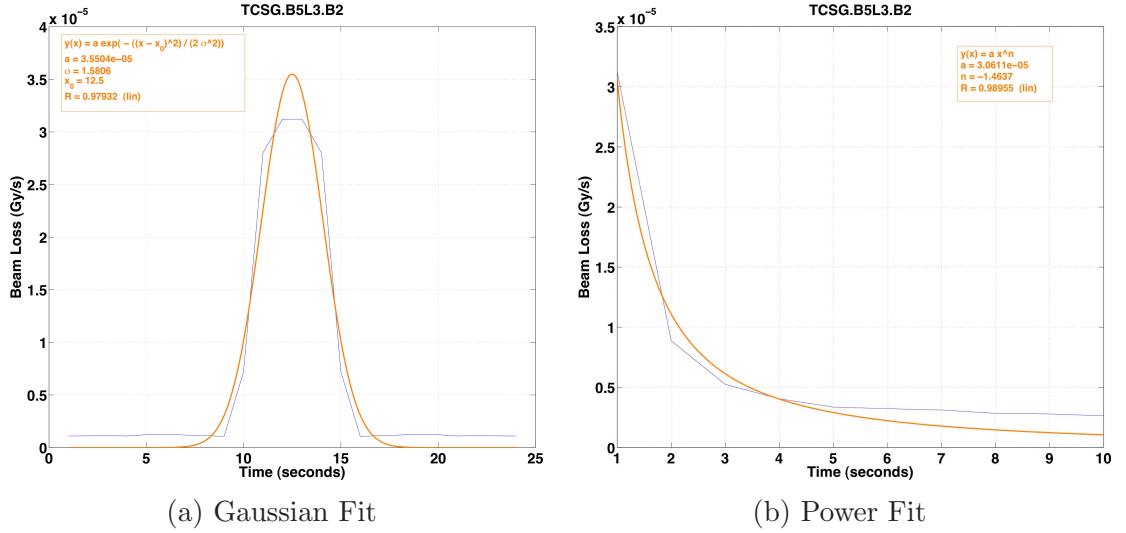
Figure 5.6: Fitting a Gaussian function to the loss spike folded about the maximum value (a) and a power function to the temporal decay from the maximum loss value onwards (b).

Ten examples of the un-scaled data points, five from each class, are listed in Table 5.4. Optimal spikes belong to the "+1" class, while non-optimal spikes belong to the "-1" class.

Table 5.4: Examples of un-scaled observations and their feature values [83].

Sample	Input Feature Values						Class
	1	2	3	4	5	6	
1	2.2512E-05	1.12315E-06	0.95979	0.98560	-1.09249	0.99182	+1
2	1.1588E-05	6.59159E-07	1.41285	0.98964	-1.28319	0.99160	+1
3	1.1318E-05	5.18305E-07	1.31249	0.99288	-1.06120	0.98716	+1
4	2.2603E-05	1.03017E-06	1.47528	0.97375	-0.91764	0.94713	+1
5	1.6212E-05	1.21613E-06	1.28399	0.96858	-1.01171	0.98796	+1
6	2.6044E-06	2.11741E-06	15.4612	0.09631	-0.28361	0.76970	-1
7	2.9027E-06	1.76021E-06	10.5298	0.45652	-0.08469	0.34159	-1
8	6.0098E-06	3.43113E-06	3.30181	0.89405	-0.28733	0.88192	-1
9	1.5770E-06	7.91728E-06	3.16919	0.93638	0.00318	0.01111	-1
10	1.1683E-06	5.98400E-07	3.80136	0.95359	-0.58202	0.95705	-1

5.4.4 SVM training

The LIBSVM tool presented in [84] was used for training and testing of the SVM model. The first step was to linearly scale the training data to values between -1 and 1. Scaling is done to avoid attributes in larger numeric ranges dominating those in smaller ranges. The scaling factors were then used to scale the test data in the same range.

The RBF kernel was chosen as it has less hyper-parameters, and presents fewer numerical difficulties. A grid search on C and γ was performed using 5-fold cross-validation to determine the optimal values for these parameters. A value of 32768 was obtained for C, while a value of 0.125 was determined for γ. Training was performed with these parameters using the RBF kernel to produce a model.

5.4.5 Experimental results

A total of 444 samples were available, of which 222 were taken from a setup at 3.5 TeV for the tertiary collimators, and the remaining 222 samples were obtained from a setup at 3.5 TeV of the IR3 collimators. The numbers of samples for each category were chosen to maintain a 1:1 training to testing ratio. Predictions were made using the model developed in the training phase. The SVM model parameters, together with the prediction accuracy, are shown in Table 5.5. An accuracy rate of 97.3% was achieved for the training data, while 82.4% of the test data points were classified correctly. This gives an overall prediction rate of 89.9%.

Table 5.5: Final parameters of the SVM-trained beam loss spike classifier [83].

Parameter	Values
Number of Features	6
Number of Classes	2
C parameter search range	2^{-50} - 2^{50}
γ parameter search range	2^{-15} - 2^{15}
C	32768
γ	0.125
v	5
Training dataset prediction rate	97.2973%
Testing dataset prediction rate	82.4324%
Overall prediction rate	89.8649%
Type of SVM	C-SVM
Kernel	RBF

5.5 Automatic threshold selection

5.5.1 Data analysis

In the 2011 LHC run, four major alignment campaigns were carried out using the semi-automatic alignment tool [76] to determine the beam centres at the collimators during different parts of the LHC machine cycle. The alignments are performed at 450 GeV (injection energy), 3.5 TeV flat top, 3.5 TeV after the beam size is reduced (squeezed) in the experimental points and at 3.5 TeV with the beams in collisions. The thresholds at the start of each repetitive jaw movement towards the beam were input manually by the operator. This provides a lot of training data which can be exploited when attempting to find an automatic technique for setting the threshold.

When setting the threshold at time $t = 0$, the operator generally gives more importance to the most recent values ($BLM_{t=-5}$ to $BLM_{t=0}$), but must also consider values back to $BLM_{t=-19}$. This is because a spike occurring previously might still be decaying back to a steady-state value, although a fixed waiting period of ∼10 seconds is enforced before moving the same or another jaw. Mathematically, the assignment of different priorities to the data depending on their occurrence in time can be expressed by means of the exponentially weighted moving average (EWMA), which is given as follows for a 20 second window:

$$EWMA_{BLM} = \frac{\sum_{i=1}^{20} e^i \times BLM_{t=i-20}}{\sum_{i=1}^{20} e^i} \tag{5.3}$$

A total of 475 samples of the steady-state BLM signal in 20 second windows and the subsequent correct threshold set by the operator (training threshold) were extracted from the logged data. Two examples of BLM signal windows and the corresponding EWMA and threshold are shown in Table 5.6. In the first example, the signal is stable at ∼1.00×10^{-6} Gy/s, while in the second example, the window includes part of the temporal decay of a previous loss spike. The larger weights were assigned to the most recent values.

If the training thresholds are plotted as a function of the EWMA, a power fit can be applied to the data as shown in Fig. 5.7. There is a correlation coefficient of 0.96611 between the measured data and the fit. The training thresholds are discrete as the operators could select from a drop-down menu with a list of pre-determined

Table 5.6: Two examples of BLM signal windows, the corresponding EWMA, the threshold set by the operator and the calculated threshold.

$t[s]$	BLM Value [Gy/s]	BLM Value [Gy/s]
-19	1.66×10^{-6}	8.88×10^{-6}
-18	1.51×10^{-6}	8.83×10^{-6}
-17	1.39×10^{-6}	6.80×10^{-6}
-16	1.35×10^{-6}	6.90×10^{-6}
-15	1.31×10^{-6}	6.96×10^{-6}
-14	1.18×10^{-6}	6.50×10^{-6}
-13	1.31×10^{-6}	6.94×10^{-6}
-12	1.27×10^{-6}	6.76×10^{-6}
-11	1.25×10^{-6}	6.53×10^{-6}
-10	1.23×10^{-6}	6.52×10^{-6}
-9	1.19×10^{-6}	5.99×10^{-6}
-8	1.10×10^{-6}	5.50×10^{-6}
-7	1.15×10^{-6}	5.74×10^{-6}
-6	1.31×10^{-6}	5.66×10^{-6}
-5	1.12×10^{-6}	4.86×10^{-6}
-4	1.10×10^{-6}	4.02×10^{-6}
-3	1.14×10^{-6}	4.17×10^{-6}
-2	1.06×10^{-6}	4.12×10^{-6}
-1	1.00×10^{-6}	4.16×10^{-6}
0	0.97×10^{-6}	3.98×10^{-6}
EWMA	1.00×10^{-6}	4.05×10^{-6}
Training Threshold	4.00×10^{-6}	10.0×10^{-6}
Calculated Threshold	3.73×10^{-6}	12.5×10^{-6}

thresholds to speed up the alignment [76]. Based on this fit, the threshold set at the start of each jaw movement can therefore be calculated as:

$$S_i^{Thres} = 0.53584 \times (EWMA_{BLM})^{0.85916} \tag{5.4}$$

The maximum threshold that can be set is fixed at 1×10^{-4} Gy/s, which is an order of magnitude below the BLM dump thresholds. As the alignment generally takes place at 3.5 to 4 σ from the beam centre, the steady-state BLM signal ranges from 5×10^{-7} to 8×10^{-5}, and hence the maximum threshold should rarely be reached.
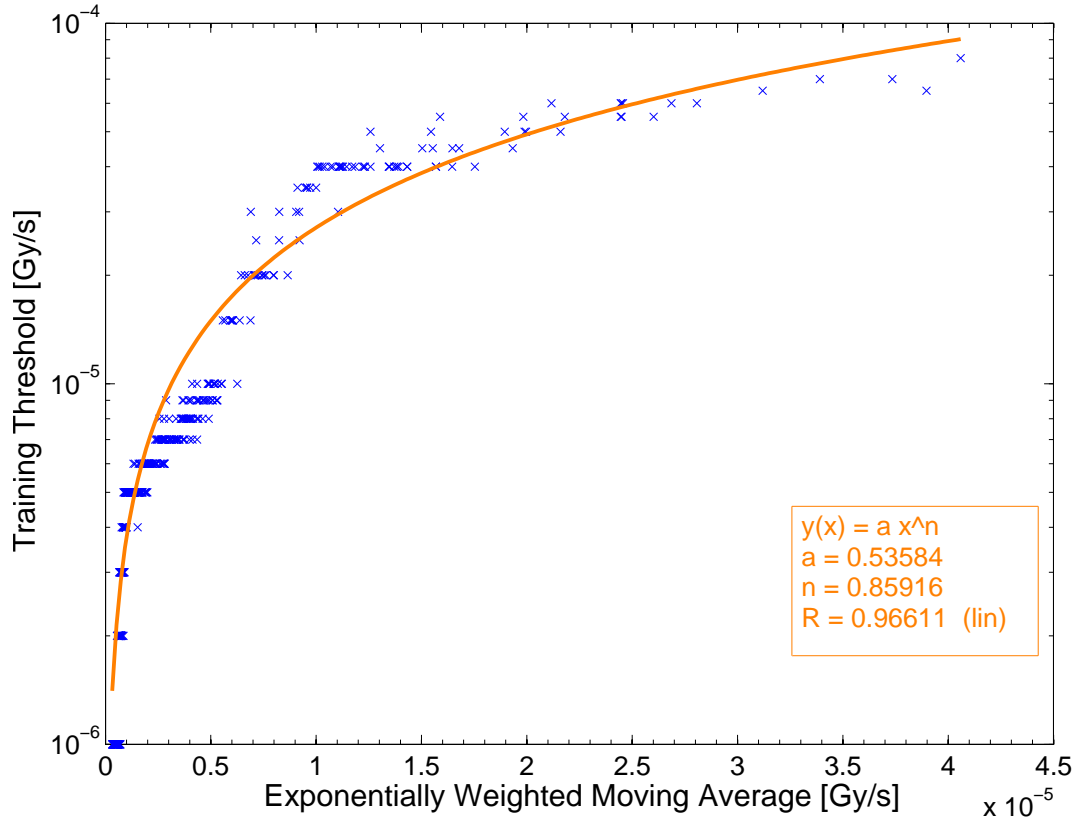
Figure 5.7: Loss thresholds applied before the start of a jaw movement as a function of the exponentially weighted moving average of the BLM signal, from [85]. A power fit can be applied to the data.

5.5.2 Results

The BLM signal threshold selection function in Eq. (5.4) was implemented into the top-level Java collimator control application. Testing was carried out during alignments held in March 2012. A plot showing the synchronized BLM signal, calculated threshold and collimator jaw gap is given in Fig. 5.8. The data are taken from an alignment of a primary collimator (TCP) at 4 TeV flat top. The jaw gap is plotted, rather than the individual jaw positions, to give a clearer picture of the small jaw movements. During the tests, no time-consuming beam dumps were triggered due to high losses, which confirms the effectiveness of the loss threshold function.
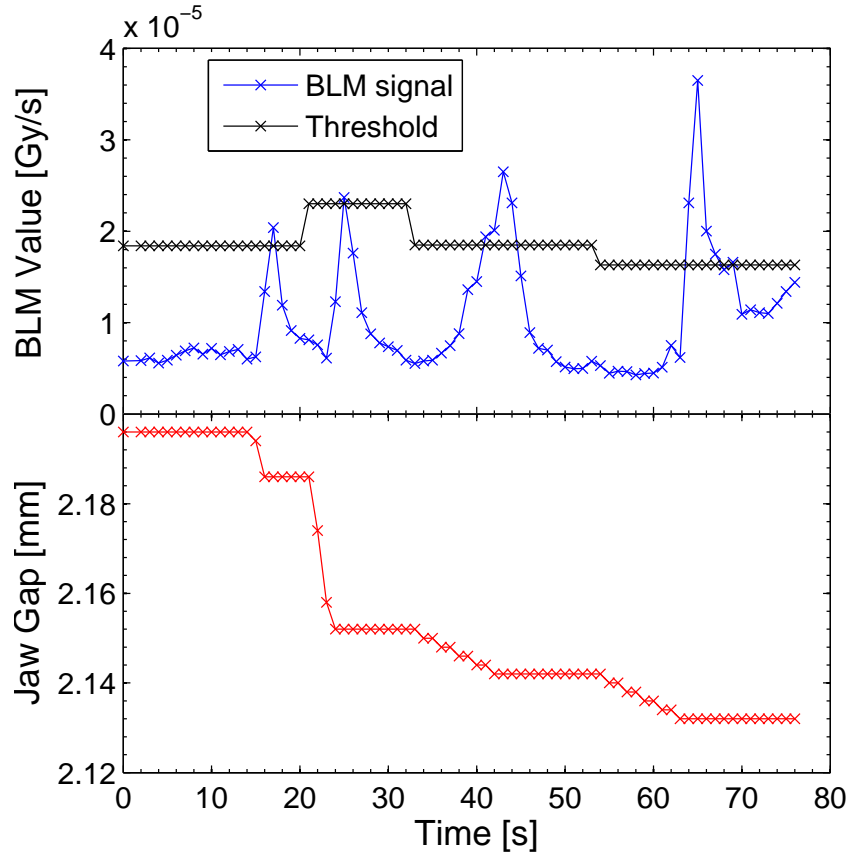
Figure 5.8: The BLM signal and calculated threshold (a) and the collimator jaw gap (b) as a function of time. The individual jaws are aligned four times, and at the start of each jaw movement a new threshold is set depending on the previous BLM values (t[0] = 08:55:57, 29.03.2012).

5.6 Coarse BPM-interpolation based alignment

An approximation to the beam centres at the collimators can be obtained from an interpolation of the orbit measured at specific locations by BPMs. These monitors are placed on each side of the warm quadrupoles, thus providing the minimum configuration that allows a linear interpolation of the closed orbit, dispersion and β functions [55].

An example of the LHC beam orbit through various points in the machine is shown in Fig. 5.9. With BPMs located at point 1 and 2, the orbit at an intermediate point S can be calculated using linear transfer matrices. The interpolation is done per plane and per segment, which is defined as the region between two BPMs. The orbit x_2 and angle x_2' at point 2 can be established from point 1 using a transfer matrix:
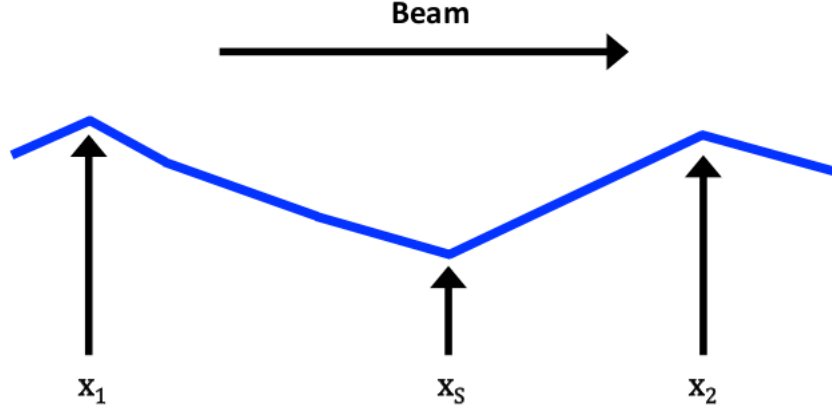
Figure 5.9: Example of the beam orbit through points 1, S and 2 (from [86]). With BPMs located at point 1 and 2, the objective of the interpolation is to find the orbit at point S.

$$\begin{pmatrix} x_2 \\ x'_2 \end{pmatrix} = M_{12} \begin{pmatrix} x_1 \\ x'_1 \end{pmatrix} = \begin{pmatrix} C_{12} & S_{12} \\ C'_{12} & S'_{12} \end{pmatrix} \begin{pmatrix} x_1 \\ x'_1 \end{pmatrix}$$

where M_{12} is the transfer matrix between point 1 and 2 with elements:

$$C_{12} = \sqrt{\frac{\beta_2}{\beta_1}} (\cos \mu_{12} + \alpha_1 \sin \mu_{12}) \tag{5.5}$$

$$C'_{12} = \frac{\alpha_1 - \alpha_2}{\sqrt{\beta_1 \beta_2}} \cos \mu_{12} - \frac{1 + \alpha_1 \alpha_2}{\sqrt{\beta_1 \beta_2}} \sin \mu_{12} \tag{5.6}$$

$$S_{12} = \sqrt{\beta_1 \beta_2} \sin \mu_{12} \tag{5.7}$$

$$S'_{12} = \sqrt{\frac{\beta_1}{\beta_2}} (\cos \mu_{12} - \alpha_2 \sin \mu_{12}) \tag{5.8}$$

where α and β are the Twiss parameters and μ is the betatronic phase advance, which were introduced in Chapter 1. Similarly for the orbit from point 1 to S:

$$\begin{pmatrix} x_S \\ x'_S \end{pmatrix} = M_{1S} \begin{pmatrix} x_1 \\ x'_1 \end{pmatrix}$$

The interpolated orbit at point S can hence be expressed as:

$$x_S = C_{1S}x_1 + S_{1S}\frac{x_2 - C_{12}x_1}{S_{12}} \tag{5.9}$$

The interpolated orbit is one of the features provided by the LHC Aperture Meter [87], an application which provides the operators with real-time information on the current machine bottlenecks. A screenshot of the Aperture Meter showing the beam orbit at IP8 is provided in Fig. 5.10.
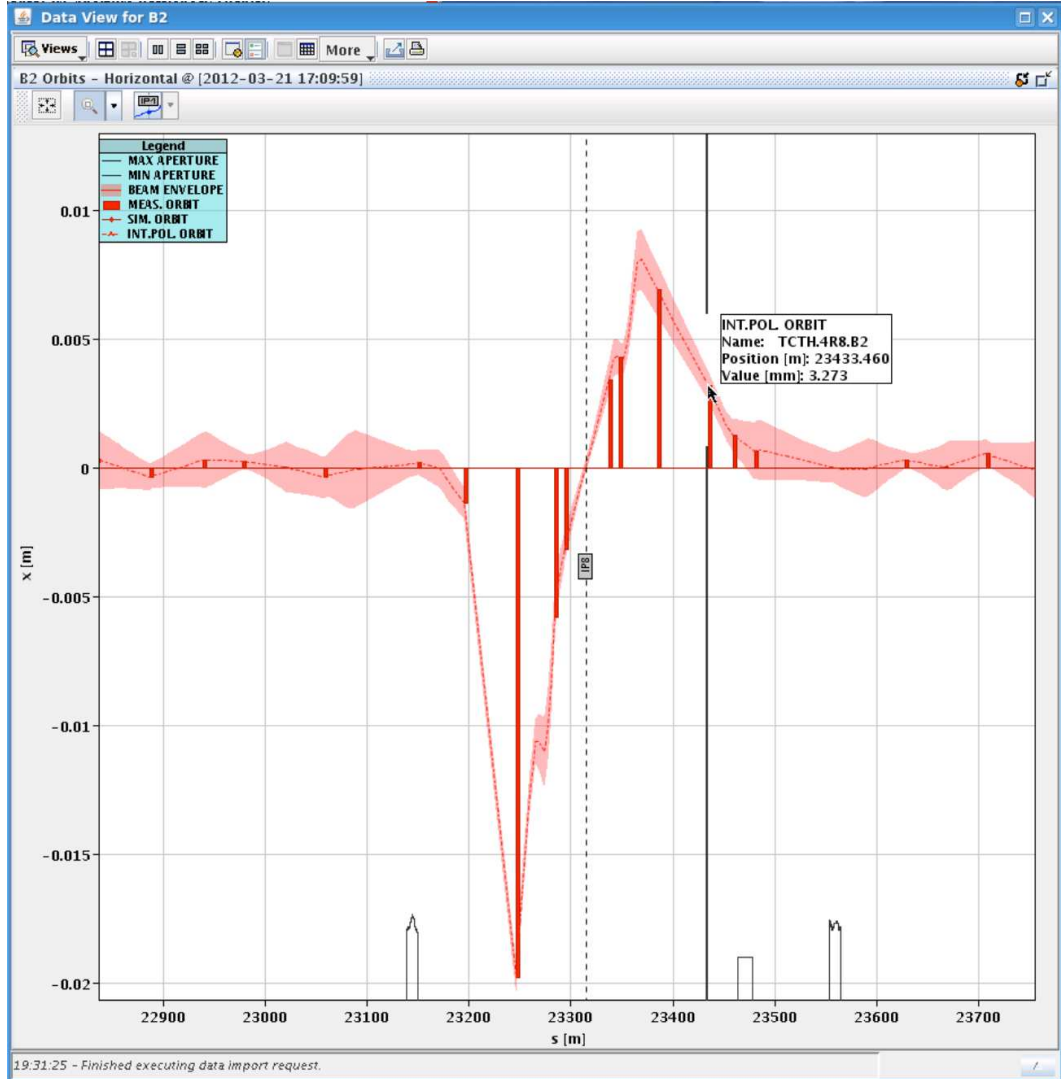
Figure 5.10: Screenshot of the LHC Aperture Meter software application, showing the beam orbit as a function of the longitudinal position in the crossing plane in IR8 surrounded by the 1 σ beam envelope. The beam energy is 4 TeV.

Finally, in order to compare to the beam centres found from beam-based collimator alignment, the interpolated orbit needs to be transformed to the collimator coordinate system:

$$\Delta_i^{int} = x_S^{hor}\cos\psi_i + x_S^{ver}\sin\psi_i \tag{5.10}$$

where ψ_i is the azimuthal tilt angle of the collimator i in the transverse plane. For B2 collimators, the sign of the horizontal component is inverted. The interpolation is highly dependent on the BPMs selected, and invalid monitors which give erroneous readings need to be removed from the calculation. The interpolation accuracy derives from the linearity of the BPM system (1% of the half radius, corresponding to $\sim130\mu$m for arc BPMs).

5.6.1   Comparison results

The interpolated orbit at each collimator was extracted for the same timestamp at which the collimator was aligned. Both datasets are acquired and logged at a rate of 1 Hz. Comparison results are presented, showing the averages over multiple alignments for two stages in the LHC machine cycle when the alignment is performed, for data from the 2011 and 2012 runs.

5.6.1.1   Results in 2011

Comparison results for 2011 are shown as histograms in Fig. 5.11a and Fig. 5.11b, for collimators with operational jaw half-gaps above $6.3\,\sigma$. The absolute differences generally lie within ±1 mm, but large differences can be observed for the tertiary collimators (TCTs). The large differences at these locations are likely due to a poorer performance of the BPMs located in this region.
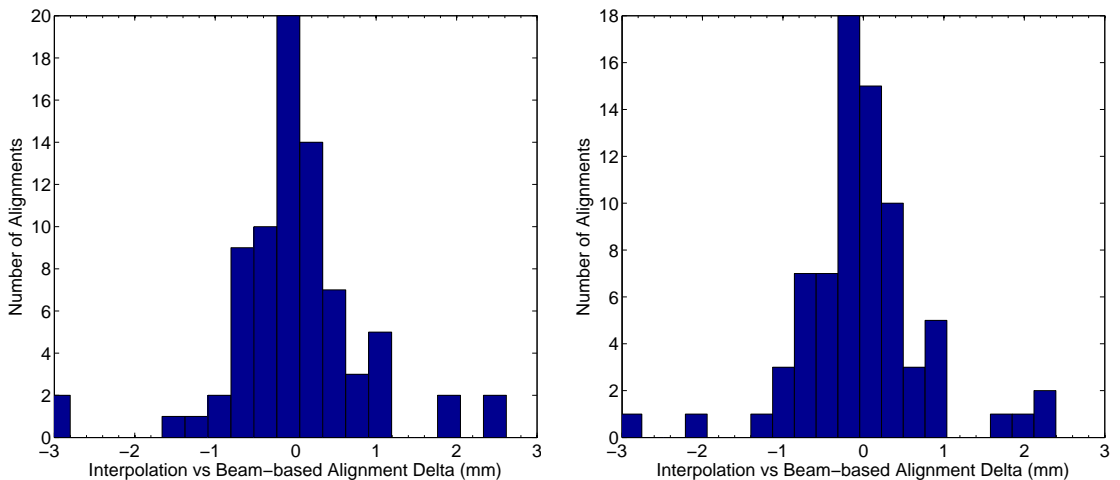
(a) Measurements at Injection (450 GeV)   (b) Measurements at Flat Top (3.5 TeV)

Figure 5.11: Absolute differences between the BPM-interpolated and the beam-based centres at the LHC collimators in 2011. The values at the extremities are those for the TCTs.

The statistics for the 2011 run are presented in Table 5.7. The TCTs are excluded from the analysis due to the poorer interpolation quality, as well as collimators already close to the beam at top energy, such as the TCPs and IR7 TCSGs. The absolute average for the injection dataset corresponds to 0.007 mm, while for flat top the absolute average is -0.059 mm. The standard deviation is 0.577 mm at injection and 0.542 mm at flat top. The largest beam centre shift at flat top (excluding the TCPs, IR7 TCSGs and TCTs) occurs at the TCLA.C6R7.B1, where 1.752 mm corresponds to 3.428 σ.

Table 5.7: BPM-interpolation and beam-based comparison statistics for 2011. The values for TCT and IR7 TCP collimators are removed from both datasets, and the IR7 TCSG values are also removed from the flat top dataset.

Dataset	Mean (mm)	Std Dev (mm)	Max (mm)	Max Shift (σ)
Injection	0.007	0.577	1.884	1.245
Flat Top	-0.059	0.542	1.752	3.428

5.6.1.2   Results in 2012

A similar analysis was performed for the collimator alignments in 2012 (see Fig. 5.12a and Fig. 5.12b). Once again, large absolute differences were observed for the TCTs. The statistics for the 2012 run listed in Table 5.8 show an average of -0.063 mm and 0.031 mm for the injection and flat top datasets respectively. The standard deviation is 0.484 mm and injection and 0.537 mm at flat top. The largest beam centre shift at flat top (excluding the TCPs, IR7 TCSGs and TCTs) occurs once again at the TCLA.C6R7.B1, where 1.942 mm corresponds to 3.977 σ.

5.6.2   BPM-interpolation guided alignment tool

The reproducible correlation between the measured and interpolated centres can be exploited during the alignment. This is done by moving in the jaws in one step at a rate of 2 mm/s from the initial positions to a safe margin around the beam without scraping any beam, instead of using the automatic setup tool with small step sizes. As it is not possible to accurately measure the beam size at the collimators without aligning them, the jaws can be opened to a half gap which considers the initial cut made by a reference collimator (IR7 TCP) and a safety margin. Based on these parameters and the nominal 1 σ beam size, the left and right jaws are moved to the settings:

(a) Measurements at Injection (450 GeV) (b) Measurements at Flat Top (4 TeV)
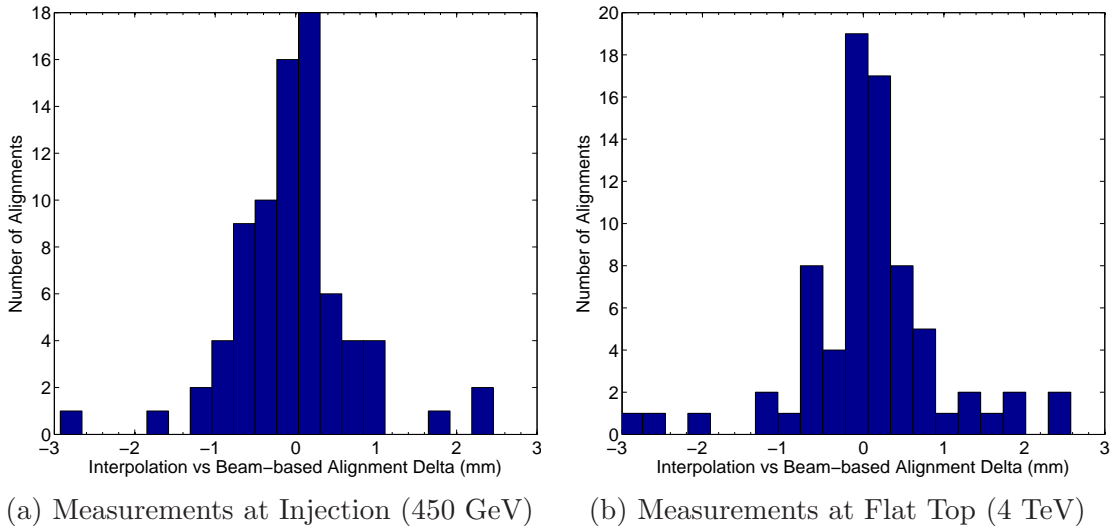
Figure 5.12: Absolute differences between the BPM-interpolated and the beam-based centres at the LHC collimators in 2012. The values at the extremities are those for the TCTs.

Table 5.8: BPM-interpolation and beam-based comparison statistics for 2012. The values for TCT and IR7 TCP collimators are removed from both datasets, while the IR7 TCSG values are removed from the flat top dataset.

Dataset	Mean (mm)	Std Dev (mm)	Max (mm)	Max Shift (σ)
Injection	-0.063	0.484	1.129	0.560
Flat Top	0.031	0.537	1.942	3.977

$$x_i^L = x_i^{int.} + (N_{TCP} + N_{margin}) \times \sigma_i^n + \sigma_i^{m,int.} \qquad (5.11)$$

$$x_i^R = x_i^{int.} - (N_{TCP} + N_{margin}) \times \sigma_i^n - \sigma_i^{m,int.} \qquad (5.12)$$

where $x_i^{int.}$ is the interpolated beam centre at collimator i, N_{TCP} is the half-gap of the IR7 TCP in units of σ, σ_i^n is the nominal 1 σ beam size at collimator i and $\sigma_i^{m,int.}$ is the standard error between the interpolated and the measured centre from beam-based alignment per collimator, based on the empirical analysis. Once the IR7 TCPs in both beams are aligned, at a half gap usually between 3 and 4 σ, then a further safety margin N_{margin} is applied (the maximum recorded shift on a collimator-by-collimator basis) over and above the cut made by the TCP.

The software tool was written in Java, and was integrated into the top-level collimator control application. When the user starts the tool, a query is made to the LHC Aperture Meter, which returns the interpolated beam centres updated
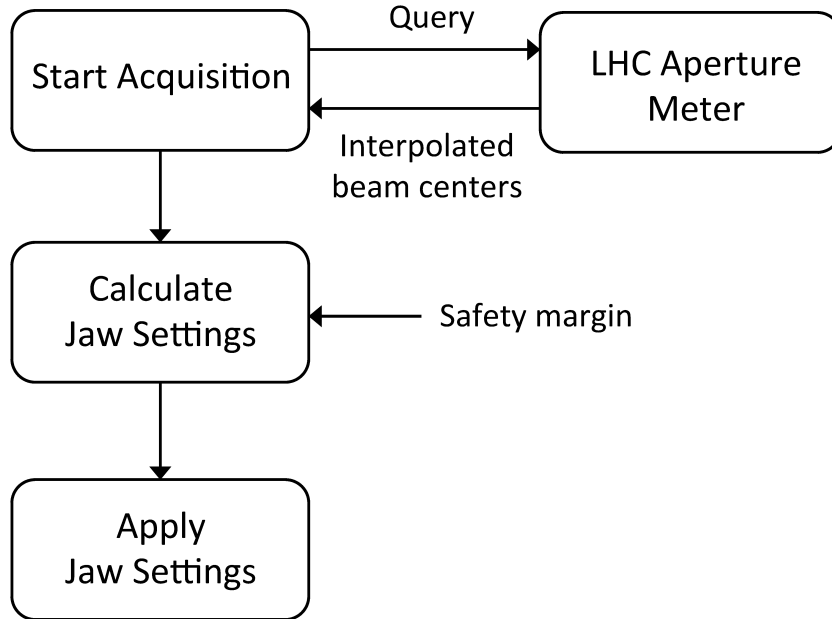
Figure 5.13: Flowchart of how the tool acquires the interpolated BPM readings and applies the tighter jaw settings based on a safety margin defined by the user, from [88].

at a rate of 1 Hz. Once a safety margin is selected, the tool calculates the new tighter settings which will be sent to the hardware (see flowchart of the operation in Fig. 5.13). A screenshot of the GUI used to move in the collimators based on these values is given in Fig. 5.14. The checkboxes on the right-hand side allow the user to prevent the tool from moving the jaws if they are not selected.

5.6.3 Experimental results

The tool was tested during an LHC MD study performed at 450 GeV in April 2012 [89]. In the study, 23 horizontal collimators in IR3 and IR7 in both beams were moved from the initial parking positions to tighter settings around the interpolated orbit. The TCTs were not aligned during this feasibility study, as the interpolation is known to be worse at these collimator locations due to a less reliable BPM signal. The TCP cut was made at 4.2 σ, and the value of the safety margin was ~2 σ to give an overall half gap of ~6.2 σ. The initial and final jaw positions in mm and beam σ are shown in Fig. 5.15a and Fig. 5.15b.

If these collimators were to reach the tighter settings using the automatic setup tool, the elapsed time would be much larger. Typically, if a step of 5 μm is made every 1 s, the time taken for all 23 collimators aligned during the MD to reach the tighter settings would be 27 minutes. In this case, therefore, the tool provided

Collimator	BPM Center	Current Left	Current Right	New Left	New Right	
TCSG.A5L7.B1	−0.373	2.105	−2.585	2.112	−2.858	☐
TCP.C6R7.B2	0.150	2.030	−0.990	2.509	−2.210	☐
TCSG.6L7.B2	−0.421	3.180	−3.435	2.979	−3.821	☑
TCLA.7L3.B2	−0.164	5.205	−5.545	1.491	−1.819	☑
TCLA.6L3.B2	0.410	5.350	−6.125	2.616	−1.796	☑
TCLA.B5L3.B2	−0.089	5.055	−7.360	2.278	−2.456	☑
TCSG.B5L3.B2	−0.150	2.940	−3.680	1.374	−1.674	☑
TCSG.A5L3.B2	−0.160	2.510	−3.405	1.227	−1.548	☑
TCSG.4L3.B2	−0.214	1.985	−2.595	0.916	−1.344	☑
TCSG.5R3.B2	−0.168	2.865	−3.740	1.353	−1.688	☑
TCP.6R3.B2	−0.114	3.850	−4.030	2.107	−2.336	☑
TCLA.A7L7.B2	−0.114	2.620	−1.245	1.532	−1.760	☑
TCLA.D6L7.B2	0.328	2.105	−1.730	1.965	−1.308	☑
TCLA.B6L7.B2	−0.032	3.115	−2.890	2.389	−2.454	☑
TCSG.B4R7.B2	−0.268	1.165	−3.280	2.098	−2.635	☑
TCP.B6R7.B2	0.167	1.045	−1.515	2.203	−1.868	☐
TCSG.A5R7.B2	−0.069	2.885	−1.805	2.416	−2.554	☐

☑ Select All

Half Gap (sigma) 6 ▼

Center Delta (mm) 0.5 ▼

Acquire   Move   Stop

Figure 5.14: Screenshot of the GUI used to set the collimator jaws around the BPM-interpolated orbit, from [88].

a speed-up by a factor 400 as it would take 4 seconds for the jaws to move from the initial to the final positions at the maximum speed of 2 mm/s. The automatic setup tool was then used to move the jaws further inwards until they touched the beam halo and the alignment was completed. Considering also the beam-based alignment of the IR3 TCPs (for the momentum halo cut) and the IR7 TCPs (to define the betatron halo for alignment), the setup for a total of 27 collimators

(a) Initial and final jaw half gaps in mm

(b) Initial and final jaw half gaps in σ
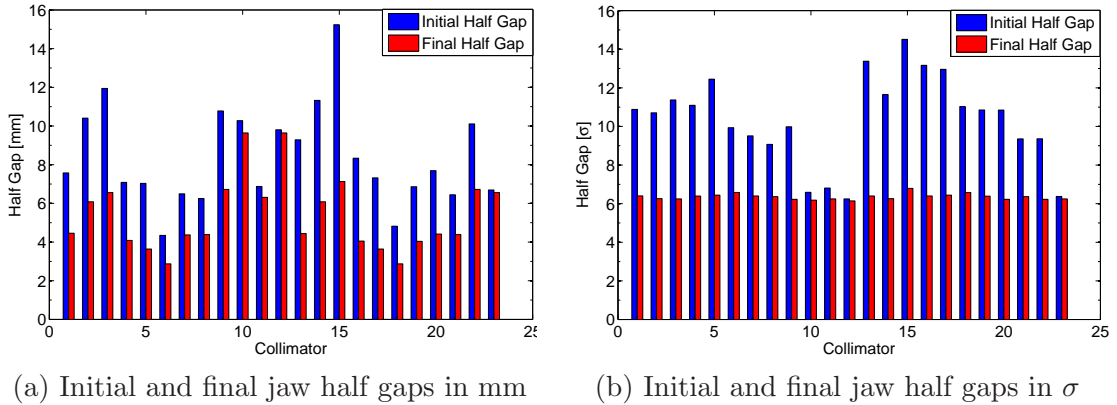
Figure 5.15: Comparison of the initial parking positions and the tighter half gaps after the tool was executed, in units of mm (a) and σ (b). Note the large change for collimators initially positioned with a half gap of more than 10 σ.

including the BPM-interpolation guided initialization lasted 1 hour 45 minutes. If this time is scaled with the total number of collimators (86), an extrapolated setup time of 5.5 hours is reached, which is 2 hours less than the previous best time achieved.

The time gain is more than the expected 27 minutes, as the time spent by the algorithm resuming the alignment after BLM signal crosstalk during the automatic setup [76] is greatly minimized, as all the collimators are quite close to the beam. The crosstalk in the BLM signal occurs when one collimator out of a group of simultaneously moving collimators touches the beam edge, and the resulting loss spike is detected also on the BLM detectors immediately downstream of the other collimators. At the start of an alignment without BPM-based initialization, some collimators may already be close to the beam. Each time crosstalk occurs, the stepwise movement of other collimators much further from the beam is halted as the parallel alignment algorithm sequentially re-aligns each stopped collimator to identify which one is touching the beam.

5.7 Alignment task sequencer

Each of the above algorithms is executed for as many times as there are collimator planes that need to be aligned. The software structure responsible for ensuring that all collimators are aligned plane by plane, and that each algorithm is called in order is called the *alignment task sequencer*. A flowchart of the alignment task sequencer is provided in Fig. 5.16.
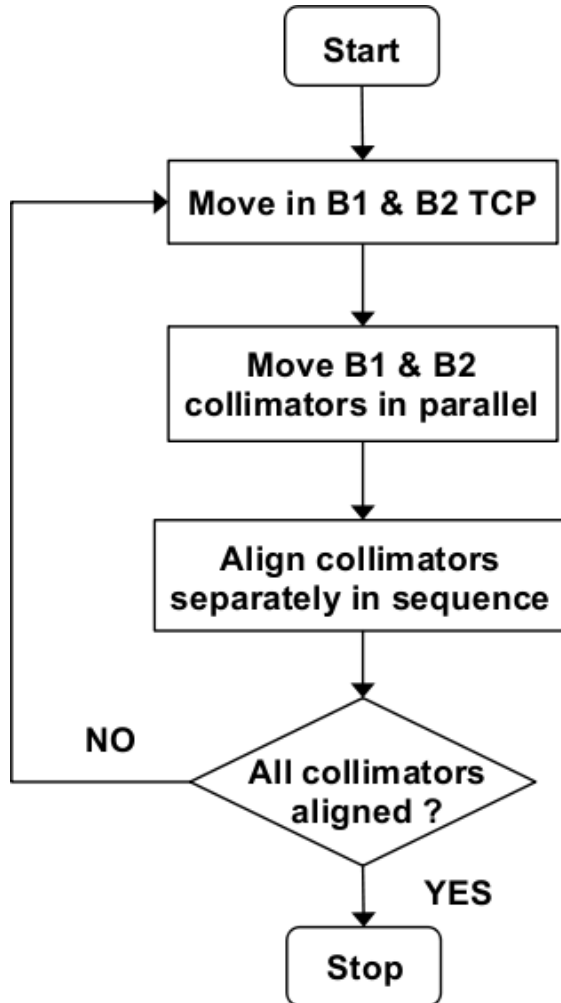
Figure 5.16: Flowchart of the alignment task sequencer operation.

5.8 BPM-Based successive approximation algorithm

A faster alignment and online monitoring of the local beam position can be achieved with embedded BPM pick-up buttons, introduced in Section 3.2.3. A prototype collimator equipped with embedded BPMs was installed in the SPS in January 2010. The collimator is set up to clean beam in the horizontal plane. A number of beam tests have been performed in the past couple of years to verify the alignment accuracy and compare the results achieved to those of the BLM-based technique [90, 91].

5.8.1 BPM measurement corrections

5.8.1.1 BPM electronics calibration

The asymmetry between the cables and the two electronics channels, which process signals from one pair of BPMs, introduces gains and offsets to the measured data [92]. The corrected electrode signal is hence obtained as:

$$V_j^{corr} = g_j V_j + o_j \tag{5.13}$$

where j denotes the channel index corresponding to a particular jaw corner, g is the gain and o is the offset. The asymmetry errors are independent of the BPM aperture and the beam offset. The parameters g_j and o_j (by default 1.0 and 0.0 respectively) can be determined experimentally by swapping the opposite BPM channels and measuring the electrode signals in these two configurations [93]. The beam position is assumed to be constant during the test. Consider two channels A and B, where V_{1A} and V_{1B} are signals from electrodes A and B when the channels are connected in a 'straight' configuration, and V_{2A} and V_{2B} are the signals from the same electrodes when the channels are connected in a 'crossed' configuration. Therefore if $g_A = 1$, then:

$$g_B = \frac{V_{2B} - V_{1B}}{V_{1A} - V_{2A}} \tag{5.14}$$

The offset is determined in a similar manner, with $o_A = 0$ and:

$$o_B = \frac{V_{1A}V_{2B} - V_{1B}V_{2A}}{V_{1A} - V_{2A}} \tag{5.15}$$

Five measurements were taken (see Fig. 5.17), and the values for each channel are listed in Table 5.9. The standard deviation of the gains is 3×10^{-4} arb. units, while that for offsets is 7×10^{-5} arb. units.

5.8.1.2 Measured BPM non-linearities

A collimator jaw scan was performed to characterize the BPM readout for selected jaw gaps and beam offsets in order to validate the simulations. At the start of
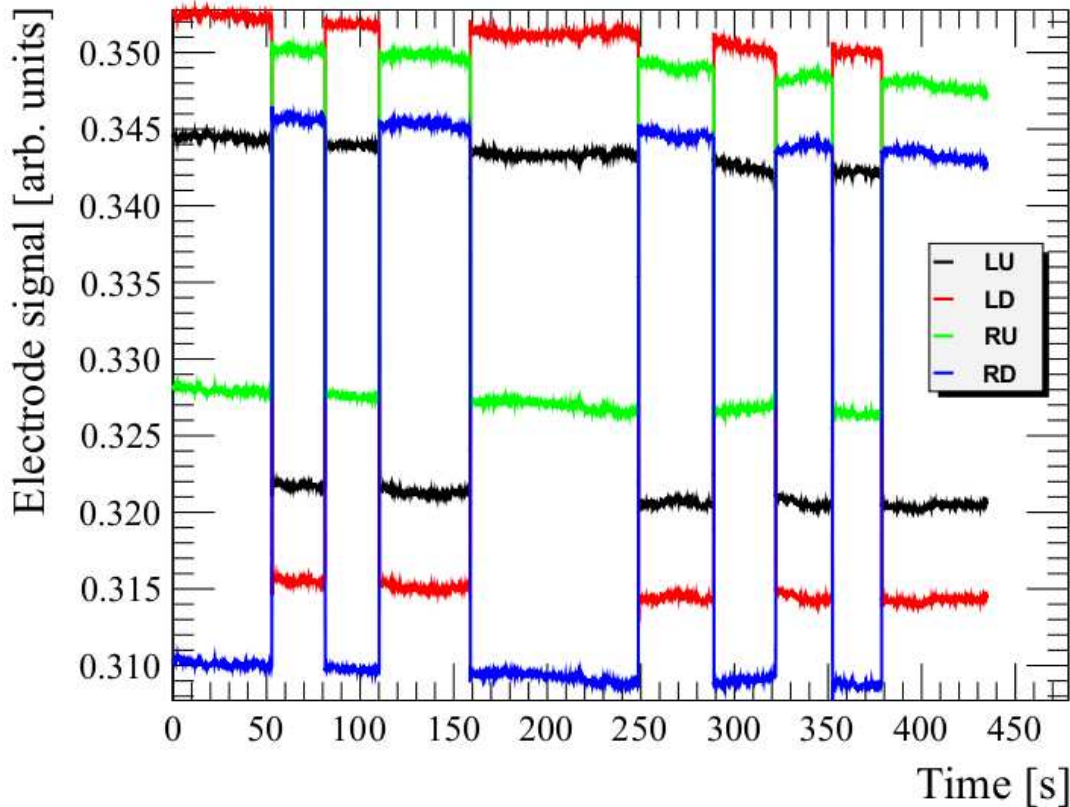
Figure 5.17: BPM electrode signals and collimator jaw positions during the electronics calibration test. The BPM channels are flipped five times at a constant jaw gap of 30 mm. The slight decrease in the signal amplitudes over time is due to the intensity decrease from normal beam losses.

Table 5.9: Gain and offset coefficients applied to the received electrode data to counter for asymmetries in the acquisition electronics. The coefficients were verified to be very similar at different jaw gaps.

Coefficient	Value
G_{LU}	1.0
G_{RU}	1.00508
G_{LD}	1.0
G_{RD}	0.97936
O_{LU}	0.0
O_{RU}	0.00409
O_{LD}	0.0
O_{RD}	0.00077

scan, the jaws were centred around the beam using feedback from BLM detectors with gain and offset calibration correction switched on. A horizontal jaw sweep was done by simultaneously moving the jaws around the coasting beam, keeping parallelism and fixed gap. The jaws were moved in m steps of ΔJ, which include a subset of identical simulated beam steps of $n \times \Delta X$ within $\pm G/2$.

The scan was executed automatically by the same application software used to test the alignment procedure. The collimator jaws were first opened to parking positions (± 30 mm), and then were shifted by 0.5 mm every 3 s. When one of the jaws reaches a pre-defined limit set to avoid beam scraping, the jaws are moved back to the starting point and the jaw gap is reduced by 1 mm. The procedure is repeated until a minimum jaw gap is reached. Results from a typical collimator scan are shown in Fig. 5.18. The measured beam axis X_{abs} is shown with and without BPM non-linearity correction. The corrected beam axis data are constant except for periodic noise which occurs when the jaws are moved from the end of the scan back to the starting point. The jaw movement is non-linear in time, but a linear interpolation is used to synchronize the 1 Hz collimator data to the 10 Hz BPM electrode data for plotting purposes.

To correlate the measured jaw scan results with simulations, it is necessary to translate the jaw sweep into a beam sweep. If the jaws are positioned at locations

$$J_{L,R,m} = J_{L,R} + m \times \Delta J \qquad (5.16)$$

where m is an iterator over each scan point, then the original "moving" beam locations can be considered at

$$X_{beam,m} = J_{c,m} = (J_{R,m} + J_{L,m})/2 \qquad (5.17)$$

and the linearity factor L_f can be calculated as in Eq. D.3. There is a very good agreement between the simulated characteristic (Fig. D.2) and measured non-linear relationship between the jaw centre and X_{raw} (Fig. 5.19). The measured linearity factors are shown in Fig. 5.20 and their values match within a few decimal places with simulated L_f (Fig. D.3). However, several differences are present due to orbit drifts and beam intensity decrease. The latter results in a gradual attenuation of the electrode signals over scan time. With the polynomial non-linearity correction switched on, the moving collimator sees the beam axis as stable (bottom plot in Fig. 5.18), which is not the case if the linear position is used. The collimator BPMs have a great potential to be added in online orbit monitoring and the LHC beam interlock system.
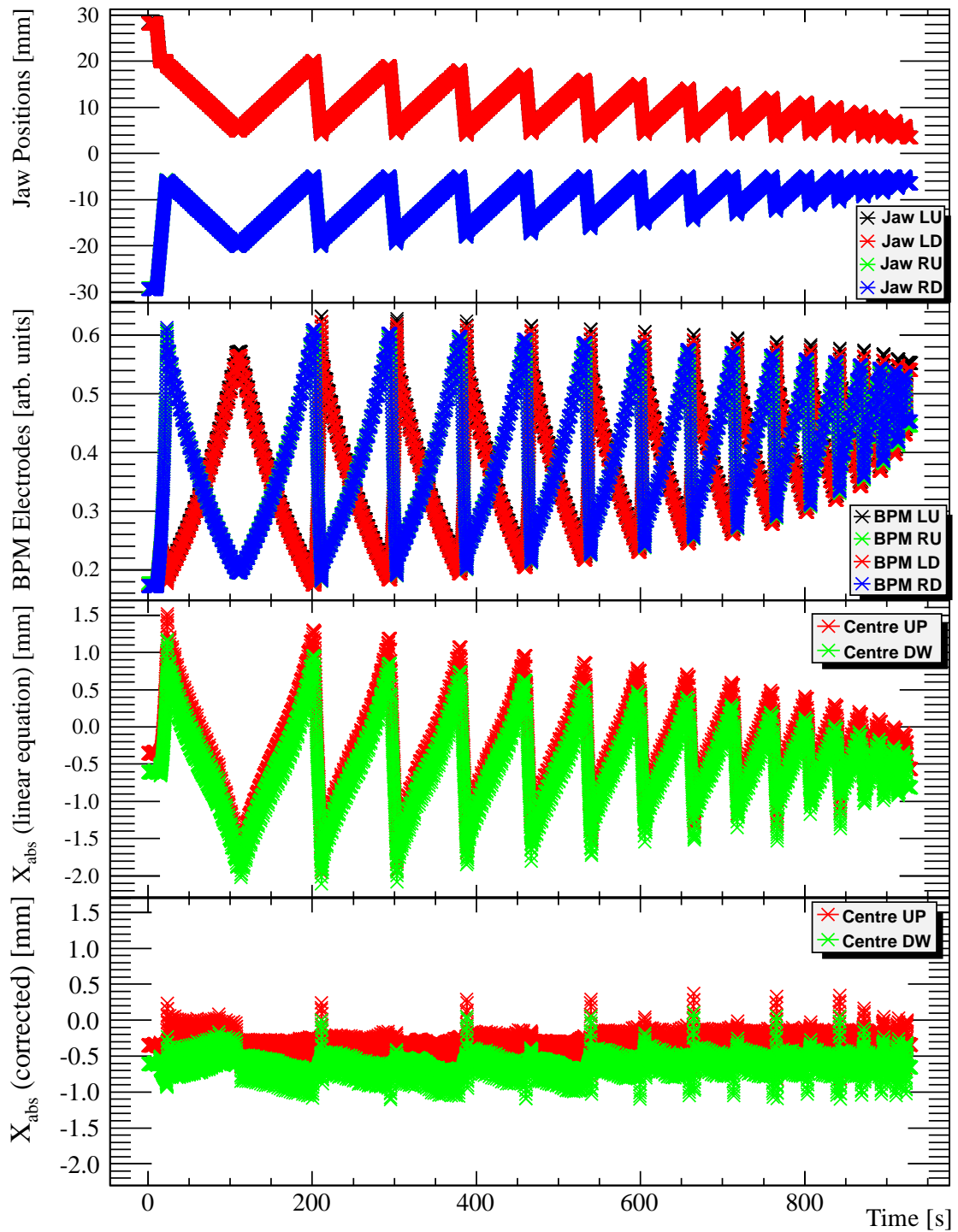
Figure 5.18: Automatic collimator scan, where the jaw centre is changed by 0.5 mm every 3 s, and the jaw gap is reduced by 1 mm at the end of each iteration. The raw, linearized and corrected by polynomial electrode signals are shown for comparison.
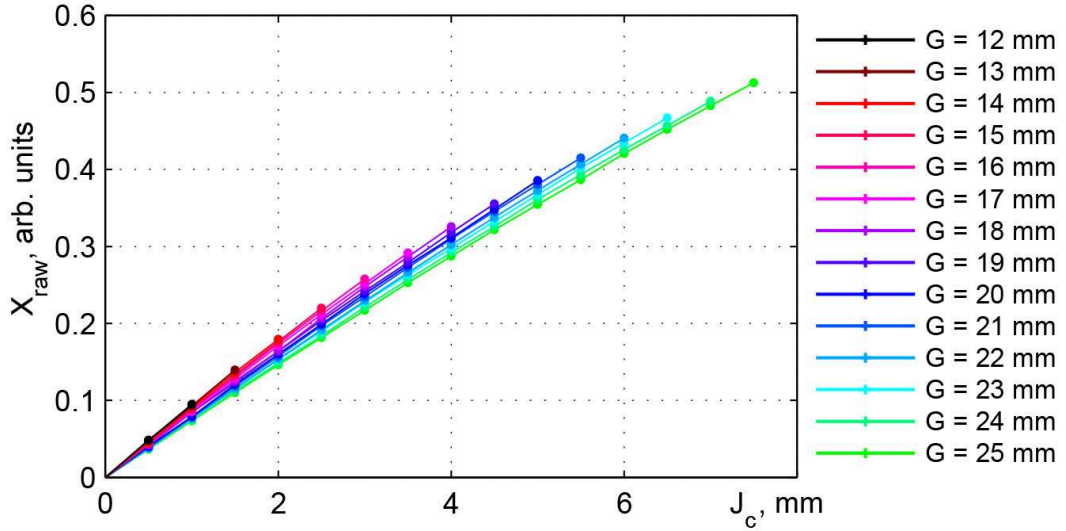
Figure 5.19: Measured non-linear relationship between the upstream jaw centre and X_{raw} as a function of the beam offsets and G.
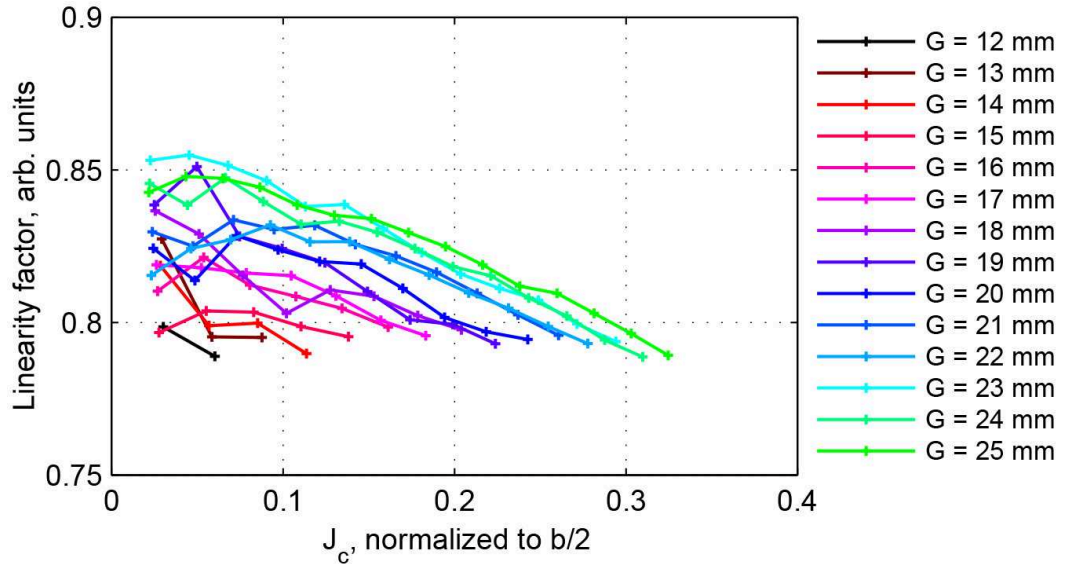
Figure 5.20: Measured linearity factors for the BPM characteristics plots in Fig. 5.19

.

5.8.2 BPM-based alignment algorithm

The objective of the alignment is to minimize X_{bpm} in Eq. (3.5). A successive approximation algorithm was developed to automatically align the collimator jaws around the beam centre from any starting jaw gap and beam offset. A flowchart of the algorithm is shown in Fig. 5.21. The first step is to estimate what would be the aligned position for the jaw furthest from the beam, J_i:

$$J_i = 2X_{bpm} + J_{i-1} \tag{5.18}$$

where i is an iterator over the successive approximation steps and J_{i-1} is the current jaw position. Once the jaw is reaches the supposedly aligned position, a new estimate is obtained for the beam centre using Eq. (3.5). The loop has two terminating conditions. The first is when the measured beam centre is below the error which can be specified as an input parameter: $|X_{bpm}| \leq X_{error}$. The second is when the jaw gap decreases below a minimum gap: $G \leq G_{min}$. This is done to ensure that the jaws do not inadvertently scrape away the beam during the alignment procedure. If $G = G_{min}$, the algorithm attempts to continue the alignment by moving the jaw closest to the beam outwards, rather than the jaw farthest from the beam inwards.
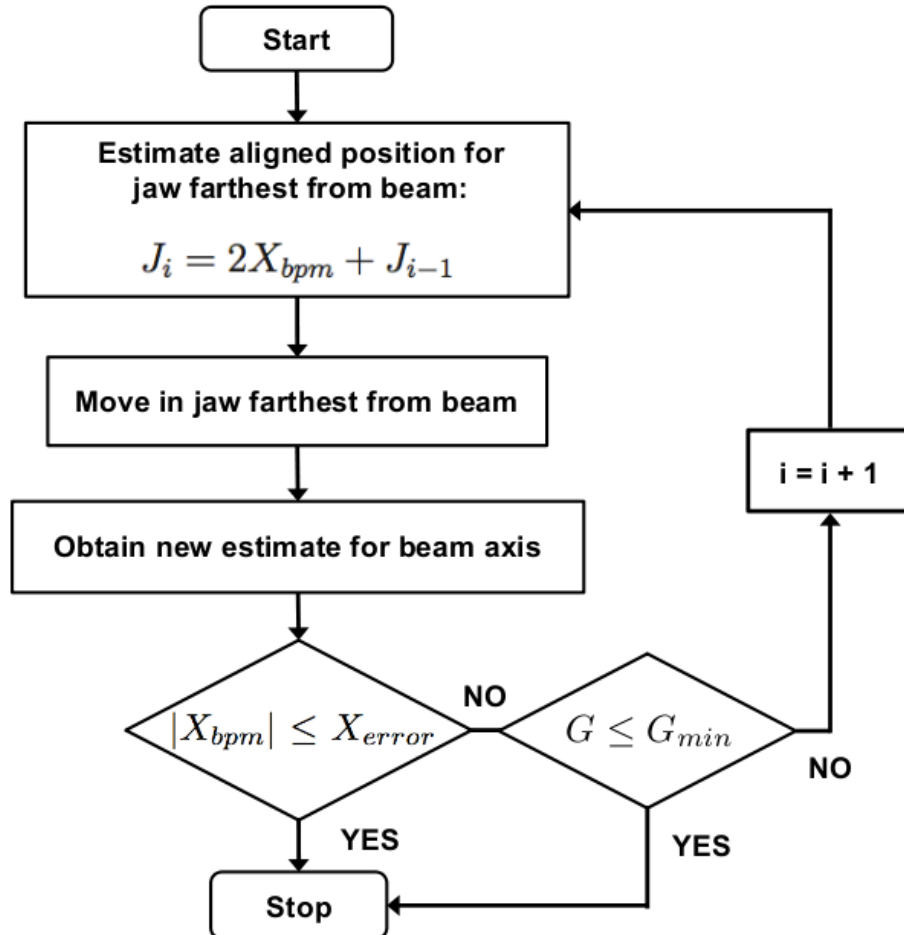
Figure 5.21: Flowchart of the BPM-based successive approximation alignment algorithm, from [94].

The alignment algorithm was implemented in the existing Java application used to control LHC prototype collimator in SPS [40]. The algorithm implementation

is flexible and allows the use of both the linear and the corrected measured beam centres. In addition, the gains and offsets for the electronics as well as the BPM non-linearity polynomial coefficients can be modified on the fly if necessary.

5.8.3   Results

5.8.3.1   Beam parameters during the tests

Alignment trials were conducted with circulating beam at an energy of 270 GeV. One LHC-type bunch with an injection intensity of 1.2×10^{11} p was circulating in the SPS.

5.8.3.2   BPM-based alignment

The alignment parameters were changed for each alignment, and are listed in Table 5.10. Two types of starting jaw positions were considered. In the first case, the jaws are initially set at parking positions around the zero position. In the second case, the jaws are initially positioned off-centre, with $|J_c| > 3.5$ mm. The alignment time is strongly influenced by the time interval between each step and the alignment accuracy required, and initial jaw gap to a lesser degree, as the BPM non-linearities are proportional to the jaw gap. The shortest alignment time achieved was $\sim$20 s, a factor 6 improvement over the best achieved alignment time of $\sim$120 s with the BLM-based technique. The collimator jaw corner positions, raw electrode signals and measured beam centre during a typical automatic alignment are shown in Fig. 5.22. Approximately 11 and 4 steps are required with the left and right jaws respectively until they are finally aligned after 30 s.

Table 5.10:   Alignment parameters and the corresponding alignment times achieved.

Parameter	Alignment Trials									
	1	**2**	**3**	**4**	**5**	**6**	**7**	**8**	**9**	**10**
Step Interval [s]	5	2	2	5	1	2	1	1	1	1
Accuracy [μm]	5	1	5	5	5	1	10	5	1	1
Initial Jaw Gap [mm]	50	60	60	48	35	35	35	21	21	35.5
Initial Jaw Centre [mm]	0.00	0.00	0.00	6.00	7.50	7.50	-7.50	-3.50	4.50	12.25
Final Jaw Gap [mm]	35.93	43.15	58.50	35.37	19.93	19.65	20.45	13.90	11.39	10.44
Alignment Time [s]	47	105	29	81	17	52	23	26	24	34
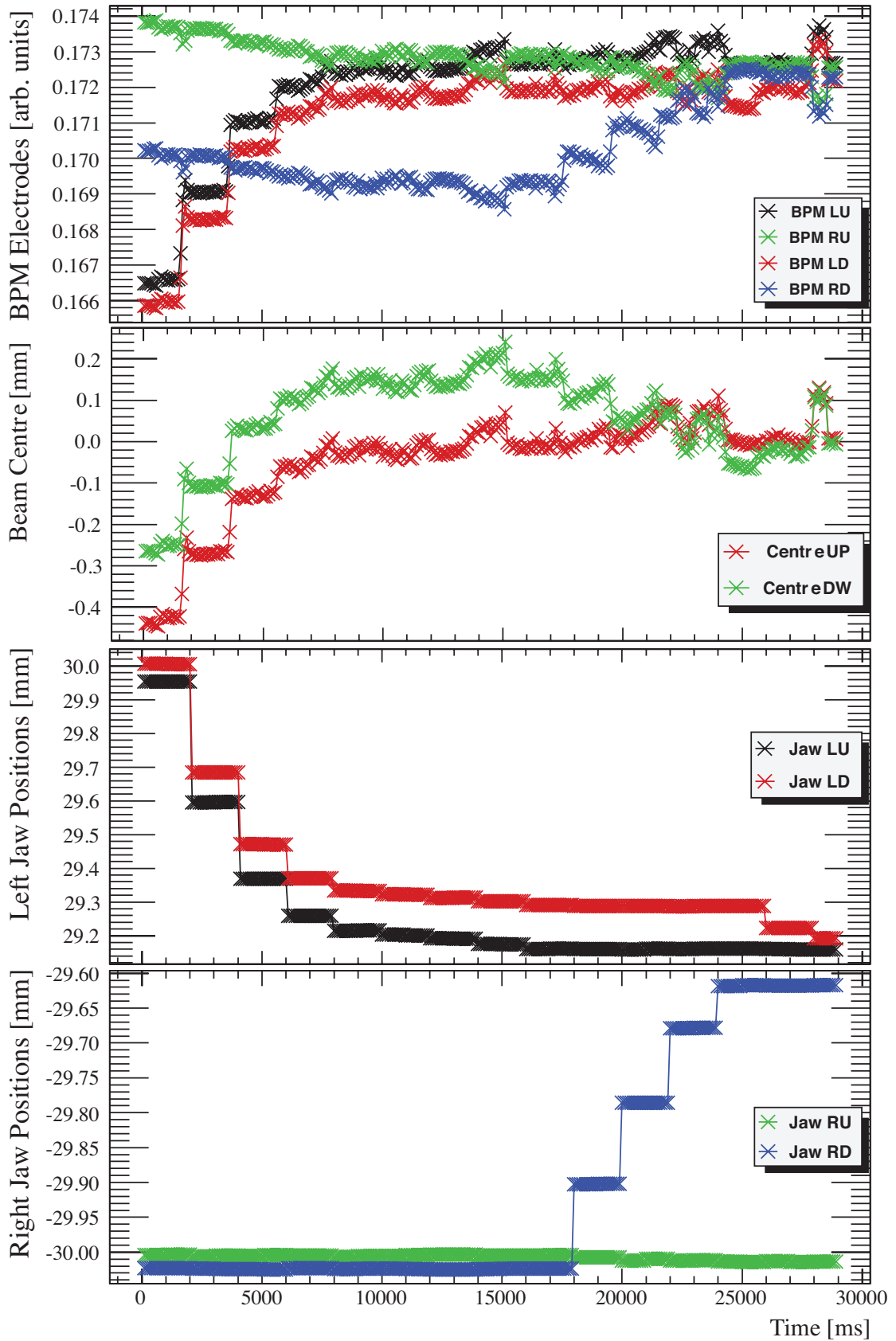
Figure 5.22: Collimator jaw corner positions, raw electrode signals and measured beam centre during a typical automatic alignment in the SPS experiment.

5.8.3.3 Comparison with BLM-based alignment

For each new fill, the jaws were aligned using feedback from the BLM detectors. This involves moving each jaw in steps of 50 to 100 μm until a loss spike is observed in the closest BLM detector downstream. A comparison of the beam centres measured with the BPM-based and BLM-based techniques is shown in Fig. 5.23. The average of the upstream and downstream positions are plotted for the BPM-based alignments, as the jaw corners were not aligned individually in the BLM-based alignments. The centres are in agreement within less than 150 μm in most instances, although larger deviations are observed in the second fill possibly due to orbit drifts. It is important to note that the design positioning tolerance of the BPM pick-up buttons with respect to the jaw surface is of 50 μm [95]. However, systematic calibration with BLM-based alignment in the LHC should reduce this inaccuracy to 10 μm. This, combined with the inaccuracies introduced by the large jaw step size required due to the larger beam sizes in the SPS, provides a valid explanation for the differences in the beam centre measurements between BLM-based and BPM-based alignment.
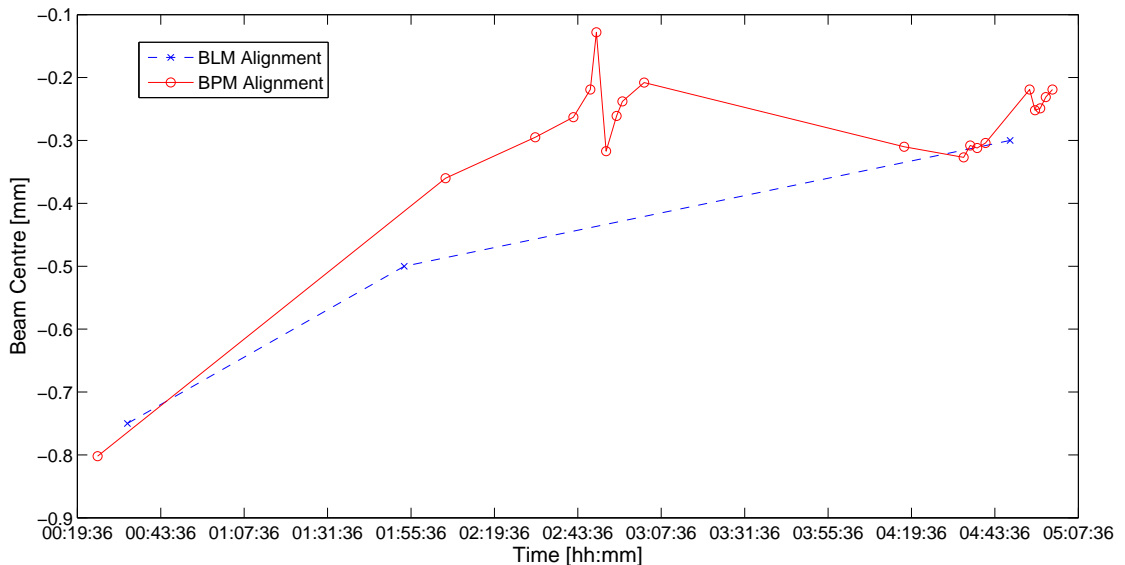
Figure 5.23: Comparison of beam centres measured using BLM-based and BPM-based alignment. The SPS was re-filled two times at 00:20 and 01:34.

5.8.3.4 Effects of beam offsets in the orthogonal plane

The BPMs are positioned in the SPS prototype collimator to measure the beam offset in the horizontal plane. Vertical beam offsets could affect the measurements (see Eq. (3.5)). Hence, a test was conducted to verify the extent of the

measurement errors. The first step was to position the jaws symmetrically around the beam using the automatic BPM-based alignment algorithm. Then, vertical orbit bumps of $+2.5$ mm followed by -2.5 mm were introduced at the collimator location. The change in the measured BPM electrodes and the corresponding shift in the measured beam centres (taking into account a collimator jaw gap of 20 mm) are shown in Fig. 5.24. A shift of ~ 50 μm was detected, which is not negligible for operational purposes. Future work is required to address this issue, although as concluded in Appendix D, the BPM non-linearity of small vertical offsets can be handled by the correction polynomial $Poly52$ without problems. The effect in the downstream corner BPM electrode signals is more evident for the negative orbit bump, and vice-versa for the positive orbit bump, as the bump cannot be applied at the same longitudinal position in both cases.
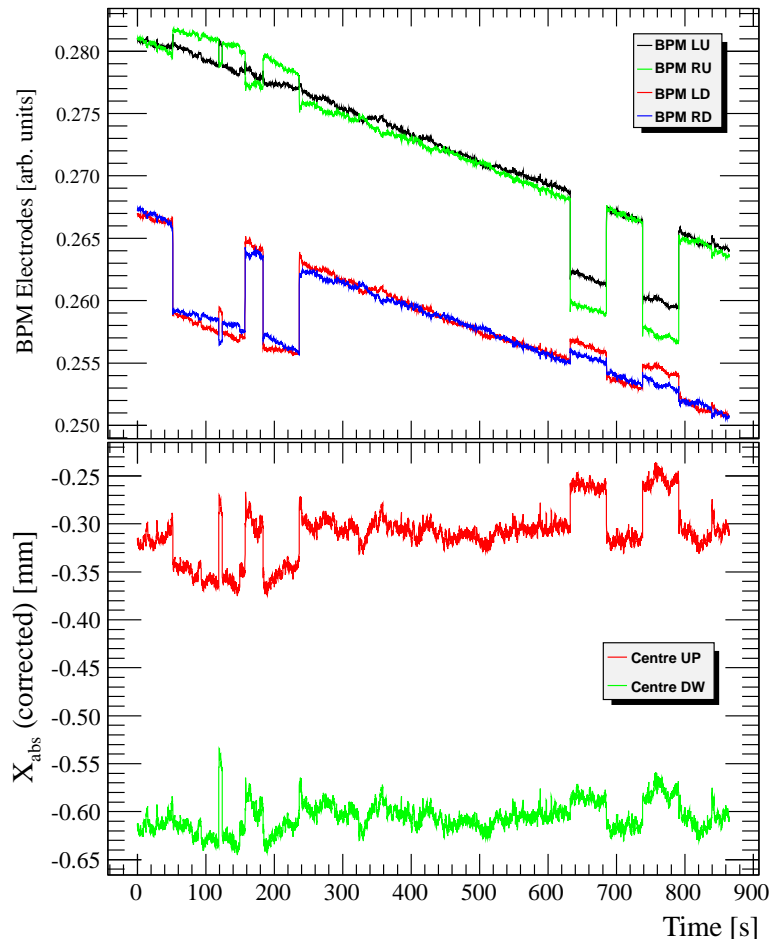
Figure 5.24: Change in the measured BPM electrode signals and the resulting beam centre due to vertical orbit bumps of $+2.5$ mm (100-300 s, ON-OFF-ON) and -2.5 mm (650-850 s, ON-OFF-ON).

Chapter 6

Software Implementation and Validation

6.1 Software development methodology

All software was designed and implemented using the Agile software development methodology [96]. The Agile methodology is characterized by 12 features, which include rapid delivery of useful software, ability to adapt to changing requirements and close cooperation between all players. These features were well-suited to the context of LHC operation. One reason for adopting this methodology was that the date and time of the next collimator alignment was never known until a few days beforehand. Indeed, many times tentative dates were brought forward or postponed, and hence by nature the development and testing schedule had to be very flexible.

6.2 Software development tools

The Beams Department at CERN uses the following tools for software development:

- Java programming language for user application development

- The Eclipse Integrated Development Environment (IDE)

- Subversion (SVN) for version management

- The Common Build build and release management tool [97], based on Apache Ant [98]

The build process generates a Java Network Launching Protocol (JNLP) file, which can be launched in the CCC via Java Web Start, an application deployment technology.

6.3 BLM-based alignment software application

The BLM-based alignment application is based on the original LHC collimator control software [40] as used in the 2010 LHC alignments.

6.3.1 Data acquisition

6.3.1.1 LHC collimation data

Collimator motor position and LVDT data are acquired by subscribing to the *RequiredAbsolutePosition* and *MeasuredCornerPositions* parameters via the Java API for Parameter Control (JAPC) framework [99]. The data are published at a frequency of 1 Hz.

6.3.1.2 Standard LHC BLM data

The signals from all BLM detectors associated with the collimators are obtained from a data concentrator [100] at a frequency of 1 Hz. A full list of the BLM detector names is available in Appendix B.

6.3.1.3 Fast LHC BLM data

Each BLM crate in the LHC tunnel sends a UDP packet simultaneously, every 82 ms, to the specified server machine *cs-ccr-logging2*. The UDP packet transmission flow is shown in Fig. 6.1. A list of the header fields in each packet is provided in Table 6.1. The header is used to identify which packet corresponds to which BLM detector at the server machine.

Table 6.1: Fast BLM UDP packet header field names and sizes.

Name	Size (bytes)	Data Type
IP	2	unsigned int
Position	2	unsigned int
timestamp	8	long long

The data are sent in a 16x16 array, where each element is 4 bytes. The following equation is used to convert between the received data in integer format and the actual signal in Gy/s for the IC BLM detectors:
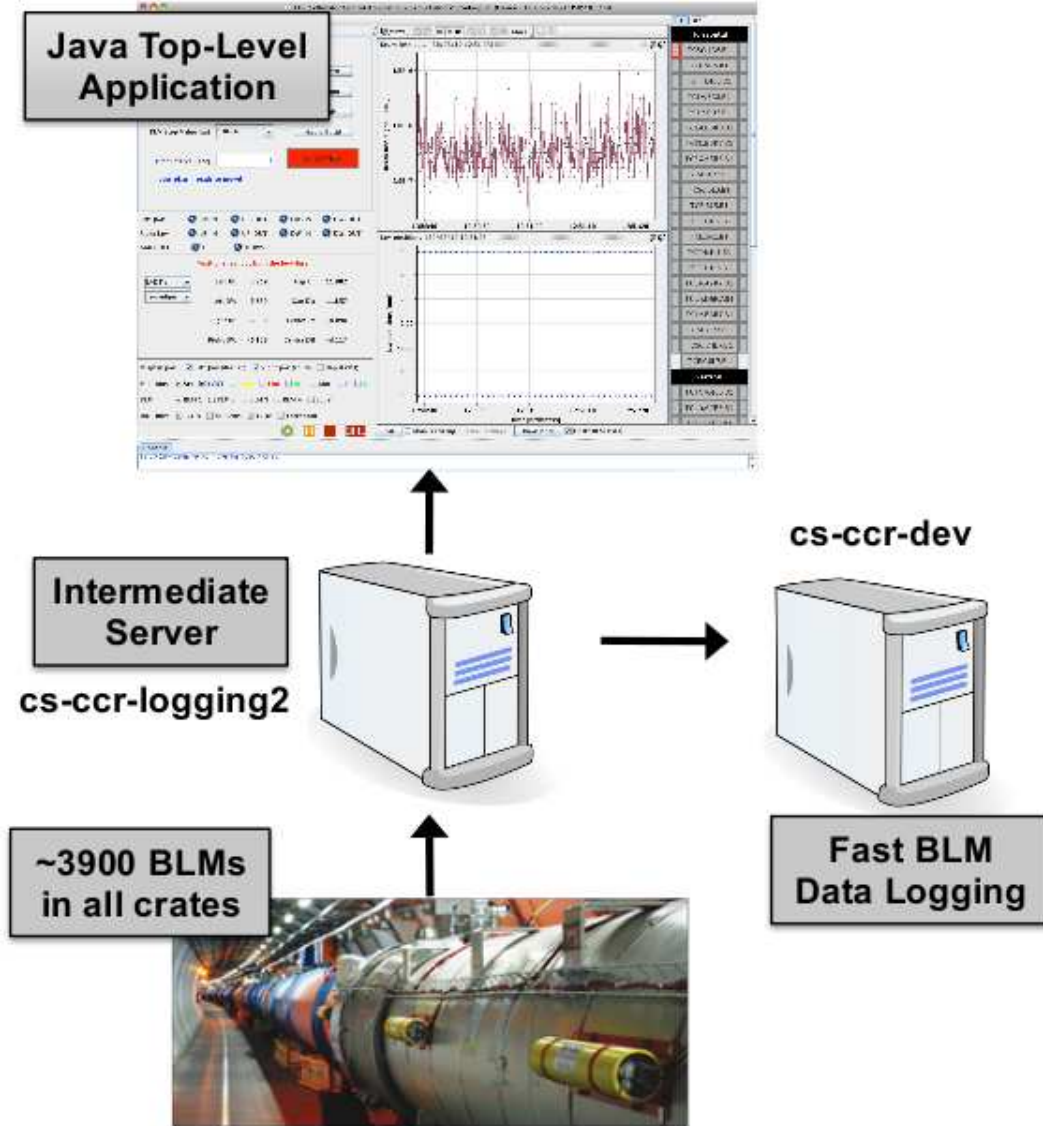
Figure 6.1: Fast BLM data UDP packet flow.

$$S_{fast,IC} = S_{rx} \times \frac{F_{Gy,IC}}{81.92 \times 10^{-3}} \tag{6.1}$$

where $F_{Gy,IC} = 3.62 \times 10^{-9}$ is the conversion factor to Gy for ICs. The server machine then forwards the data to the Java top-level application in the CCC. The BLM data can also be logged on the CCC machines for offline analysis.

6.3.2 Graphical User Interface

A screenshot of the original main GUI of the LHC collimator application as operated from the CCC in 2010 is available in Fig. 6.2.

Figure 6.2: Screenshot of the original main application GUI in 2010.

86

The B1 and B2 collimator layout names are displayed in blue and red respectively, in alphabetical order. The MDC and PRS state is shown for each collimator, the colour coding for which is described in detail in Section 6.5.1. From this screen, the user can launch the user interface for an individual collimator, by clicking on one of the displayed collimators, and then clicking on *App Launcher* followed by *Launch application*. The BLM signal is displayed in the top right panel, with the collimator left and right jaw positions in the panel below it. In the top left corner, three tabs allow the user to input the individual jaw corner positions, set both corners of each jaw to the same position, or apply increments to the jaw positions. All the inputs are transmitted to the MDC. The bottom left panel displays the PRS data, and allows the user to add or remove data shown in the collimator position plot. A screenshot is shown in Fig. 6.3.
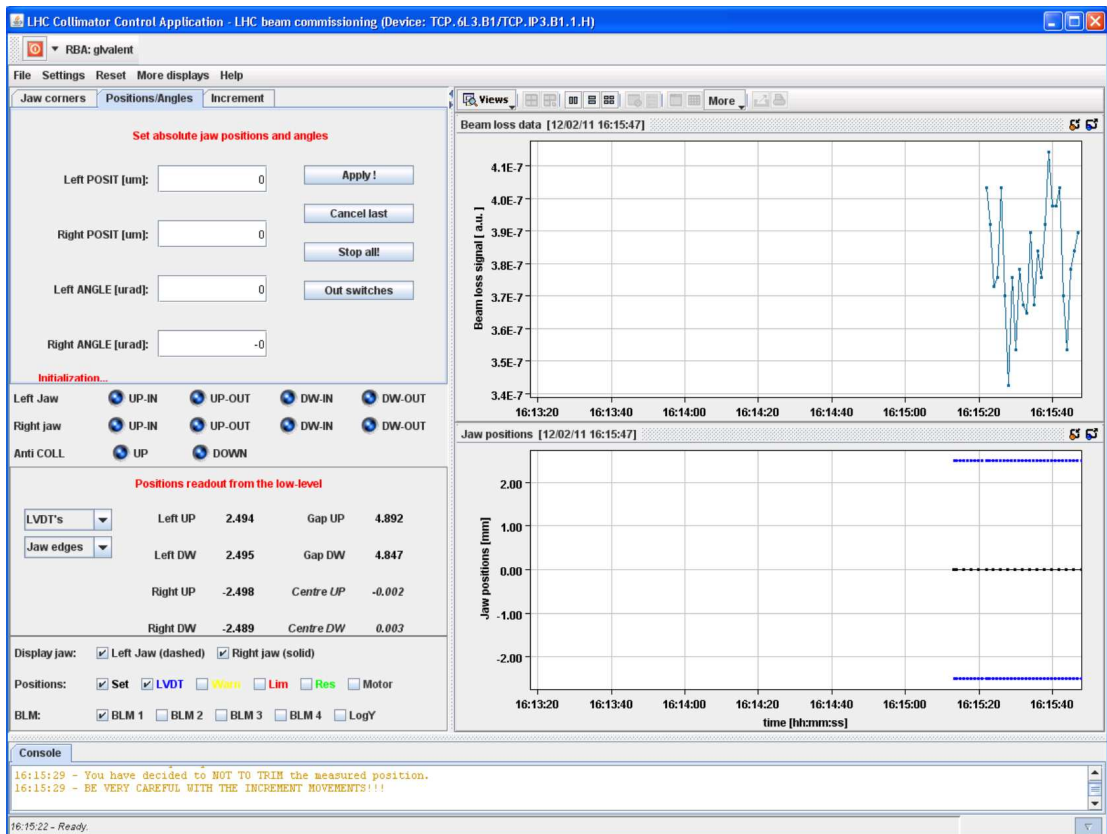
Figure 6.3: Screenshot of the original collimator controller window in 2010.

The software application was modified in this thesis to cater for the alignment algorithms, while maintaining backward-compatibility with all the previous functionality. The collimators are now displayed in 6 groupings, divided by beam and plane (see screenshot in Fig. 6.4). A search feature allows for a requested collimator name to be highlighted to avoid time-consuming visual scanning of all the names until the correct one is located.
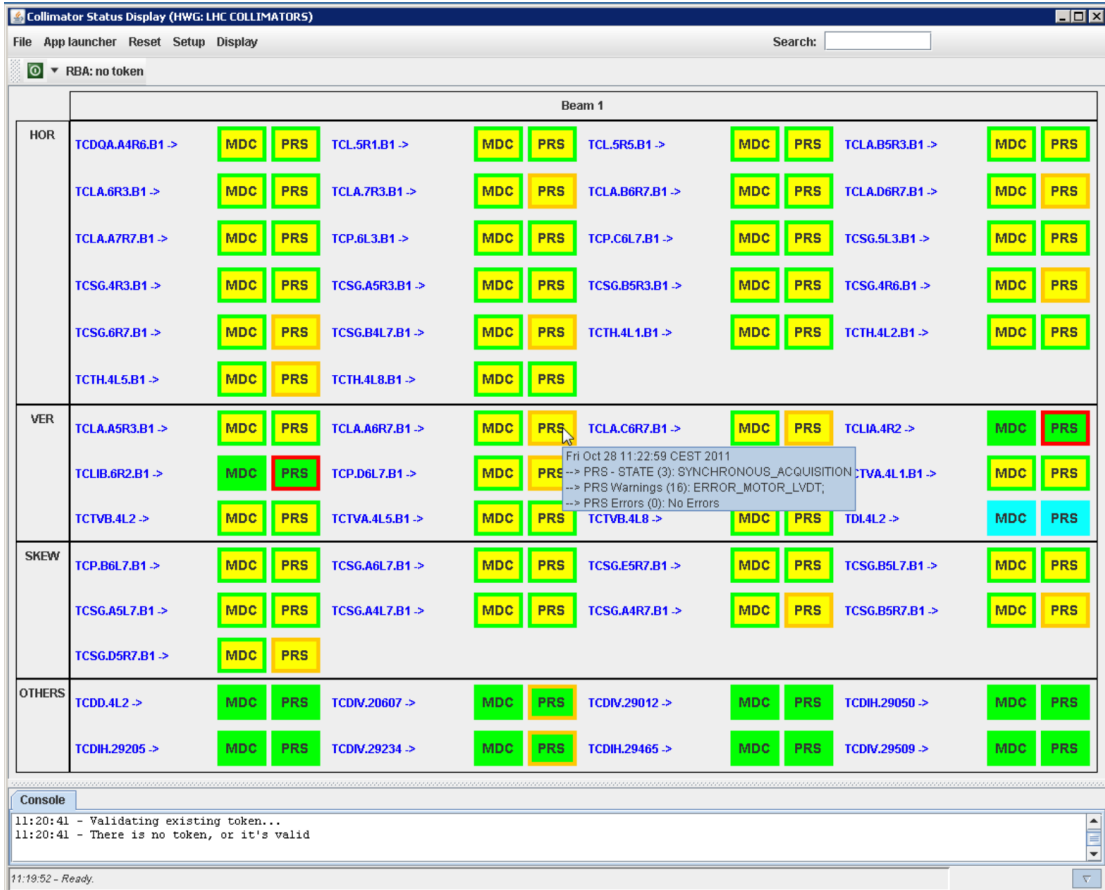
Figure 6.4: Screenshot of the main application GUI. Only B1 collimators are shown for clarity.

Apart from opening windows for individual collimators, the user may decide to start an alignment of several collimators by clicking on the *Setup* drop-down menu in the top-left hand corner. The user then has the option to create a new setup or load an existing setup. The second option is useful if the alignment needs to be resumed after a beam dump, so that all previously measured and saved values are loaded. If a new setup is created, the user is presented with a collimator selection interface (see Fig. 6.5), to be able to select the collimators for alignment. The names are colour-coded in red, blue and green for horizontal, vertical and skew respectively.

The user is then directed to the next screen, which involves selection of the hierarchy settings N_σ for each collimator family. Pre-defined default settings for a selected machine mode are loaded from a configuration file, and can be modified directly from the window if necessary. A screenshot is shown in Fig. 6.6.
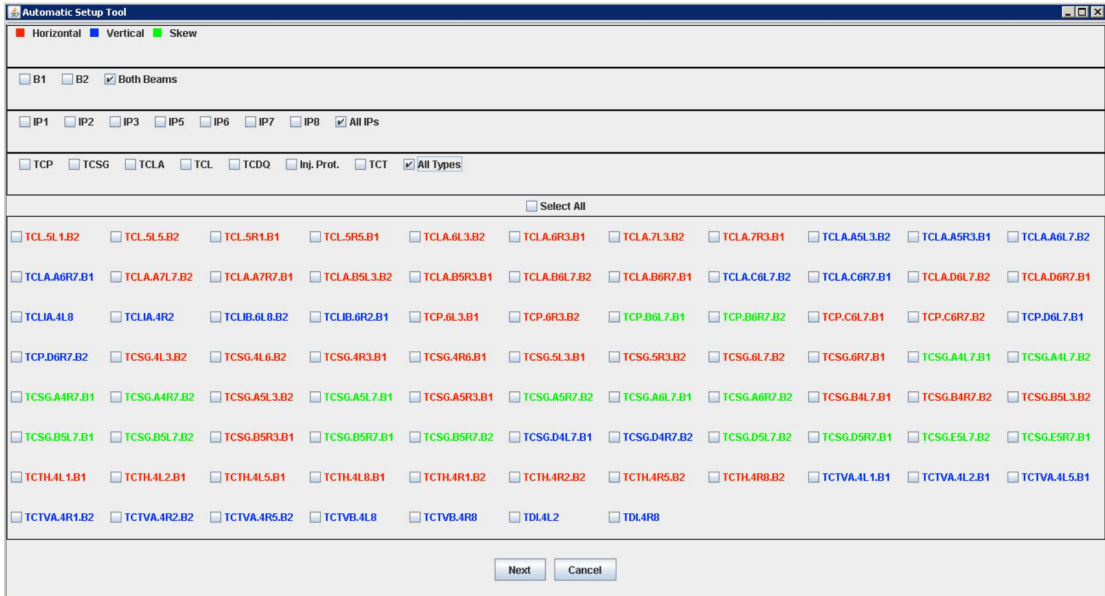
Figure 6.5: The collimator selector GUI allows the user to include any combination of collimator names in the alignment sequence.
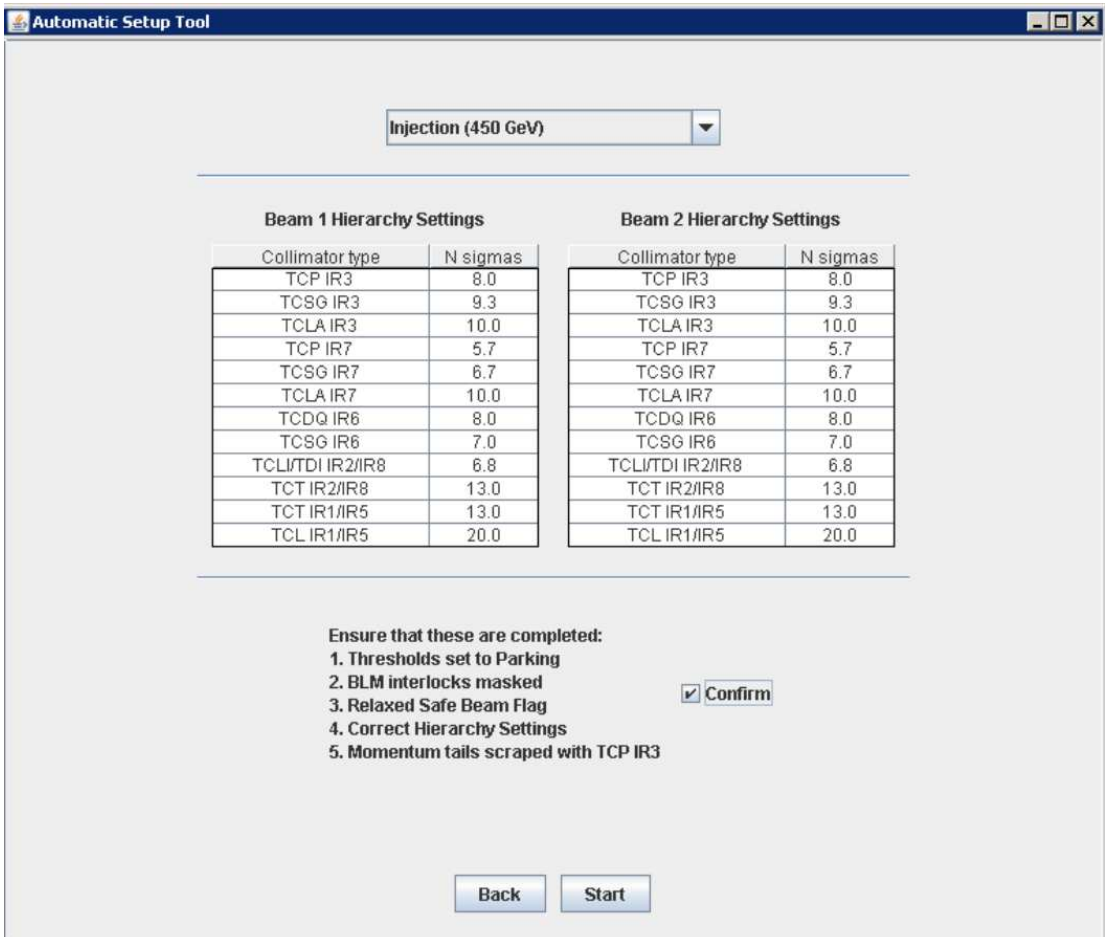
Figure 6.6: The collimator settings window enables selection of the machine mode and hierarchy settings for collimator families. Pre-defined default settings for a selected machine mode can be modified directly from the window if necessary.

Once all the alignment parameters are defined, the collimator controller window is launched (see screenshot in Fig. 6.7). On the right is the list of collimators selected for setup, in the sequence defined in Appendix A. The smaller boxes on either side of the names represent the TCP in the same plane, which needs to be re-aligned before each regular collimator is aligned. The collimators highlighted in turquoise have already been aligned. Table 6.2 lists the various colour codes selected, as well as the state they represent.
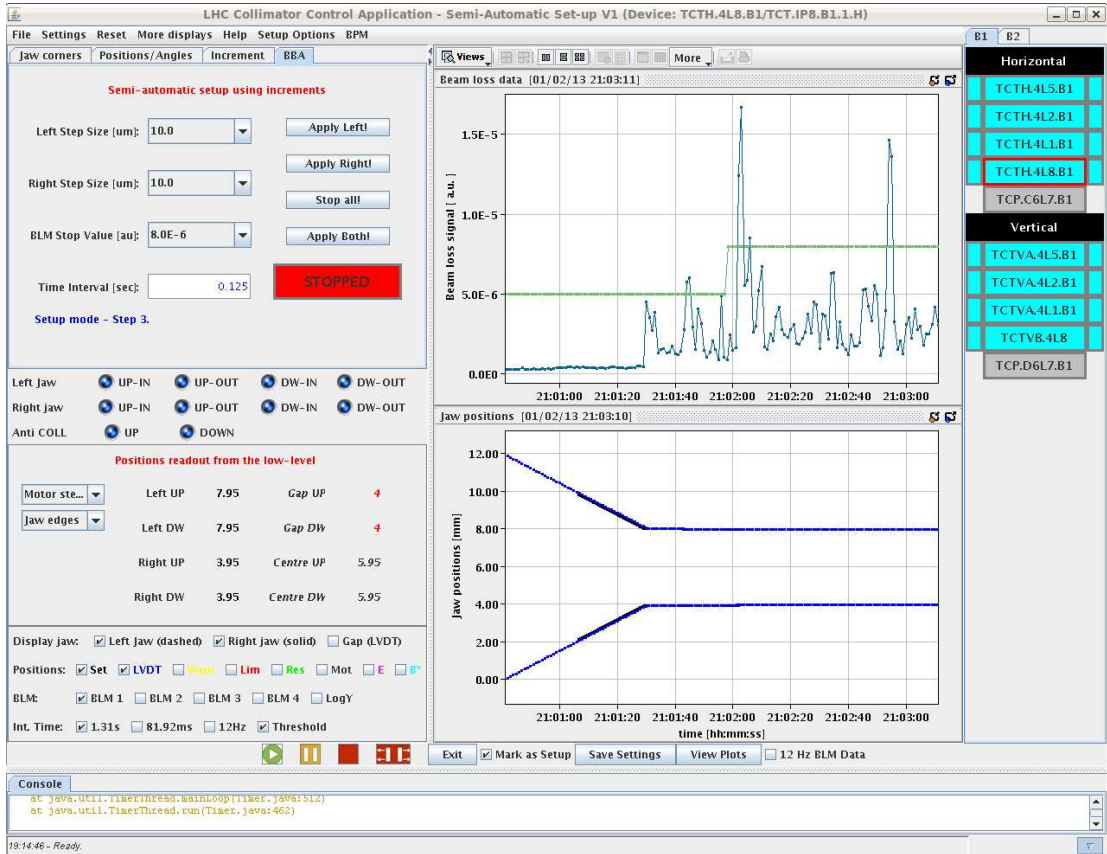
Figure 6.7: Screenshot of the collimator controller window.

Table 6.2: Colour coding used to identify the different alignment states of an individual collimator.

Colour	State
Gray	Not moved yet
Green	Collimator jaw(s) moving
Red	Collimator jaw has just stopped moving, decision in process
Yellow	One or both jaws have touched the beam, collimator not aligned
Turquoise	Collimator is declared to be aligned

Other additions include display of the applied BLM threshold (seen in green in the BLM plot), and the energy and β^* limits, which were introduced in the 2012 LHC run. The 1 Hz and 12.5 Hz BLM data can be displayed separately or together. A

new tab for beam-based alignment (BBA) is implemented. Therefore, the operator can align an individual collimator in a semi-automatic fashion, by inputting the left and right jaw step sizes as well as the loss threshold and the time interval in the top left panel.

At the start of the alignment, the collimators can be moved to tighter settings around the BPM-interpolated settings by clicking on *BPM* in the menu at the top, which launches the window in Fig. 5.14. The alignment sequencer can then be launched by clicking on the green *play* icon at the bottom of Fig. 6.7. Implementing the algorithm presented in Fig. 5.16, the sequencer performs the various stages of the alignment, starting off with parallel alignment of all collimators, and then sequentially fine-tuning each one to get the beam centres and beam sizes. The sequencer can be paused or stopped at any time by clicking on the appropriate buttons in the bottom panel.

One disadvantage of the above GUI is that only one BLM - collimator position plot can be viewed at any one time. To view the same plot for other collimators, the user can click on the collimator names shown in the list on the right-hand side. In case the user would like to have a global view of the alignment (especially perhaps during parallel alignment), clicking on the *View Plots* button opens a separate window (screenshot shown in Fig. 6.8), which displays the BLM signal, collimator positions and alignment status for each collimator.
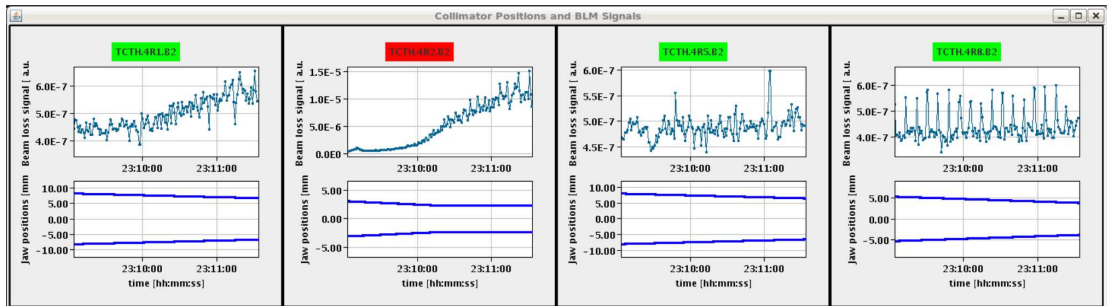
Figure 6.8: Screenshot of the multi-view window, showing the BLM signals, jaw positions and alignment status for each collimator.

The beam-based data measured during the alignment can be viewed by clicking on *Display* in the main application window. A typical example of a setup sheet with data from a TCT alignment in February 2013 is given in Fig. 6.9. The alignment sequencer automatically populates the sheet, but nevertheless it remains fully editable. Depending on whether the alignment is carried out at injection or top energy, the user can choose whether the equations that calculate the positions to open the jaws to after alignment (step 4 in the alignment procedure) rely on the measured or the nominal beam size.

Collimator Setup Sheet - Beam 1 (/user/slops/data/LHC_DATA/OP_DATA/LHCCollimators/Setups/Setup_2013-02-01_1/Collimator_Setup_Sheet_4000GeV-collisions_2013-02-01_19-14-16_B1_ONGOING.txt)

File Edit Options

Geometric Emittance: 8.21E-10
Setup N Sigma: 4.5
RMS Momentum Deviation: 3.06E-4

Number	Status	Collimator Name	Angle (deg)	JAW L Calib (mm)	JAW R Calib (mm)	LVDT gap	Gap Offset (mm)	Half Gap Meas (mm)	Eff sigma in coll plane	JAW L Setting (mm)	JAW R Setting (mm)	Target HALF GAP sigma	Pos
Horizontal													
9	True	TCP.C6L7.B1	0.00	1.020	-1.525	2.474	-0.252	1.272	n/a	n/a	n/a	3.62	197
10	True	TCTH.4L5.B1	0.00	-1.895	-7.975	6.067	-4.935	3.040	0.942	4.482	-14.352	10.00	131
11	True	TCP.C6L7.B1	0.00	0.895	-1.425	2.249	-0.265	1.160	n/a	n/a	n/a	3.30	197
36	True	TCP.C6L7.B1	0.00	0.895	-1.425	2.250	-0.265	1.160	0.352	0.895	-1.425	3.30	197
37	True	TCTH.4L2.B1	0.00	2.950	-2.275	5.191	0.338	2.612	0.791	8.249	-7.574	10.00	321
38	True	TCP.C6L7.B1	0.00	0.855	-1.405	2.190	-0.275	1.130	n/a	n/a	n/a	3.21	197
42	True	TCP.C6L7.B1	0.00	0.855	-1.405	2.189	-0.275	1.130	0.352	0.855	-1.405	3.21	197
43	True	TCTH.4L1.B1	0.00	3.500	-2.115	5.569	0.692	2.808	0.942	10.110	-8.725	10.00	265
44	True	TCP.C6L7.B1	0.00	0.815	-1.365	2.109	-0.275	1.090	n/a	n/a	n/a	3.10	197
45	True	TCP.C6L7.B1	0.00	0.815	-1.365	2.109	-0.275	1.090	0.352	0.815	-1.365	3.10	197
46	True	TCTH.4L8.B1	0.00	7.680	4.260	3.400	5.970	1.710	0.551	12.579	-0.639	12.000	231
47	True	TCP.C6L7.B1	0.00	0.785	-1.325	2.038	-0.270	1.055	n/a	-0.270	-0.270	3.00	197
Vertical													
0	True	TCP.D6L7.B1	90.01	1.035	-0.585	1.596	0.225	0.810	n/a	n/a	n/a	3.20	197
1	True	TCTVA.4L5.B1	90.01	2.505	-1.355	3.852	0.575	1.930	0.600	6.572	-5.422	10.00	131
2	True	TCP.D6L7.B1	90.01	0.980	-0.540	1.496	0.220	0.760	n/a	n/a	n/a	3.00	197
12	True	TCP.D6L7.B1	90.01	0.980	-0.540	1.487	0.220	0.760	n/a	n/a	n/a	3.00	197
13	True	TCTVA.4L2.B1	90.01	0.620	-4.760	5.343	-2.070	2.690	0.840	6.332	-10.472	10.00	325
14	True	TCP.D6L7.B1	90.01	0.965	-0.530	1.464	0.217	0.748	n/a	n/a	n/a	2.95	197
18	True	TCP.D6L7.B1	90.01	0.965	-0.530	1.464	0.217	0.748	n/a	n/a	n/a	2.95	197
19	True	TCTVA.4L1.B1	90.01	4.460	0.450	3.977	2.455	2.005	0.600	8.452	-3.542	10.00	265
20	True	TCP.D6L7.B1	90.01	0.955	-0.520	1.445	0.217	0.738	n/a	n/a	n/a	2.91	197
21	True	TCP.D6L7.B1	90.01	0.955	-0.520	1.445	0.217	0.738	n/a	n/a	n/a	2.91	197
22	True	TCTVB.4L8	90.01	2.025	-1.895	3.883	0.065	1.960	0.650	7.862	-7.732	12.000	232
23	True	TCP.D6L7.B1	90.01	0.940	-0.500	1.405	0.220	0.720	n/a	0.220	0.220	2.84	197
Skew													

Figure 6.9: Screenshot of the collimator setup sheet after a TCT alignment in February 2013.

6.3.3   Data logging

All data generated by the collimator application, including inputs and outputs provided to the various algorithms are logged for offline analysis.

6.4   BPM-based alignment software application

The BPM-based alignment application is based on the original SPS collimator control software [40] as used in the 2010-2011 SPS beam tests.

6.4.1   Data acquisition

6.4.1.1   SPS collimation and BLM data

A set-up similar to that for LHC collimators is used.

6.4.1.2   BPM data acquisition

The BPM pick-up button signals are processed by electronics based on compensated diode detectors. Two diode orbit front-end prototypes were built and tested in the laboratory and with beam [92]. In this technique the diode detectors convert nanosecond pulses from BPM electrodes into slowly varying signals, which are low-pass filtered to 10 Hz and sent to a 24-bit ADC with a sampling frequency of 11.7 kHz, averaged down and sent through an Ethernet link by a simple microcontroller. This type of electronics is also intended for installation in the LHC for the standard BPMs [101].

The ADC samples are averaged by a programmable factor, and are sent as User Datagram Protocol (UDP) network packets by a built-in microcontroller in the SPS tunnel to an intermediate server. Data from the LU, LD, RU and RD BPM electrodes are included in the packet payload. The server forwards the packets on request to the collimator application running in the CCC or the data logging application. Each packet has a 48 byte header, to which a maximum of 992 bytes of data can be appended. The individual header field names and sizes are provided in Table 6.3. In the software application, the raw electrode data are decoded as follows. The first step is to extract the full-scale range:

Table 6.3: BPM UDP packet header field names and sizes.

Name	Size (bytes)	Data Type
Packet Type	12	byte array
Authorization Key	8	byte array
Source Host Number	4	int
Send Time (s)	4	unsigned long
Send Time (μs)	4	unsigned long
Acquisition Timestamp	8	unsigned long long
Sequence number	4	unsigned long
ADC sample number	2	UINT16
Averaging factor	2	UINT16

$$R_{fs} = k_{avg} \times \frac{2^{24}}{2^{\lceil \log_2 (k_{avg} \times 2^{24}/2^{32}) \rceil}} \tag{6.2}$$

where k_{avg} is the averaging factor. The data rate is determined by the averaging factor and the ADC clock frequency f_{ADC} of 11719 Hz as follows:

$$DR = \frac{f_{ADC}}{k_{avg}} \tag{6.3}$$

The electrode signals are then obtained by dividing the received data D by the full scale range:

$$V_j = \frac{D_j}{R_{fs}} \tag{6.4}$$

where j denotes the jaw corner. For the beam tests with the prototype collimator, the averaging mode was used with one data sample sent per UDP at a rate of 10 Hz ($k_{avg} = 1172$). The UDP packet transmission flow is shown in Fig. 6.10.

6.4.2 Graphical User Interface

The user interface and data acquisition of the BPM-based alignment top-level software application is based on the BLM-based alignment application used in 2010. A screenshot of the application as used in the alignment configuration is shown in Fig. 6.11. Six plots are shown, namely the BLM signal, collimator jaw positions, BPM electrode signals, the beam position as calculated by Eq. (3.4), the tilt (see Eq. (3.7)), and the absolute beam position obtained through Eq. (3.2).
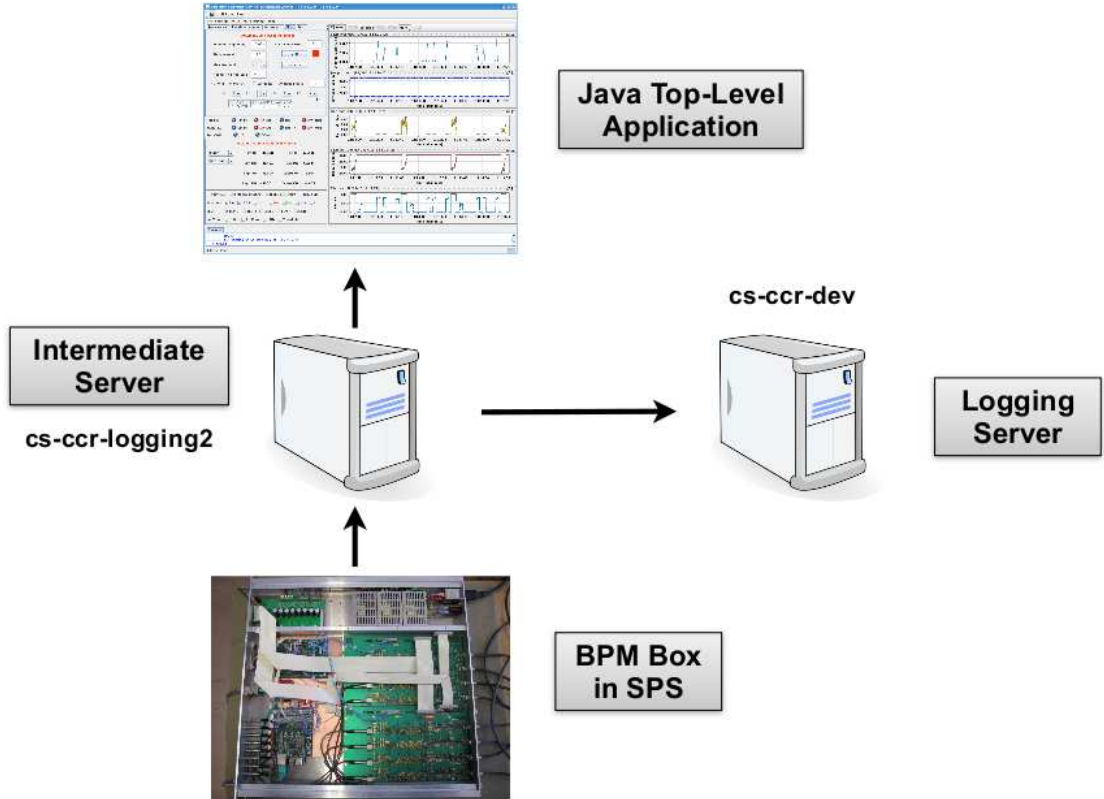
Figure 6.10: SPS BPM data UDP packet flow.

The number and positioning of the plots displayed can be easily modified for clarity. The alignment parameters described in Section 5.8.3.2 are inputted in the top-left panel. The table at the bottom provides data related to the received UDP packets, namely the sequence number, ADC sample number and the averaging factor $k_{avg} = 1172$. The coloured square indicates the alignment status, using the same colour coding as described in Table 6.2.

The application can be used in collimator scan mode by moving on to the next tab (see Fig. 6.12). All input parameters related to the scan are inserted in the top-left panel. An example of the table generated automatically by the collimator scan is visible in Fig. 6.13. As mentioned in Section 5.8.2, the BPM non-linearity coefficients and electronics calibration factors can be modified on the fly. The user interface that provides this is shown in Fig. 6.14.

6.4.3 Data logging

All data generated by the application, including alignments, collimator scans and changes of coefficients and calibration factors are logged for offline analysis.
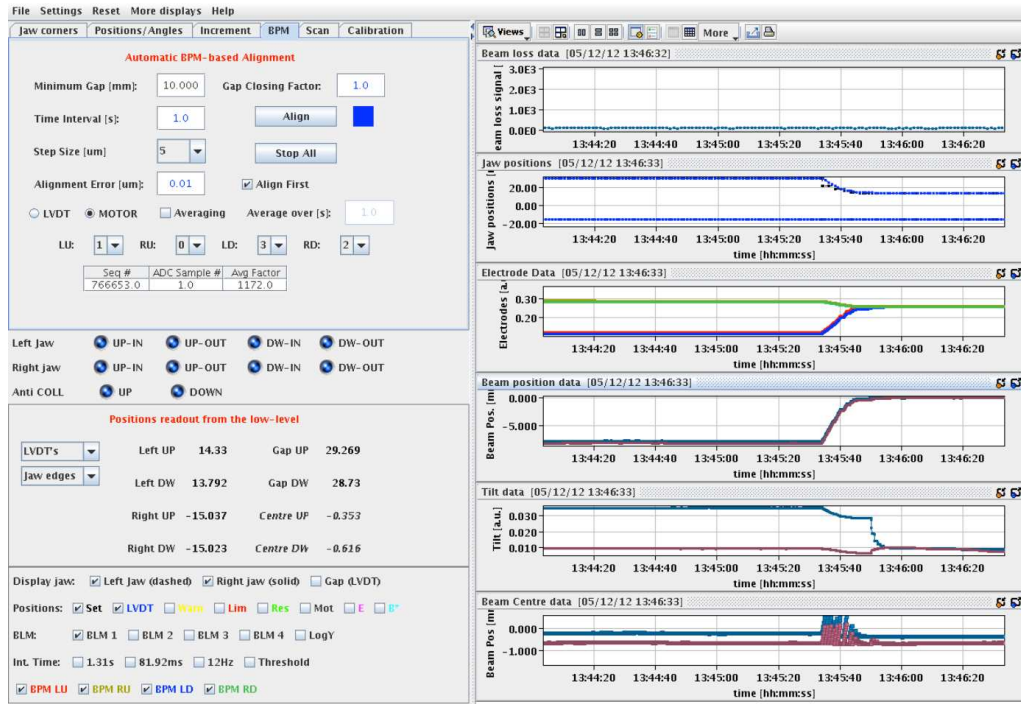
Figure 6.11: A screenshot of the BPM-based alignment application, showing the alignment input parameters in the top-left panel.
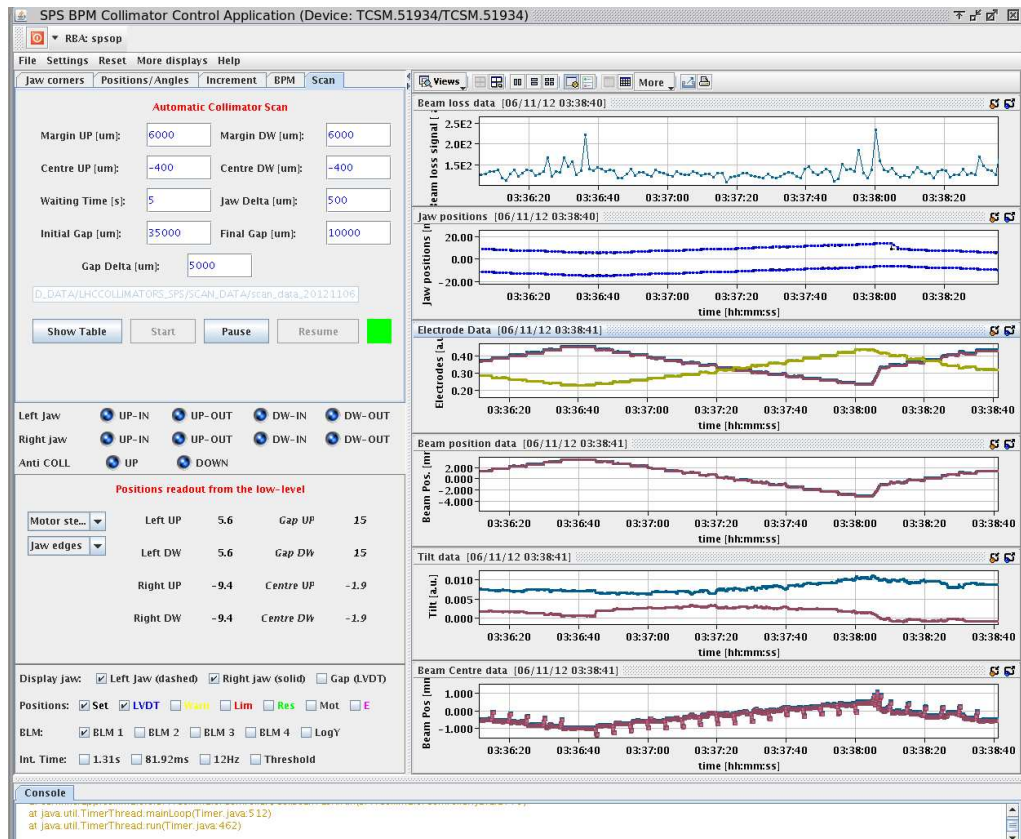
Figure 6.12: A screenshot BPM-based alignment application, showing the collimator scan input parameters in the top-left panel.

Gap	Jaw Centre	E–LU	E–LD	E–RU	E–RD	MOT–LU	MOT–LD	MOT–RU	MOT–RD	Timestamp	Status	Comments
20.000	−3.900	0.457752	0.230674	0.451284	0.230275	6.100	6.100	−13.900	−13.900	1352169404734	OK	
20.000	−3.400	0.440484	0.239969	0.434682	0.239042	6.600	6.600	−13.400	−13.400	1352169409734	OK	
20.000	−2.900	0.424193	0.249607	0.418708	0.248423	7.100	7.100	−12.900	−12.900	1352169414734	OK	
20.000	−2.400	0.409188	0.258993	0.404055	0.257636	7.600	7.600	−12.400	−12.400	1352169419734	OK	
20.000	−1.900	0.389387	0.272601	0.384095	0.271196	8.100	8.100	−11.900	−11.900	1352169424735	OK	
20.000	−1.400	0.373723	0.284210	0.368504	0.282689	8.600	8.600	−11.400	−11.400	1352169429736	OK	
20.000	−0.900	0.360777	0.294490	0.355880	0.292684	9.100	9.100	−10.900	−10.900	1352169434736	OK	
20.000	−0.400	0.347305	0.305787	0.342471	0.303974	9.600	9.600	−10.400	−10.400	1352169439735	OK	
20.000	0.100	0.332178	0.319579	0.327270	0.317834	10.100	10.100	−9.900	−9.900	1352169444736	OK	
20.000	0.600	0.317862	0.333743	0.312996	0.331880	10.600	10.600	−9.400	−9.400	1352169449736	OK	
20.000	1.100	0.304732	0.347760	0.299832	0.345840	11.100	11.100	−8.900	−8.900	1352169454736	OK	
20.000	1.600	0.297896	0.355114	0.293433	0.353008	11.600	11.600	−8.400	−8.400	1352169459736	OK	
20.000	2.100	0.281991	0.374420	0.277244	0.372584	12.100	12.100	−7.900	−7.900	1352169464737	OK	
20.000	2.600	0.269919	0.390359	0.265120	0.388466	12.600	12.600	−7.400	−7.400	1352169469737	OK	
20.000	3.100	0.257948	0.407439	0.253074	0.405691	13.100	13.100	−6.900	−6.900	1352169474738	OK	
15.000	3.600	0.247847	0.422733	0.243015	0.421192	13.600	13.600	−6.400	−6.400	1352169479738	OK	
15.000	1.100	0.236788	0.441594	0.231670	0.440474	8.600	8.600	−6.400	−6.400	1352169484737	OK	
15.000	0.600	0.338576	0.415719	0.332015	0.415926	8.100	8.100	−6.900	−6.900	1352169489737	OK	
15.000	0.100	0.352817	0.400205	0.346048	0.400666	7.600	7.600	−7.400	−7.400	1352169494737	OK	
15.000	−0.400	0.365121	0.386877	0.357950	0.387377	7.100	7.100	−7.900	−7.900	1352169499737	OK	
15.000	−0.900	0.386530	0.365281	0.379534	0.365582	6.600	6.600	−8.400	−8.400	1352169504737	OK	
15.000	−1.400	0.407243	0.346298	0.400219	0.346599	6.100	6.100	−8.900	−8.900	1352169509737	OK	
15.000	−1.900	0.420581	0.335000	0.412978	0.335507	5.600	5.600	−9.400	−9.400	1352169514738	OK	
15.000	−1.900	0.438445	0.320782	0.430812	0.321246	5.600	5.600	−9.400	−9.400	1352169519738	OK	
15.000	−1.400	0.443316	0.316763	0.436424	0.316772	6.100	6.100	−8.900	−8.900	1352169524738	OK	

Figure 6.13: A screenshot of the table automatically generated by the collimator scan.
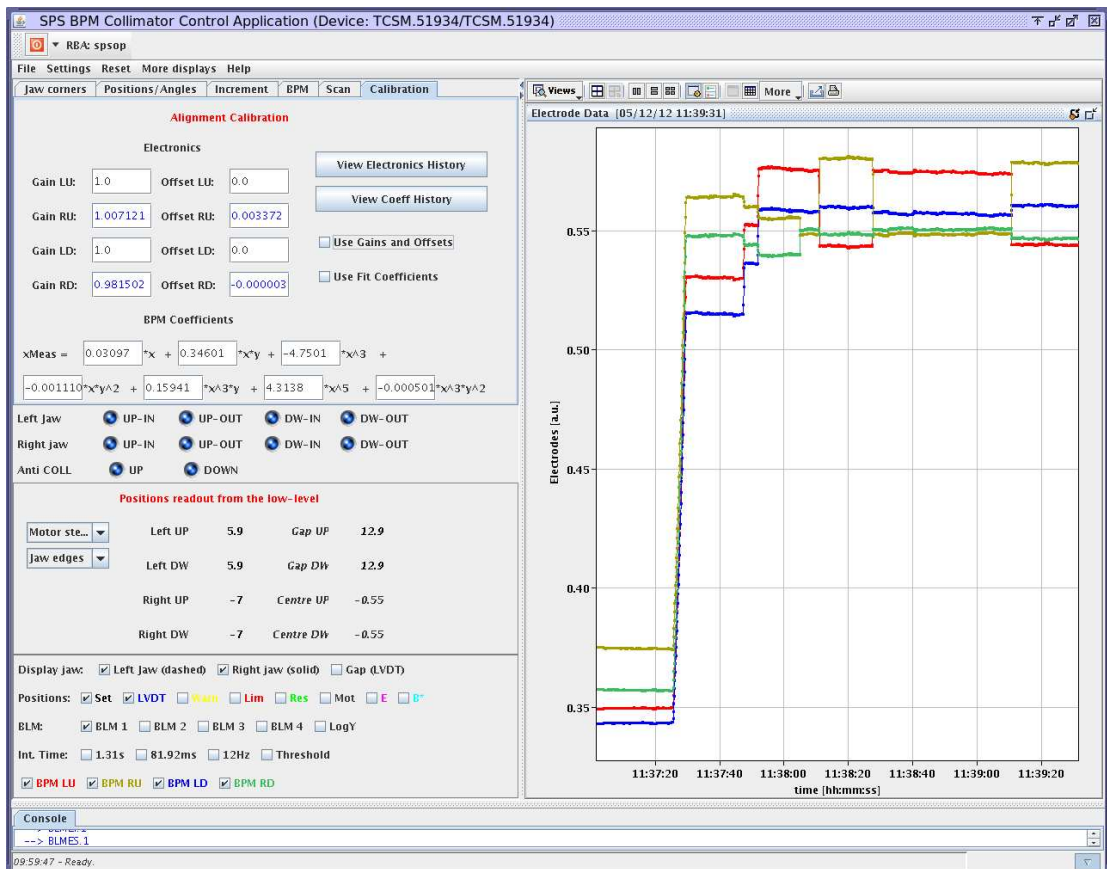
Figure 6.14: A screenshot BPM-based alignment application, showing the adjustable BPM non-linearities and electronics errors correction parameters in the top-left panel.

6.5 Collimator system fixed display

A fixed display was developed to provide an overview of the status of the LHC collimation system at all times during operation [102]. The display is shown overhead in the CCC for the benefit of the LHC operators, and is also available online for the general public [103].

6.5.1 Monitored LSA parameters

A list of the parameters monitored from the LSA database by the display is given below.

- CollimatorStatus#prsState

- CollimatorStatus#mdcState

- MeasuredCornerPositions#lvdt_left_upstream

- MeasuredCornerPositions#lvdt_left_downstream

- MeasuredCornerPositions#lvdt_right_upstream

- MeasuredCornerPositions#lvdt_right_downstream

- MeasuredCornerPositions#mdcWarnings

- MeasuredCornerPositions#prsWarnings

- MeasuredCornerPositions#mdcErrors

- MeasuredCornerPositions#prsErrors

- BeamMode_LHC

The MDC and PRS error and warning bits and the corresponding descriptions are provided in Table 6.4 to Table 6.7. A description of the colour codes for parameters 1 and 2 is provided in Table 6.8, while the colour codes for parameters 7 to 10 are provided in Table 6.9.

Table 6.4: MDC errors (by courtesy of A. Masi)

FESA Bit Name	Bit	Description
FPGA_STUCK	0	The FPGA is stuck
CPU_STUCK	1	The PXI CPU is stuck
LEFT_UP_RESOLVER_STEP_LOST	2	LU resolver detected lost motor steps
LEFT_DOWN_RESOLVER_STEP_LOST	3	LD resolver detected lost motor steps
RIGHT_UP_RESOLVER_STEP_LOST	4	RU resolver detected lost motor steps
RIGHT_DOWN_RESOLVER_STEP_LOST	5	RD resolver detected lost motor steps
LEFT_JAW_STOPPED	6	The left jaw motion was stopped
RIGHT_JAW_STOPPED	7	The right jaw motion was stopped
ALL_SWITCHES_ACTIVE	8	All switches active, electrical problem
INNER_SWITCH_ACTIVE	9	At least one inner end-switch is active
ANTICO_SWITCH_ACTIVE	10	At least one anti-collision end-switch is active
INTERLOCK_B1A_ACTIVE	11	B1 A beam permit is/was removed
INTERLOCK_B1B_ACTIVE	12	B1 B beam permit is/was removed
INTERLOCK_B2A_ACTIVE	13	B2 A beam permit is/was removed
INTERLOCK_B2B_ACTIVE	14	B2 B beam permit is/was removed
DRIVERS_DISABLED	15	Motor drivers are disabled, the collimator cannot move
TUNE_N_ABORTED	16	The "tune n" command was aborted
NOT_INITIALIZED	17	MDC system is not initialized by the FESA class
OFFLINE_MODE	18	MDC is running in offline mode

Table 6.5: MDC warnings (by courtesy of A. Masi)

FESA Bit Name	Bit	Description
POSITION_NOT_REACHED_SWITCH_ACTIVE	0	Requested position not reached
OUTER_SWITCHES_ACTIVE	1	At least one outer end-switch is active
EXPERT_MODE	2	Collimator controlled by expert
RESOLVER_OUT_OF_RANGE	3	At least one axis has a difference between resolvers and controller more than the threshold

Table 6.6: PRS errors (by courtesy of A. Masi)

FESA Bit Name	Bit	Description
FPGA_STUCK	0	The FPGA is stuck
CPU_STUCK	1	The PXI CPU is stuck
PROFILE_OUT_OF_ENERGY	2	LVDT position out of energy limits
POSITION_OUT_OF_CONSTANT_LIMITS	3	LVDT position out of constants limits
PROFILE_OUT_OF_DUMP_LIMIT_FUNCTION	4	LVDT position out of dump limits (during profile execution)
INTERLOCK_B1A_ACTIVE	5	B1 A beam permit is/was removed
INTERLOCK_B1B_ACTIVE	6	B1 B beam permit is/was removed
INTERLOCK_B2A_ACTIVE	7	B2 A beam permit is/was removed
INTERLOCK_B2B_ACTIVE	8	B2 B beam permit is/was removed
MDC_RIGHT_JAW_STOPPED	9	PRS stopped the right jaw motion on MDC
MDC_LEFT_JAW_STOPPED	10	PRS stopped the left jaw motion on MDC
ENERGY_TIMEOUT	11	Energy limits sent by FESA class not received in due time
INTERLOCK_INJA_ACTIVE	12	Beam permit on channel injection A is/was removed (interlock)
INTERLOCK_INJB_ACTIVE	13	Beam permit on channel injection B is/was removed (interlock)
OFFLINE_MODE	14	PRS operating in offline mode
PROFILE_OUT_OF_BETA_STAR	15	LVDT position out of β^* limits
BETA_STAR_TIMEOUT	16	β^* limits sent by FESA class not received in due time

Table 6.7: PRS warnings (by courtesy of A. Masi)

FESA Bit Name	Bit	Description
POSITION_OUT_OF_WARNING_CONSTANTS	0	LVDT position out of constant warning limits
PROFILE_OUT_OF_FUNCT_WARNING_LIMITS	1	LVDT position out of profile warning limits
POSITION_OUT_OF_WARNING_ENERGY_LIMIT	2	LVDT position out of energy warning limits
EXPERT_MODE	3	Collimator controlled by expert
ERROR_MOTOR_LVDT	4	LVDT-controller difference is more than the threshold

Table 6.8: Colour codes for the collimator statuses.

Colour	Description
Green	WAITING_COMMANDS
Yellow	MOTION_EXECUTION
Red	UNCONFIGURED
Purple	ARMED

Table 6.9: Colour codes for the MDC/PRS warning and errors.

Colour	Description
Green	No PRS/MDC Warnings or Errors
Yellow	PRS and/or MDC Warnings
Red	PRS and/or MDC Errors

6.5.2 Display layout

The left and right jaws of each collimator are represented horizontally inside a box (Fig. 6.15). The average of the LVDT upstream and downstream measurement values of each jaw are calculated. Two boxes representing the jaws are placed inside the main box, and are sized such that they give an accurate impression of the gap between the jaws, which is depicted in white. The maximum retraction position that can be displayed is 30 mm. The jaw boxes are coloured according to the status of the collimator. Bracketing the jaws are the MDC settings and PRS status boxes, as well as the left and right jaw average LVDT values in mm.

Figure 6.15: Single collimator display box. The following parameters are displayed (from left to right): average of LU and LD LVDT jaw positions, MDC status, collimator status, collimator name, PRS status, average of RU and RD LVDT jaw positions. The white space gives an accurate impression of the jaw gap.

Two screens are created, one per beam. The collimator boxes are grouped by IP and ordered by their location (s position in metres) in the ring. The border colour coding reflects the standard convention for the beam being displayed (blue for B1, red for B2). Screenshots of the collimator display during stable beams are shown in Fig. 6.16a and Fig. 6.16b. The status of the injection protection collimators is red because their jaw positions are outside the injection limits, therefore preventing injection.
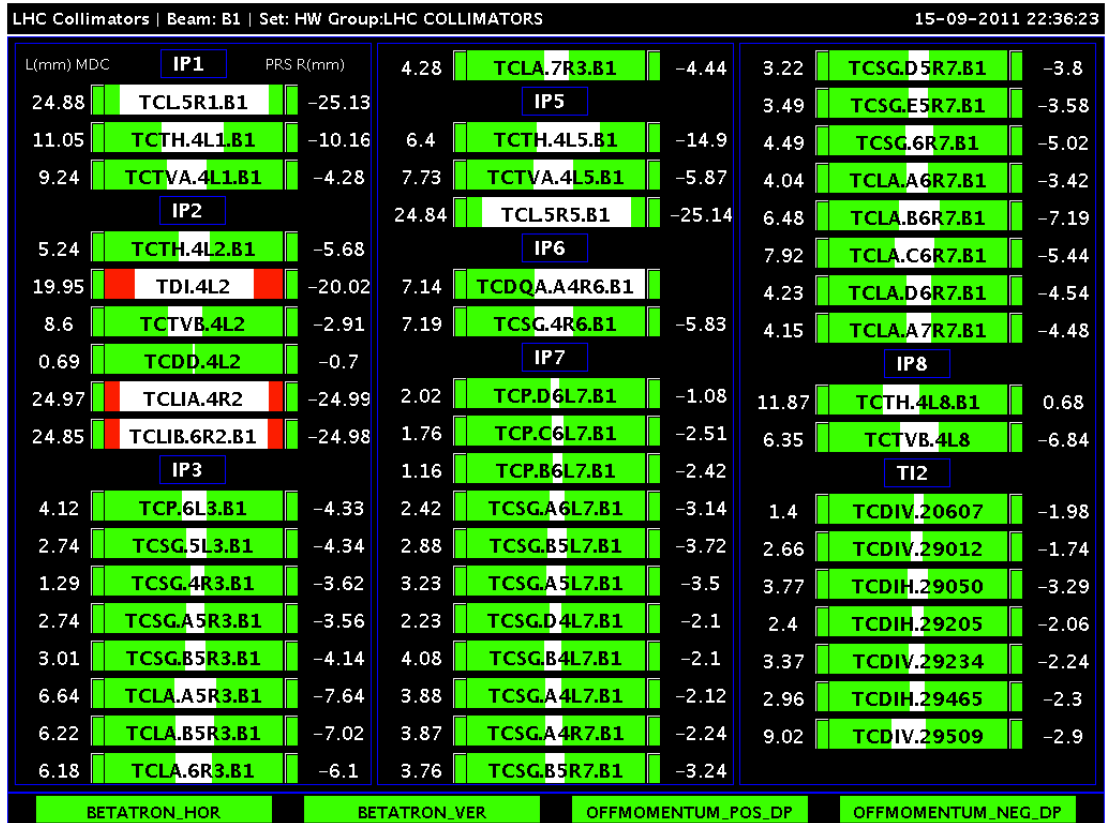
(a) Collimator fixed display B1
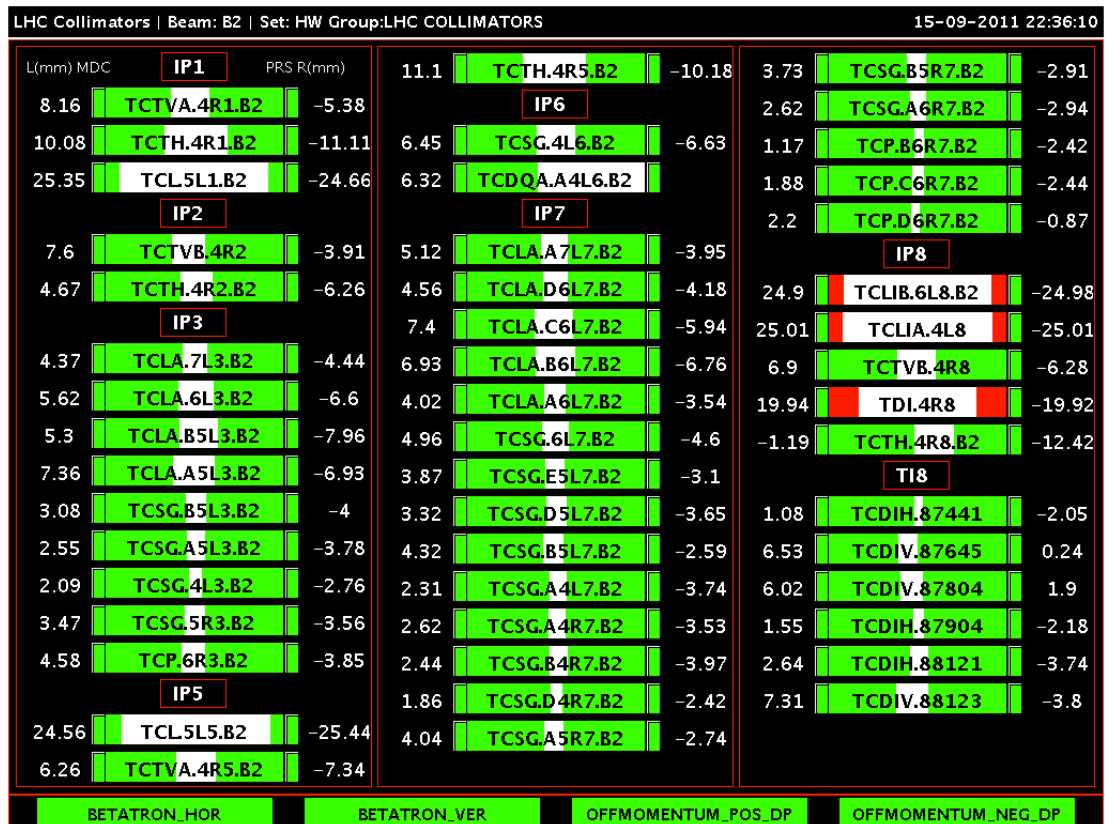
(b) Collimator fixed display B2
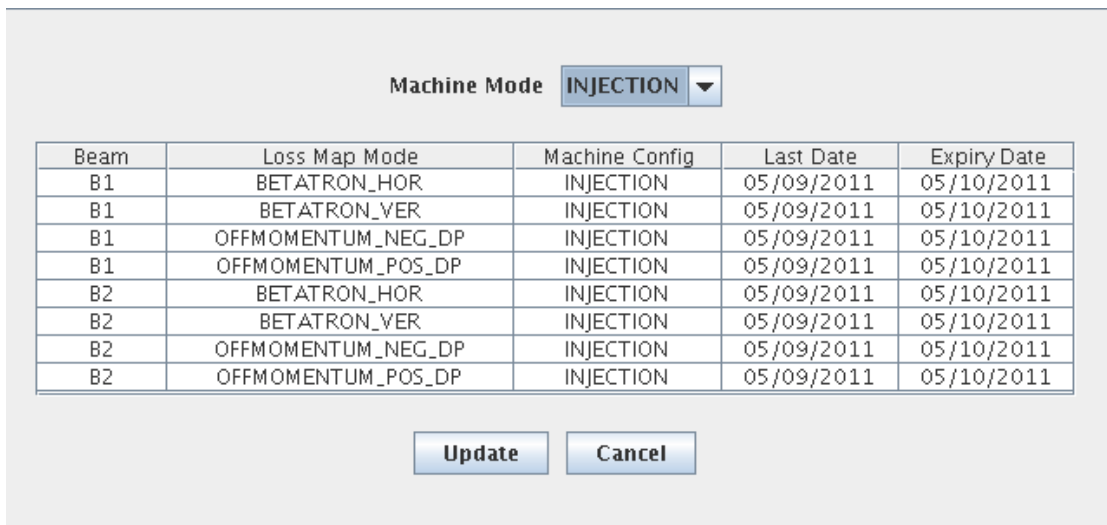
Figure 6.16: LHC collimator vistar fixed display.

6.5.3 Beam loss map validity

The collimation system is qualified regularly by performing betatron (horizontal and vertical) and momentum (positive and negative) beam loss maps. Therefore, the four loss maps per beam are:

- Betatron Horizontal

- Betatron Vertical

- Positive Off-Momentum

- Negative Off-Momentum

Qualification of the hierarchy is done at four stages of the machine cycle: injection, flat top, after the squeeze and during collisions. This leads to a total of 32 loss maps for both beams. The loss map validity start and stop dates are stored in a table in the LSA database. Typically in 2012, 3 months were set for the injection, flat top and squeezed loss maps, and 1 month was set for the expiry of the physics loss maps. If more than one week is left until the deadline, the status is green. With one week or less to go, the status turns yellow, and if the validity period is expired the status turns red. The status is intended simply for informational purposes and does not affect the collimation system operation in any way. The loss map validity dates can be updated from an application (GUI displayed in Fig. 6.17) when the system is qualified again. The validity statuses for the four types of loss maps per beam are displayed at the bottom of the fixed display.

Figure 6.17: Loss Map Validity GUI.

The loss map status is updated on change of the LHC Beam Mode, based on the mappings shown in Table 6.10.

Table 6.10: Mapping from loss map machine configuration to LHC beam mode.

Loss Map Beam Mode	LHC Beam Mode
INJECTION	INJECTION PROBE BEAM
	INJECTION SETUP BEAM
	INJECTION PHYSICS BEAM
	INJECT AND DUMP
	CYCLING
	RECOVERY
	CIRCULATE AND DUMP
	NO BEAM
	PREPARE RAMP
	SETUP
	ABORT
	BEAM DUMP
FLAT TOP	FLAT TOP
	RAMP
SQUEEZE	SQUEEZE
PHYSICS	ADJUST
	STABLE
	BEAM DUMP WARNING
	UNSTABLE BEAMS

6.6 Software validation

The alignment and fixed display software were tested using standard techniques on multiple levels. Testing at the individual module level is known as "unit testing", while testing performed over all the modules operating as a whole program is called "integration testing" [104]. The defensive programming feature offered by the Java environment, namely the exceptions mechanism, was exploited to ease the debugging and validation process. All possible runtime errors related to parameter subscription, network connections, input/output and user input formats are handled. The implementation of the individual algorithms were tested using the black-box and glass-box approaches.

6.6.1   Black-box testing

The black-box approach involves generation of test inputs without any regard for the internal implementation. It is particularly useful as the test inputs do not need to be changed if the underlying implementation is modified. Test data was derived from real alignments in the case of the feedback loop, and from data used in generating the models in the case of the threshold selection, pattern recognition and BPM-interpolation beam centre approximation algorithms. The tests ensured that:

- the loss threshold was correctly selected based on the empirical model;

- the feedback loop correctly stopped the jaw movement if the losses exceeded the predefined threshold;

- the pattern recognition module correctly classified the loss spikes as it had in the SVM model;

- the calculation of the tighter jaw positions around the BPM-interpolated orbit is correct;

- the beam centre calculated from the BPM electrode signals and the jaw positions is correct.

In addition, the BPM-based alignment algorithm was tested using the following equations kindly provided by M. Gasior, which simulate the electrode signals for the left and right pick-up buttons:

$$V_L = \frac{B^2}{(B + X_{beam})^2} \tag{6.5}$$

$$V_R = \frac{B^2}{(B - X_{beam})^2} \tag{6.6}$$

where B is the BPM aperture and X_{beam} is the fixed beam position, using the same notation as defined in Section 3.2.3 and Appendix D.

6.6.2   Glass-box testing

Glass-box testing complements black-box testing by ensuring that each path in the code is exercised by at least one test (path-completeness). This testing approach was used to validate all possible user actions in the individual GUI modules, as well as to perform integration testing and ensure that the GUI, algorithm modules and alignment sequencer all work together as expected. The static testing and Application Programming Interface (API) testing techniques, which involved code walkthroughs and individual testing of class functionality respectively, were used.

Chapter 7

Modeling and Simulation of Collimator Setup

7.1 Motivation

An accurate analysis of the BLM signals can allow for a comparison between the measured beam losses and the losses predicted by simulation models. This data can also be used for a simulator that produces a realistic BLM signal response for a given collimator movement. Such a simulator is important as it would provide adequate training for machine learning-based algorithms before they are deployed with real beam. Given certain observed correlations of beam loss patterns with energy, such as the temporal decay, a model could be set up to predict the losses that will be observed during setup with 7 TeV beams.

Static and dynamic models were developed. The static model assumes a fixed Gaussian distribution of the beam particles, and was built using data from collimator scrapings performed in 2011. A collimator scraping is performed by moving in a jaw in steps with a certain step time interval until part or all of the beam is scraped away. The main disadvantage of this model is that the beam tails are in fact non-Gaussian, and only the beam core can be approximated by a Gaussian curve. On the other hand, the dynamic model provides a more realistic approach, as the BLM signal is predicted from beam diffusion coefficients measured in 2012, and is independent of the beam distribution.

7.2 Modeling of BLM signals during setup

The typical beam loss signal during collimator setup is similar to the example in Fig. 7.1. The loss pattern can be divided into four components, where each component is due to a beam physics process which must be understood for modeling purposes:
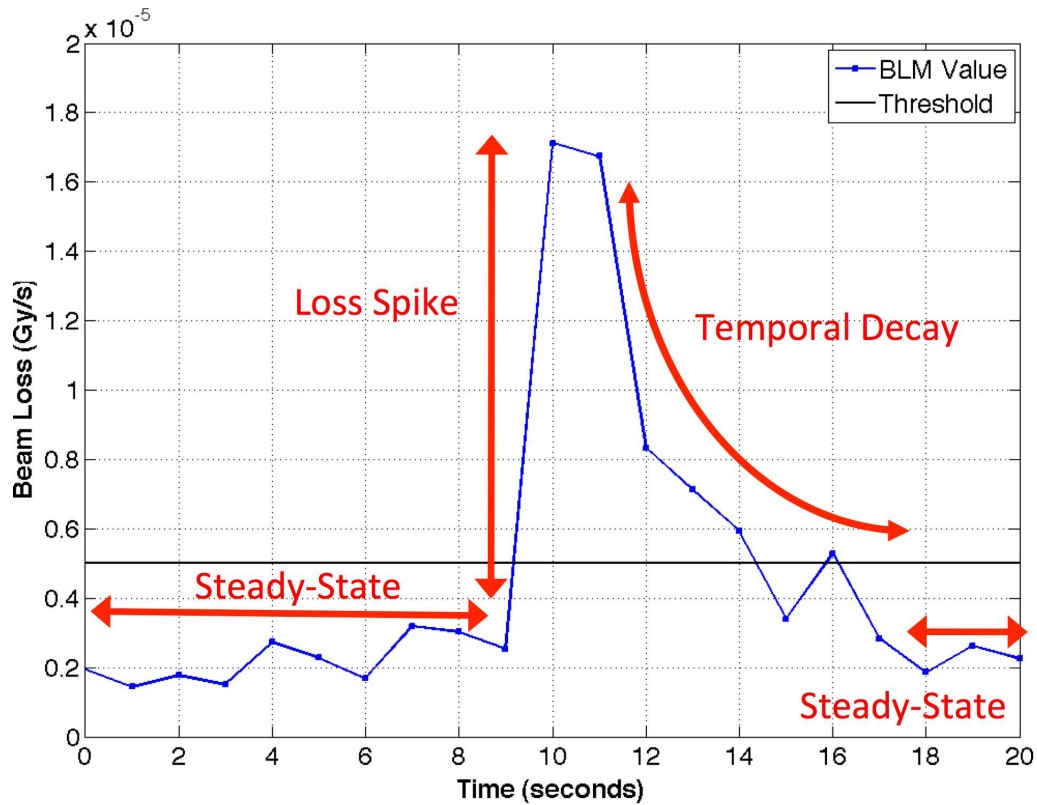
Figure 7.1: The components of a typical clear BLM signal when the collimator jaw touches the beam halo [105].

1. Steady-state signal before the spike

2. Loss spike

3. Temporal decay in the losses

4. Steady-state signal after the losses have decayed

BLM signal crosstalk is another phenomenon that must be modeled on a global scale (see Fig. 5.2). Crosstalk occurs when a collimator jaw touches the beam, which causes beam loss spikes to appear in multiple BLM detectors, some of which may be associated with other collimators. These collimators may be stopped by the beam loss feedback algorithm, and hence understanding which collimators are likely to be stopped in the event of another collimator touching the beam is key to building an accurate simulator.

7.3 Steady-state BLM signal

The steady-state BLM signal is due to a continuous scraping process where halo particles are constantly scattered away from the beam core when the jaw positions are fixed. Intuitively, the further a jaw cuts into the beam halo, the more the steady-state signal increases as the density of the particles near the jaw increases. An empirical analysis was performed, using data from four major alignments in 2011 and 2013, at beam energies of 450 GeV, 3500 GeV and 4000 GeV.

A steady-state sample is defined to be the average of the last 5 s of values of a collimator BLM detector when no collimator was moving in the previous 10 s. A script was written to extract hundreds of samples for each collimator BLM detector. In many cases, the jaws were stationary for more than 10 s, and hence multiple samples were collected for a given jaw half gap in units of beam σ. Polynomial fits of the form:

$$y = a + \frac{b}{x + c} \tag{7.1}$$

were applied to plots of the samples as a function of the jaw half gap for each collimator, where a, b and c are fitting parameters and x is the sample data. The average BLM signal before and after the loss spike was found to decrease exponentially with the collimator jaw half gap (see Fig. 7.2). An empirical model for this component of the BLM signal can therefore be developed. For simulation purposes, the steady-state loss rate is calculated from the fit equation depending on the distance of the jaw from the beam centre.

7.4 Static model of spike and decay

7.4.1 BLM loss spike

Particles in high-intensity beams are assumed to have a Gaussian distribution in the transverse plane [106]. Figure 7.3 illustrates the new beam particle distribution after a round jaw cut in units of beam σ of $n_\sigma = 2.0$ and $n_\sigma = 2.5$. The effects of a single-sided, single-turn cut and a round cut of the beam distribution after multiple turns are shown in Fig. 7.4. A model described in [107] attempts to predict the beam losses that occur during injection, when beam is transferred from the
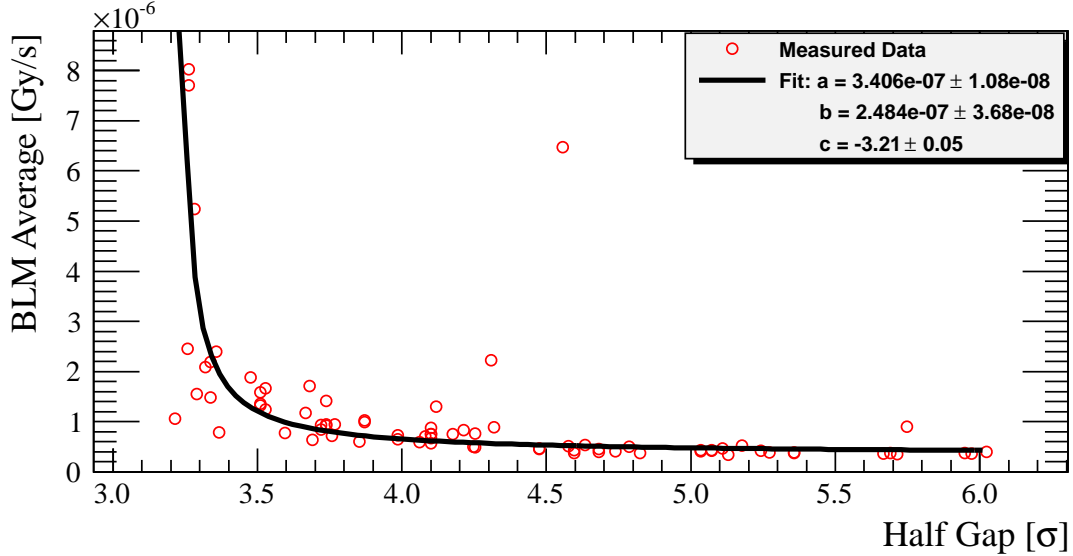
Figure 7.2: Polynomial fit applied to the average BLM steady-state signal as a function of the jaw half gap. The data are for the TCP.C6L7.B1 collimator.

SPS to the LHC via collimator-equipped transfer lines with fixed jaw positions. This work attempts to extend this model to beam losses observed during scraping and collimator setup, where multiple jaw movements of 5 μm to 40 μm every few seconds are common. The fraction of particles lost after scraping, $F_{lost}(n_\sigma)$, can be expressed in terms of the collimator jaw position x and the beam centre x_0 as follows:

$$F_{lost}(n_\sigma) = e^{-n_\sigma^2/2} = e^{\frac{-\frac{1}{2}(x-x_0)^2}{\sigma_x^2}} \tag{7.2}$$

The distribution of the beam following a cut of n_σ in terms of the collimator jaw position x and the 1 σ beam size in mm is then:

$$y = \frac{e^{\frac{-x^2}{2\sigma_x^2}}}{\sqrt{2\pi}} \text{erf}\left(\frac{\sqrt{n_\sigma^2 - \frac{x^2}{\sigma_x^2}}}{2}\right) \times N_0 \tag{7.3}$$

where N_0 is the beam intensity. A detailed derivation is available in Appendix E.

7.4.2 Comparison with measured data

In July 2011, a beam distribution MD experiment was performed with 450 GeV beams to study the population of the beam using collimator scrapings. The left
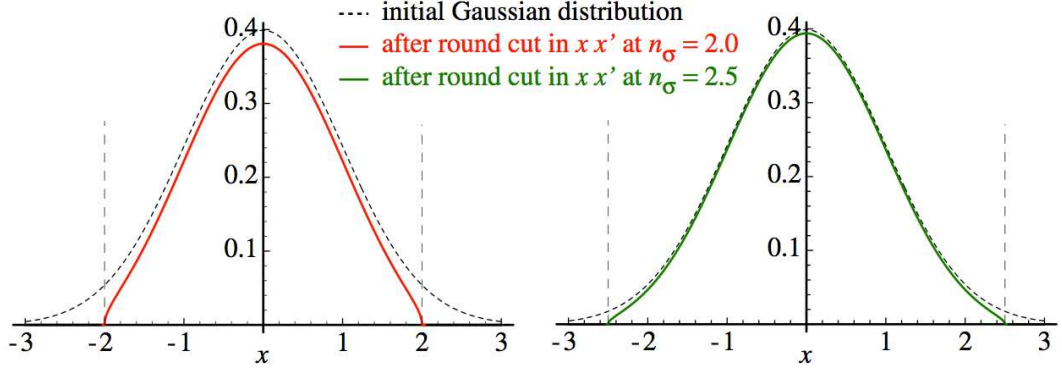
Figure 7.3: Gaussian beam profile in the x plane before (dashed line) and after (solid line) collimation at $n_\sigma = 2.0$ (a) and $n_\sigma = 2.5$ (b). From [107].
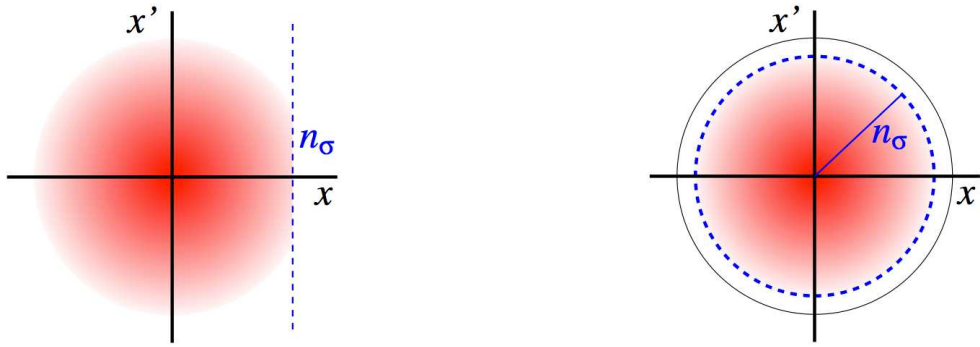
Figure 7.4: Single-sided cut of the beam distribution in the x, x' phase space after a single turn (a), and round cut of the beam distribution after multiple turns (b). From [107].

jaws of the primary collimators were moved in separately in 40 μm steps every 4 seconds. The model described in the previous section was implemented in MATLAB to determine whether the measurement data were reproduced. A list of the parameters for each primary collimator is shown in Table 7.1.

Table 7.1: Measured beam scraping parameters.

Collimator	Model Parameters				
	Emittance (μm)	σ_x (mm)	x_0 (mm)	N_0 (p)	f_i^{calib} (p/Gy)
TCP.C6L7.B1	1.4	0.663	- 0.280	1.37E11	1.25E12
TCP.C6R7.B2	1.8	0.730	- 0.160	1.18E11	1.26E12
TCP.D6L7.B1	1.4	0.478	0.470	1.24E11	1.20E12
TCP.D6R7.B2	1.9	0.542	0.650	1.32E11	1.13E12
TCP.B6L7.B1	1.3	0.540	- 0.640	1.25E11	1.94E12
TCP.B6R7.B2	2.0	0.654	- 0.635	1.10E11	1.75E12

Table 7.2 presents a comparison of the measured and the simulated beam intensity lost in the scraping. The same data are plotted as a function of the collimator jaw half gap in mm in Fig. 7.5. The measured lost intensity N_{meas}^{lost} at each step

Table 7.2: Comparison of the lost intensity (measured and simulated data) during the scraping.

Collimator	N_0 (p)	N_{sim}^{lost} (p)	N_{meas}^{lost} (p)
TCP.C6L7.B1	1.37E11	1.37E11	1.37E11
TCP.C6R7.B2	1.18E11	1.18E11	1.18E11
TCP.D6L7.B1	1.24E11	1.24E11	1.27E11
TCP.D6R7.B2	1.32E11	1.32E11	1.32E11
TCP.B6L7.B1	1.25E11	1.25E11	1.25E11
TCP.B6R7.B2	1.10E11	1.10E11	1.10E11

was derived from the decrease in the beam intensity measured by the Fast Beam Current Transformer (FBCT) over a 4 second period following each step, to allow the FBCT signal to stabilize. On the other hand, the simulated lost intensity is calculated by integrating over the scraping range:

$$N_{sim}^{lost} = \int_{x_0}^{x_{start}} F_{lost}(n_\sigma)dx \qquad (7.4)$$

where x_{start} is the jaw position at the start of the scraping. Since all the beam was scraped away by the collimator jaw, if the intensity lost at each jaw step is integrated over the whole scraping, the initial intensity should result. The simulated and measured lost intensity are identical to the initial intensity. The slight increase in the intensity signal at 0 mm is due to a delay in the jaw movement when moving from 0.58 mm to 0.54 mm (which in terms of half gap as shown on the plot translates to a movement from 0.11 mm to 0.07 mm). The effect of the delayed jaw movement is seen in both the simulated and measured data.
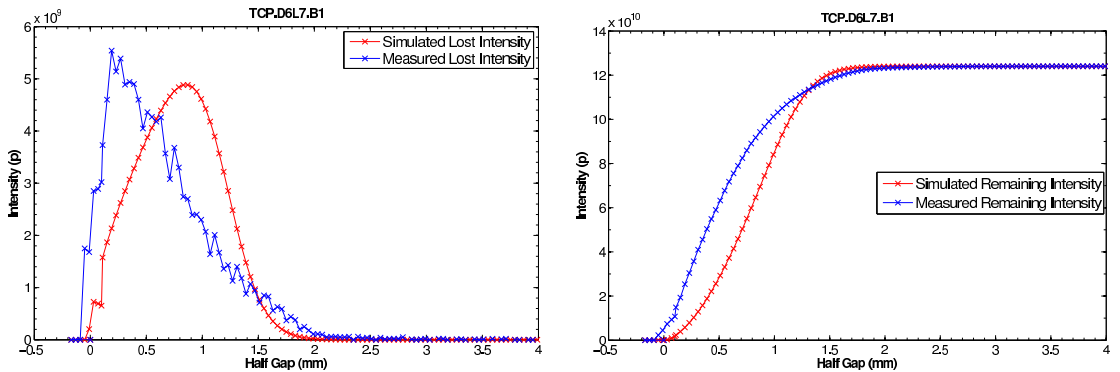
(a) Lost intensity (without error compensation)

(b) Remaining intensity (without error compensation)

Figure 7.5: Measured and simulated intensity every 4 seconds as a function of the collimator jaw half gap (without error compensation).

112

Table 7.3: Variance for different distributions after beam cuts.

Particle Distribution	$1\,\sigma$ beam size (mm)
Original	1.05
$5\,\sigma$ cut	1.05
$4\,\sigma$ cut	1.0499
$3\,\sigma$ cut	1.0447
$2\,\sigma$ cut	0.97136
$1\,\sigma$ cut	0.64101

As the model assumes that there are no losses before the jaw movement, and the summation is performed from $-\infty$, the measured data can be approximated further by subtracting some losses from the fraction of lost particles given by the model:

$$F_{lost}(n_\sigma) = e^{-n_\sigma^2/2} = e^{\frac{-\frac{1}{2}(x-x_0)^2}{\sigma_x^2}} - e^{\frac{-\frac{1}{2}(x+a-x_0)^2}{\sigma_x^2}} \tag{7.5}$$

The best fit to the measured data was found with a fitting parameter $a = 0.15$. Comparisons of the error-compensated simulated intensity to the measured data are shown in Fig. 7.6 and Fig. 7.7. Small shifts in the x-axis can be observed for the simulated data when compared to the measured data. This is because the beam centre assumed in the simulation is the one determined in the setup held in March 2011. However, by July 2011 (when the scraping MD was performed), the beam centre shifted by a few tens of μm. The BLM signal (Gy/s) can now be obtained from the loss rate (p/s) using the calibration factor [79]:

$$S_i(t) = \frac{R_i(t)}{f_i^{calib}} \tag{7.6}$$

Each measured and simulated data point in Fig. 7.8a to Fig. 7.8f corresponds to the BLM signal spike value obtained every 4 seconds when the jaw is moved in. In Fig. 7.9, the effect of various jaw cuts into the beam on the resulting particle distribution is plotted. Table 7.3 shows the corresponding $1\,\sigma$ beam size in mm, which is obtained from a Gaussian fit to the particle distribution. The simulated decrease in the intensity is therefore given by:

$$N_i = N_{i-1} \times (1 - F_{lost}(n_\sigma)) \tag{7.7}$$

(a) Lost intensity (TCP.D6L7.B1)　　　(b) Remaining intensity (TCP.D6L7.B1)
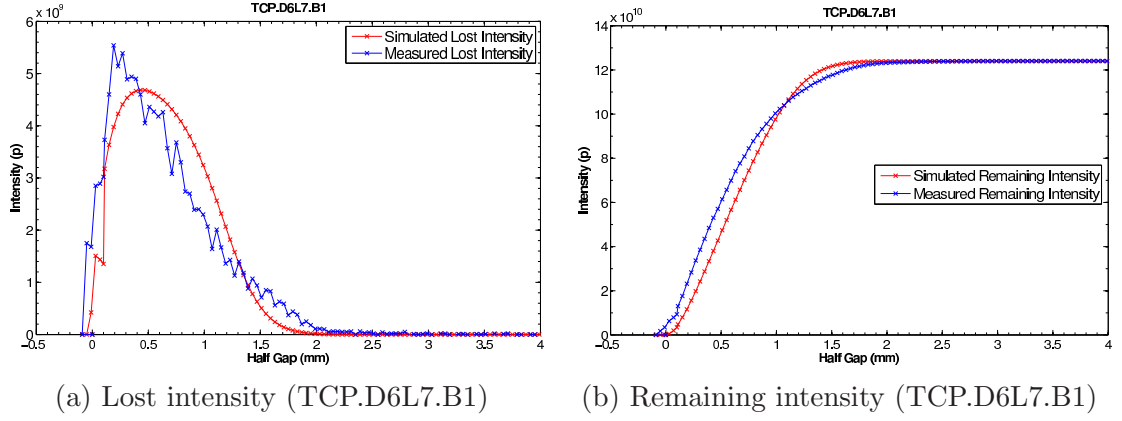
Figure 7.6: Measured and simulated intensity every 4 seconds as a function of the collimator jaw half gap (TCP.D6L7.B1), from [108].

(a) Lost intensity (TCP.D6R7.B2)　　　(b) Remaining intensity (TCP.D6R7.B2)
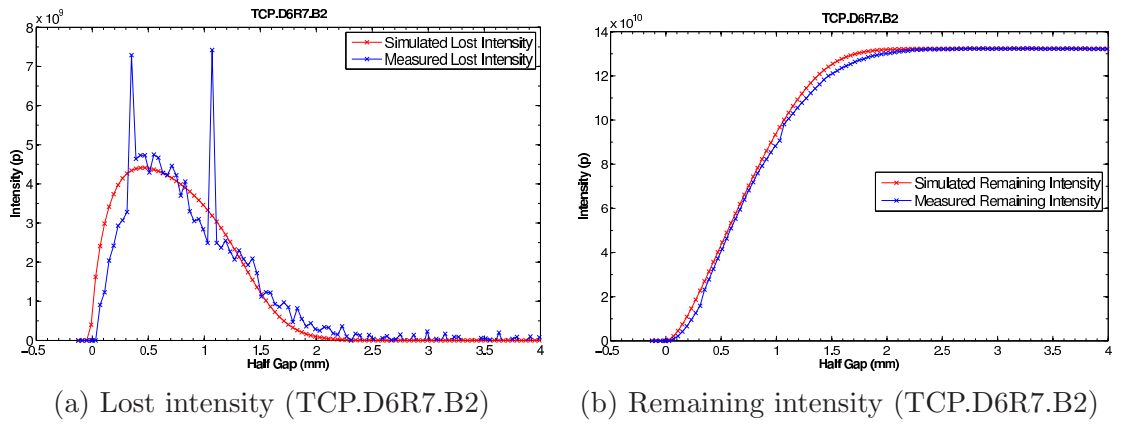
Figure 7.7: Measured and simulated intensity every 4 seconds as a function of the collimator jaw half gap (TCP.D6R7.B2).

7.4.3　Temporal decay in the losses

Rather than attempting to understand the underlying physics processes which could explain the temporal decay, it was sufficient for the purposes of the static model to perform an empirical analysis. The fit parameters are:

- Amplitude a

- Power coefficient n

- Error between fit and data R

A number of loss spike samples were collected (299 at 450 GeV and 262 at 3.5 TeV), and a polynomial curve of the form $y = ax^n$ was fit to each sample in MATLAB using the Ezyfit curve-fitting tool. Two examples are show in Fig. 7.10. In addition, all samples were visually examined to determine the decay time, which is

114

(a) BLM loss spike (TCP.B6L7.B1)

(b) BLM loss spike (TCP.B6R7.B2)

(c) BLM loss spike (TCP.C6L7.B1)

(d) BLM loss spike (TCP.C6R7.B21)

(e) BLM loss spike (TCP.D6L7.B1)

(f) BLM loss spike (TCP.D6R7.B2)
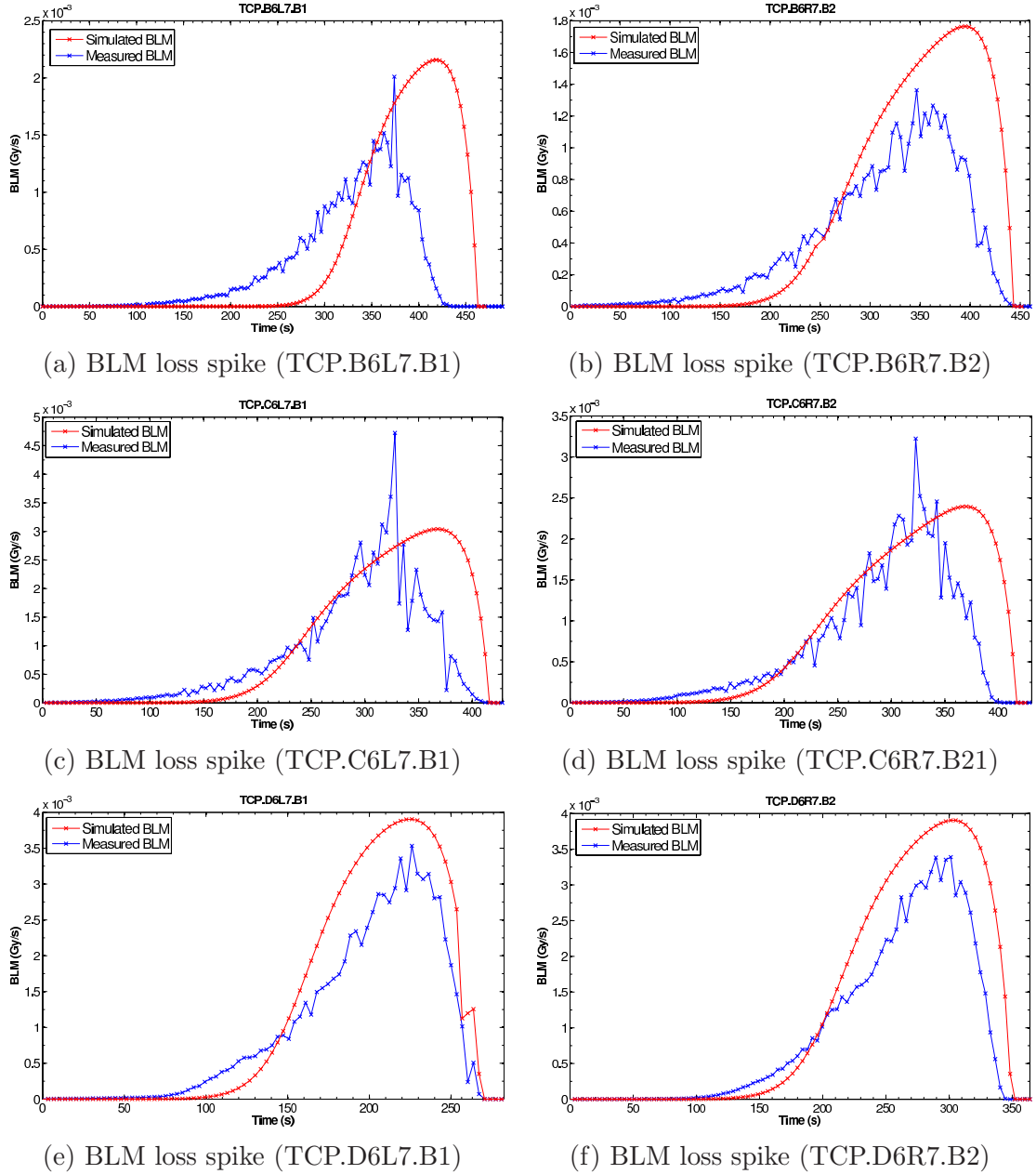
Figure 7.8: Measured and simulated BLM spike every 4 seconds calculated from the loss rate for the primary collimators.

the time taken for the losses to decrease to a quasi-constant level (the steady-state BLM signal). For example, in Fig. 7.10b, the decay time is 5 seconds.

From the collimator setup data, no correlations were observed between various setup parameters and the fit parameters, for example the step size and spike height, or the half gap and the decay time. This is because during the setup, precautions are taken to achieve uniform loss spikes and losses below the dump threshold. To be able to generate loss values which decay exponentially, it is sufficient to randomly generate a power coefficient for each loss spike, as the maximum loss
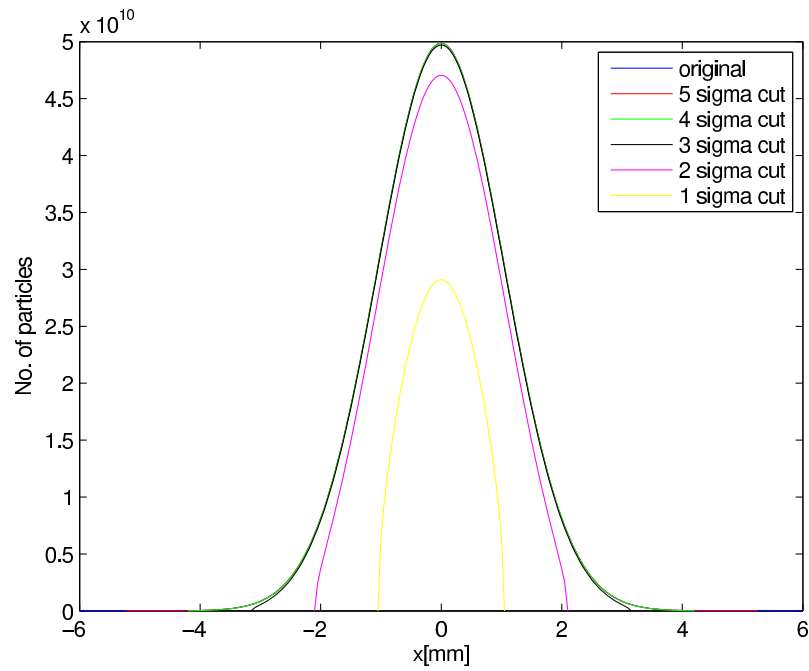
Figure 7.9: Different beam cuts and the corresponding particle distribution.
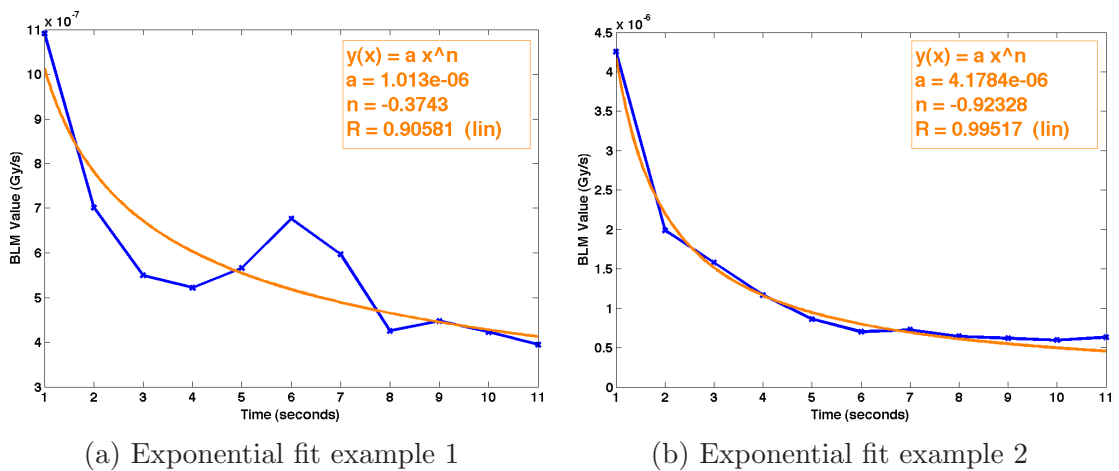
(a) Exponential fit example 1

(b) Exponential fit example 2

Figure 7.10: Examples of polynomial fits to the temporal decay.

Table 7.4: Empirical modeling of the temporal decay at 450 GeV and 3.5 TeV, showing the mean and error bars where applicable.

Parameter	450 GeV	3.5 TeV
Jaw Step Size (μm)	10 - 20	5 - 10
Decay Time (s)	5.22 ± 0.16	7.86 ± 0.16
Amplitude a (Gy/s)	1.29E-05 ± 9.83E-07	1.22E-05 ± 1.10E-06
Power coefficient n	-0.747 ± 0.021	-0.571 ± 0.035
Error coefficient R	0.887 ± 0.051	0.927 ± 0.006

value (a) will have been generated by the Gaussian beam distribution model discussed previously. A log-normal distribution of the power coefficients can be observed when plotting histograms of this data for both beam energies (Fig. 7.11). The parameters μ and σ of each data set were obtained using maximum likelihood estimation.
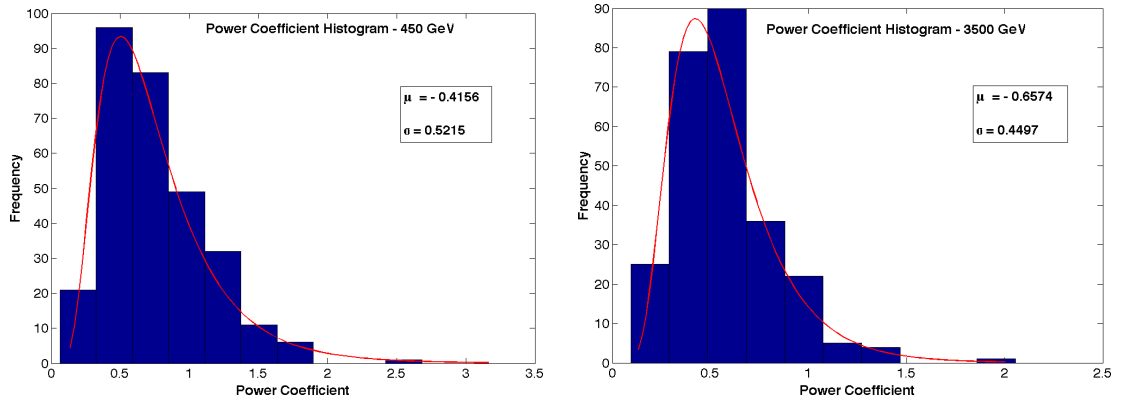
(a) Power coefficient histogram (450 GeV)   (b) Power coefficient histogram (3.5 TeV)

Figure 7.11: Log-normal distribution of the power coefficients at 450 GeV and 3.5 TeV.

7.5 Dynamic model of spike and decay

A diffusion model of the time evolution of loss rates caused by a collimator jaw step was developed in [109]. It builds upon the model of Ref. [110] and its assumptions: (1) constant diffusion rate within the range of the step and (2) linear halo distribution tails. These hypotheses allow one to obtain analytical expressions for the solutions of the diffusion equation and for the corresponding loss rates as a function of time. The model in [109] addresses some of the limitations of the previous model and expands it in the following ways:

1. losses before, during and after the collimator step are predicted;

2. different steady-state rates before and after are accounted for;

3. determination of the model parameters (diffusion coefficient, tail population, detector calibration and background rate) is more precise and robust against statistical fluctuations in the data, parameter correlations and initial parameter values in the fits.

These calculations are the basis for the measurement of transverse beam diffusion rates as a function of particle amplitude with collimator scans. Following Ref. [110], the evolution in time t of a beam of particles with phase-space density $f(J, t)$ as described by the diffusion equation is considered:

$$\partial_t f = \partial_J(D\partial_J f) \tag{7.8}$$

where J is the Hamiltonian action and D is the diffusion coefficient. The particle flux at a given location $J = J'$ is $\phi = -D \times [\partial_J f]_{J=J'}$. During a collimator step, the action limit $J_c = x_c^2/2\beta_c$, corresponding to the collimator half gap x_c at a ring location where the amplitude function is β_c, changes from its intial value J_{ci} to its final value J_{cf} in a time t^s. The step in action is therefore $\Delta J \equiv J_{cf} - J_{ci}$. In the LHC, typical steps in collimator half gaps (Δx_c) are 10 μm in 5 ms, and the amplitude function is tens of meters. It is assumed that the collimator steps are small enough so that the diffusion coefficient can be treated as a constant in that region. If D is constant, the local diffusion equation becomes $\partial_t f = D\partial_{JJ} f$. With these definitions, the particle loss rate at the collimator is equal to the flux at that location:

$$L = -D \times [\partial_J f]_{J=J_c} \tag{7.9}$$

The loss rate evolution measured by the BLM detectors can be expressed in terms of the particle loss rate L, a calibration constant k and a background term B:

$$S = kL + B \tag{7.10}$$

The local losses are proportional to the gradient of the distribution function at the collimator. The value of the gradient at the collimator for inward and outward steps, denoted by the I and O subscripts respectively, is given by:

$$\partial_J f_I(J_c, t) = -A_i + 2(A_i - A_c)P(\frac{-J_c}{w}) - \frac{2A_i(J_{ci} - J_c)}{\sqrt{2\pi}w}$$
$$+ \frac{2(A_i J_{ci} - A_c J_c)e^{[-\frac{1}{2}(\frac{J_c}{w})^2]}}{\sqrt{2\pi}w} \tag{7.11}$$

$$\partial_J f_O(J_c, t) = -2A_i P(\frac{J_{ci} - J_c}{w}) + 2(A_i - A_c)P(\frac{-J_c}{w})$$
$$+ 2\frac{A_i J_{ci} - A_c J_c}{\sqrt{2\pi}w}e^{[-\frac{1}{2}(\frac{J_c}{w})^2]} \tag{7.12}$$

The parameters A_i and A_f are the slopes of the distribution function before and after the step, with A_c varying linearly between A_i and A_f as the collimator moves. The function $P(x)$ is the cumulative Gaussian distribution, and the w term is defined as $w \equiv \sqrt{2Dt}$.

7.5.1 Experimental procedure

7.5.1.1 Beam parameters and machine configuration

The beam parameters, including the beam energy, starting intensity and β-functions in the experimental interaction points (β^*) for each scraping configuration are shown in Table 7.5. One nominal bunch (1.2×10^{11} protons) per beam was used.

Table 7.5: The beam parameters at the start of both scraping configurations [111].

Parameter	Separated Beams	Colliding Beams
Energy [GeV]	4000	4000
Intensity B1 [10^{11} p]	1.29	1.14
Intensity B2 [p]	1.07	0.74
β^* IP1/5 [cm]	60	60
β^* IP2/8 [cm]	300	300

7.5.1.2 Beam test programme

The MD [112] started off with squeezed, non-colliding beams at an energy of 4 TeV. The IR7 primary and secondary collimators were retracted from their nominal

settings of 4.3 σ and 6.3 σ respectively to 7 σ away from the beam centre, in order to have a larger scan range. The beam centres at these collimators were measured during beam-based alignments in March 2012, and are used throughout the 2012 LHC run. The centres are checked regularly via beam loss maps, and are stable thanks to the reproducibility of the machine. The maximum deviations of the beam centres at the horizontal and vertical TCPs with respect to the first alignments in the 2012 LHC run were measured to be 160 μm (0.45 σ) and 110 μm (0.43 σ) respectively. The beam size is calculated from the nominal beta functions at the individual collimators, with a beam emittance of 3.5 μm in both horizontal and vertical planes. An overview of the settings of the collimators not used for scraping during the beam study are shown in Table 7.6. The settings for these collimators, except the TCPs and TCSGs in IR7, are the same as used in normal operation.

Table 7.6: The settings of the collimators not used for scraping throughout the beam study (grouped by families), for both scraping configurations [111].

Collimator Family	Description	Half Gap [σ]
TCP IR3	Primary collimator	12
TCSG IR3	Secondary collimator	15.6
TCLA IR3	Absorber	17.6
TCP IR7	Primary collimator	7
TCSG IR7	Secondary collimator	7
TCLA IR7	Absorber	8.3
TCSG IR6	Secondary collimator	7.1
TCDQ IR6	Dump protection	7.6
TCT IR1/5	Tertiary collimator	9
TCT IR2/8	Tertiary collimator	12
TCL IR1/5	Luminosity Debris Absorber	out

In the study, the left jaws of the TCP.D6L7.B1 (vertical plane) and the TCP.C6R7.B2 (horizontal plane) collimators were moved in steps of 5 μm to 20 μm, thus performing a single-sided scraping. The β functions and nominal beam sizes at these collimators are provided in Table 7.7. Primary collimators on either side of IR7 were chosen for scraping the counter-rotating beams. Scraping could be done simultaneously for the two beams (see Fig. 7.12) because the distance between the collimators used for scraping ensured negligible crosstalk between beam loss measurements. For each beam, the jaws were moved in as soon as the beam losses from the previous step had decayed back to a steady-state (approximately every 10 to 40 seconds). The decay time is inversely proportional to the distance from the beam orbit.

Table 7.7: The β functions and 1 σ nominal beam sizes at the collimators used in the scraping [111].

Collimator	β (m)	1 σ (mm)
TCP.D6L7.B1	78.26	0.253
TCP.C6R7.B2	150.36	0.351
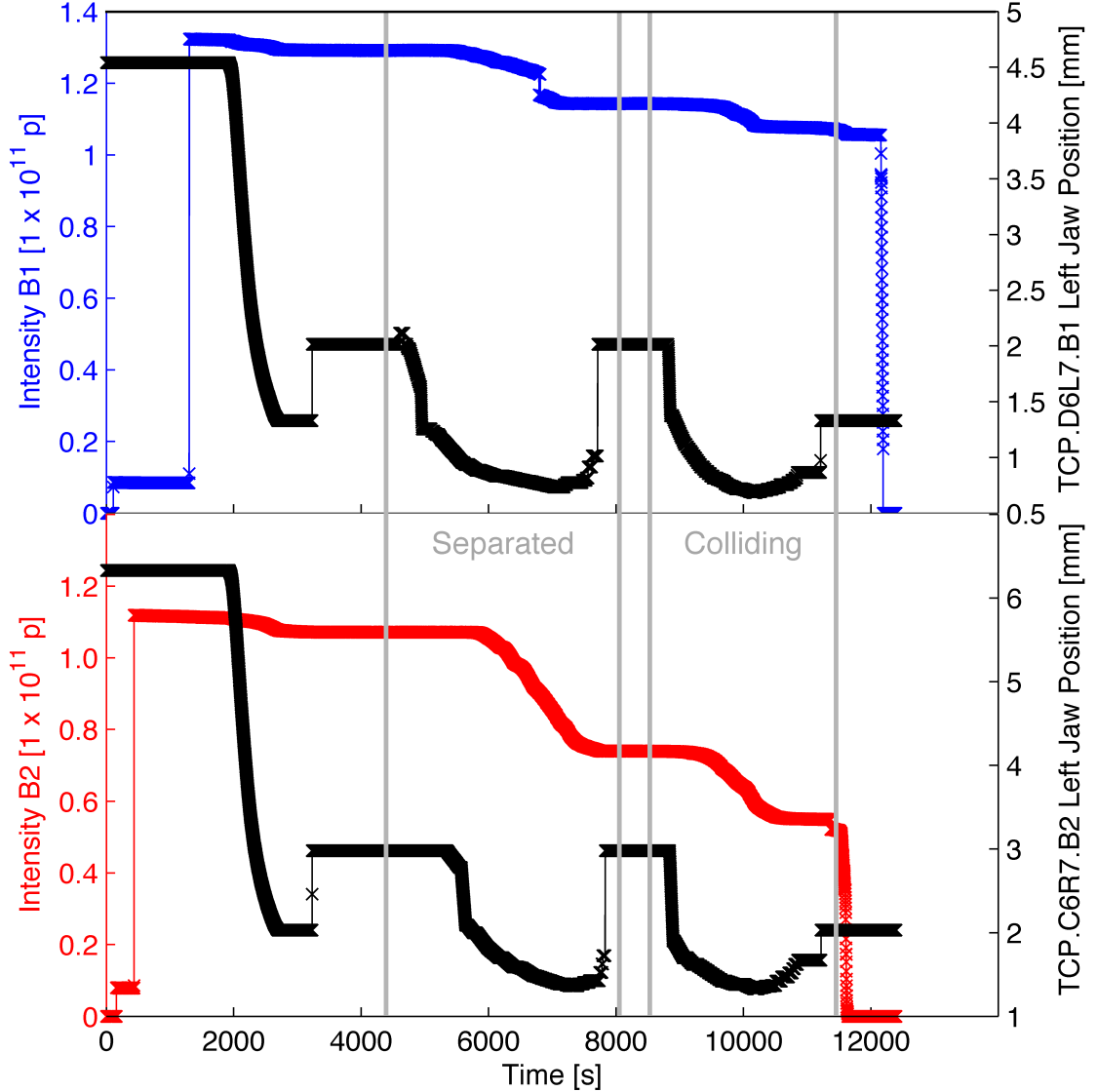
Figure 7.12: The beam intensities and the left jaw collimator positions as a function of time (t[0] = 22.06.2012 04:30:00). Scraping with the left jaws of the TCP.D6L7.B1 (vertical plane) and TCP.C6R7.B2 (horizontal plane) was performed with squeezed non-colliding and colliding beams [111].

The jaws were left for a few minutes in the beam after they had reached their final inward position, to allow the losses to stabilize. Subsequently, the jaws were moved out in steps of 20 μm to 100 μm, with the next step being taken when a steady-state loss rate was observed. The beams were then brought into collisions, and the procedure was repeated. The beam intensities and left jaw collimator positions as

a function of time are shown in Fig. 7.12. The initial and final jaw positions for each scraping in terms of the nominal beam size are provided in Table 7.8.

Table 7.8: The initial (1) and final (2) collimator jaw nominal half gaps in units of σ for the different scrapings. The beam centres determined in beam-based alignments in March 2012 and used during operation are assumed for the calculation [111].

Collimator	Separated Beams	Colliding Beams
TCP.D6L7.B1 (1)	7.00 σ	7.00 σ
TCP.D6L7.B1 (2)	1.96 σ	2.41 σ
TCP.C6R7.B2 (1)	7.00 σ	7.00 σ
TCP.C6R7.B2 (2)	1.76 σ	2.31 σ

7.5.1.3 Measured variables

The halo diffusion model depends on beam intensities, beam emittances, collimator positions and local losses, which need to be recorded. The measured variables are the following:

- **Intensity:** The FBCT data are logged at a rate of 1 Hz and 50 Hz.

- **Wire-scan emittances:** Three sets of wire scans were taken: (1) non-colliding beams, before scraping; (2) non-colliding beams, after scraping; (3) colliding beams before scraping. Some measurements were not accurate due to saturation.

- **Synchrotron-light emittances:** Synchrotron-light emittance measurements (BSRT) were logged continuously every 3 seconds.

- **Collimator positions:** The left and right collimator jaw positions were logged at a rate of 1 Hz. The jaws were kept to the zero angle throughout the study. The plots in Fig. 7.12 show the beam intensity and positions of the IR7 primary collimators used for scraping.

- **Beam losses:** The BLM data were acquired at a rate of 1 Hz (1.3 s integration time) and 12.5 Hz (82 ms integration time). The typical background signal is 2×10^{-7} Gy/s, with a noise of 10^{-8} Gy/s. The signal varies from 10^{-7} Gy/s to 10^{-3} Gy/s (close to the beam dump threshold), as the collimator jaw cuts deeper into the beam halo.

7.5.2 Data analysis

The local losses measured by the immediately downstream BLM detectors and the collimator jaw positions throughout the beam study are shown in Fig. 7.13 for the two scraping tests done for each beam. A comparison of the responses of the 4 BLM detectors immediately downstream of the collimator of interest is shown in Fig. 7.14. As expected, similar loss profiles with different offsets and spike amplitudes are observed for the different monitors.

7.5.2.1 Intensity-beam loss calibration

The BLM detectors measure beam losses in terms of ionizing radiation, and the resulting signal can be calibrated to determine the losses in terms of protons. Calibration factors which allow conversion from beam loss in Gy/s to p/s are useful in determining the beam lifetime, as the BLM detectors allow for more precise measurements when the loss levels are low. The background losses (the B parameter in the fit model) are determined during "quiet time", with no beam in the machine (between 2012-06-22 05:28:00 and 2012-06-22 05:48:00). For the local B1 BLM detectors the background level is 1.81×10^{-6} Gy/s, and 1.06×10^{-6} Gy/s for B2.

For calibrating the response of this group of BLM detectors (conversion from Gy/s to protons/s), the experiment time is subdivided into 20-second intervals (40 μm groupings of the collimator half gap) to obtain the average collimator position, local loss rate and intensity decay rate. The 20-second period was chosen to obtain a better resolution in the intensity decrease, as for some individual loss spikes (particularly at a larger jaw distance from the beam centre) the intensity decrease is close to the FBCT resolution.
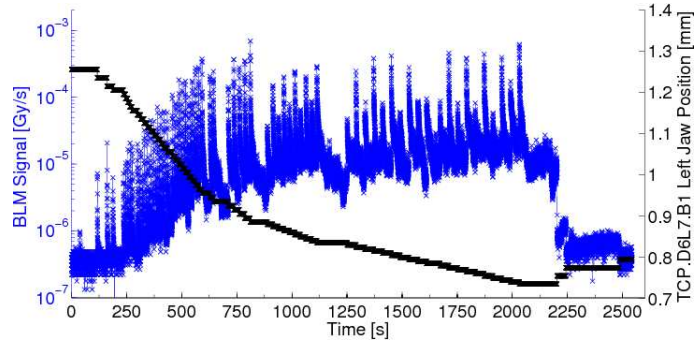
(a) BLM data and TCP.D6L7.B1 left jaw positions (separated beams)
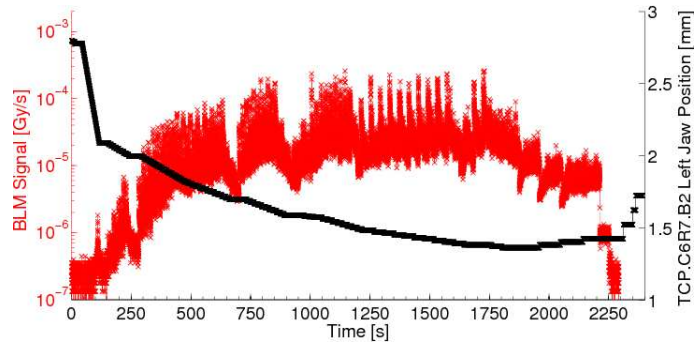
(b) BLM data and TCP.C6R7.B2 left jaw positions (separated beams)
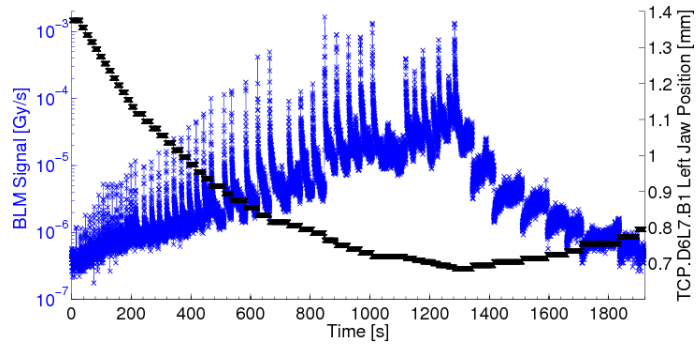
(c) BLM data and TCP.D6L7.B1 left jaw positions (colliding beams)
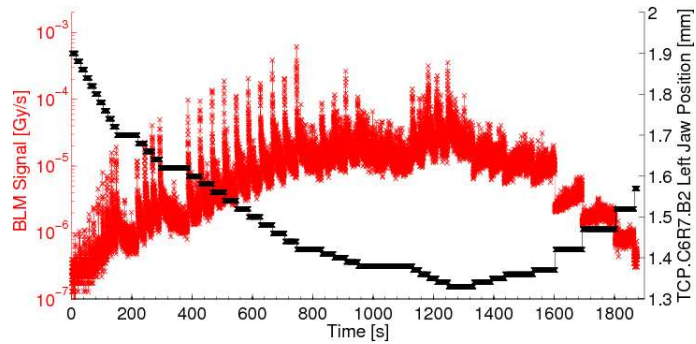
(d) BLM data and TCP.C6R7.B2 left jaw positions (colliding beams)

Figure 7.13: The collimator positions and associated BLM signals as a function of time with separated beams (t[0] = 22.06.2012 06:00:00) and colliding beams (t[0] = 22.06.2012 07:00:00) [111].

124
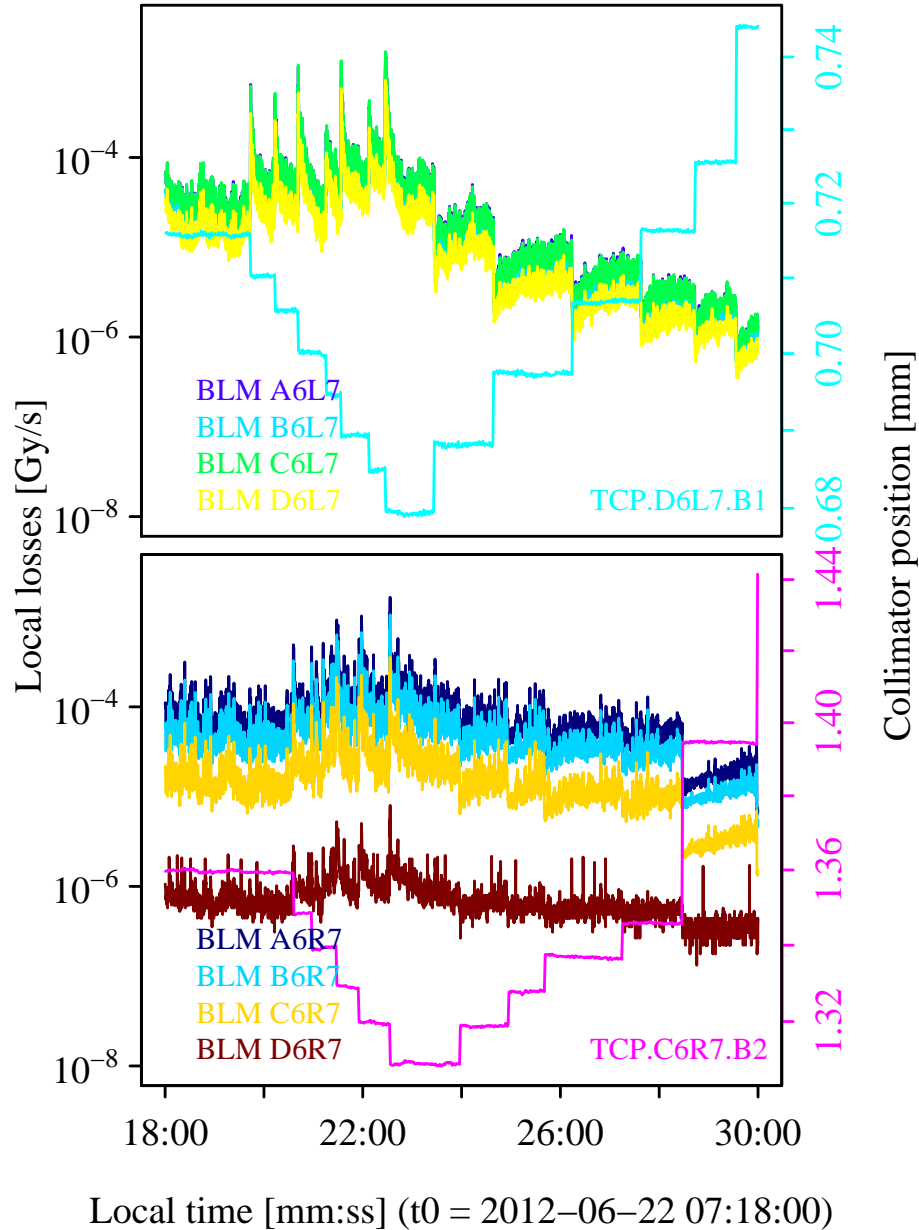
Figure 7.14: Collimator jaw positions (right axis) and beam losses at different BLM detectors immediately downstream of the collimator used for scraping (left axis) as a function of time, for a portion of the collimator scan.

Figure 7.15 shows the BLM detector calibration constant as a function of the collimator half gap. The calibration factor, or "local loss detection efficiency", varies by more than 2 orders of magnitude. It clearly exposes the threshold when most of the losses occur locally - a half gap of 0.8 mm in the vertical plane and 1.5 mm horizontally. As expected, the efficiency in collisions is lower, when a larger beam fraction is lost at the experimental interaction points. This is particularly obvious in the horizontal case. For the purposes of the diffusion analysis, these numbers are an experimental measurement of the k parameter in
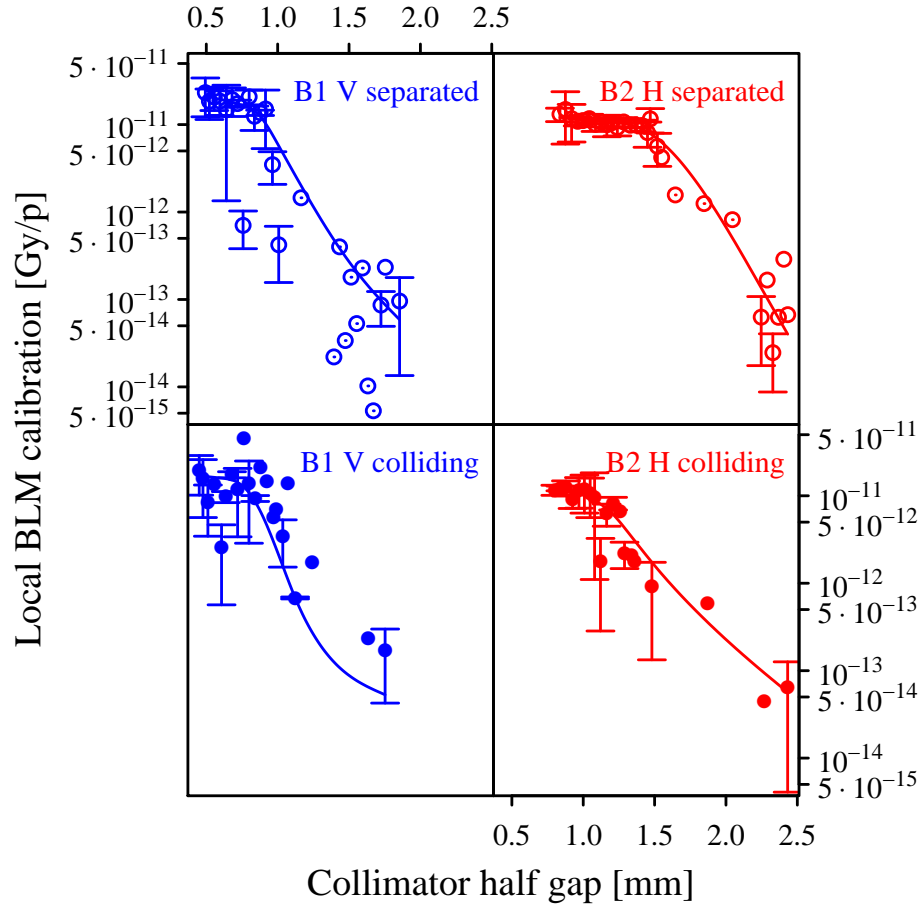
Figure 7.15: Local loss monitor calibration as a function of collimator position [111].

Eq. (7.10). In Fig. 7.15, the measurements of k as a function of collimator position are interpolated with a smooth spline with 4 degrees of freedom.

The dose-intensity calibration factors were also obtained using the information on the BLM spikes over intervals of 1 s from the jaw movement, with the BLM detector taken to be the one downstream closest to the collimator. The advantage in this case is that any intensity decrease caused by beam losses at the collimator can be directly correlated to the loss spike under study. This type of analysis is more sensitive to 'beam cleaning', i.e. the fast, multi-turn beam losses caused by an inward collimator step that would be present even in a linear machine and in the absence of diffusion processes. The BLM and intensity data were extracted for each loss spike interval. The dose in Gy was calculated as the average loss signal for the peak integrated over ~1 s, as shown in Fig. 7.16a and Fig. 7.16c. The intensity lost over the same time period was also determined (see examples in Fig. 7.16b and Fig. 7.16d). The particle loss was calculated as a percentage of the intensity recorded by the FBCT before the loss spike, and is shown as a function of the jaw gap in mm in Fig. 7.18a and 7.18b.

(a) BLM spike B1

(b) FBCT signal B1

(c) BLM spike B2
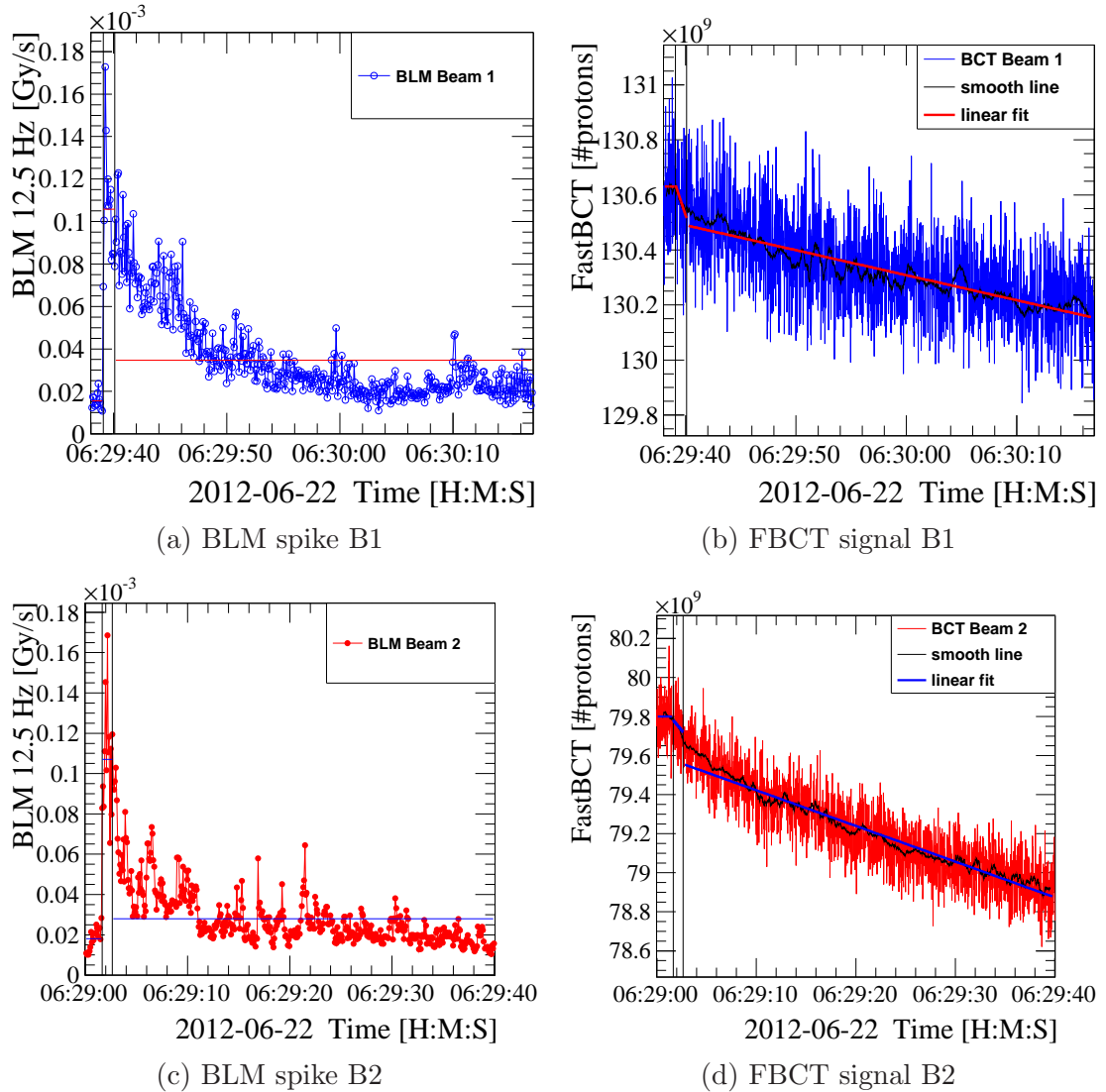
(d) FBCT signal B2

Figure 7.16: Examples of fits made to the BLM and FBCT signals during loss spikes following a B1 ((a) and (b)) and B2 ((c) and (d)) collimator jaw movement respectively. The dose in Gy is calculated by integrating the BLM signal over ~1 s and the intensity lost in the same period is determined to calculate the calibration factor for each loss spike [111].

The calibration factors in Gy/p are shown in Fig. 7.17. The values compare well with those found during the 2011 scraping study for the same collimators (8.3×10^{-13} Gy/p, see [79]). The apparent difference in scale between Fig. 7.17 and Fig. 7.15 is because the former plot takes into account only the closest BLM detector to the collimator, while the latter considers the four closest downstream BLM detectors. The particle loss was calculated for a given jaw half gap by integrating over the static Gaussian beam distribution for the jaw step size used. The nominal beam sizes at the collimator locations are considered for the beam distribution calculation.
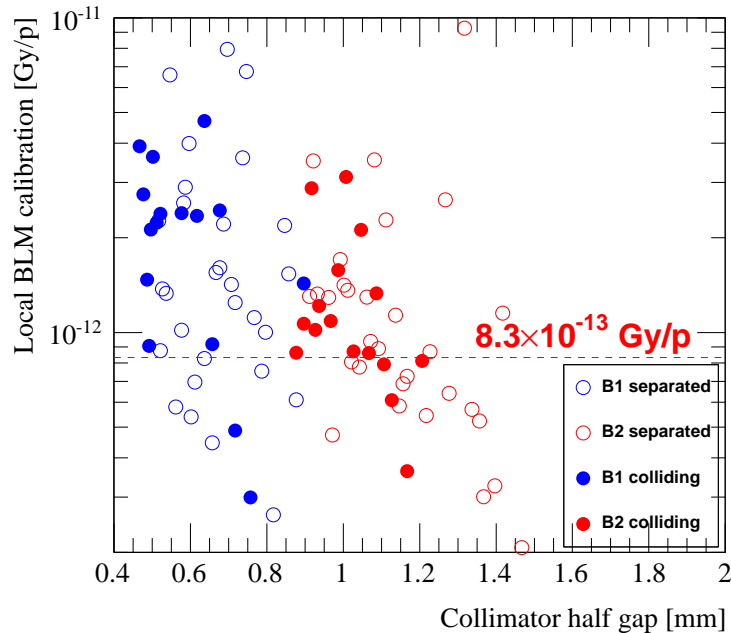
Figure 7.17: The calibration factors calculated for each loss spike in units of Gy/p, as a function of the collimator half gap in mm. The red dotted line indicates the calibration factor found in the 2011 scraping study for reference.

Figures 7.18c and 7.18d show the BLM signal in arbitrary units, which is calculated by multiplying the ratio of the dose to the intensity before the jaw movement by the average calibration factor of 1.2×10^{12} p/Gy and an additional factor. The additional factor ($\sim$0.65) was necessary to scale the resulting BLM signal to the static distribution curves, which are the same as in Figs. 7.18a and 7.18b. The factor derives partly from the uncertainty in the calibration factor and partly from an offset between the FBCT signal and the actual intensity in the LHC. The discontinuities in the static distribution curves are due to different jaw step sizes being used throughout the beam study.

7.5.2.2 Evolution of beam emittance

The objective of measuring the beam emittances is to determine the beam sizes at the collimator positions and estimate the core diffusion rates. The initial emittances are calculated from the wire-scan (see Table 7.9) and the synchrotron-light data. Both wire-scan and synchrotron-light emittance measurements are affected by the scraping of the tails (Fig. 7.19). The emittances measured at the start of the beam study (2012-06-22 06:08:00) are used to convert the collimator gaps into beam sigmas. The statistical uncertainty is calculated from the difference between inward and outward wire movement. The average of the synchrotron-light measurements is used, with a statistical uncertainty deduced from the spread in data points.

(a) Particle loss (separated beams)

(b) Particle loss (colliding beams)

(c) Local BLM signal (separated beams)

(d) Local BLM signal (colliding beams)
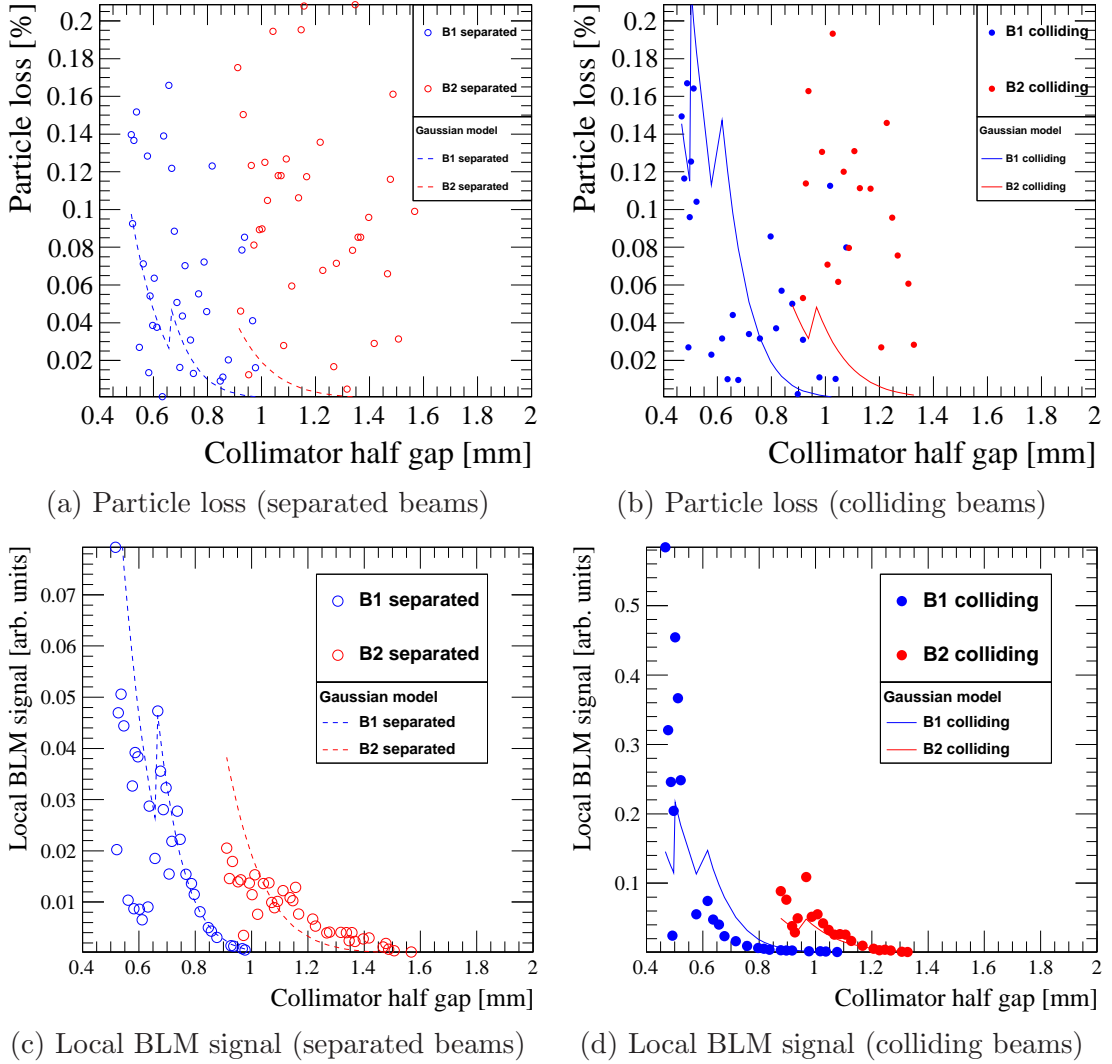
Figure 7.18: Particle loss as a percentage of the intensity measured before the loss spike ((a) and (b)) and local BLM signal ((c) and (d)), with comparison to the static beam distribution at the start of scraping. The discontinuities in the static distribution curves are due to different jaw step sizes being used throughout the beam study [111].

The final emittance value is obtained by averaging wire scan and synchrotron-light data. Its error is the combination in quadrature of the statistical errors plus a systematic error due to the difference between the two techniques. Results are reported in Table 7.10. The beam sizes at the collimators calculated from the initial emittances are 0.156 mm (B1 vertical) and 0.270 mm (B2 horizontal). The emittance growth rates $\gamma = \dot{\epsilon}/\epsilon$ are deduced from the slope of the synchrotron-light data before 2012-06-22 06:08:00. According to the diffusion model, the slope of the diffusion coefficient in the beam core is related to the growth rate of the geometrical emittance: $D' = dD/dJ = \dot{\epsilon}$. These slopes are presented in Table 7.10. In Section 7.5.3, diffusion coefficients calculated from these slopes ($D = D' \cdot J =$

Table 7.9: Normalized, 1 σ wire-scan emittances: (1) Non-colliding beams before scraping, (2) Non-colliding beams after scraping, (3) Colliding beams before scraping [111].

Type	**Time**	ϵ_x^{B1} [μm]	ϵ_y^{B1} [μm]	ϵ_x^{B2} [μm]	ϵ_y^{B2} [μm]
(1)	05:53	1.92	1.36	1.69	1.73
(2)	06:47	1.80	1.23	1.20	1.21
(3)	07:01	1.71	1.45	1.28	1.26

Table 7.10: Initial emittances (wire scan, synch-light, average), emittance growth rates (EGR) γ, and diffusion slopes D' [111].

Plane	**Emittance** [μm]						**EGR** [1/s]		**Diffusion** [μm/s]	
	ϵ_{ws}	$\delta\epsilon_{ws}$	ϵ_{sl}	$\delta\epsilon_{ws}$	ϵ	$\delta\epsilon$	γ	$\delta\gamma$	D'	$\delta D'$
B1 H	1.92	1.3e-02	2.15	9.6e-03	2.03	0.07	5.23e-05	1.50e-05	2.49e-08	7.4e-09
B1 V	1.36	2.0e-03	1.29	4.7e-03	1.33	0.02	1.70e-05	1.00e-05	5.27e-09	3.2e-09
B2 H	1.69	6.6e-03	2.43	1.3e-02	2.06	0.21	5.37e-05	1.90e-05	2.60e-08	9.6e-09
B2 V	1.73	4.6e-02	1.98	1.2e-02	1.85	0.09	1.10e-05	1.70e-05	4.79e-09	7.2e-09

$\dot{\epsilon} \cdot J$) are compared with the measured diffusion coefficients in the halo. One would expect halo diffusion to be at least as large as core diffusion, or larger if there are additional diffusion mechanisms at increasing amplitudes, such as magnet nonlinearities or resonances.

7.5.2.3   Parametric fits of the diffusion model

The model described in Section 7.5 is used to perform fits to the inward and outward jaw movements separately. The initial values for the fit parameters are determined as follows. The steady-state rates are evaluated by averaging the losses before the step (-0.5 s from the step or earlier) and after (4 s after or later). The starting point for the diffusion coefficient is the value obtained from the decay 3 s after the step (where the losses are $\approx 1/\sqrt{t}$). The time of the step, t_0, is known from the time stamps of the collimator position (with 1 s resolution) and from the increase in the losses (80 ms resolution). The duration of the step t^s is estimated from the step size and the nominal jaw speed, 2 mm/s. The step time and duration can also be left as free parameters within some reasonable limits.

The distribution of the response variable (loss rate) is not Gaussian, as one can see for instance from Fig. 7.14, because of instrumental effects (such as beam jitter and mechanical vibrations) and because of the Poissonian nature of the shower process. For this reason, fit parameters are determined by minimizing not a χ^2, but the sum of absolute deviations of the model from the data (robust estimation). For
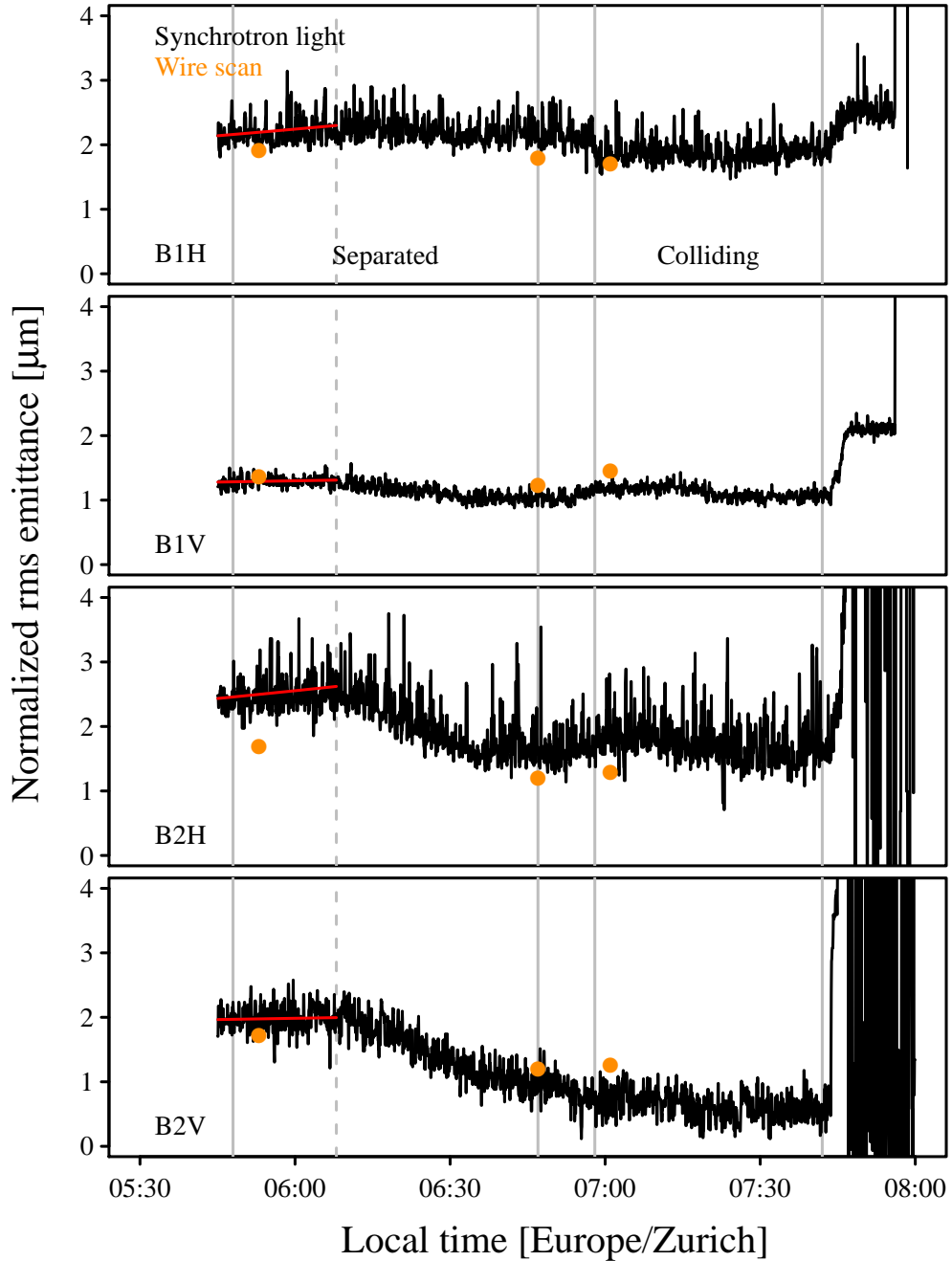
Figure 7.19: Synchrotron-light and wire-scan emittances over the course of the study [111].

the same reason, a first estimate of the statistical errors comes from the Hessian matrix of the χ^2 function, but the final error analysis is done by bootstrapping. For each step, bootstrapping is done by resampling the data points with replacement and repeating the fit 3 times with the same initial parameters. The final results are the median of the fit results and the uncertainties come from their spread.

Examples of the fit results are plotted in Fig. 7.20 for inward and outward jaw movements. Not all fits converged: in some cases, the model cannot explain the

first few seconds of losses after the step. This seems to be due to the losses decaying differently from $1/\sqrt{t}$, as shown in the first column of the plots. This fact could be a combination of instrumental effects (the details of the collimator movement) and pure beam removal/cleaning. But in general, the model seems to reproduce the main features of the loss evolution with time quite well. Less data are available for the outward movement, as the losses were found to quickly decrease to the background level when a half gap of 2.2 σ for B1 and 2.8 σ for B2 was reached.

7.5.3   Results

The diffusion coefficients as a function of action are shown in Fig. 7.21 for all 4 cases: horizontal and vertical, separated and colliding beams. With separated beams, the diffusion in the B2 horizontal plane is higher than that in the B1 vertical plane. In the horizontal plane, there seems to be little difference between the separated and colliding cases, while in the vertical plane, collisions enhance diffusion by about two orders of magnitude. The reason for this is not fully understood. A possible explanation is due to the larger emittances measured in the horizontal plane in B1. If there is sufficient coupling, with the beams in collisions, diffusion could be enhanced also in the vertical plane in B1, as B2 has lower emittances. Unfortunately, collimator scans could not be performed for using the horizontal B1 and vertical B2 collimators, and hence no generalizations can be drawn from a lack of measurements.

A significant systematic effect is the larger diffusion rates obtained from the outward steps. They are not understood, but are probably due to the fact that, after scraping, a different beam population is being sampled. A comparison of inward and outward steps was motivated both by practical and physical reasons. Practical considerations included checking for instrumental systematic effects. Moreover, outward steps should be independent of fast, multi-turn particle removal or perturbations of the beam density distribution induced by the collimators. From the physical point of view, if phase space contains particles trapped in islands and motion is not completely stochastic, one may expect different removal and repopulation rates for a given amplitude. In practice, these effects are difficult to disentangle.

The grey curves in Fig. 7.21 are not an interpolation of the data: they represent the dependence $D(J)$ that one would obtain from the core emittance growth rates (Table 7.10). This comparison allows one to draw several conclusions: (1) the diffusion rates measured with the collimator scan technique have reasonable values
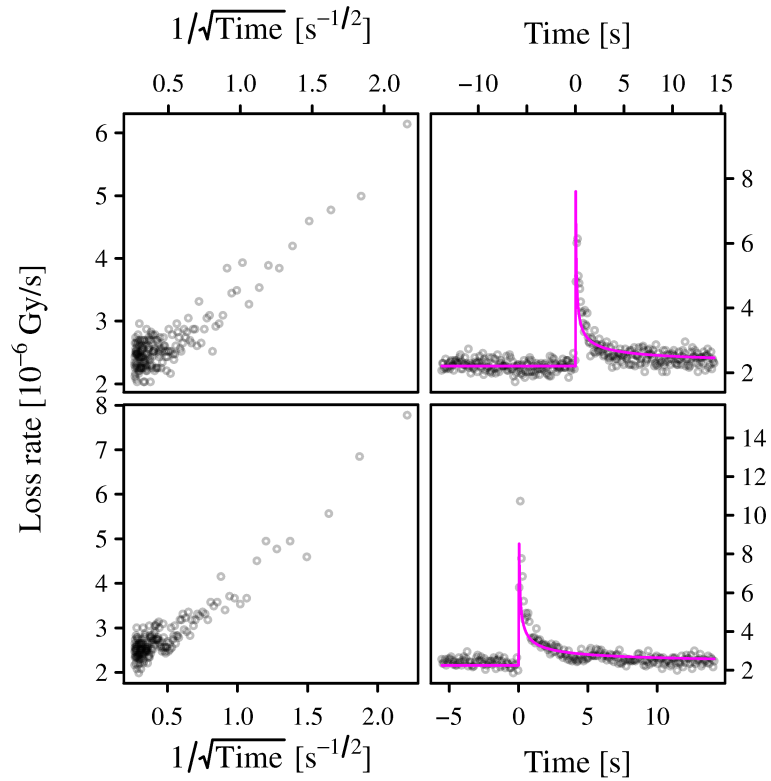
(a) Inward collimator jaw movement
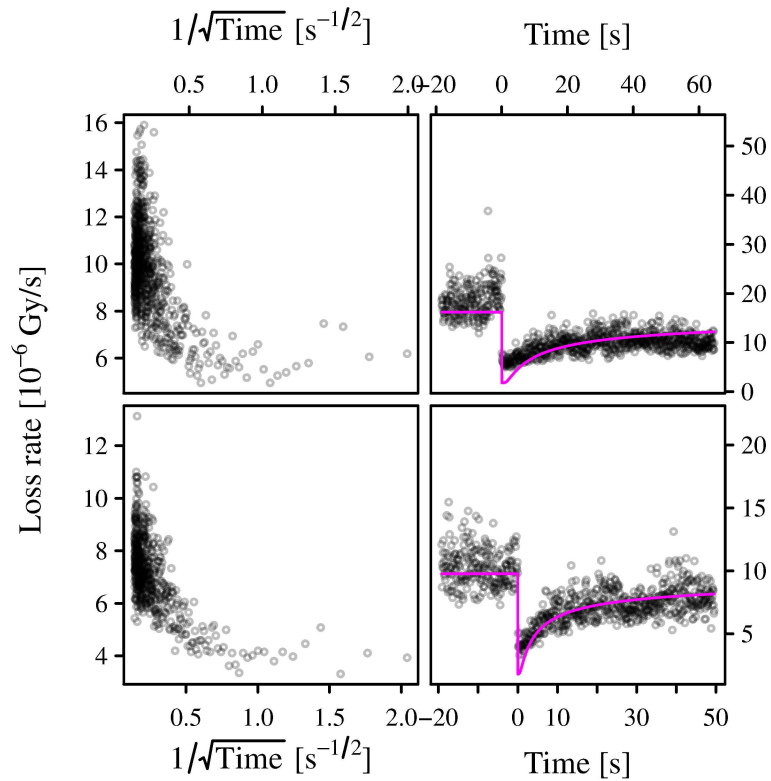
(b) Outward collimator jaw movement

Figure 7.20: Examples of the loss decay part of the spike plotted as a function of $1/\sqrt{t}$ (a), a diffusion model fit to an inward step (b), for inward and outward jaw movements, from [111].
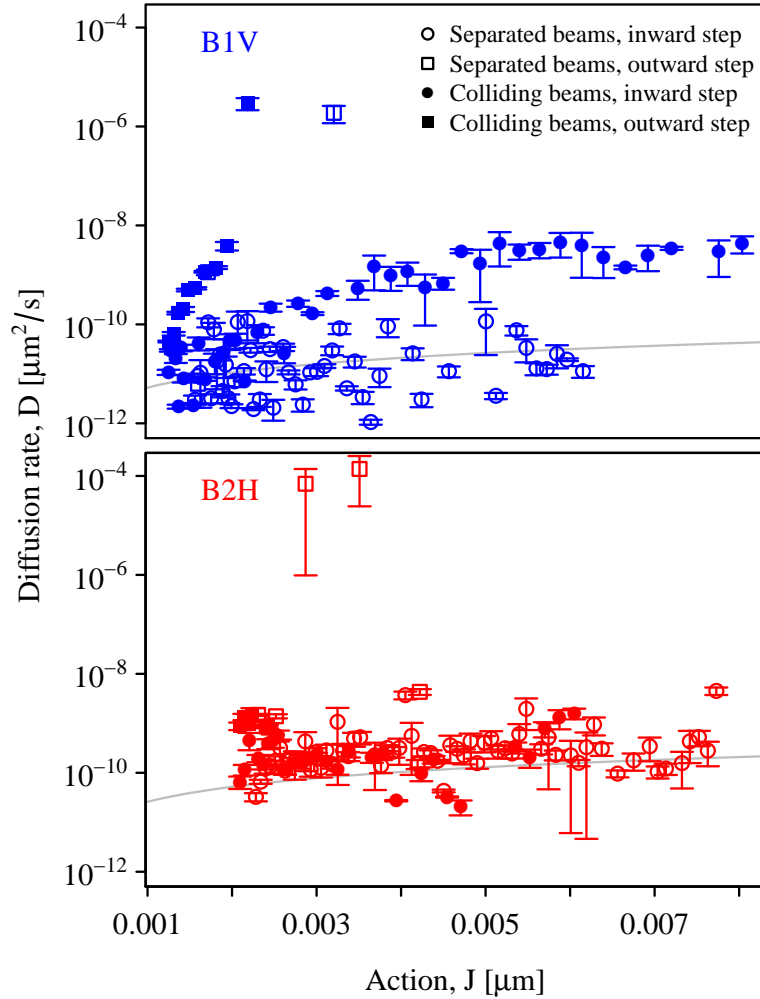
Figure 7.21: Diffusion coefficient as a function of action from the collimator scan (points), compared with the expectation from core emittance growth rates (lines).

for B2 horizontal; (2) without collisions, the beam halo in the LHC diffuses almost like the core up to large amplitudes; (3) no significant dynamic aperture effects (sharp rises in diffusion rate) are observed in the amplitude range explored in these experiments. The B1 vertical diffusion rate is approximately 100 times larger with colliding beams.

From the diffusion coefficients as a function of amplitude, one can calculate the distribution of impact parameters, i.e. the depth at which particles impinge on the collimators. These distributions can affect the efficiency of a collimator system [24]. Impact parameters from diffusion coefficients can be calculated in two ways [73]. The first uses a Monte Carlo technique to generate particles near a collimator, propagating their trajectories including diffusion, and calculating their distributions when they reach the collimators. The second method uses an analytical form of the impact parameter distribution based on the diffusion phenomenology. In both cases, the average impact parameter is found to scale

with the diffusion coefficient as $D^{2/5}$. Although the detailed analysis is beyond the scope of this work, average impact parameters in the range between 0.02 to 0.3 μm are obtained for diffusion coefficients of 1.2×10^{-11} to 3.6×10^{-9} μm^2/s, for actions of 0.002 to 0.008 μm. These results are consistent with the assumptions commonly used for the LHC collimation system design and performance evaluation [113].

7.6 BLM signal crosstalk

An empirical model of the ratios of the spikes in BLM signals of stationary collimators to the spike in the BLM signal of an aligned collimator was constructed, based on data from four major alignments in 2011 and 2012 held at beam energies of 450 GeV, 3.5 TeV and 4 TeV. A script was written to extract 620 spike samples of 21 s each from the alignment data. The script ensures that only one collimator was moving in the 21-second interval, and extracts its BLM signal as well as the BLM signal for all other collimator BLM detectors with a peak amplitude for the same timestamp of $> 1 \times 10^{-6}$ Gy/s. Examples of such samples is shown in Fig. 7.22a and Fig. 7.22b.

Each of these 620 plots was then verified manually to ensure that only signals with a similar pattern to that of the aligned collimator were processed further. The ratios, or *factors*, between the spike of the aligned collimator and the spikes of the other collimators were calculated and plotted as a function of the relative distance from the aligned collimator. An example of this *crosstalk map* is shown in Fig. 7.23.

The relative positions, jaw half gap of the primary and ratios were fed into RapidMiner, a software suite which allows for quick data import, processing and output [114]. The k-NN algorithm was used to develop a model that can predict the factor that must be applied to the BLM signal of an aligned collimator, for another collimator BLM detector at a given relative distance and with a given jaw half gap. This algorithm performs a regression which predicts a value depending on the closest class. A test-to-train ratio of 50/50 was used. A screenshot of the setup in Rapid Miner is provided in Fig. 7.24. Note that for BLM detectors associated with collimators in the opposite beam, the jaw half gap parameter is weighted to 0. A value of $k = 1$ was chosen for the smallest Root Mean Square Error (RMSE), to achieve the most accurate model. One model was obtained for each collimator BLM detector. A table showing the typical inputs and predicted factors is shown in Table 7.11.
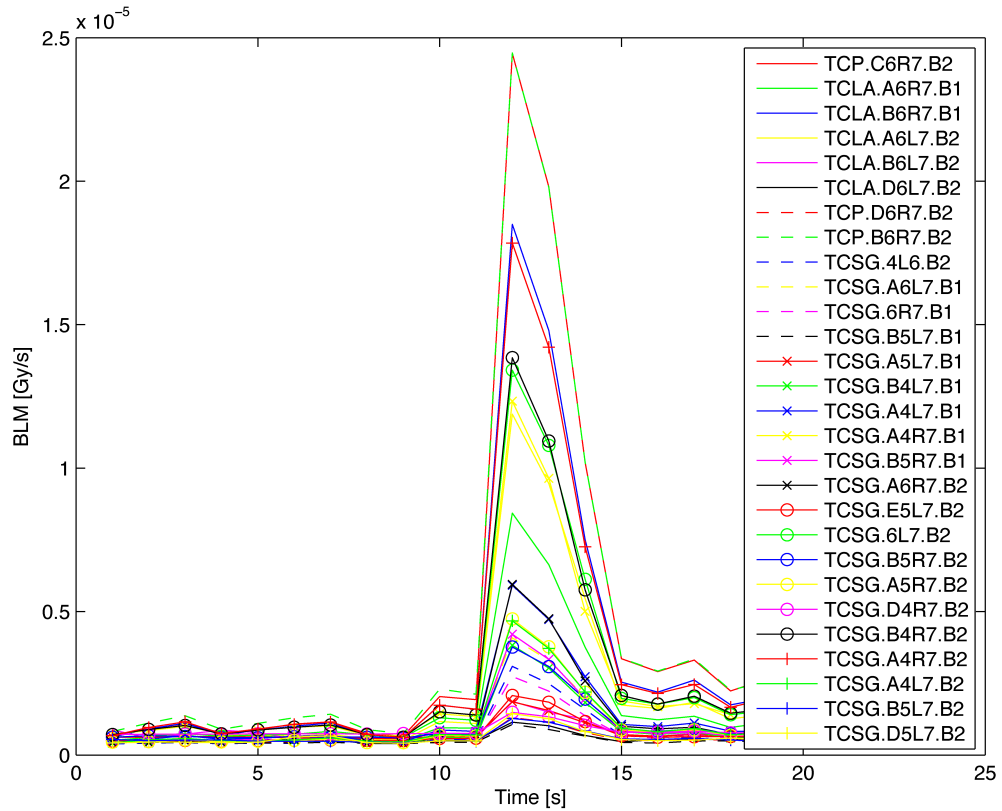
(a) Aligned collimator: TCP.C6R7.B2
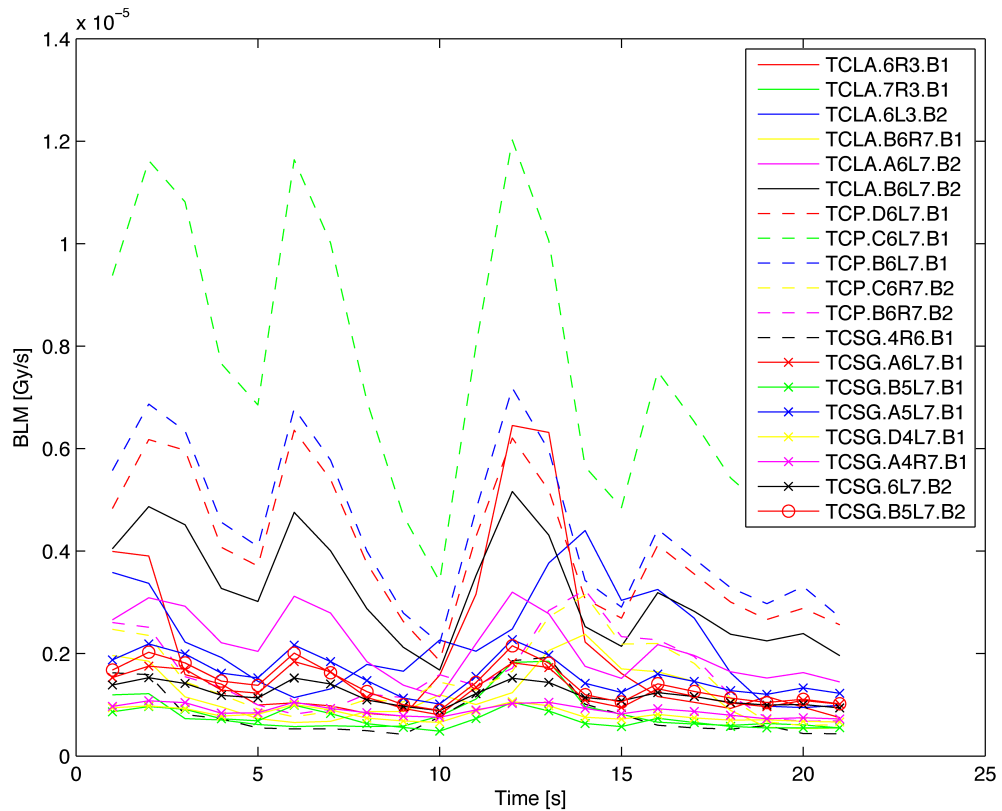
(b) Aligned collimator: TCLA.6R3.B1

Figure 7.22: Superimposition of the highest BLM signals following an alignment of the TCP.C6R7.B2 and TCLA.6R3.B1 (marked in solid red lines in the respective plots).
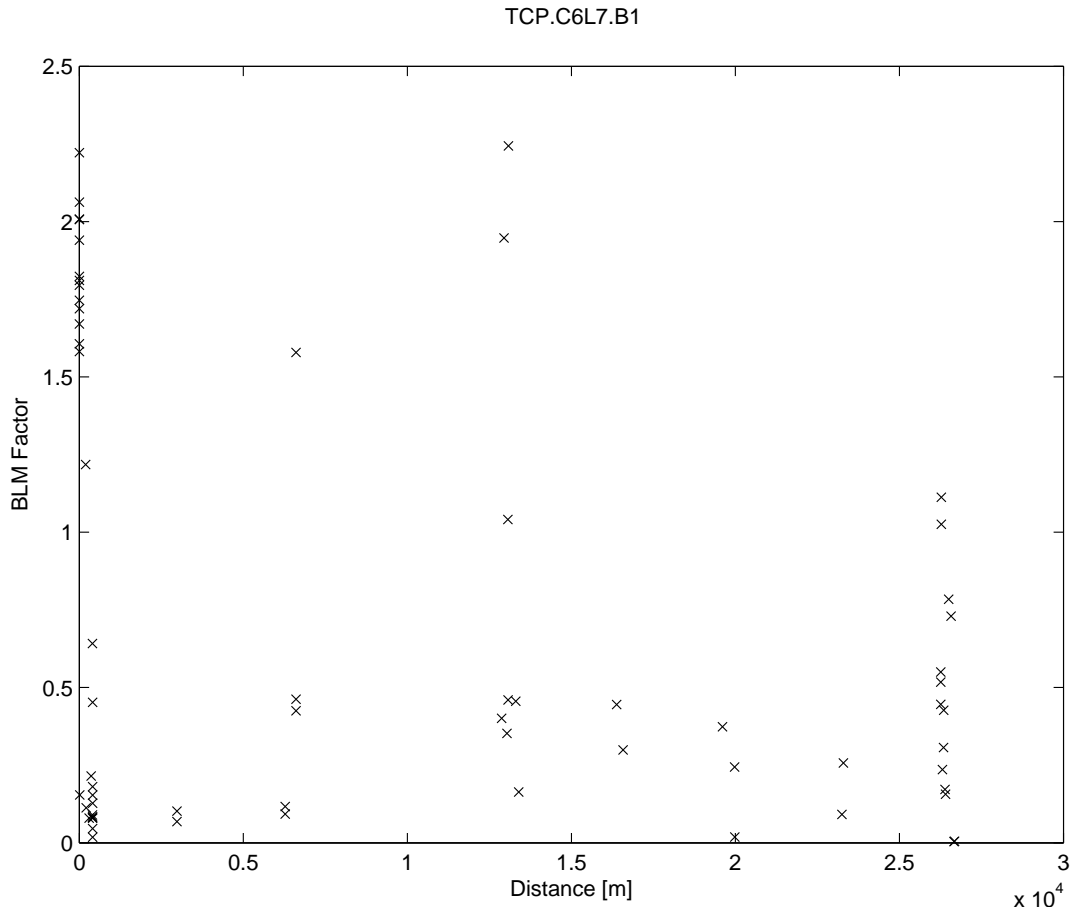
Figure 7.23: Crosstalk map for the TCP.C6L7.B1.

Test Position [m]	Test Gap [mm]	Test Factor	Predicted Factor
13036	4.552	1.185	0.352
12876	4.090	0.516	0.401
26343	4.552	0.628	0.307
26279	4.552	1.577	1.112

Table 7.11: Typical input values and the 1-NN prediction. The RMSE value for the whole dataset is 1.15, corresponding to an error of 17%.
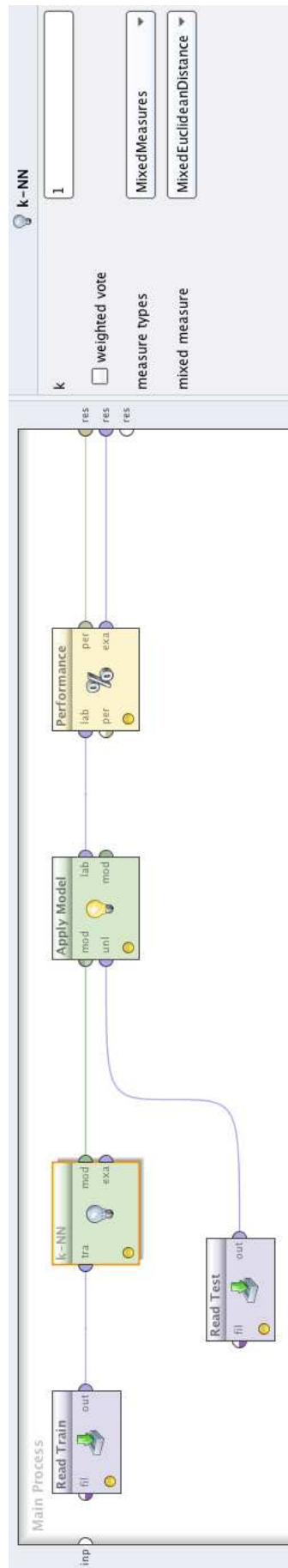
Figure 7.24: Rapid Miner prediction setup.

138

7.7 Collimator setup simulator

7.7.1 Simulator algorithm

Four "alignment policies" were developed, each of which combines the algorithms described in Chapter 5 to attempt to align the collimators in the shortest time possible. A policy is defined as a subgroup of several alignment algorithms, and one of the objectives of the simulator will be to determine which policy achieves the least alignment time. Four alignment policies were considered:

- **Policy 1:**

    - Sequential alignment algorithm.

- **Policy 2:**

    - Parallel alignment algorithm.

    - Sequential alignment algorithm.

- **Policy 3:**

    - Movement of all collimators with a half gap larger than $6\,\sigma$ from parking to tighter settings based on BPM-interpolation.

    - Parallel alignment algorithm.

    - Sequential alignment algorithm.

- **Policy 4:**

    - Movement of all collimators with a half gap larger than $6\,\sigma$ from parking to tighter settings based on BPM-interpolation.

    - Parallel alignment algorithm utilizing knowledge of crosstalk factors.

    - Sequential alignment algorithm.

The setup simulator was based on the existing GUI developed for the operational collimator application. However, the collimator and BLM data acquisition modules were adapted to transmit and receive data to and from the simulator engine. The simulator algorithm works as follows. First, an initialization procedure is executed:

- Choose beam centres randomly from a uniform distribution in the range of ± 300 μm, based on past alignment data.

- Calculate beam size at the collimators for a given geometrical emittance.

- Set the jaws to the initial positions around the beam centre, in order that they respect the four-stage hierarchy.

- Initialize the BLM signals for each collimator to the steady-state signals given the starting jaw positions.

The initial beam halo is defined to be at 3.5 σ, and no loss spikes are simulated for jaw movements above this limit. After the first jaw touches the beam, the halo is defined by the jaw closest to the beam. The initialization procedure is followed by a loop which aligns all the selected collimators according to the desired alignment policy (P_s):

1. If P_s == 3 or 4, start by moving the jaws at a half gap of > 6 σ from parking to a tighter setting of $\sim$ 6 σ around the interpolated centre. The interpolated centre is generated by choosing a random value in the ±500 μm range around the measured data.

2. If P_s == 2, 3 or 4:

   - set the BLM thresholds using the threshold selection algorithm.
     - if P_s == 2 or 3, move both jaws of all collimators in the horizontal plane until one of the jaws exceeds the 3.5 σ limit.
     - if P_s == 4, move both jaws of collimators which have crosstalk factors <1 with respect to the collimator closest to the beam in units of nominal σ in the horizontal plane, until one of the jaws exceeds the 3.5 σ limit.
   - generate a spike and temporal decay with the diffusion model.
   - generate crosstalk using the k-NN model, and check if the thresholds of other BLM detectors are also exceeded.
   - if yes, execute the crosstalk recovery algorithm:
     - stop all collimators. Then move each collimator one by one until the one at the beam is identified.

140

> – then resume parallel alignment of the remaining collimators which
>   are still far from the beam.

3. Then, or if $P_s == 1$, repeat step 2, instead aligning the TCP in the same
   plane as the collimator C to be aligned, followed by alignment of collimator
   C, and so on until all collimators in the same plane are aligned.

4. Repeat steps 1-3 for all horizontal, vertical and skew collimators.

For every collimator movement, a command transmission delay of 0.125 s is
considered to simulate the delay between the alignment software application
running in the CCC and the hardware in the LHC tunnel. The beam intensity is
simulated by converting the BLM signal at the collimator closest to the beam to
p/s using the calibration factors provided in Table 7.1.

7.7.2 Simulator implementation

The simulator was written in MATLAB. All algorithms described in Section 5 are
implemented in the simulator. A screenshot of the GUI is shown in Fig. 7.25.
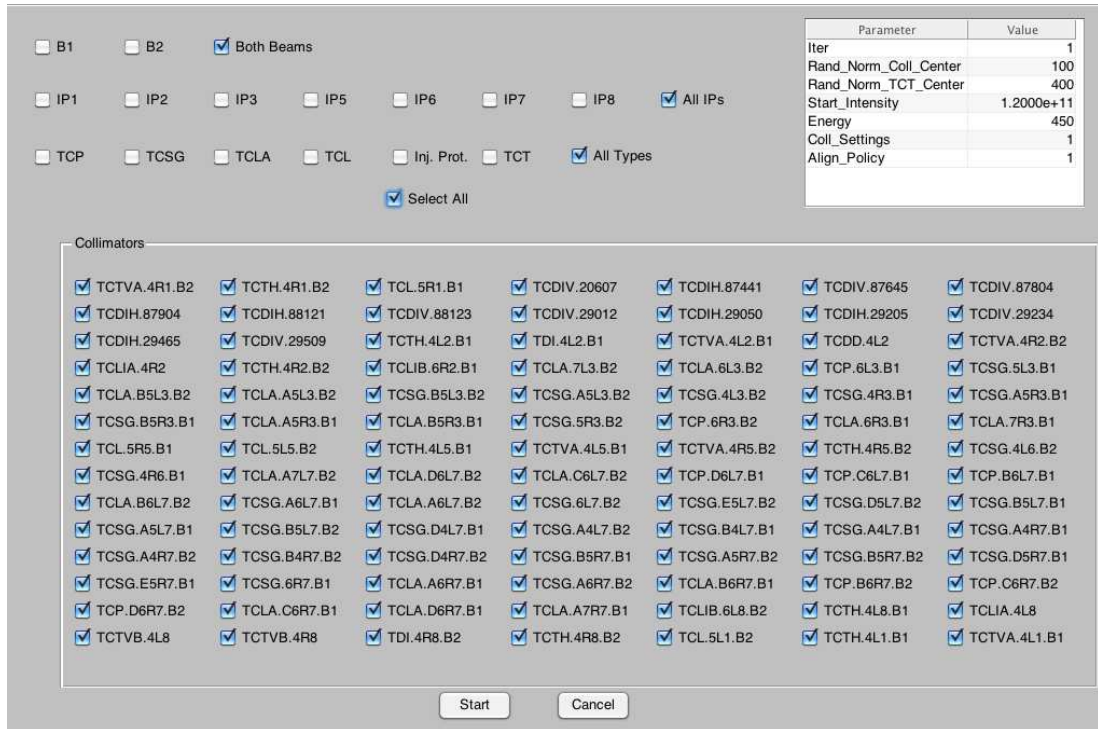
Figure 7.25: Simulator GUI.

Chapter 8

Simulation and Operational Results

8.1   Simulation results

Simulations were performed for various beam energies and collimator settings using the simulator described in Chapter 7. For each policy and beam energy, the simulation was run for 50 times to obtain the final results in a Montecarlo fashion. The collimators were divided into subgroups which are frequently aligned, such as the IR7 or TCT collimators. In each case, no simulations were performed for the TCT collimator subgroup for Policy 3 and Policy 4, as there is a poor comparison between the BPM-interpolated and the measured beam centres at these collimators, and hence the algorithm that moves the jaws from the initial settings to the tighter settings in one step cannot be used. The simulation outputs are the following:

- jaw positions for each collimator

- BLM signal for each collimator BLM detector

- beam intensities

- final collimation depth in σ

Typical simulation results showing the jaw positions and BLM signal as a function of time are shown in Fig. 8.1a. Crosstalk appears during the sequential stage as the alignment is being done in parallel with a collimator in the other beam. A zoom of the final sequential alignment is shown in Fig. 8.1b. The simulated beam intensities throughout an alignment are provided in Fig. 8.2. An initial beam intensity of 1.2×10^{11} was used throughout the simulations. Note that no beam instabilities or normal beam loss are taken into account, hence the smooth decrease over time.

(a) Full alignment

(b) Zoom into sequential alignment

Figure 8.1: Simulation results for the alignment of the TCLA.A6R7.B1 using Policy 1. The zoom into the sequential stage provides a better view of the simulated loss spikes and temporal decay. The impulses are BLM signal crosstalk generated by other moving collimators, with the temporal decay not being plotted for clarity.

143
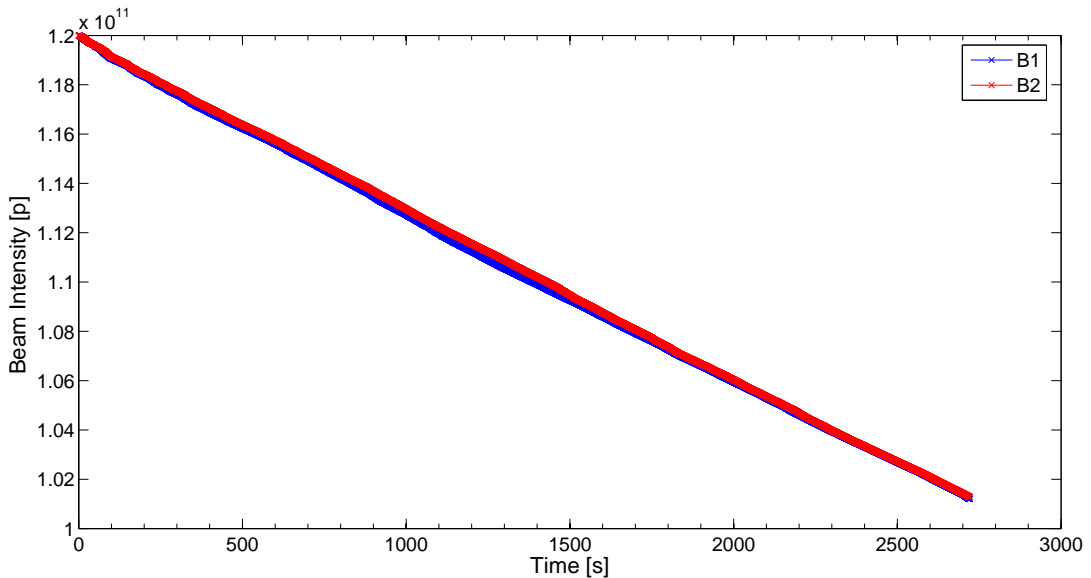
Figure 8.2: Simulated beam intensities for Policy 1 for an alignment of all collimators.

8.1.1 Results at 450 GeV

The jaw step size is 10 μm, and the injection settings were used. Initial centres were taken from the 2011 450 GeV alignment dataset. The total number of steps and average number of steps taken by each collimator are shown in Fig. 8.3a and Fig. 8.3b respectively.

The number of steps is divided by the maximum jaw movement rate of 8 Hz to obtain the time in s, and hence the plots in Fig. 8.4a and Fig. 8.4b are generated.
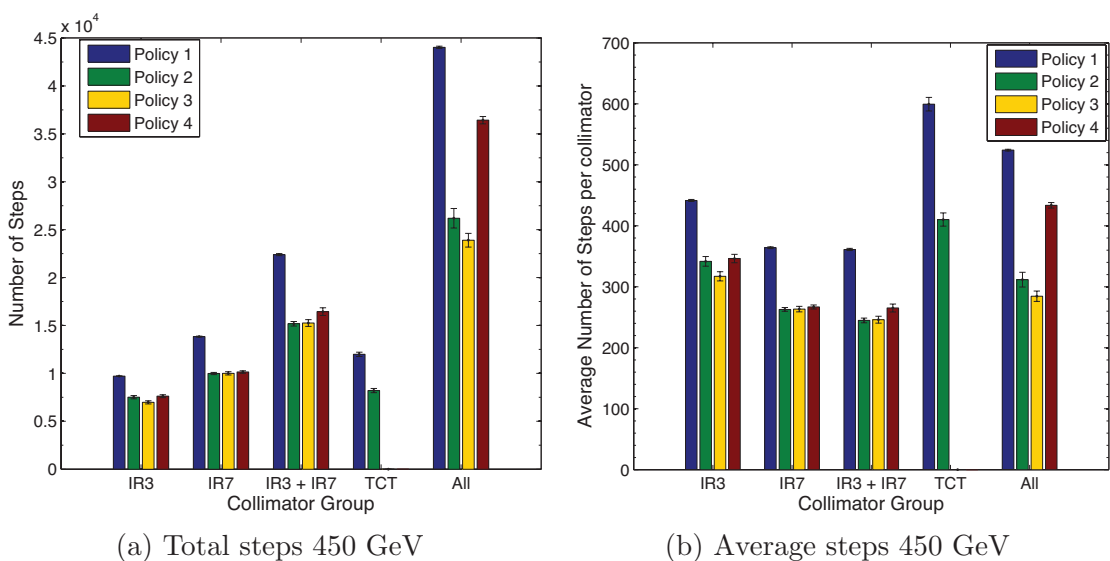
(a) Total steps 450 GeV

(b) Average steps 450 GeV

Figure 8.3: Total number of steps (a) and average number of steps (b) per collimator at 450 GeV.

(a) Total time 450 GeV

(b) Average time 450 GeV
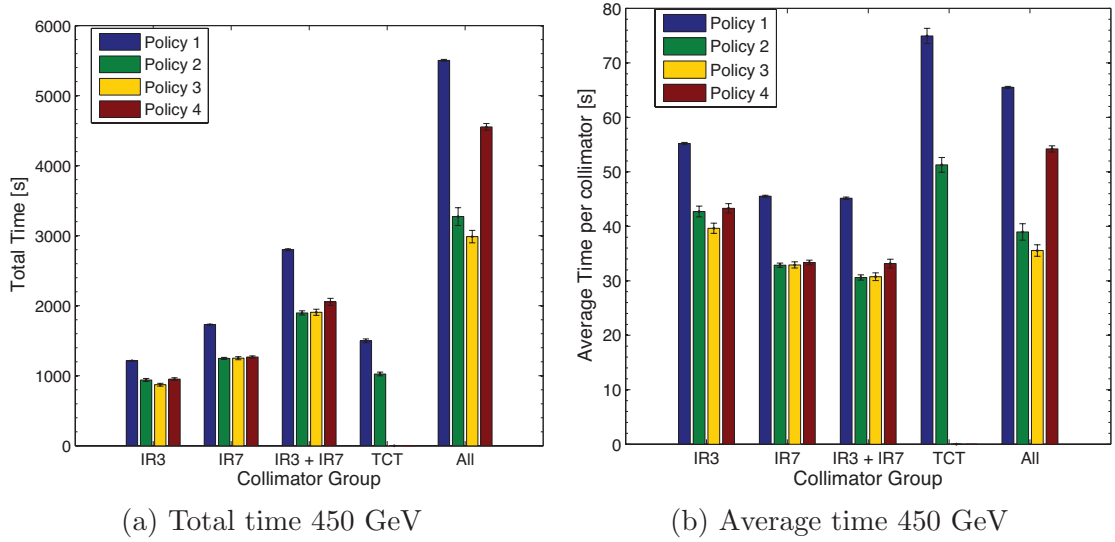
Figure 8.4: Total time (a) and average time (b) required per collimator at 450 GeV.

The final beam intensities for B1 and B2 at the end of the alignment are provided in Fig. 8.5a and Fig. 8.5b respectively.

(a) Final Intensity B1 450 GeV

(b) Final Intensity B2 450 GeV
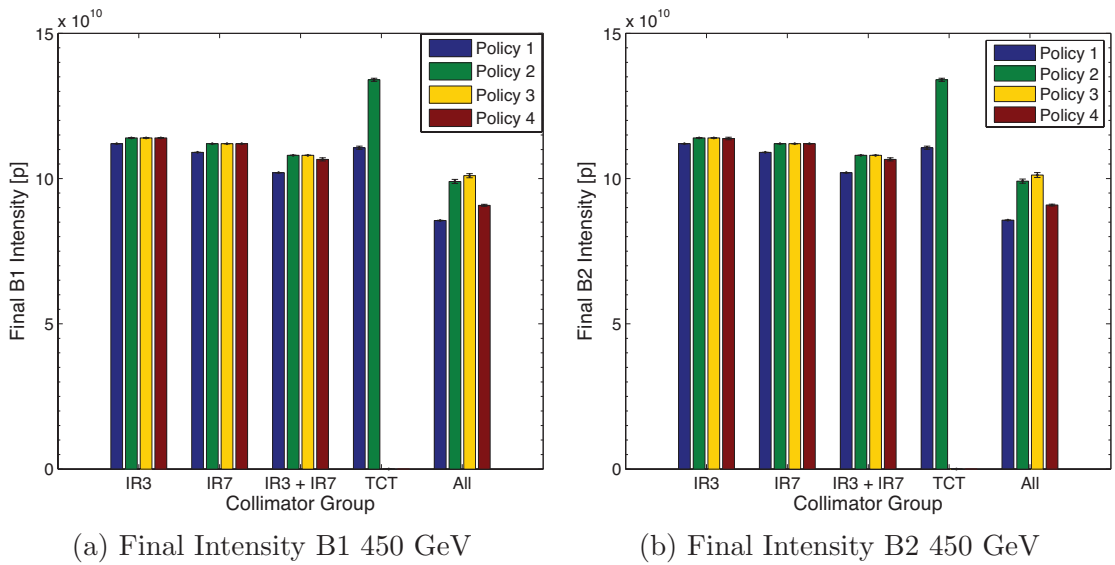
Figure 8.5: Final B1 (a) and B2 (b) intensities at 450 GeV.

The final collimation depth and the actual time required to complete the simulations are shown in Fig. 8.6a and Fig. 8.6b respectively.

(a) Final collimation depth 450 GeV

(b) Simulation time required 450 GeV
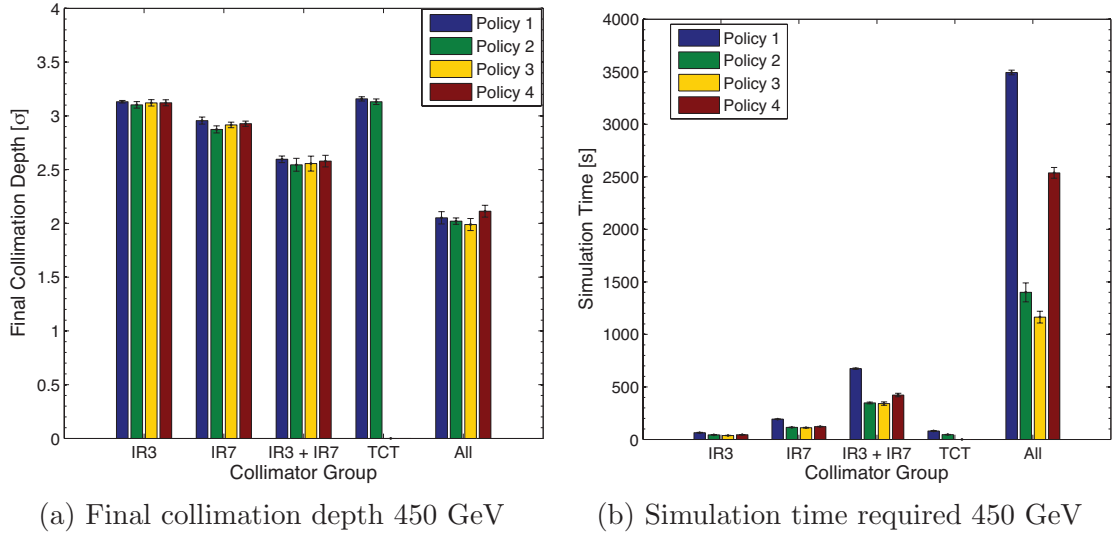
Figure 8.6: Final collimation depth (a) and simulation time required (b) at 450 GeV.

8.1.2 Results at 4000 GeV

The jaw step size is 5 μm, and the tight settings at 4 TeV were used. Initial centres were taken from the 2012 4000 GeV alignment dataset. The total number of steps and average number of steps taken by each collimator are shown in Fig. 8.7a and Fig. 8.7b respectively.

(a) Total steps 4000 GeV

(b) Average steps 4000 GeV
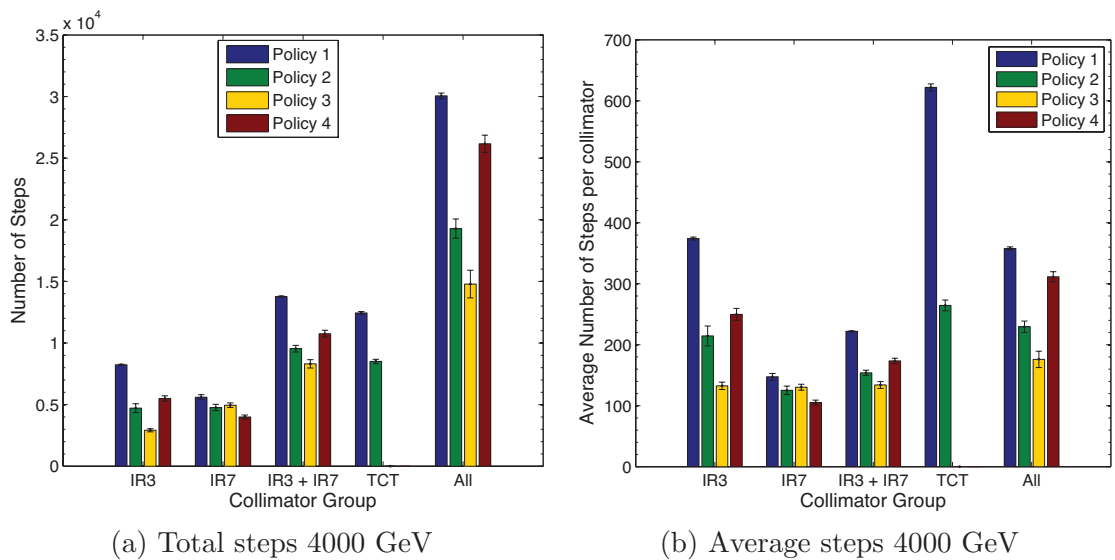
Figure 8.7: Total number of steps (a) and average number of steps (b) per collimator at 4000 GeV.

(a) Total time 4000 GeV

(b) Average time 4000 GeV
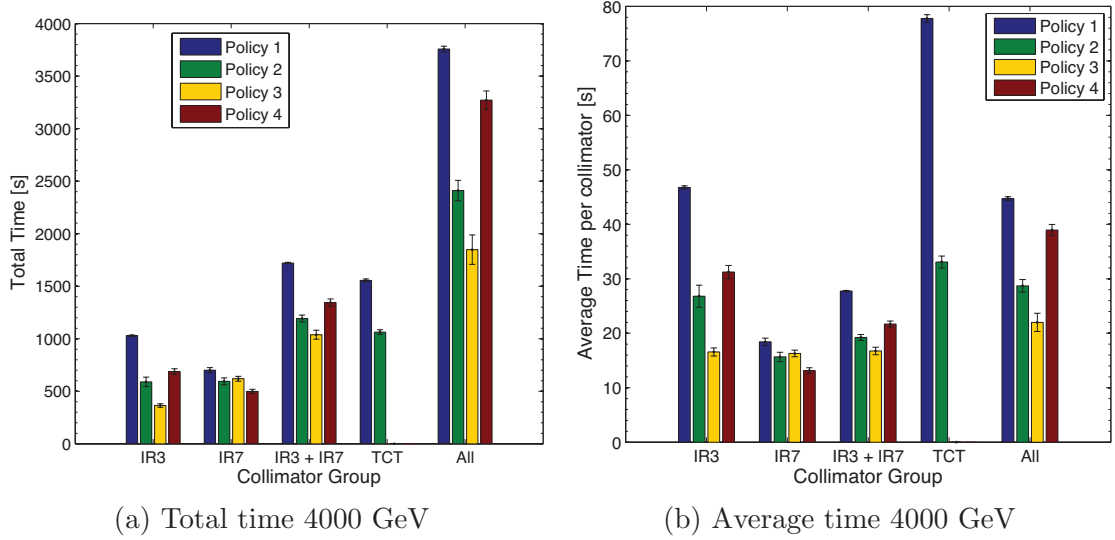
Figure 8.8: Total time (a) and average time (b) required per collimator at 4000 GeV.

The number of steps is divided by the maximum jaw movement rate of 8 Hz to obtain the time in s, and hence the plots in Fig. 8.8a and Fig. 8.8b are generated.

The final beam intensities for B1 and B2 at the end of the alignment are provided in Fig. 8.9a and Fig. 8.9b respectively.

(a) Final Intensity B1 4000 GeV

(b) Final Intensity B2 4000 GeV
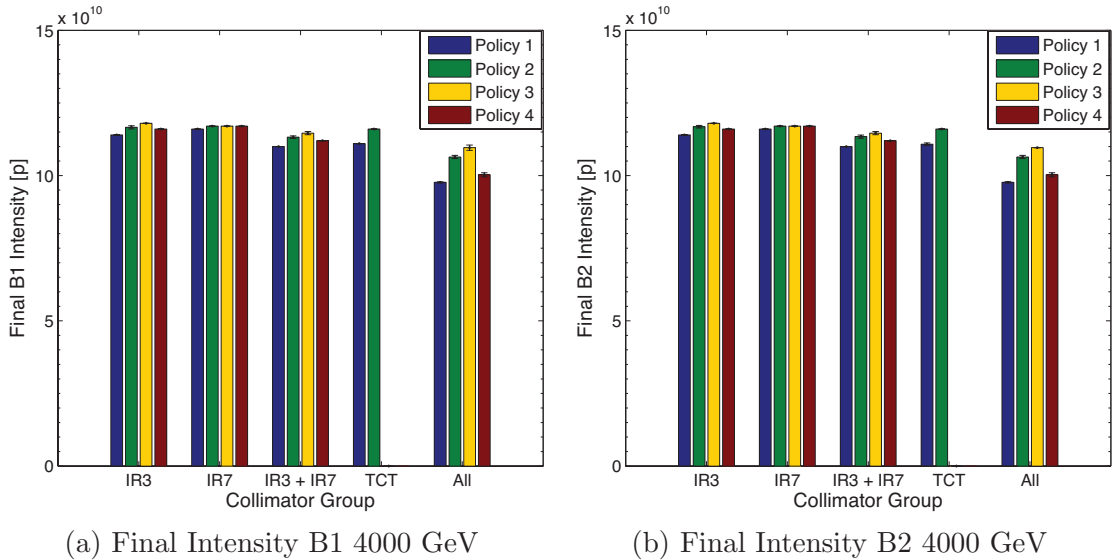
Figure 8.9: Final B1 (a) and B2 (b) intensities at 4000 GeV.

The final collimation depth and the actual time required to complete the simulations are shown in Fig. 8.10a and Fig. 8.10b respectively.

147

(a) Final collimation depth 4000 GeV

(b) Simulation time required 4000 GeV
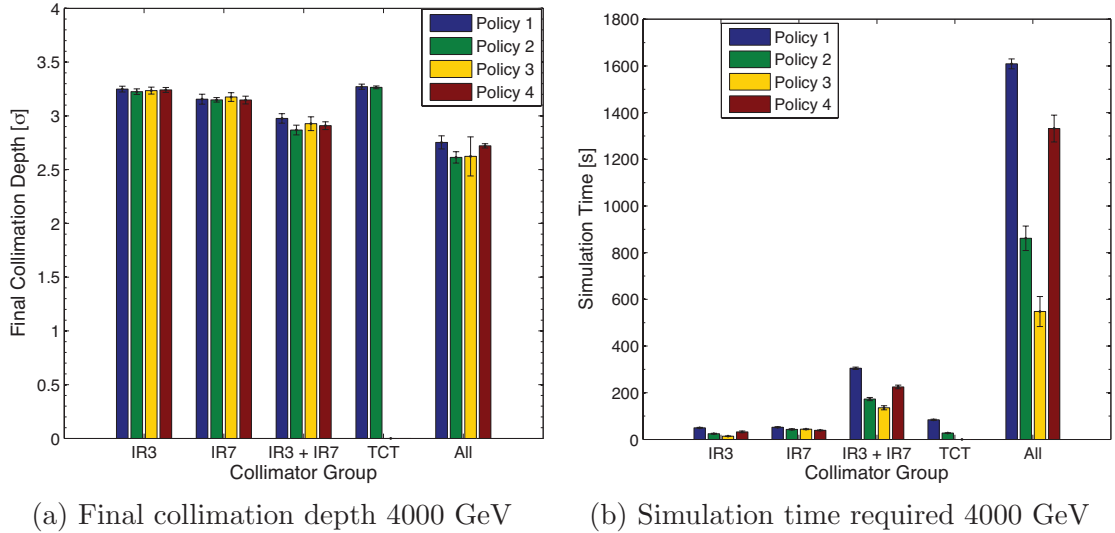
Figure 8.10: Final collimation depth (a) and simulation time required (b) at 4000 GeV.

8.1.3 Results at 7000 GeV

The jaw step size is 5 μm, and the tight settings at 7 TeV were used. Initial centres were taken from the 2012 4000 GeV alignment dataset. The total number of steps and average number of steps taken by each collimator are shown in Fig. 8.11a and Fig. 8.11b respectively.

(a) Total steps 7000 GeV

(b) Average steps 7000 GeV
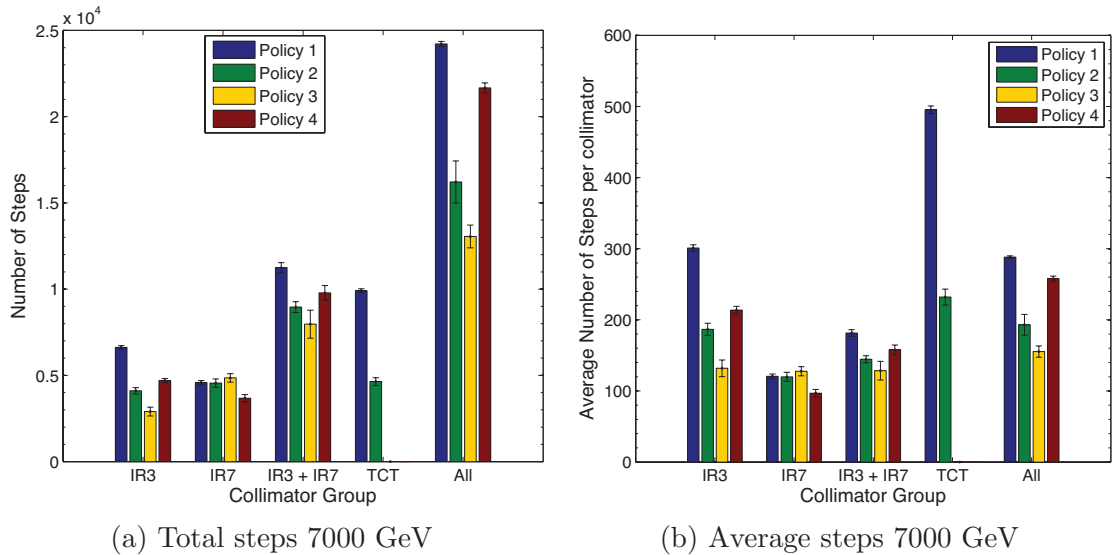
Figure 8.11: Total number of steps (a) and average number of steps (b) per collimator at 7000 GeV.

The number of steps is divided by the maximum jaw movement rate of 8 Hz to obtain the time in s, and hence the plots in Fig. 8.12a and Fig. 8.12b are generated.

(a) Total time 7000 GeV

(b) Average time 7000 GeV
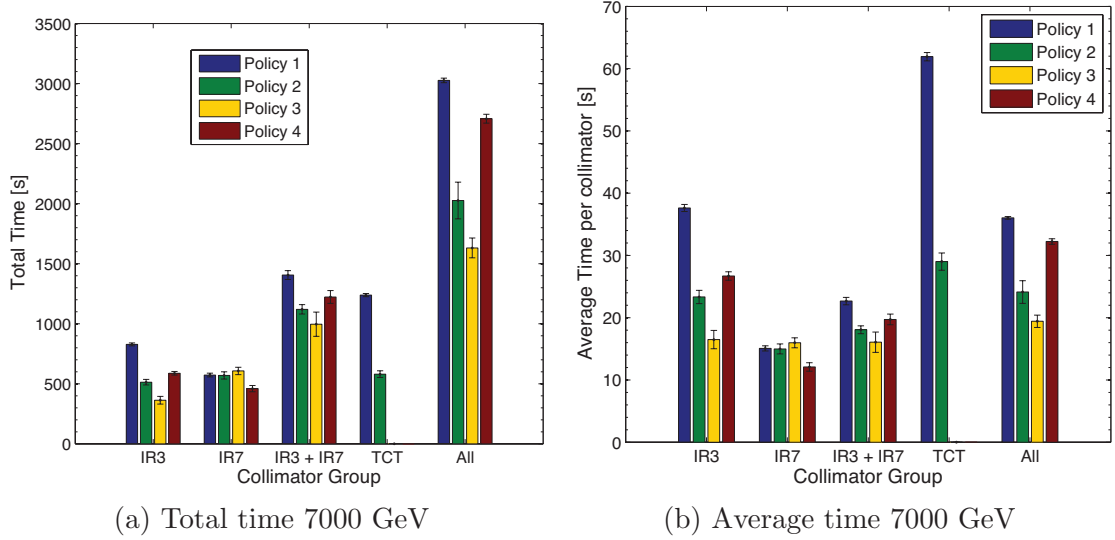
Figure 8.12: Total time (a) and average time (b) required per collimator at 7000 GeV.

The final beam intensities for B1 and B2 at the end of the alignment are provided in Fig. 8.13a and Fig. 8.13b respectively.

(a) Final Intensity B1 7000 GeV

(b) Final Intensity B2 7000 GeV
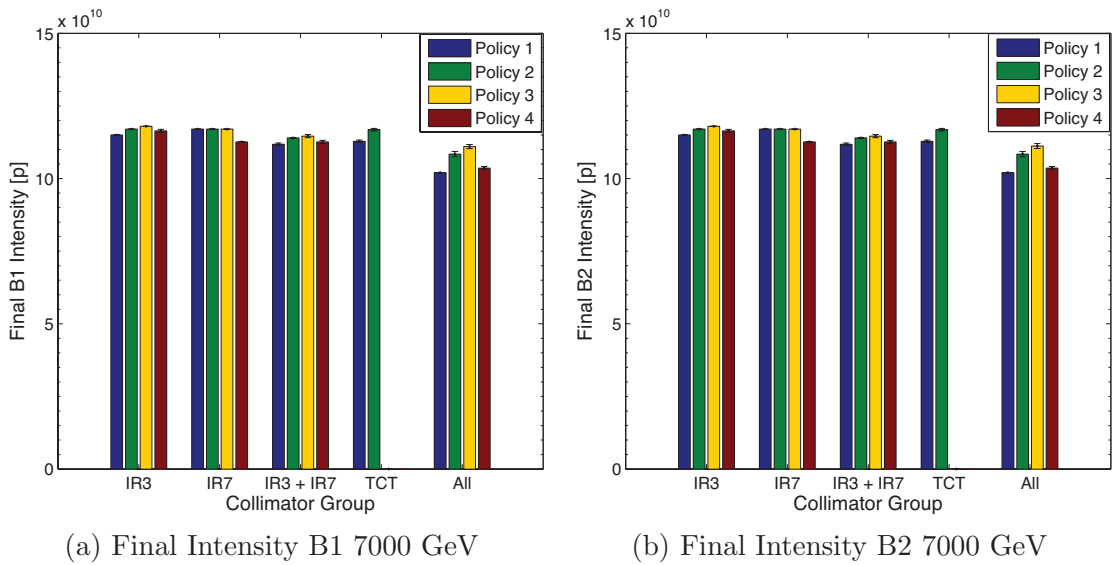
Figure 8.13: Final B1 (a) and B2 (b) intensities at 7000 GeV.

The final collimation depth and the actual time required to complete the simulations are shown in Fig. 8.14a and Fig. 8.14b respectively.

(a) Final collimation depth 7000 GeV

(b) Simulation time required 7000 GeV
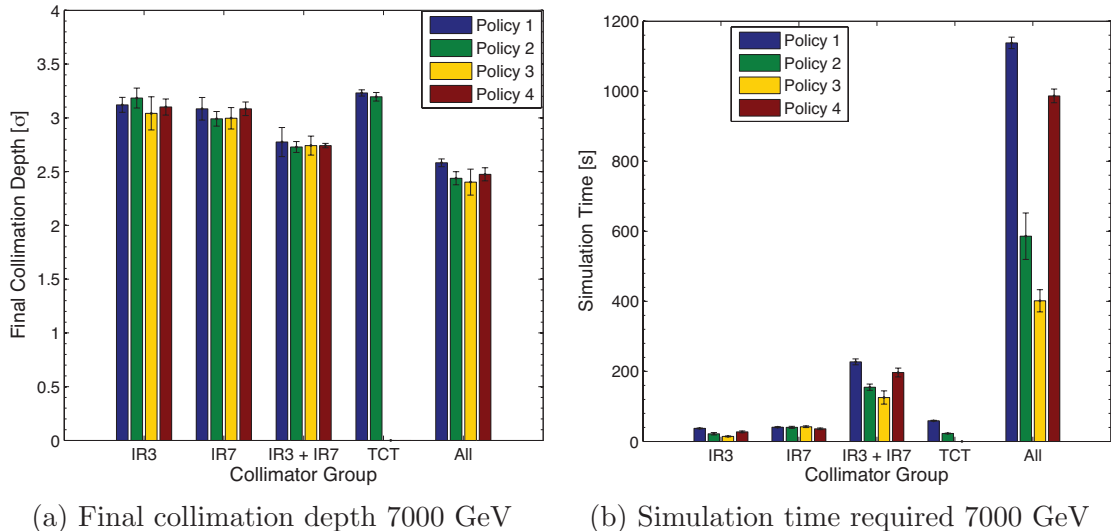
Figure 8.14: Final collimation depth (a) and simulation time required (b) at 7000 GeV.

8.1.4 Interpretation of simulated results

For every simulation, the jaw centres determined during the simulation agree with the initially generated beam centres within the specified jaw step size (5 - 10 μm). Independently of the beam energy or collimator subgroup, Policy 3 achieves the quickest alignment time. It appears that Policy 4 performs even worse than Policy 2. Recall that Policy 4 and Policy 3 are similar, except that Policy 4 attempts to speed up the alignment by using knowledge of the crosstalk factors to align selected subgroups of collimators in parallel. A possible explanation for this is that although the subgroup of collimators with low crosstalk factors with respect to the closest collimator to the beam move for extended periods of time without crosstalk interruptions, the gain achieved by moving all collimators in parallel albeit more frequent interruptions is larger.

8.2 Operational results

Data from a typical alignment of the TCP.C6R7.B2 are shown in Fig. 8.15. Both jaws are moved in, followed by an alignment of the left and right jaws individually. The same beam centre is found as the data are taken from the sequential phase where the IR7 TCPs are systematically realigned after each collimator to obtain information about the local beam size.
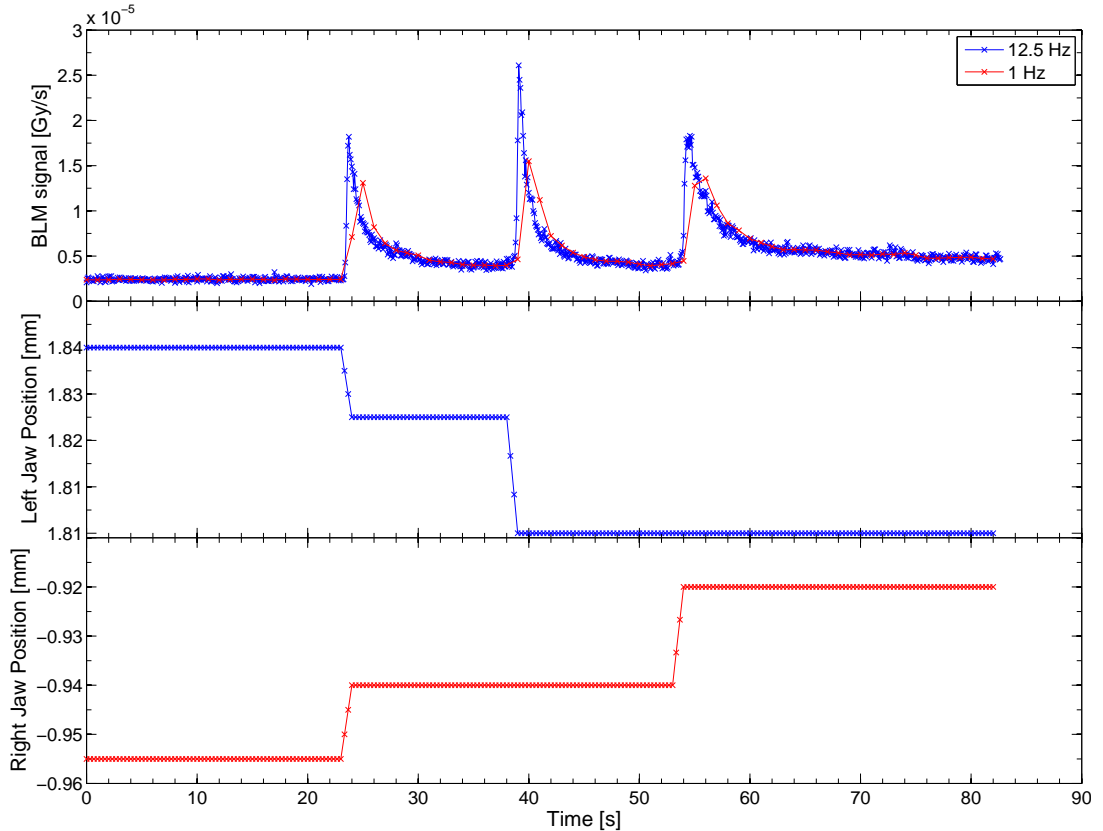
Figure 8.15: Measured data from the alignment of a TCP.C6R7.B2 collimator, including superimposed the fast (12.5 Hz) and slow (1 Hz) BLM data, as well as the left and right jaw positions.

8.2.1 Inferred beam sizes

The beam size ratio is the ratio of the inferred beam size in σ to the nominal beam size in σ. The nominal and inferred beam sizes are calculated using equations (4.4) and (4.8). The variation in the ratio of the inferred beam size to the nominal beam size can indicate the accuracy and stability of manual and automatic collimator alignment. However, this is true only if certain machine parameters remain constant, such as the β-beat. Ideally, the beam size ratio is unity.

The plots in Figs. 8.16a to 8.18b contrast the beam size ratios obtained during collimator setups for the p-p 2010-2012 runs at 450 GeV and 3.5 TeV / 4 TeV. Histograms for the same data are shown in Fig. 8.17a to Fig. 8.19b. The beam size ratios measured at 450 GeV in 2012 are much closer to unity when compared to the data for 2010 and 2011, due to the usage of smaller jaw step sizes and hence better accuracy permitted by the faster alignment speed. The beam size ratios in IR3 are generally larger than 1. This could be due to the fact that there is a high dispersion in this region, which means that, independently of the alignment, the small energy errors on all particles contribute to the measured beam size. Over-populated tails may also affect the beam size measurements.

151
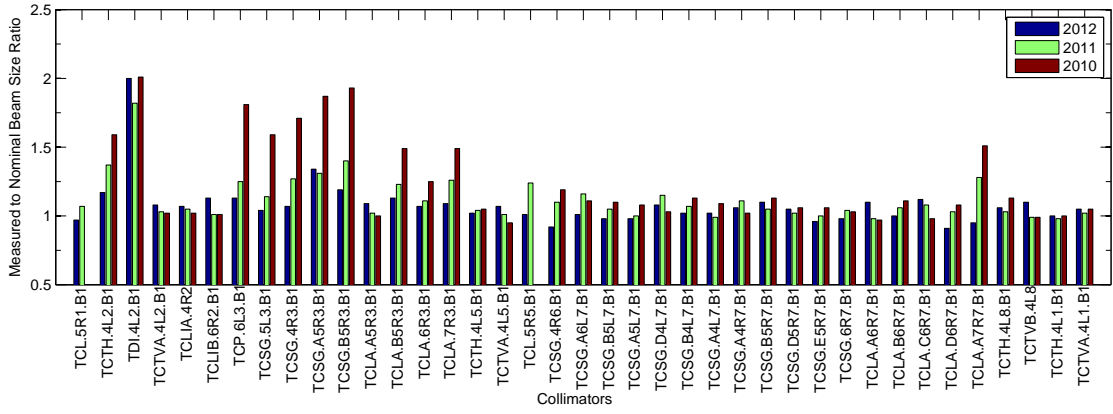
(a) 450 GeV B1 beam size ratios
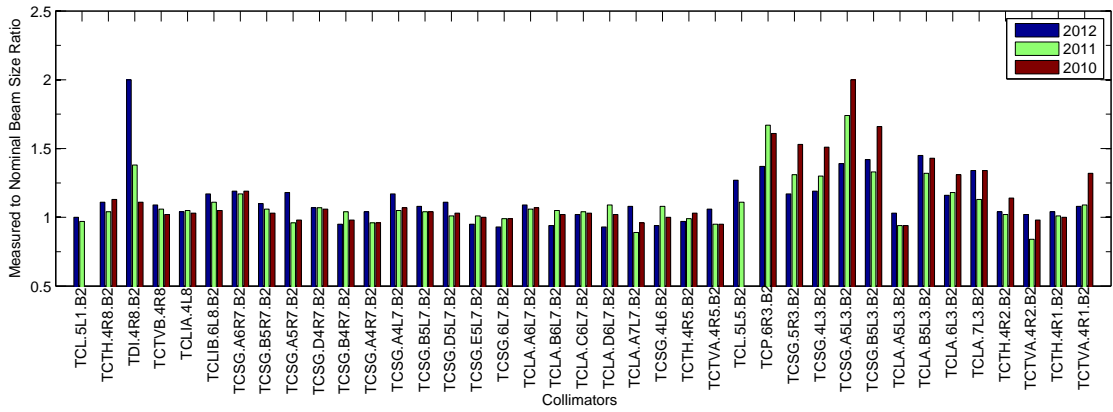
(b) 450 GeV B2 beam size ratios

Figure 8.16: Beam size ratios at 450 GeV between 2010 and 2012 for the B1 (a) and B2 (b) collimators.
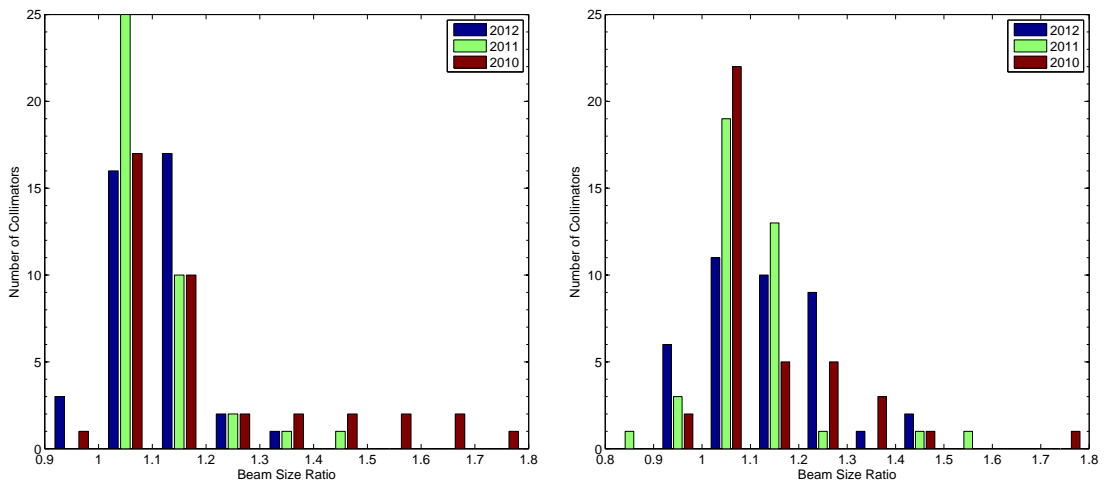
(a) 450 GeV B1 beam size ratios histogram (b) 450 GeV B2 beam size ratios histogram

Figure 8.17: Histogram of the beam size ratios at 450 GeV between 2010 and 2012 for the B1 (a) and B2 (b) collimators.
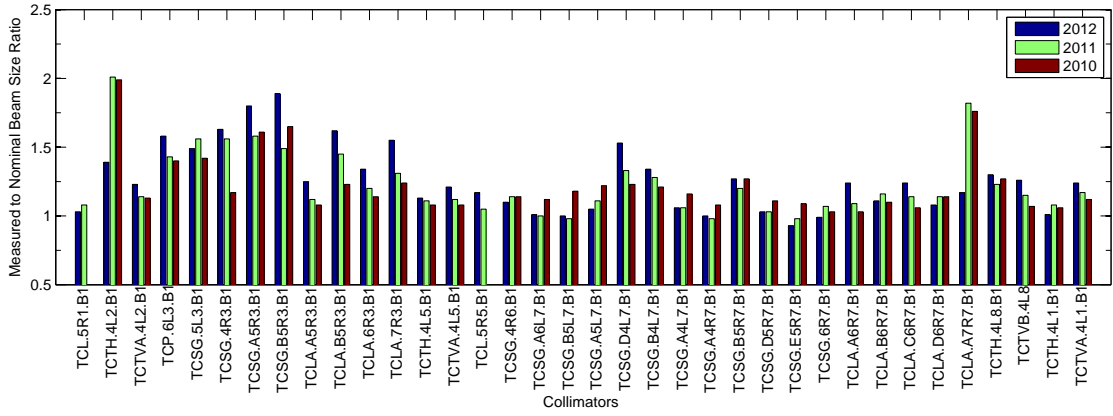
(a) Top energy B1 beam size ratios
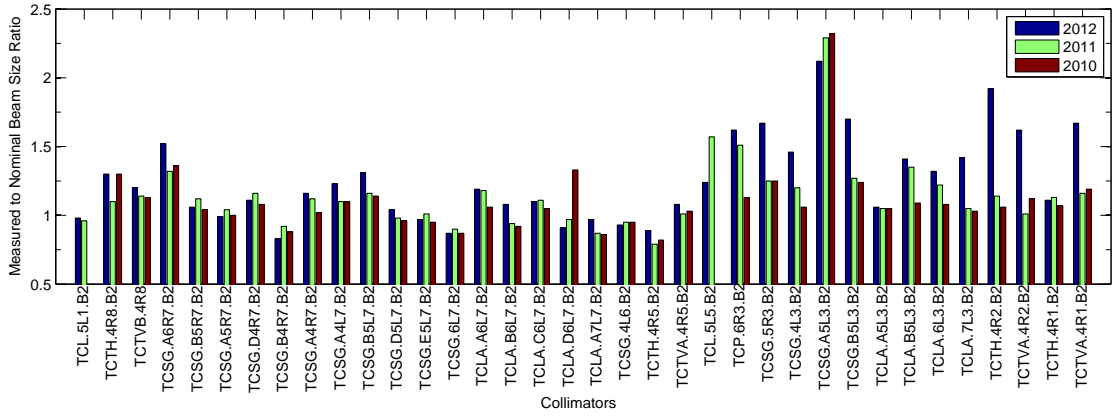
(b) Top energy B2 beam size ratios

Figure 8.18: Beam size ratios at top energy (3.5 TeV / 4 TeV) between 2010 and 2012 for the B1 (a) and B2 (b) collimators.
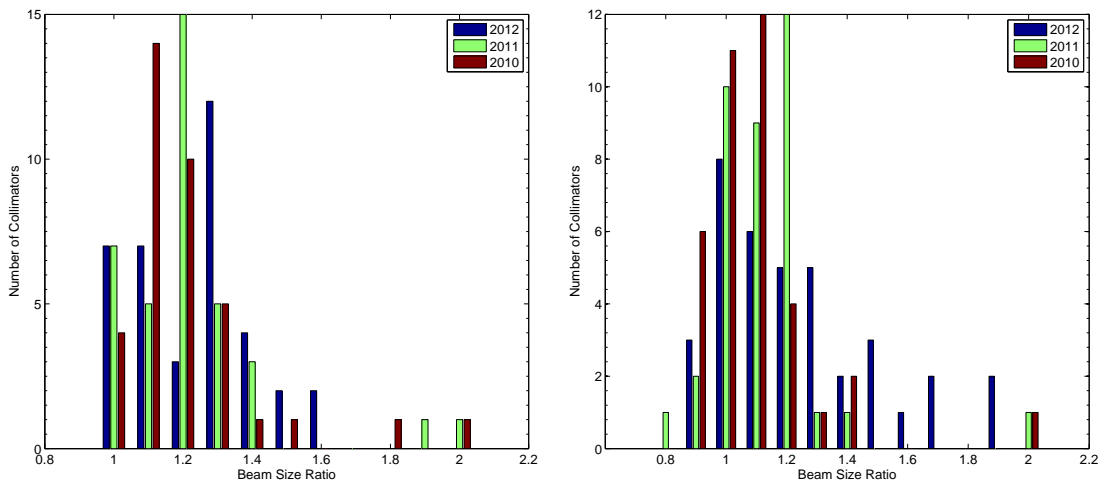
(a) Top energy B1 beam size ratios histogram

(b) Top energy B2 beam size ratios histogram

Figure 8.19: Histogram of the beam size ratios at top energy (3.5 TeV / 4 TeV) between 2010 and 2012 for the B1 (a) and B2 (b) collimators.

8.2.2 Beam intensity loss during setup

Throughout collimator setup, a certain amount of beam intensity must be maintained to obtain reproducible beam loss spikes when aligning the jaws. In addition, minimizing the intensity lost can allow for more alignments to be performed at different stages of the machine cycle within the same fill. These alignments may even be followed by a full set of qualification loss maps if enough intensity is left.

In the 2010 run, large step sizes (40 μm) and human error occasionally led to substantial sudden decreases in the beam intensity, if not beam dumps, as illustrated in Fig. 8.20a. Automatic setup allows for smaller step sizes and safer setup, leading to a smoother 'shaving' of the beam shown in Fig. 8.20b.

(a) B1 intensity
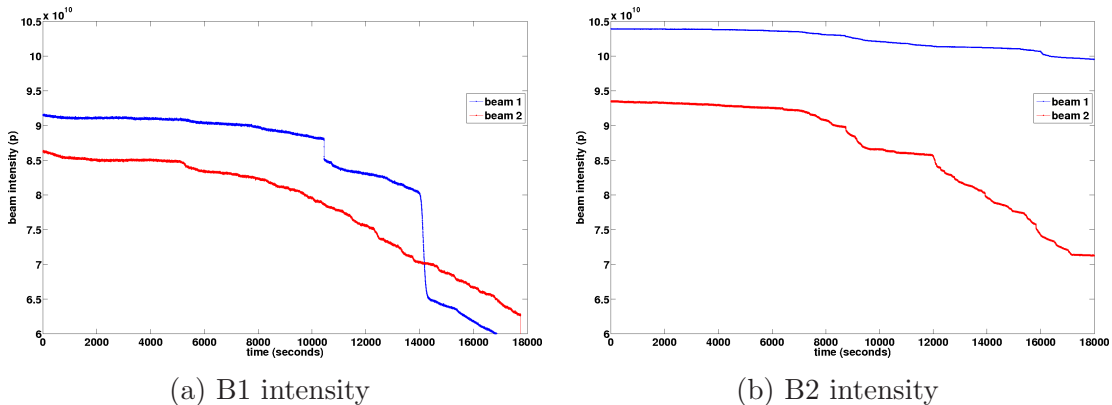
(b) B2 intensity

Figure 8.20: Variation of beam intensity during manual (a) and automatic (b) setup at 3.5 TeV [115, 76]. T(0) for manual setup corresponds to 13.06.2010 07:30:00, while T(0) for automatic setup corresponds to 07.03.2011 21:30:00.

8.2.3 Setup times

The time taken to set up collimators is the most important indicator of the efficiency of a setup algorithm. The average time per collimator $T_{average}$ and the total time required T_{setup} are defined as follows:

$$T_{average} = \frac{T_{beam}}{C} \tag{8.1}$$

$$T_{setup} = T_{beam} + d \times T_{turnaround} \tag{8.2}$$

where T_{beam} is the beam time used for setup, C is the number of collimators and d is the number of beam dumps caused by collimator setup. The turnaround time $T_{turnaround}$ is the time consumed from the point of beam dump until the machine is cycled back to the setup operating point. The average LHC turnaround times used for this analysis are presented in Table 8.1.

Table 8.1: Average turnaround times in the 2010 LHC proton run from [116].

Operating Point	Turnaround Time (hours)
Injection	3.00
Flat top	3.57
Squeezed	4.26
Collisions	4.48

The alignment times achieved for the 2010-2013 period are listed in Tables 8.2a to 8.2d. The results given in Table 8.2b indicate an increase in the setup time by a factor of 2 for the 2011 450 GeV setup compared to 2010, but this was due to the time required to test the new software. The two beam dumps recorded for the 2011 450 GeV setup were caused by human error when using the manual alignment technique during a phased changeover from manual to semi-automatic software. After debugging was carried out, an improvement by a factor of 1.5 in setup time at 3.5 TeV flat top was registered.

For the March 2011 setups with squeezed beams, before and after going into collisions, the software was upgraded to allow both jaws to move in parallel to the beam. A speed-up by a factor of 4 to 6 for both modes respectively was achieved. No beam dumps were recorded from 2011 onwards, establishing the safety of the feedback algorithm used in automatic alignment. Fast BLM data (12.5 Hz versus the previous 1 Hz) were introduced in a phased manner during the March 2012 alignments, thus allowing the maximum jaw movement rate of 8 Hz to be used. The measured beam centres and beam sizes for individual collimators from two alignments at injection and top energy in 2012 are listed in Appendix C.

The evolution of the alignment times achieved at top energy is shown in Fig. 8.21. A superimposed timeline illustrates the phased introduction of the alignment algorithms. The last two points are extrapolated from an alignment of half the collimation system in IR6 and IR7. The minimum time required for alignment is defined mainly by the time necessary for the loss spikes to decay back to steady-state during alignment. Considering a total of 86 collimators, two jaws per collimator, the fact that the reference collimator needs to be re-aligned for each collimator, and a spike decay time of 15 seconds, then a lower bound of ∼1.5 hours is obtained. The jaw movement rate plays a minor role: the difference

between moving a jaw for a typical 6 mm in 5 μm steps at 1 Hz and at 8 Hz is around 15 minutes. A similar plot was generated for the evolution of the TCT alignment times (see Fig. 8.22).

Table 8.2: Comparison of setup times, number of beam dumps d and collimators aligned C in the 2010-2013 period.

Dates	Setup Type	Species	$T_{average}$ (mins)	T_{setup} (hours)	d	C
05-07 May	Injection	p-p	5.88	11.02	1	82
12-16 Jun	Flat top	p-p	10.28	27.98	4	80
17-18 Jun	Squeezed	p-p	12.00	8.26	1	20
20 Jun	Collisions	p-p	12.00	8.48	1	20
07 Sep	Injection	p-p	11.01	3.67	0	20
12-13 Sep	Flat Top	p-p	16.36	5.18	0	19
15 Sep	Flat Top	p-p	7.85	1.57	0	12
18 Sep	Collisions	p-p	8.01	2.67	0	20
05 Nov	Injection	Pb-Pb	9.21	3.07	0	20
07 Nov	Collisions	Pb-Pb	9.54	7.66	1	20
		Sub-total	10.21 (Average)	79.56	8	313

(a) Alignments in 2010

Dates	Setup Type	Species	$T_{average}$ (mins)	T_{setup} (hours)	d	C
25 Feb-01 Mar	Injection	p-p	8.73	18.52	2	86
06-08 Mar	Flat top	p-p	13.33	17.77	0	80
11 Mar	Squeezed	p-p	6.00	2.00	0	20
11 Mar	Collisions	p-p	4.00	1.33	0	20
02 Apr	Injection	p-p	8.04	0.67	0	5
03 Apr	Injection	p-p	8.47	1.27	0	9
03 Apr	Flat Top	p-p	6.96	0.58	0	5
02 Jul	Flat Top	p-p	9.27	3.4 0	0	22
03 Sep	Squeezed	p-p	8.75	1.75	0	12
03 Sep	Collisions	p-p	7.50	1.5 0	0	12
04 Sep	Injection	p-p	9.00	1.2 0	0	8
05 Sep	Flat Top	p-p	7.50	1.00	0	8
05 Sep	Collisions	p-p	5.40	0.72	0	8
06 Nov	Squeezed	Pb-Pb	2.10	0.70	0	20
06 Nov	Collisions	Pb-Pb	2.40	0.80	0	20
28 Nov	Collisions	Pb-Pb	9.00	0.60	0	4
		Sub-total	7.28 (Average)	53.81	2	339

(b) Alignments in 2011

Dates	Setup Type	Species	$T_{average}$ (mins)	T_{setup} (hours)	d	C
21 Mar	Injection	p-p	6.98	10.00	0	86
29 Mar	Flat top	p-p	5.63	7.50	0	80
30 Mar	Collisions	p-p	7.50	3.00	0	24
31 Mar	Squeezed	p-p	8.19	2.73	0	20
21 Apr	Injection	p-p	3.89	1.75	0	27
22 Apr	Squeezed	p-p	15.00	1.50	0	6
30 Apr	Collisions	p-p	6.75	0.90	0	8
07 Jul	Collisions	p-p	5.50	1.10	0	12
16 Jul	Collisions	p-p	4.56	1.52	0	20
13 Aug	Injection	p-p	4.73	0.63	0	8
13 Aug	Flat Top	p-p	6.60	0.88	0	8
14 Aug	Squeezed	p-p	7.88	1.05	0	8
14 Aug	Collisions	p-p	4.73	0.63	0	8
09 Oct	Squeezed	p-p	1.61	1.07	0	40
22 Nov	Collisions	p-p	3.51	1.17	0	20
28 Nov	Squeezed	p-p	3.00	0.50	0	10
11 Dec	Collisions	p-p	3.50	1.40	0	24
11 Dec	Squeezed	p-p	1.50	0.50	0	20
		Sub-total	5.61 (Average)	37.83	0	429

(c) Alignments in 2012

Dates	Setup Type	Species	$T_{average}$ (mins)	T_{setup} (hours)	d	C
17 Jan	Flat Top	p-Pb	1.62	1.08	0	40
18 Jan	Squeezed	p-Pb	3.00	1.00	0	20
18 Jan	Collisions	p-Pb	3.00	1.00	0	20
28 Jan	Collisions	p-Pb	1.73	0.23	0	8
01 Feb	Collisions	Pb-p	4.95	1.65	0	20
10 Feb	Collisions	p-p	2.70	1.08	0	24
		Sub-total	2.83 (Average)	6.04	0	132

(d) Alignments in 2013
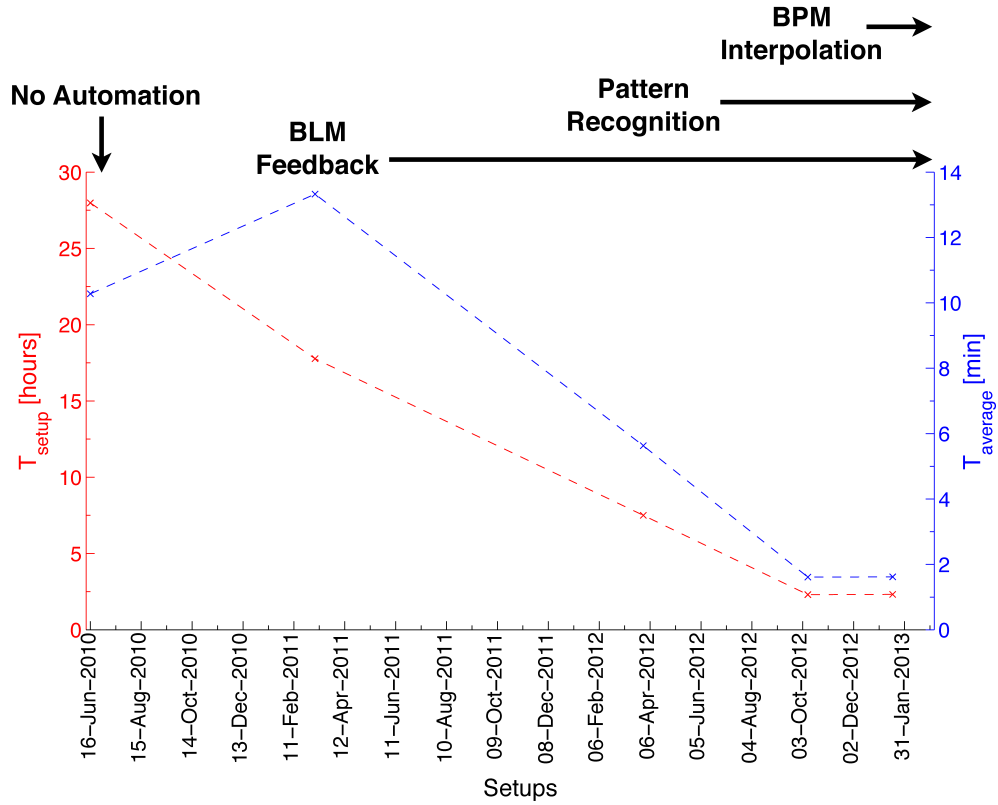
Figure 8.21: Evolution of T_{setup} and $T_{average}$ for full alignments at flat top over the 2010-2013 LHC run. A timeline showing the introduction of the various algorithms is superimposed.
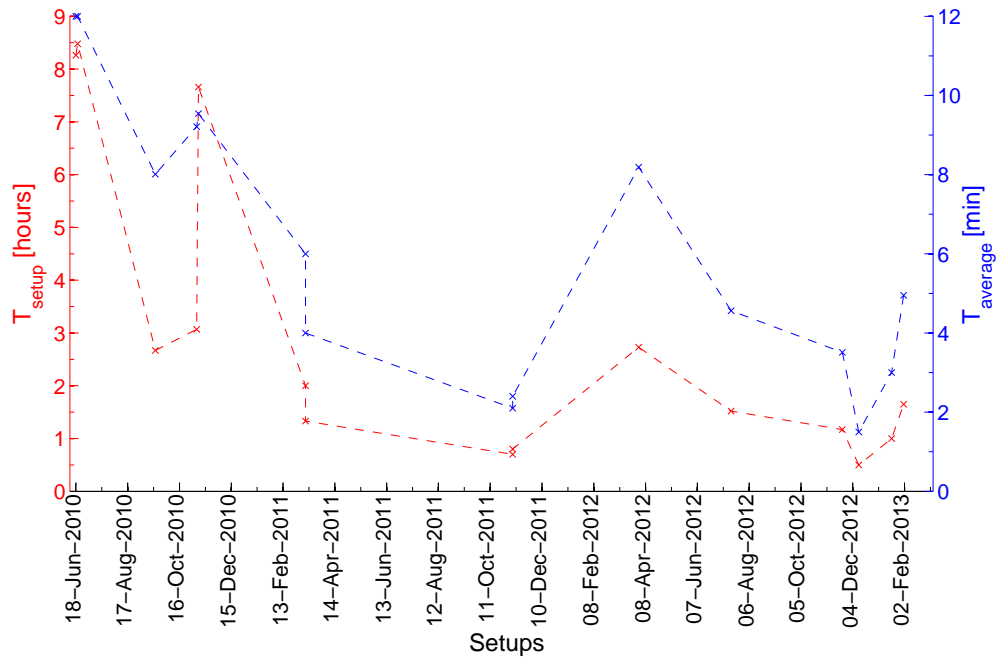
Figure 8.22: Evolution of T_{setup} and $T_{average}$ for TCT alignments with squeezed separated and colliding beams over the 2010-2013 LHC run.

8.2.4 Misaligned collimators

Possible misalignments of the collimator jaws in the tunnel are the major source of error that could affect the measurements. This is because the alignment procedure assumes that the jaws are parallel to the beam trajectory during the setup. Figure 8.23 shows a jaw with an angular offset of α_i with respect to the beam axis. The n_1 parameter refers to the cut of the primary collimator into the beam in units of σ during the alignment, σ_i^r is the real beam size at the collimator and L_i is the length of the jaw in metres. There are three independent position measurements for each jaw, namely a motor step counter, a resolver and a LVDT [39]. A scale error Δ_i exists due to a difference between the position sent using the counter and the resolver to the motor and the actual position as read out from the LVDT. When possible measurement errors are taken into account, the measured gap is [117]:

$$G_i = \frac{2n_1\sigma_i^r}{\cos(\alpha_i)} + \Delta_i + \tan(\alpha_i) \times L_i \tag{8.3}$$

Rearranging Eq. (8.3), the real beam size at collimator i for small misalignment angles is given by:

$$\sigma_i^r = \frac{G_i - \Delta_i - \alpha_i \times L_i}{2n_1} \tag{8.4}$$
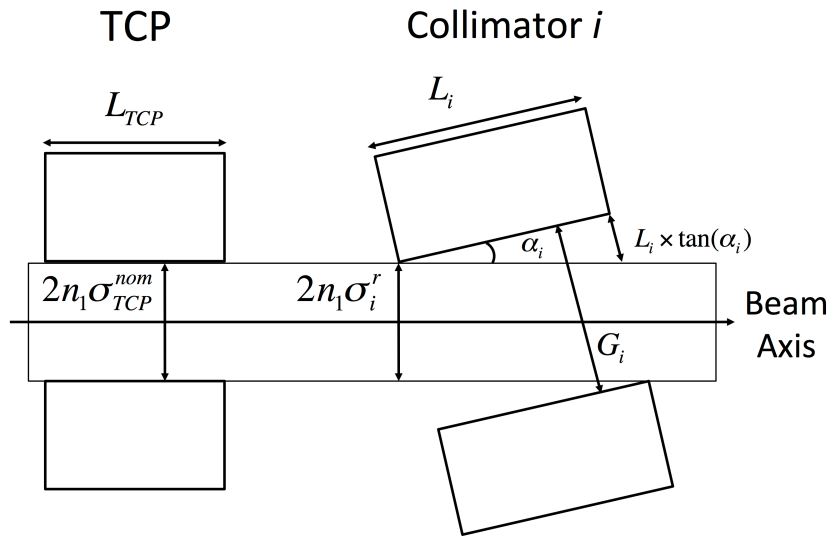
Figure 8.23: Schematic of the position of the jaws of a collimator i misaligned by an angle α_i, which introduces an error in the measured gap [117, 76]. The reference primary collimator is assumed to be perfectly aligned.

The inferred beam size is expressed as:

$$\sigma_i^{inf} = \frac{G_i}{2n_1} \qquad (8.5)$$

Assuming a perfect reference primary alignment, the error in the beam size at collimator i is the difference between the real beam size, given by Eq. (8.4), and the inferred beam size:

$$\Delta\sigma_i = \frac{\Delta_i + \alpha_i \times L_i}{2n_1} \qquad (8.6)$$

The error can be minimized by working at the maximum n_1. However, this does not provide much room as the primary collimators should not be opened beyond $6\,\sigma$ at 3.5 TeV due to machine protection requirements. The value for n_1 during the setup decreases over time as the jaws cut further into the beam. Considering typical values for beam-based alignment, a scale error of 0.05 mm, angle error of 0.1 mrad and a collimator length of 1 m result in an error of 0.025 mm for $n_1 = 3$. This amounts to an error of 2.38% at 450 GeV and $\sim$7% at 3.5 TeV.

Another error source is the β-beat, which can be corrected to between 10% and 20% in the LHC [118]. If this error is included in Eq. (4.4), then the error from the β-beat alone in the inferred beam size is between 5% and 10%, which is independent of energy. The contribution to the error by the angle of the n-sigma beam envelope is typically 20-50 μrad, which is less than the measured misalignment angle of 1.6 mrad. For the current LHC configuration, this contribution is ignored, especially as the alignment of the jaw corners is not done separately.

At both 450 GeV and 3.5 TeV, large beam size ratios were observed for the TCLA.A7R7.B1, TCTH.4L2.B1 and TCSG.A5L3.B2 collimators. An inspection in the LHC tunnel revealed that the tanks housing these collimators were misaligned by an angle of approximately 1.6 mrad. After their positions were corrected, beam-based alignment was performed again and the beam size ratios decreased by 38%, 35% and 39% respectively at 3.5 TeV. The predicted misalignment angles for these collimators were calculated using equation (8.6), assuming a scale error of 0.05 mm, and ignoring the small contribution of the β-beat to the measured gap error.

The results for the inferred and nominal beam sizes at 3.5 TeV are given in Table 8.3a, while Table 8.3b displays the recalculated values after the re-alignment

Table 8.3: Predicted misalignment angles for the collimators with the highest beam size ratios [76]. The difference between the nominal and the inferred beam sizes at these collimators, and hence the predicted misalignment angle, decreases after tunnel realignment.

Collimator	σ_i^{inf} (mm)	σ_i^{nom} (mm)	n_1	α_i (mrad)
TCTH.4L2.B1	0.844	0.420	3.63	3.0
TCLA.A7L7.B1	0.890	0.490	4.40	3.4
TCSG.A5L3.B2	0.928	0.486	3.68	3.2

(a) Before tunnel alignment

Collimator	σ_i^{inf} (mm)	σ_i^{nom} (mm)	n_1	α_i (mrad)
TCTH.4L2.B1	0.564	0.420	4.38	1.2
TCLA.A7L7.B1	0.554	0.490	4.64	0.5
TCSG.A5L3.B2	0.566	0.486	4.56	0.6

(b) After tunnel alignment

in the tunnel. The predicted misalignment angles were found to agree within a factor 2 assuming no further misalignments of the jaws with respect to the tanks. The decrease in the beam size ratios after the tunnel re-alignment means that the model can be used as an indication of the correct positioning of the collimators in the tunnel.

8.2.5 Settings qualification

As explained in Chapter 4, all settings are qualified by beam loss maps. After the loss maps are executed in the CCC, the approximate timestamps are noted down in the eLogbook. In an offline analysis, a program is used to search for the highest beam losses within a ± 10 s range of the approximate timestamp. Beam loss data at this timestamp are plotted as a function of the longitudinal position to create the loss map. The signal background (typically 3×10^{-7} Gy/s) is subtracted, and the data are normalized to the highest loss, generally the IR7 TCP for betatron loss maps and the IR3 TCP for momentum loss maps.

A typical betatron loss map produced after a collimator alignment at 4 TeV flat top in March 2012 is shown in Fig. 8.24a, with B1 travelling from left to right of the plot. A zoom into IR7 is given in Fig. 8.24b. The inefficiency of the collimation system for betatron cleaning is determined as the leakage fraction of primary particles to the cold aperture in Q8. In Fig. 8.24b, the inefficiency is calculated as 8×10^{-5}, a factor 7.5 below the design cleaning inefficiency at 7 TeV of 6×10^{-4}. On the other hand, a typical momentum loss map for the same alignment is provided in Fig. 8.25a, with a zoom into IR3 in Fig. 8.25b.

betatron losses B1 4000GeV hor norm F (2012.03.29, 14:42:40)

(a) Betatron loss map (full ring)

betatron losses B1 4000GeV hor norm IR7 (2012.03.29, 14:42:40)

(b) Betatron loss map (zoom in IR7)
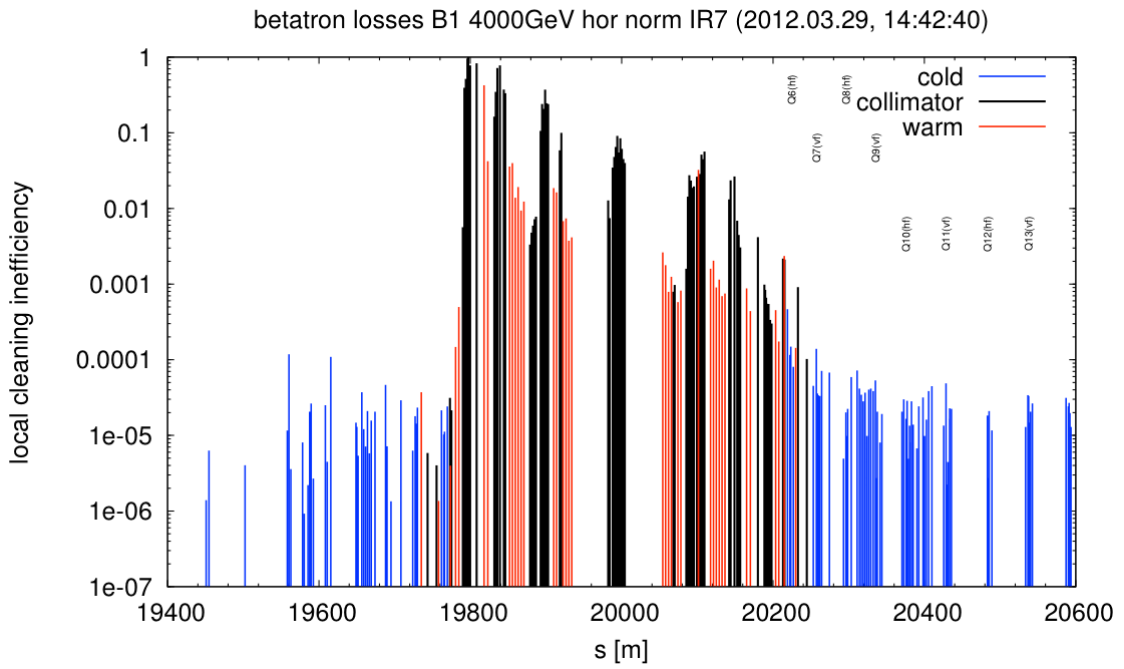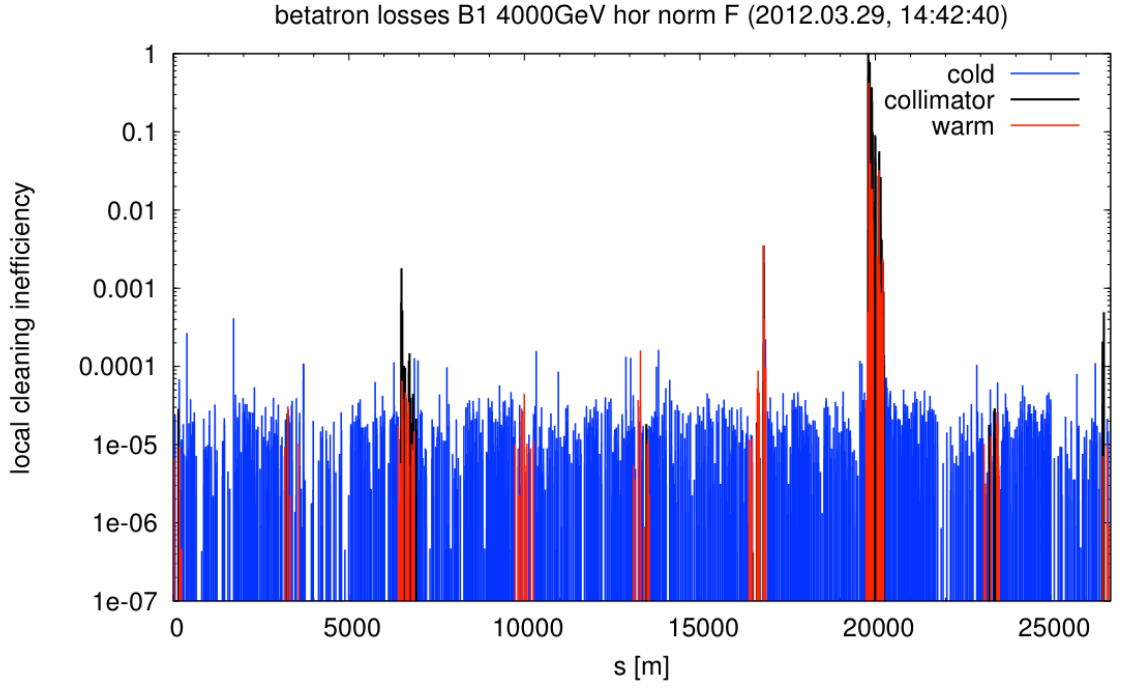
Figure 8.24: Betatron loss map of the whole LHC ring (a) and zoom in IR7 (b).
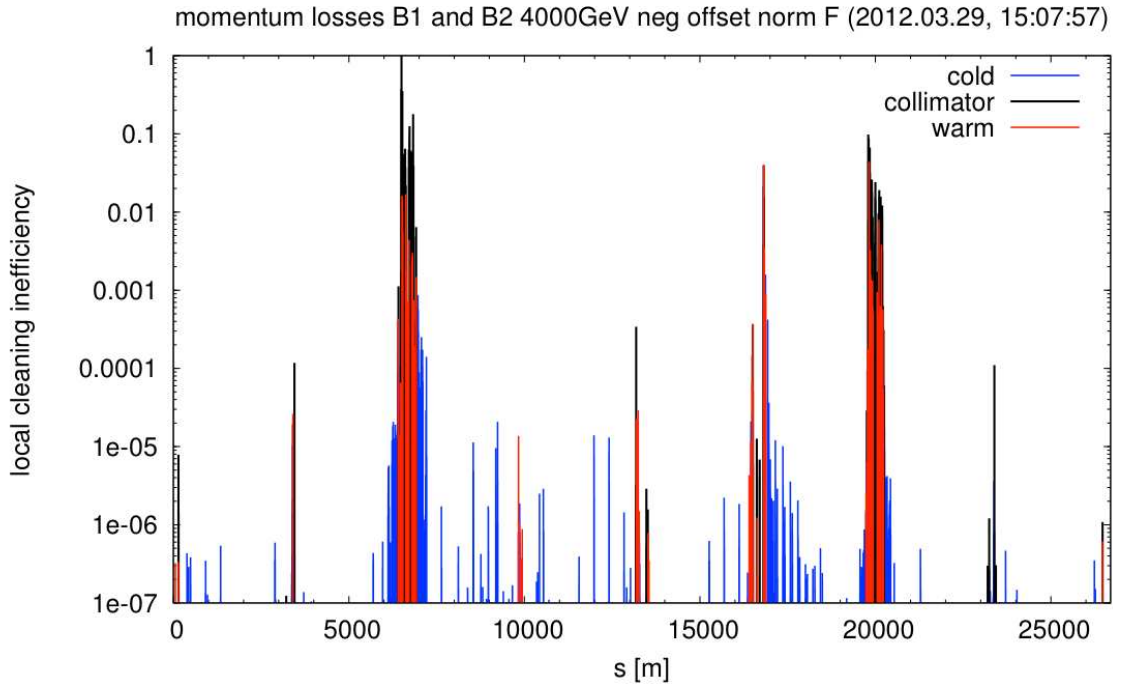
(a) Momentum loss map (full ring)
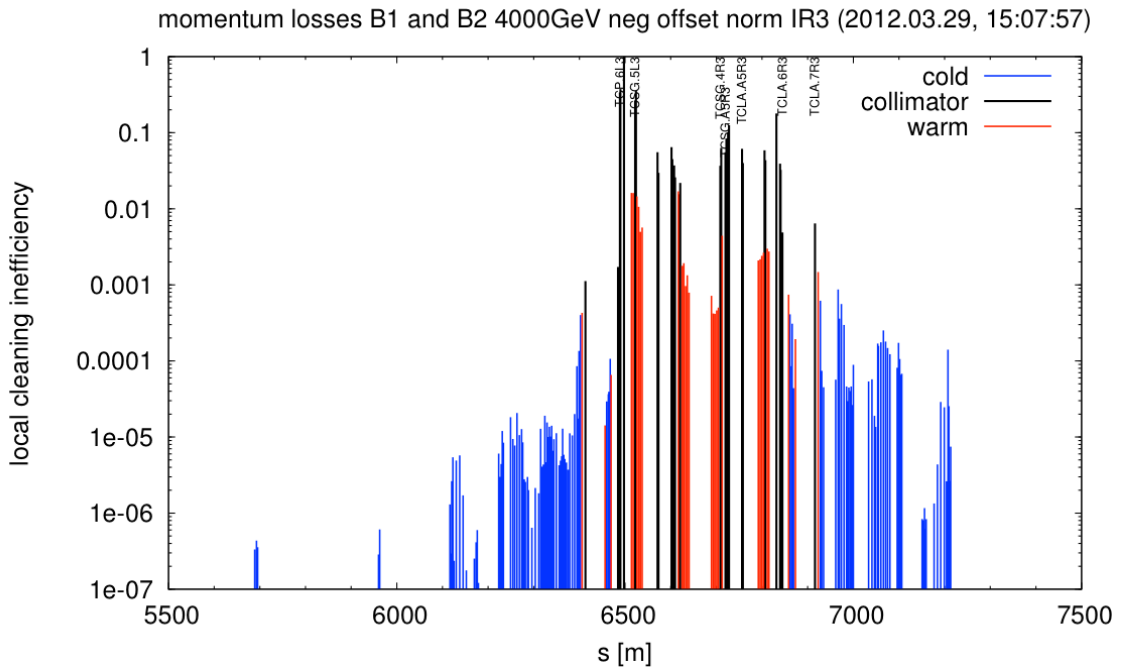
(b) Momentum loss map (zoom in IR3)

Figure 8.25: Momentum loss map of the whole LHC ring (a) and zoom in IR3 (b).

The hierarchy is correct for both IR3 and IR7, as the highest losses are observed in the primary collimators, followed in decreasing order of magnitude by the losses in the secondary collimators and the absorbers. The stability of the IR7 cleaning inefficiency over the 2010-2013 LHC runs is shown in Fig. 8.26. The introduction of the tight collimator settings in 2012 provided an improvement in the cleaning efficiency from 99.97% to 99.993%.
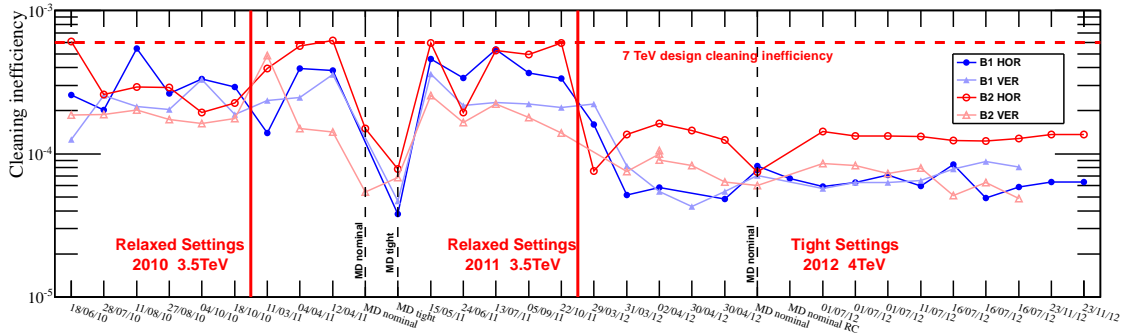
Figure 8.26: Evolution of the LHC collimation cleaning inefficiency from 2010 to 2013, from [119].

8.2.6 Alignment errors

A beam centre measurement error of 700 μm occurred during an alignment of the TCLA.A6L7.B2 collimator (vertical plane) in January 2013 [120]. The spike recognition algorithm described in Section 5.4 incorrectly classified a loss spike to be optimal, when in fact the loss signal was probably due to beam jitter or mechanical vibrations. The error was picked up in the ensuing loss map performed to qualify the newly-established beam-based parameters (see Fig. 8.27).
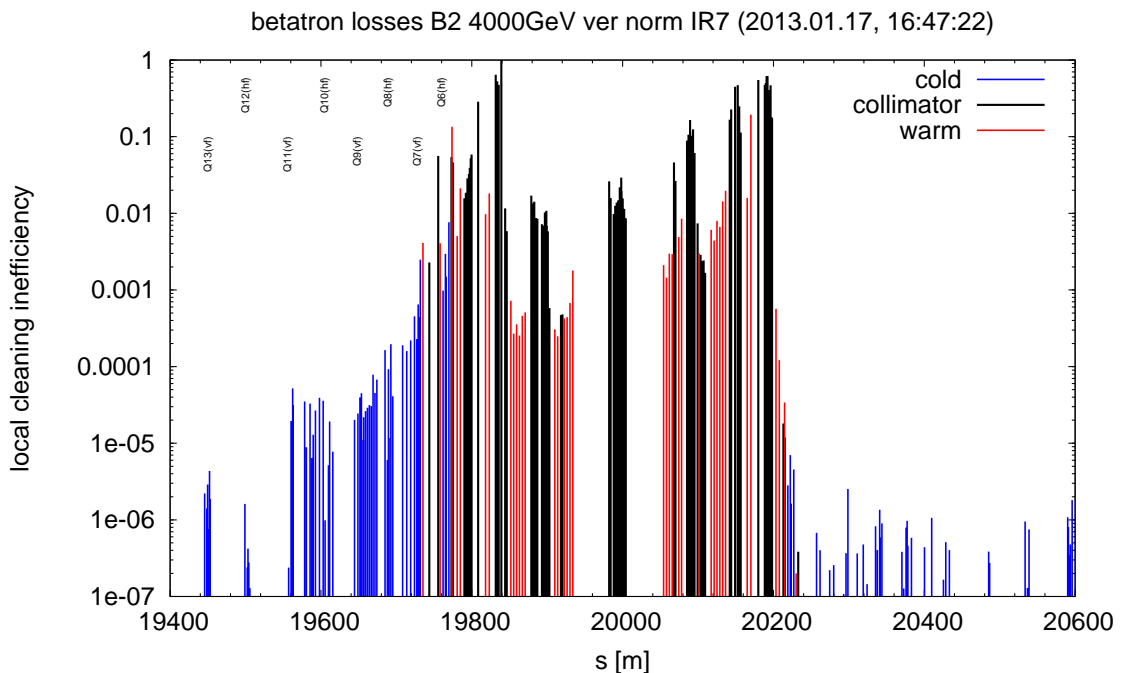
Figure 8.27: Vertical betatron loss map zoom in IR7 following an alignment error of the TCLA.A6L7.B2.

A hierarchy violation is clearly evident in IR7, with the TCLA.A6L7.B2 acting as a primary collimator. Future errors related to spike detection might be avoided if the jaw is moved in further after an optimal spike is detected, and the jaw is considered to be aligned only if the second spike is also optimal.

8.2.7 Stability of beam-based alignment settings

The stability of the alignment settings is essential for maximal efficiency of the collimation system. A few comparisons of the beam centres of the IR3 collimators are presented in Fig. 8.28. These collimators were aligned in the 3.5 TeV flat top setup in March 2011, and re-aligned in July 2011 during an LHC MD study.
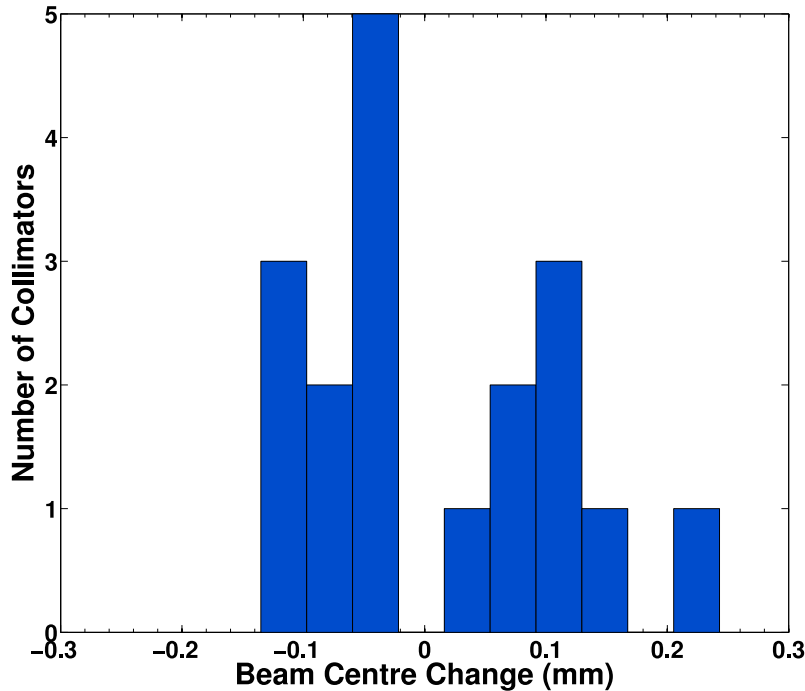
Figure 8.28: Change in the beam centres for the IR3 B1 and B2 collimators over four months of LHC operation [121].

In the second setup, attempts were made to correct the beam orbit as close as possible to the orbit established in the first setup. The results show that the centres of the collimators measured in the second setup are within less than 135 μm from the previous values, except the TCSG.5L3.B1, for which a 243 μm shift was registered. Regular monitoring of the collimation system through beam loss maps has shown that the shifts in the centres of this order do not reduce the cleaning efficiency of the system.

In 2012, the IR6 and IR7 collimators in both beams were aligned on two occasions: at the start of the LHC run in March, and for a beam study in October. The beam sizes and beam centres measured during the beam study were compared to the values achieved in the March alignment. The beam size ratios are shown in Fig. 8.29, with the beam centres in units of mm and σ in Fig. 8.30 and Fig. 8.31 respectively. The collimator names shown on the x-axis are arranged in order of longitudinal position in the LHC. The largest change in the beam centre is of

0.185 mm (corresponding to 0.507 σ), with the average change being 0.043 mm (0.146 σ) for B1 and 0.089 mm (0.243 σ) for B2. The similarity in the measured values is a reflection of the excellent stability of the LHC, and is the reason why a full collimation system alignment needs to be performed only yearly for a given set of machine parameters.
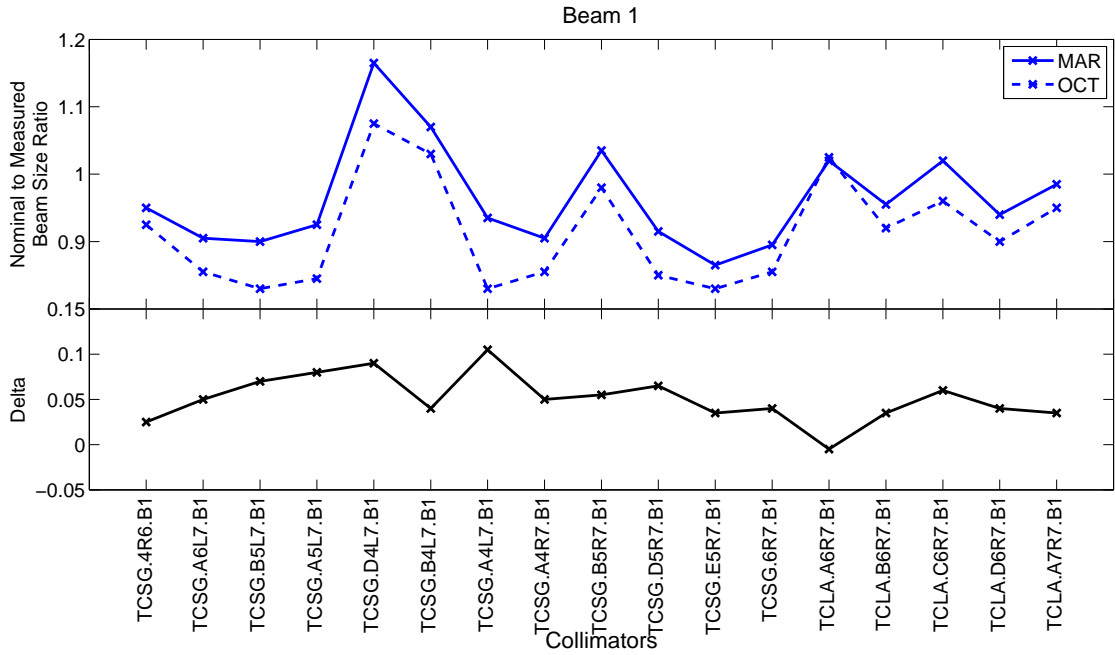
(a) B1 beam size ratios
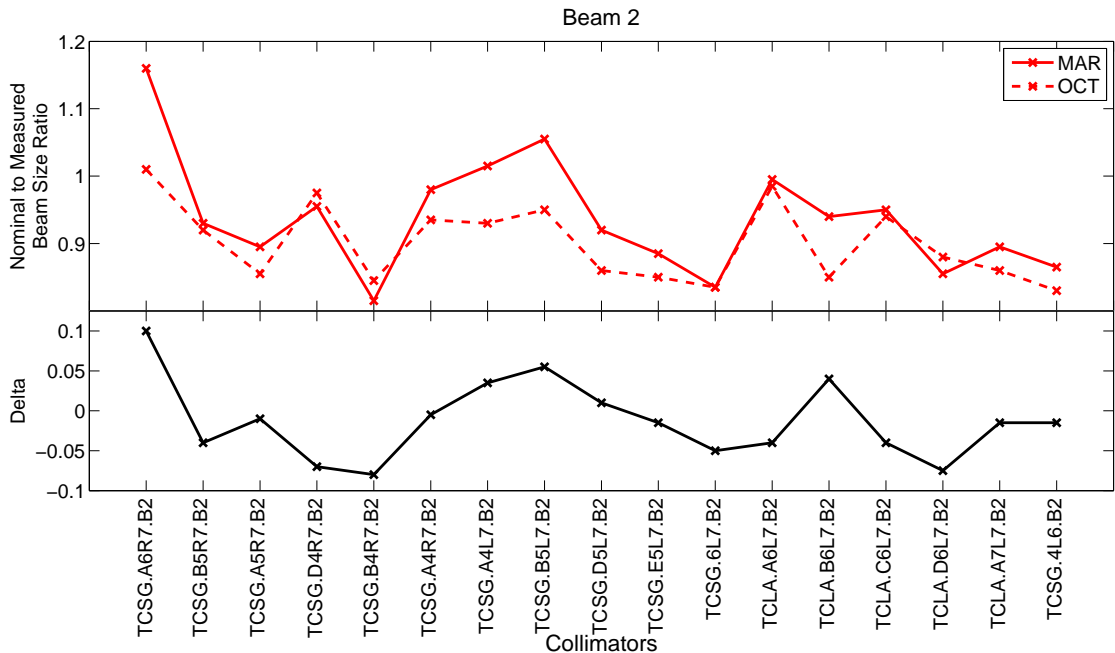
(b) B2 beam size ratios

Figure 8.29: Comparison of measured beam size ratios in IR7. The alignments were performed in March and October 2012.
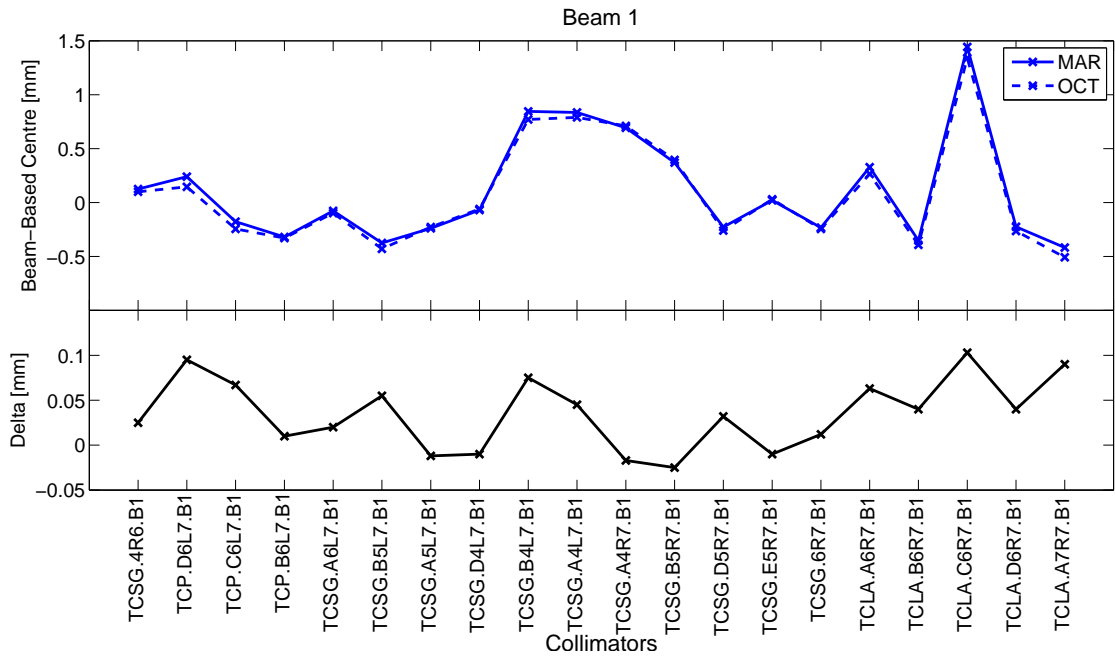
(a) Measured centres in mm (B1)
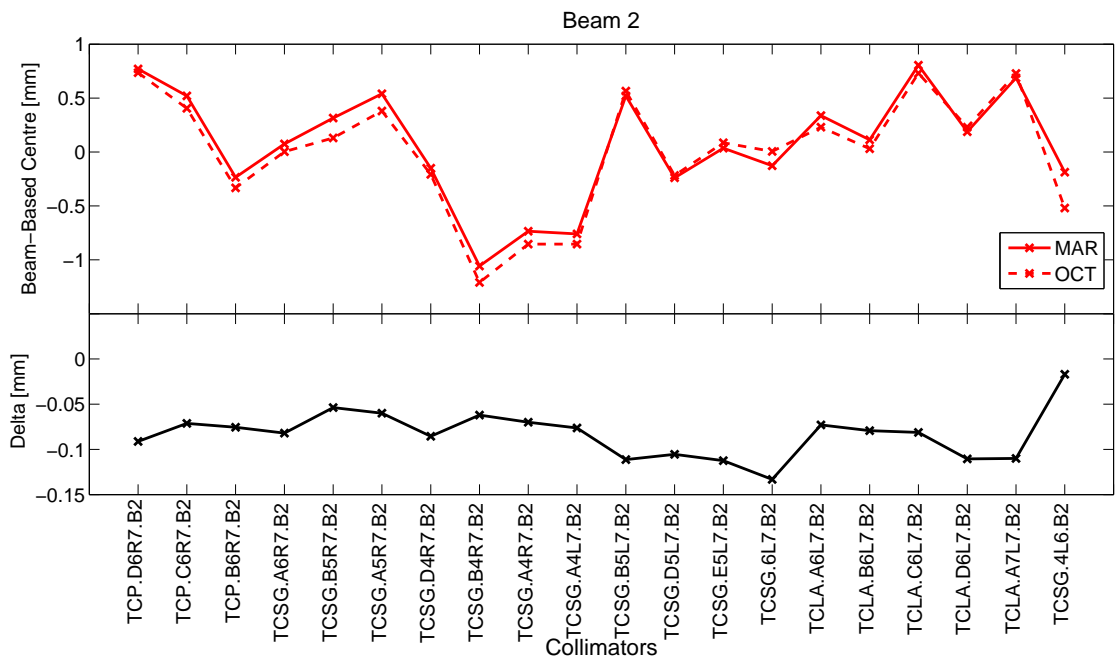
(b) Measured centres in mm (B2)

Figure 8.30: Comparison of measured beam centres in units of mm in IR7. The alignments were performed in March and October 2012.
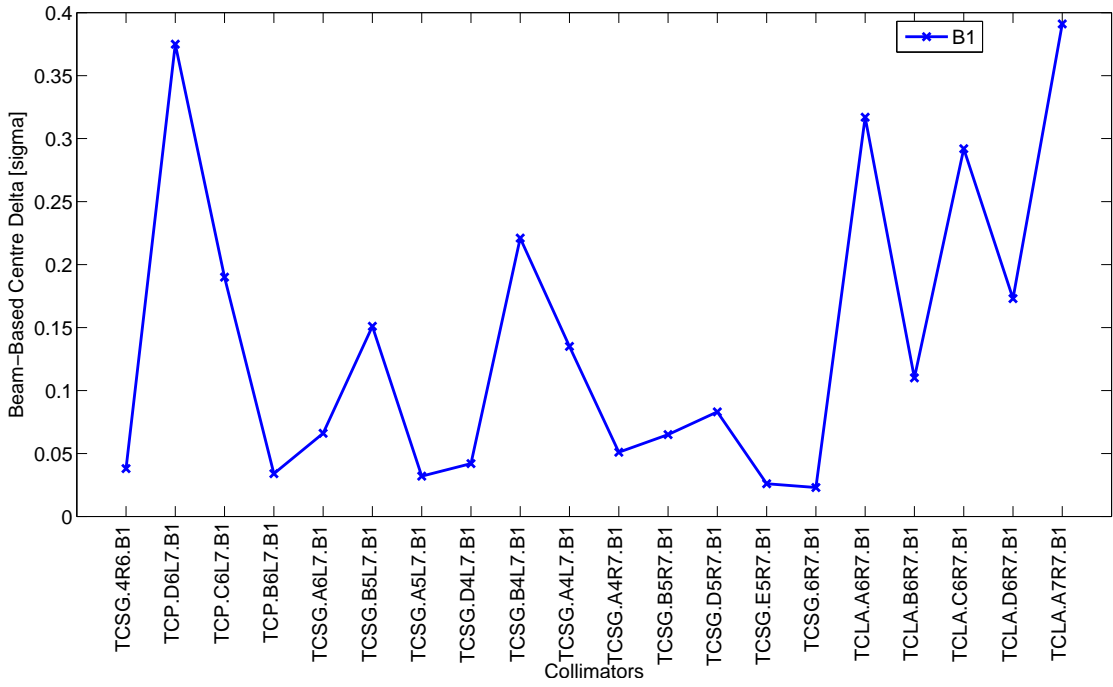
(a) Absolute difference of the measured centres in beam σ (B1)
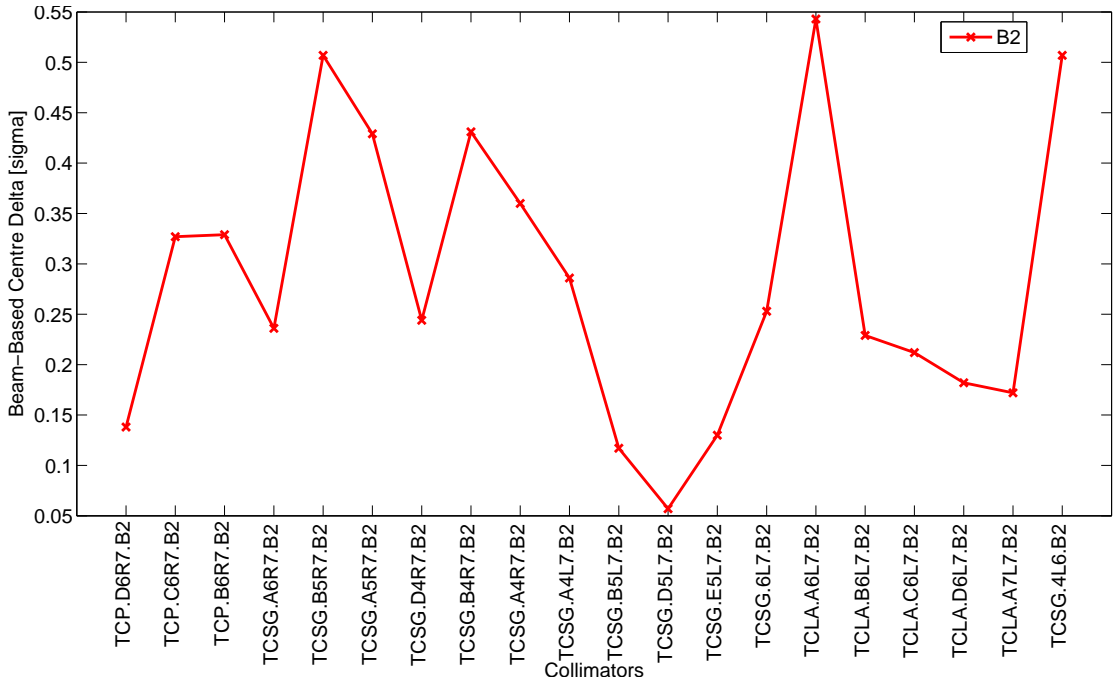
(b) Absolute difference of the measured centres in beam σ (B2)

Figure 8.31: Absolute difference of the measured beam centres in units of beam σ in IR7. The alignments were performed in March and October 2012.

8.2.8 Orbit stability at the TCPs

The horizontal and vertical primary collimators in IR7 are the collimators that are aligned most frequently during the year, being the reference collimators. The beam centres measured at the TCPs during all alignments held in the 2010-2012 period
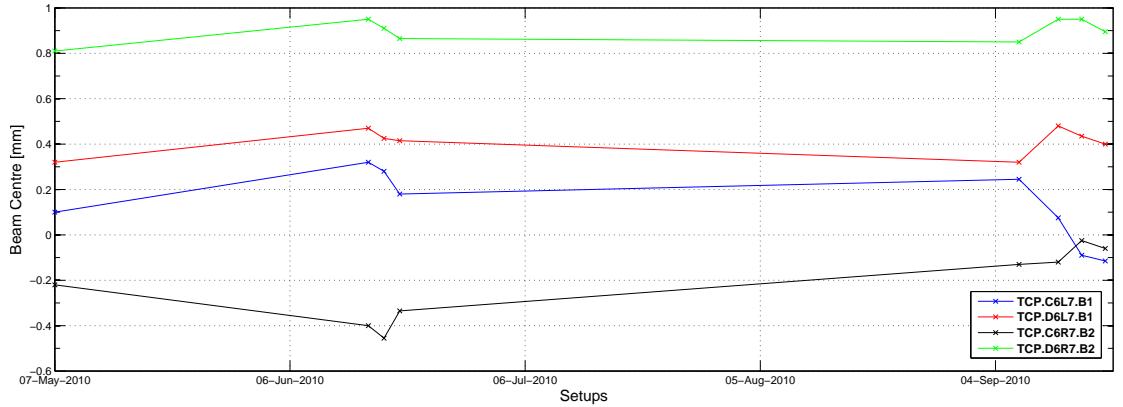
(a) 2010
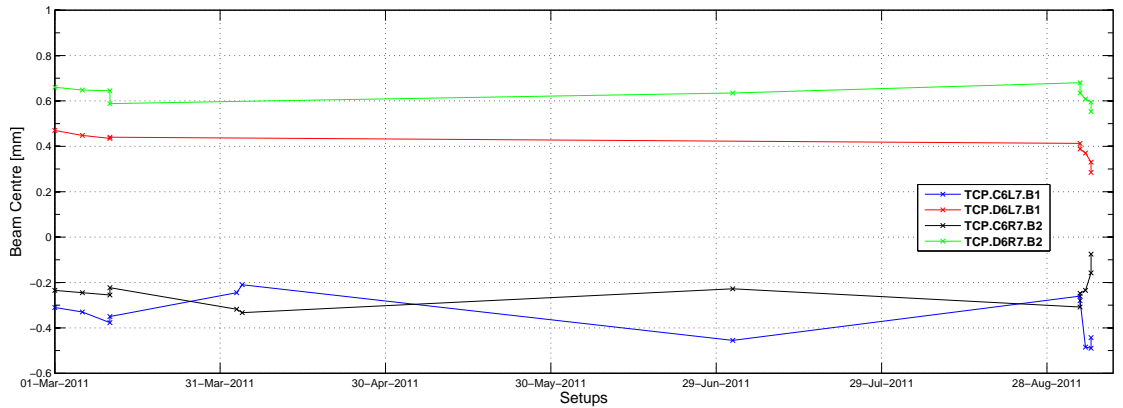
(b) 2011
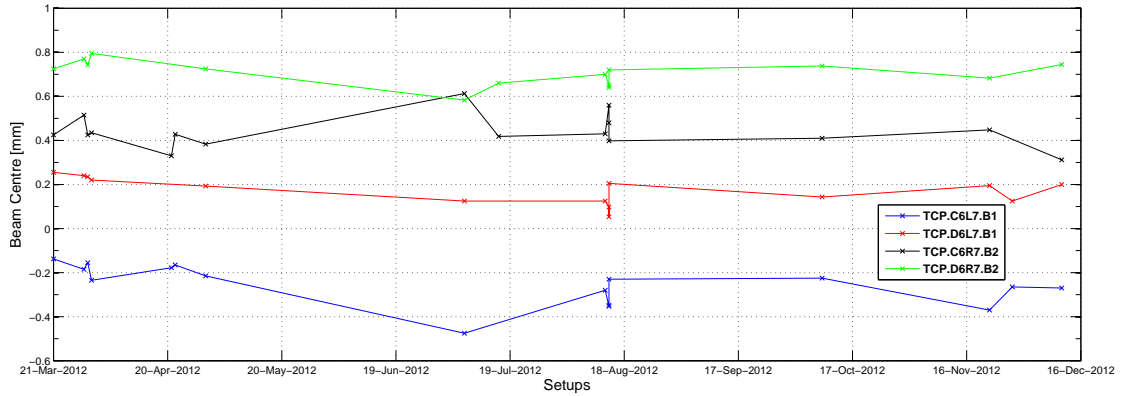
(c) 2012

Figure 8.32: Orbit stability at the TCPs during the 2010-2012 LHC runs [122].

are shown in Fig. 8.32. The beam orbit at the IR7 TCPs is not changed throughout the year, as is done for the orbit at the TCTs, and hence is expected to remain constant. Nevertheless, certain patterns are noticed in the data. For example, there appear to be correlated shifts in the measured centres in one plane or one beam. This could be the effect of systematic misalignments of the quadrupole magnets over time. The variations in the orbit are of the order of a few hundred micrometers, which can be attributed to various effects such as ground motion and the ambient temperature in the tunnel [62].

8.2.9 Orbit stability at the TCTs

The TCTs need to be re-aligned whenever the orbit or optics configurations at the experimental IPs are changed. Table 8.4 lists the configuration changes performed for the collisions beam process in the 2012 LHC run.

Table 8.4: Configuration changes performed for the collisions beam process in the 2012 run [122].

Date	Reason for Alignment	Crossing angle [μrad] in IP1V/2V/5H/8H/8V	Optics [m] in IP1/2/5/8
30/03/2012	Start of run	-145/-90/145/0/90	0.6/3.0/0.6/3.0
07/07/2012	$\beta^* = 90$m	0/-90/0/-220/0	90/10/90/10
16/07/2012	Van der Meer scans	0/-90/0/200/0	11/10/11/10
22/11/2012	Van der Meer scans	0/145/0/-220/0	11/10/11/10
11/12/2012	25 ns bunch spacing	-145/145/145/220/0	1/3/1/3

In this analysis, the BPM-interpolated orbit at the TCTs is extracted using the LHC Aperture Meter [87]. As the absolute interpolated orbit is poor at the TCT locations due to larger distances from the BPM locations [123], the change between the interpolated orbit at flat top (FT) and collisions (CO) were compared with the change in the measured orbit at the same operating points in the machine cycle. The comparison results are shown in Fig. 8.33 and Fig. 8.34, with separate plots for the TCTs in each IR.

As expected, the beam centres at the TCTs shown in Fig. 8.33a - 8.34b change as a function of the crossing angles in Table 8.4. For instance, van der Meer scans were performed on the 16/07/2012 and on the 22/11/2012. In between these dates, the IP2 vertical crossing angle was changed from -90 μrad to 145 μrad, while the IP8 horizontal crossing angle was changed from 200 μrad to -220 μrad. The beam centres measured on the 22/11/2012 at all TCTs, except the IP2 TCTVs and the IP8 TCTHs, remained the same as the values measured on the 16/07/2012 (within 100 μm).
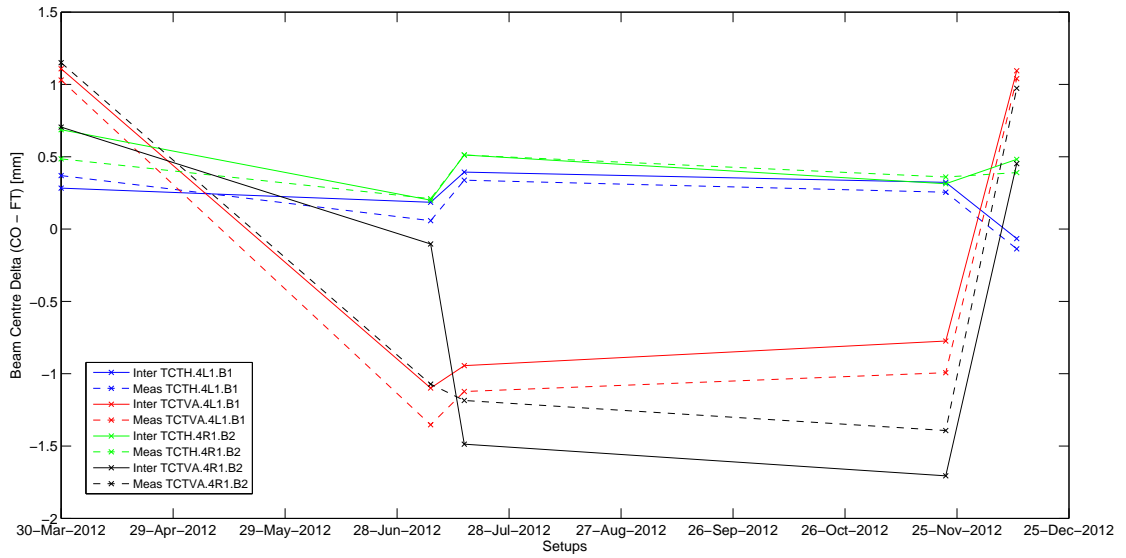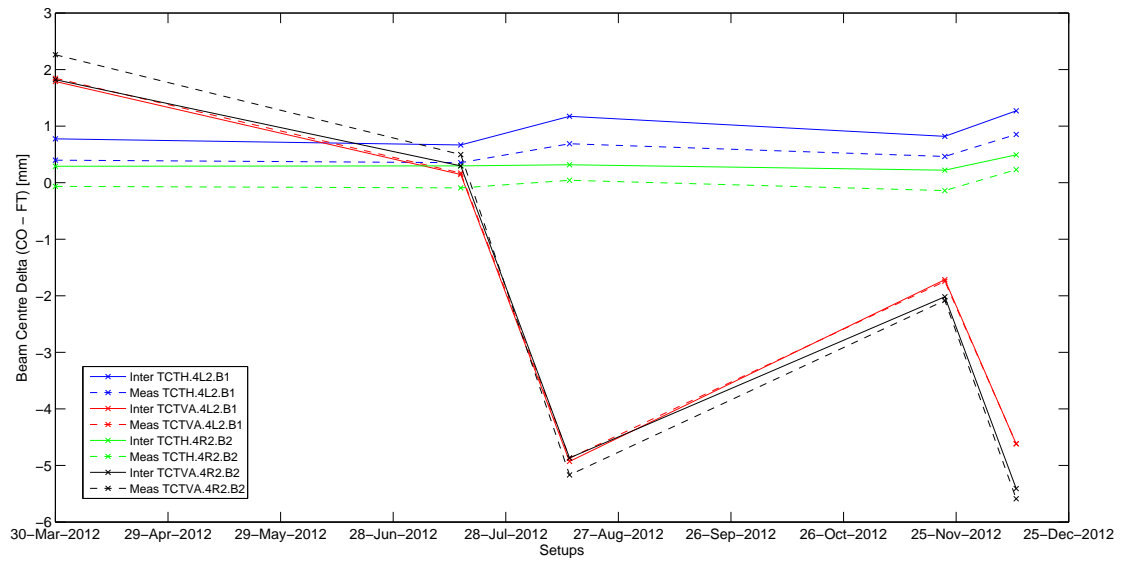
(a) TCT IR1

(b) TCT IR2

Figure 8.33: Orbit stability at the IR1 and IR2 TCTs during the 2012 LHC run.
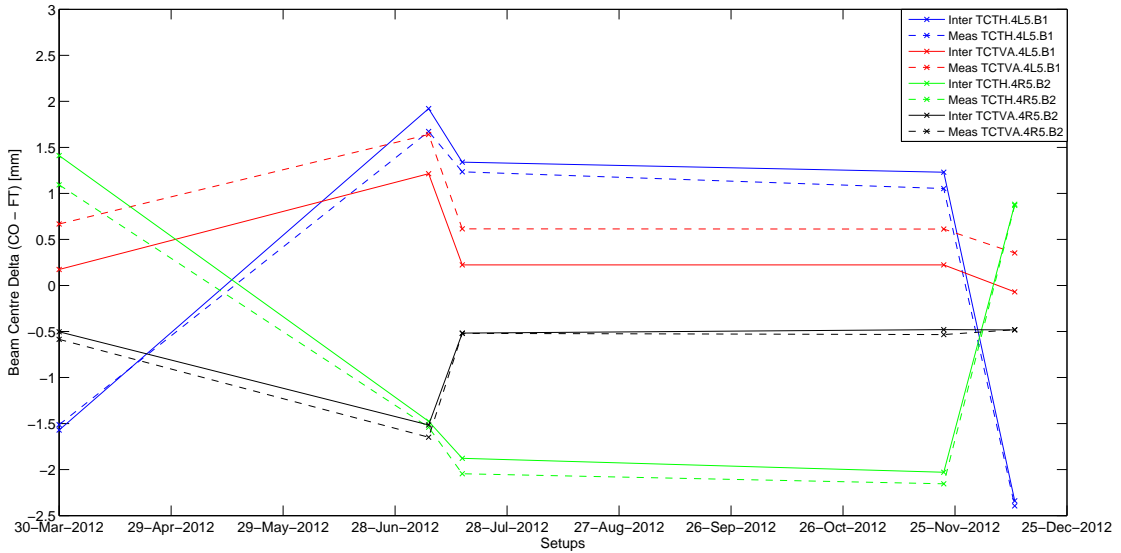
(a) TCT IR5
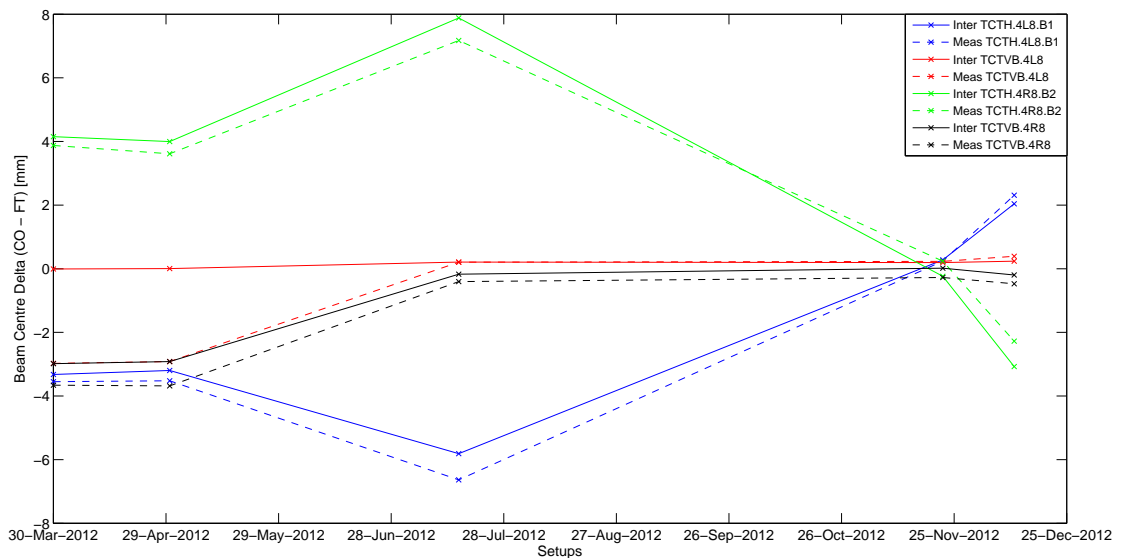
(b) TCT IR8

Figure 8.34: Orbit stability at the IR5 and IR8 TCTs during the 2012 LHC run [122].

8.2.10 Alignment performance overview

An overview of the collimator setup performance gain with automatic setup is illustrated in Fig. 8.35. The number of aligned collimators increased over the years due to frequent changes in the optics and crossing angles (see Fig. 8.35b). The 2013 run lasted for only 1 month, which explains the reduced number of alignments. The time used for setup decreased by over 40 hours, as shown in Fig. 8.35a. The reduction in the alignment time is one of the contributors to the increase in machine availability for physics production, which increased from 16% in 2010 to 36.5% in 2012 [124, 21]. Figure 8.35c indicates an improvement in

the accuracy of beam-based alignment by a factor 8, as well as in its safety (see Fig. 8.35d) as there were no beam dumps during alignment at top energy.

(a) Setup time

(b) Aligned collimators

(c) Setup accuracy

(d) Beam dumps
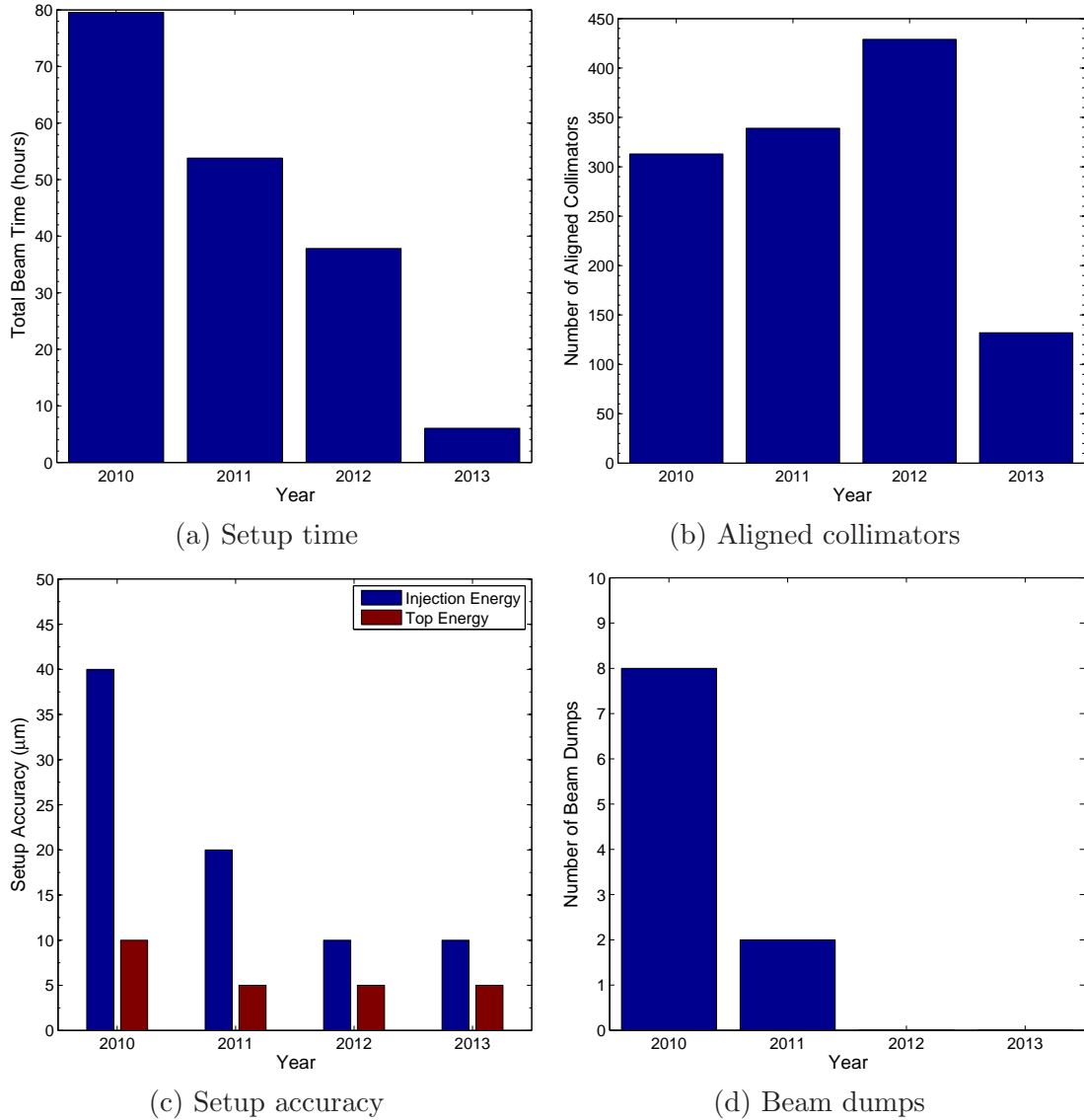
Figure 8.35: Summary of the performance gains with automatic alignment [122].

8.3 Comparison of simulation and measurement results

The measured and simulated alignment times agree within less than a factor of 2 for Policy 1 and 2, and approximately a factor 4 for Policy 3, as shown in Fig. 8.36. The measured data were taken from the alignments at top energy in March 2011, March 2012 and October 2012. Policy 4 is not included in the comparison as only simulation results exist. In practice, the alignment takes much

longer due to unforeseen beam instabilities, human checks, the momentum cut in IR3 and imperfect loss spikes. Nevertheless, the simulator provides a good means of validating the performance of future alignment algorithms without requiring beam, particularly in choosing which combination of alignment policies to be used for which subset of collimator which need to be aligned.

(a) Total alignment time

(b) Average alignment time
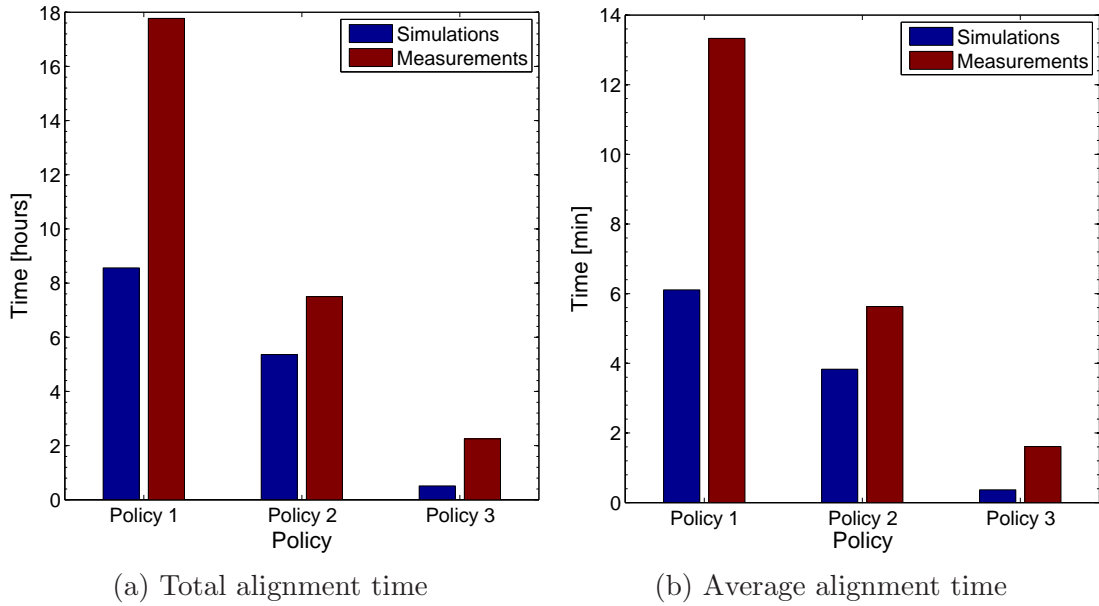
Figure 8.36: Comparison of simulated and measured alignment times for full alignments at top energy for each policy.

Chapter 9

Conclusion

9.1 Summary

With a nominal stored energy of 362 MJ and a beam momentum of 7 TeV/c, the LHC requires a beam collimation system which can operate at the highest level of cleaning efficiency, to enable operation at the design parameters. The number of collimators (86) in the LHC ring is almost an order of magnitude greater than in other accelerators such as the Tevatron, HERA and RHIC. Due to the lower beam energies, the collimation requirements in these colliders are much less stringent than at the LHC.

The performance of the LHC collimation system is highly dependent upon having the correct jaw positions throughout the machine cycle. Setting errors may cause violations in the collimation hierarchy, leading secondary collimators to intercept the primary beam halo, or inadequate protection of the beam dump and experimental regions.

Beam-based parameters, such as the beam centres and beam sizes at the collimator locations, are required as inputs to establish the jaw positions. The jaws need to be placed symmetrically around the beam centre, at the correct number of transverse beam standard deviations (σ) from the beam trajectory. These parameters are measured via beam-based collimator alignment, in which the jaws are moved in steps of a few micrometers until they touch the beam halo on either side. This occurs when a characteristic spike is observed in the signal of a BLM detector placed a few metres downstream from the collimator.

During the 2010 LHC run, before the commencement of the Ph.D. work, beam-based alignment was performed manually. In the CCC, operators used a Java application to move the jaws towards the beam, intervening for each jaw step that needed to be made. They needed to continuously examine the BLM signal and ensure that they stopped moving in the jaw before the losses exceeded the dump threshold and the beams were automatically removed from the LHC, resulting in several hours of downtime before the alignment could resume.

Once significant beam losses were observed, the operator would need to check whether the pattern was similar to the characteristic spike indicating a jaw alignment. If this was not the case, the jaw would need to be moved in further until the characteristic spike was observed. In addition, due to human constraints, the operators were restricted to moving at most two collimators simultaneously, one in each beam, and they were also required to input the measured values manually in a file and then decide which collimator to align next. This procedure took up to 30 hours to complete in 2010, which is a significant amount of beam time lost for the LHC physics programme.

Therefore, the objective of the thesis is to automate and speed up the beam-based alignment of the LHC collimators. An array of algorithms has been developed to achieve this aim. These algorithms were designed, tested and used in a phased manner during the 2011-2012 LHC runs. The implementation was done in Java in the existing top-level collimator control application.

The first step in 2011 was the introduction of a BLM-based feedback loop, that could allow for a single or parallelized movement of collimator jaws in steps towards the beam, until the losses exceeded a pre-defined stopping threshold. Initially, the threshold was set manually to gain experience with this semi-automatic algorithm. In 2012, a threshold selection algorithm was developed based on the numerous training data, therefore saving time and eliminating the possibility of operator mistakes by setting the threshold too high or too low.

Potential alignment errors introduced by premature stopping of the collimator jaws before the beam halo is reached were mitigated using a SVM-based loss spike classification algorithm. The algorithm classifies optimal spikes, displaying the typical sharp increase and decay, from non-optimal or noisy signal patterns when the stopping threshold is exceeded. A prediction accuracy of almost 90% was reached.

In addition, a tool was developed to centre the jaws from parking positions to a safe and tighter gap around the BPM-interpolated orbit at the collimator locations at the start of the alignment. This algorithm resulted in a gain of a factor 400, performing a task which would have required almost 30 minutes in a couple of seconds.

The alignment algorithms are an improvement over the state of the art at other colliders, which in the most complex case at HERA only employed a form of beam loss feedback loop. In the LHC, they have achieved the right balance between

obtaining optimal BLM signal spikes, ensuring that the losses remain below beam dump thresholds, and aligning collimators in the fastest time possible and with the greatest accuracy available (5 μm jaw step size).

The beam intensity loss during alignment is kept to a minimum, which from 2012 onwards ensured that all collimators were set up during a single fill. In addition, alignments can be performed for different stages of the machine cycle during the same fill. For example, the 16 TCTs are now set up with squeezed, separated beams, and then the beams are brought into collisions and the alignment is re-done to determine the new beam centres. This saves 2 - 4 hours which would have otherwise been required if the beams had to be dumped and re-injected after the first alignment.

The time for a full alignment of the whole collimation system has been reduced from 30 hours in the 2010 LHC run, to less than 4 hours in 2012 without triggering any beam dumps. This provided more flexibility for the operation team to perform more frequent changes to the machine configuration. More and more alignment campaigns were carried out over the years, despite the fact that the total time consumed by collimator alignment has decreased year after year. Normalizing the total alignment time to the number of collimators aligned in 2010 and 2012, the fast automated alignment is responsible for operational savings of €10.7 million per year, considering that the hourly LHC running cost is €150,000.

The collimation system hierarchy is qualified regularly to ensure that the collimators are at the right positions with respect to the beam. Qualification is performed by inducing slow (multi-turn) beam losses (betatron or momentum offsets) so that a large number of particles hit the collimators and the resulting showers are detected in the BLM detectors around the ring. Snapshots or beam loss maps can then be produced for the precise instant when the losses are maximal.

A beam centre measurement error of 700 μm occurred during an alignment of an IR7 collimator in January 2013. The spike recognition algorithm incorrectly classified a loss spike to be optimal, when in fact the loss signal was probably due to beam jitter or mechanical vibrations. The error was picked up in the ensuing loss map performed to qualify the newly-established beam-based parameters. Future errors related to spike detection might be avoided if the jaw is moved in further after an optimal spike is detected, and the jaw is considered to be aligned only if the second spike is also optimal.

In view of an eventual shift to a new collimator design, which envisages BPM pick-up buttons embedded inside the jaws of the 16 TCTs, a BPM-based algorithm was also developed and successfully validated with a mock-up collimator installed in the SPS. Alignment times of approximately 20 seconds were achieved at a safe distance from the beam, with an accuracy of 5 μm. Comparisons to the BLM-based alignment technique showed an agreement in the beam centre measurement of 150 μm. However, it is important to keep in mind that a jaw step size of 50 μm was required due to the larger beam size in the SPS, as well as that there is a design positioning tolerance of the BPM pick-up buttons with respect to the jaw surface of 50 μm. Online monitoring of the beam centres during physics fills could help in reducing the β^* reach by about 15%, due to reduced orbit tolerance requirements. Nevertheless, machine protection studies are still necessary to ensure that no additional risks are introduced.

The Java application user interface was upgraded to accommodate the new algorithms. All software was designed and implemented using the Agile software development methodology, which was well-suited to the context of LHC operation. One can now acquire jaw positions and BLM data for as many collimators as required. A faster BLM data rate of 12.5 Hz was provided through a collaboration with the beam instrumentation team, which enabled the maximum jaw movement rate of 8 Hz. However, the bottleneck in terms of alignment time is the waiting period enforced by the spike decay after a jaw touches the beam, which can last up to 15 or 20 seconds.

For an alignment of all 86 collimators, with a re-alignment of the reference collimator each time, this translates into a minimum alignment time of around 1.5 hours. On the other hand, the difference between moving a jaw by 6 mm at 1 Hz and 8 Hz is around 15 minutes. The 12.5 Hz BLM data and the 10 Hz BPM data are acquired using similar software architectures. The BLM data is transmitted via UDP packets to a server, which swallows or forwards the packets to a data logging machine and the software application running in the CCC. The BPM data is also acquired via UDP packets, from the electronics box in the SPS tunnel.

A fixed display was developed to provide an overview of the status of the LHC collimation system at all times during operation and during collimator alignment. The displayed parameters include the jaw positions, MDC and PRS statuses, and also an indication of the last time when the collimator settings were qualified via beam loss maps. The display is shown overhead in the CCC for the benefit of the LHC operators, and is also available online for the general public.

A model of the beam losses that occur during collimator alignment was developed. Two empirical analyses were performed, one assuming a static Gaussian distribution of the beam, and the other considering transverse beam halo diffusion. Both analyses rely on collimator scraping measurements in the LHC. The diffusion rates were measured for the first time in the LHC by observing the response of the beam loss rates to small inward or outward collimator steps, and the results provided experimental information on the relationship between halo population and halo dynamics, emittance growth, beam lifetime and collimation efficiency.

The beam diffusion model and empirical models of the BLM signal crosstalk and steady-state BLM signal were combined into a simulator, which can allow the testing of current and future alignment algorithms without requiring dedicated LHC beam time. Simulations were carried out for different beam energies, initial jaw positions, subgroups of collimators, and using different subsets of alignment algorithms (policies). The simulated and measured alignment times agree within a factor 2 for Policy 1 (sequential alignment) and Policy 2 (sequential and parallel alignment), and within a factor 4 for Policy 3 (coarse BPM-interpolation guided alignment followed by parallel and sequential alignment).

The parameters used to measure the LHC collimator setup accuracy and performance, such as the measured-to-nominal beam size ratio and the stability of settings over months of operation have been defined. The effect of jaw angular misalignment errors on the beam size measurement was observed, with the correction of a 1.6 mrad collimator tank misalignment in the tunnel leading to more reasonable beam size ratio values. The results also show that the automatic alignment maintains the same collimator setup quality obtained with the slower manual method.

The work described in this dissertation was adopted by CERN for the first LHC running period (2008 - 2013). It will continue to be used in future operation post-2015 after a two-year shutdown, in which the machine will be upgraded to be able to operate at the design parameters.

9.2   Suggestions for further work

In view of the envisaged LHC re-start in 2015, a few suggestions for further work are provided. Future errors related to spike detection might be avoided if the jaw is moved in further after an optimal spike is detected, and the jaw is considered to

be aligned only if the second spike is also optimal. The algorithm logic could be moved from the application to a server level, thereby reducing the processing load at the user end. The Java remote method invocation application programming interface could be used in an eventual implementation. The beam-based settings determined during the alignment could be stored directly in LSA database tables, rather than locally on disk. This would make it easier to import the measured settings directly into the beam processes.

Due to reduced error tolerances at higher beam energies, one could consider a possible BLM-based individual jaw corner alignment algorithm, which has already been achieved with the BPM-based technique in the SPS. Finally, the BPM-based alignment algorithm itself will need to be commissioned with LHC beam in preparation for operation in 2015, to determine a new set of calibration and non-linearity coefficients that need to be applied. The measured beam centres could be transmitted to the LHC beam orbit feedback system, and interlocks could be placed on the measurements to dump the beam if abnormally large orbit shifts are detected.

A. Collimator Database

Table A.1: LHC B1 collimator database. The collimators are ordered in the same sequence as used during the alignments (H = horizontal, V = vertical, S = skew).

Name	Angle [rad]	Plane	Position [m]	Material	Length [m]
TCSG.4R6.B1	0.00	H	16815.98	CFC	1.0
TCDQA.B4R6.B1	0.00	H	16812.07	CFC	6.6
TCL.5R5.B1	0.00	H	13513.55	Cu	1.0
TCTH.4L5.B1	0.00	H	13181.77	W	1.0
TCLA.7R3.B1	0.00	H	6915.18	W	1.0
TCLA.6R3.B1	0.00	H	6843.77	W	1.0
TCLA.B5R3.B1	0.00	H	6757.22	W	1.0
TCSG.B5R3.B1	0.20	H	6724.74	CFC	1.0
TCSG.A5R3.B1	2.98	H	6718.92	CFC	1.0
TCSG.4R3.B1	0.00	H	6707.53	CFC	1.0
TCSG.5L3.B1	0.00	H	6521.04	CFC	1.0
TCP.6L3.B1	0.00	H	6487.67	CFC	0.6
TCTH.4L2.B1	0.00	H	3214.49	CFC	1.0
TCL.5R1.B1	0.00	H	184.36	Cu	1.0
TCTH.4L1.B1	0.00	H	26511.36	W	1.0
TCTH.4L8.B1	0.00	H	23197.43	W	1.0
TCLA.A7R7.B1	0.00	H	20231.86	W	1.0
TCLA.D6R7.B1	0.00	H	20214.51	W	1.0
TCLA.B6R7.B1	0.00	H	20178.96	W	1.0
TCSG.6R7.B1	0.01	H	20141.02	CFC	1.0
TCSG.B4L7.B1	0.00	H	19987.16	CFC	1.0
TCP.C6L7.B1	0.00	H	19791.18	CFC	0.6
TCTVA.4L5.B1	1.57	V	13183.45	W	1.0
TCLA.A5R3.B1	1.57	V	6755.22	W	1.0
TCLIB.6R2.B1	1.57	V	3560.09	CFC	1.0
TCLIA.4R2	1.57	V	3408.18	CFC	1.0
TCTVA.4L2.B1	1.57	V	3258.95	W	1.0
TDI.4L2	1.57	V	3251.60	CFC	4.2
TCTVA.4L1.B1	1.57	V	26513.04	W	1.0
TCTVB.4L8	1.57	V	23241.89	W	1.0
TCLA.C6R7.B1	1.57	V	20212.51	W	1.0
TCLA.A6R7.B1	1.57	V	20148.09	W	1.0
TCSG.D4L7.B1	1.57	V	19917.24	CFC	1.0
TCP.D6L7.B1	1.57	V	19789.18	CFC	0.6
TCSG.E5R7.B1	2.28	S	20106.42	CFC	1.0
TCSG.D5R7.B1	0.90	S	20102.42	CFC	1.0
TCSG.B5R7.B1	2.47	S	20086.42	CFC	1.0
TCSG.A4R7.B1	0.81	S	19995.16	CFC	1.0
TCSG.A4L7.B1	2.35	S	19991.16	CFC	1.0
TCSG.A5L7.B1	0.71	S	19895.91	CFC	1.0
TCSG.B5L7.B1	2.50	S	19891.91	CFC	1.0
TCSG.A6L7.B1	2.46	S	19832.68	CFC	1.0
TCP.B6L7.B1	2.22	S	19793.18	CFC	0.6

Table A.2: LHC B2 collimator database. The collimators are ordered in the same sequence as used during the alignments (H = horizontal, V = vertical, S = skew).

Name	Angle [rad]	Plane	Position [m]	Material	Length [m]
TCTH.4R8.B2	0.00	H	46.96	W	1.0
TCL.5L1.B2	0.00	H	142.46	Cu	1.0
TCSG.6L7.B2	0.01	H	336.01	CFC	1.0
TCTH.4R1.B2	0.00	H	160.00	W	1.0
TCTH.4R2.B2	0.00	H	47.10	W	1.0
TCLA.7L3.B2	0.00	H	65.97	W	1.0
TCLA.6L3.B2	0.00	H	129.56	W	1.0
TCLA.B5L3.B2	0.00	H	151.80	W	1.0
TCSG.B5L3.B2	0.19	H	45.57	CFC	1.0
TCSG.A5L3.B2	2.98	H	35.89	CFC	1.0
TCSG.4L3.B2	0.00	H	26.20	CFC	1.0
TCSG.5R3.B2	0.00	H	54.68	CFC	1.0
TCP.6R3.B2	0.00	H	131.63	CFC	0.6
TCL.5L5.B2	0.00	H	142.37	Cu	1.0
TCTH.4R5.B2	0.00	H	160.57	W	1.0
TCSG.4L6.B2	0.00	H	523.02	CFC	1.0
TCDQA.B4L6.B2	0.00	H	510.46	CFC	6.6
TCLA.A7L7.B2	0.00	H	68.86	W	1.0
TCLA.D6L7.B2	0.00	H	65.13	W	1.0
TCLA.B6L7.B2	0.00	H	159.66	W	1.0
TCSG.B4R7.B2	0.00	H	151.47	CFC	1.0
TCP.C6R7.B2	0.00	H	150.36	CFC	0.6
TCLIB.6L8.B2	1.57	V	158.69	CFC	1.0
TCLIA.4L8	1.57	V	49.51	CFC	1.0
TCTVB.4R8	1.57	V	128.10	W	1.0
TDI.4R8.B2	1.57	V	108.75	CFC	4.2
TCTVA.4R1.B2	1.57	V	157.53	W	1.0
TCTVA.4R2.B2	1.57	V	48.29	W	1.0
TCLA.A5L3.B2	1.57	V	142.70	W	1.0
TCTVA.4R5.B2	1.57	V	158.10	W	1.0
TCLA.C6L7.B2	1.57	V	68.70	W	1.0
TCLA.A6L7.B2	1.57	V	297.30	W	1.0
TCSG.D4R7.B2	1.57	V	333.01	CFC	1.0
TCP.D6R7.B2	1.57	S	158.69	CFC	0.6
TCSG.E5L7.B2	2.28	S	241.53	CFC	1.0
TCSG.D5L7.B2	0.90	S	213.98	CFC	1.0
TCSG.B5L7.B2	2.47	S	121.88	CFC	1.0
TCSG.A4L7.B2	0.73	S	99.51	CFC	1.0
TCSG.A4R7.B2	2.31	S	139.68	CFC	1.0
TCSG.A5R7.B2	0.71	S	186.05	CFC	1.0
TCSG.B5R7.B2	2.51	S	160.07	CFC	1.0
TCSG.A6R7.B2	2.47	S	39.88	CFC	1.0
TCP.B6R7.B2	2.23	S	142.30	CFC	0.6

B. Collimator BLM Detector List

Table B.1: LHC B1 collimator BLM detector database.

BLM Name	Position [m]	Associated Collimator
BLMEI.05R1.B1E10_TCL.5R1.B1	185.6	TCL.5R1.B1
BLMEI.04L2.B1E10_TCTH.4L2.B1	3214.83	TCTH.4L2.B1
BLMEI.04L2.B1E10_TDI.4L2.B1	3248.33	TDI.4L2
BLMEI.04L2.B1E10_TCTVA.4L2.B1	3216.83	TCTVA.4L2.B1
BLMEI.06R2.B1I10_TCLIB.6R2.B1	3561.25	TCLIB.6R2.B1
BLMEI.06L3.B1I10_TCP.6L3.B1	6488.67	TCP.6L3.B1
BLMEI.05L3.B1I10_TCSG.5L3.B1	6521.99	TCSG.5L3.B1
BLMEI.04R3.B1I10_TCSG.4R3.B1	6708.58	TCSG.4R3.B1
BLMEI.05R3.B1I10_TCSG.A5R3.B1	6719.92	TCSG.A5R3.B1
BLMEI.05R3.B1I10_TCSG.B5R3.B1	6725.74	TCSG.B5R3.B1
BLMEI.05R3.B1I10_TCLA.A5R3.B1	6756.22	TCLA.A5R3.B1
BLMEI.05R3.B1I10_TCLA.B5R3.B1	6758.22	TCLA.B5R3.B1
BLMEI.06R3.B1I10_TCLA.6R3.B1	6844.77	TCLA.6R3.B1
BLMEI.07R3.B1I10_TCLA.7R3.B1	6916.18	TCLA.7R3.B1
BLMEI.04L5.B1I10_TCTH.4L5.B1	13182.76	TCTH.4L5.B1
BLMEI.04L5.B1I10_TCTVA.4L5.B1	13184.85	TCTVA.4L5.B1
BLMEI.05R5.B1E10_TCL.5R5.B1	13515.12	TCL.5R5.B1
BLMEI.04R6.B1E10_TCDQA.A4R6.B1	16808.06	TCDQA.A4R6.B1
BLMEI.04R6.B1E10_TCSG.4R6.B1	16817.86	TCSG.4R6.B1
BLMEI.06L7.B1E10_TCP.D6L7.B1	19790.18	TCP.D6L7.B1
BLMEI.06L7.B1E10_TCP.C6L7.B1	19792.18	TCP.C6L7.B1
BLMEI.06L7.B1E10_TCP.B6L7.B1	19794.18	TCP.B6L7.B1
BLMEI.06L7.B1E10_TCSG.A6L7.B1	19833.68	TCSG.A6L7.B1
BLMEI.05L7.B1E10_TCSG.B5L7.B1	19892.91	TCSG.B5L7.B1
BLMEI.05L7.B1E10_TCSG.A5L7.B1	19896.91	TCSG.A5L7.B1
BLMEI.04L7.B1E10_TCSG.D4L7.B1	19918.24	TCSG.D4L7.B1
BLMEI.04L7.B1E10_TCSG.B4L7.B1	19988.16	TCSG.B4L7.B1
BLMEI.04L7.B1E10_TCSG.A4L7.B1	19992.16	TCSG.A4L7.B1
BLMEI.04R7.B1E10_TCSG.A4R7.B1	19996.16	TCSG.A4R7.B1
BLMEI.05R7.B1E10_TCSG.B5R7.B1	20087.42	TCSG.B5R7.B1
BLMEI.05R7.B1E10_TCSG.D5R7.B1	20103.42	TCSG.D5R7.B1
BLMEI.05R7.B1E10_TCSG.E5R7.B1	20107.42	TCSG.E5R7.B1
BLMEI.06R7.B1E10_TCSG.6R7.B1	20142.02	TCSG.6R7.B1
BLMEI.06R7.B1E10_TCLA.A6R7.B1	20149.09	TCLA.A6R7.B1
BLMEI.06R7.B1E10_TCLA.B6R7.B1	20179.96	TCLA.B6R7.B1
BLMEI.06R7.B1E10_TCLA.C6R7.B1	20213.23	TCLA.C6R7.B1
BLMEI.06R7.B1E10_TCLA.D6R7.B1	20215.23	TCLA.D6R7.B1
BLMEI.07R7.B1E10_TCLA.A7R7.B1	20232.86	TCLA.A7R7.B1
BLMEI.04L8.B1E10_TCTH.4L8.B1	23198.83	TCTH.4L8.B1
BLMEI.04L8.B2I10_TCLIA.4L8	23238.05	TCLIA.4L8
BLMEI.04L8.B1E10_TCTVB.4L8	23242.79	TCTVB.4L8
BLMEI.04L1.B1I10_TCTH.4L1.B1	26512.22	TCTH.4L1.B1
BLMEI.04L1.B1I10_TCTVA.4L1.B1	26514.29	TCTVA.4L1.B1

Table B.2: LHC B2 collimator BLM detector database.

BLM Name	Position [m]	Associated Collimator
BLMEI.04R1.B2I10_TCTVA.4R1.B2	144.62	TCTVA.4R1.B2
BLMEI.04R1.B2I10_TCTH.4R1.B2	146.78	TCTH.4R1.B2
BLMEI.04R2.B2E10_TCTVA.4R2.B2	3447.41	TCTVA.4R2.B2
BLMEI.04R2.B1I10_TCLIA.4R2	3406.95	TCLIA.4R2
BLMEI.04R2.B2E10_TCTH.4R2.B2	3449.75	TCTH.4R2.B2
BLMEI.07L3.B2E10_TCLA.7L3.B2	6413.27	TCLA.7L3.B2
BLMEI.06L3.B2E10_TCLA.6L3.B2	6484.67	TCLA.6L3.B2
BLMEI.05L3.B2E10_TCLA.B5L3.B2	6571.22	TCLA.B5L3.B2
BLMEI.05L3.B2E10_TCLA.A5L3.B2	6573.22	TCLA.A5L3.B2
BLMEI.05L3.B2E10_TCSG.B5L3.B2	6603.7	TCSG.B5L3.B2
BLMEI.05L3.B2E10_TCSG.A5L3.B2	6609.52	TCSG.A5L3.B2
BLMEI.04L3.B2E10_TCSG.4L3.B2	6620.87	TCSG.4L3.B2
BLMEI.05R3.B2E10_TCSG.5R3.B2	6807.45	TCSG.5R3.B2
BLMEI.06R3.B2E10_TCP.6R3.B2	6840.77	TCP.6R3.B2
BLMEI.05L5.B2E10_TCL.5L5.B2	13143.67	TCL.5L5.B2
BLMEI.04R5.B2I10_TCTVA.4R5.B2	13474.04	TCTVA.4R5.B2
BLMEI.04R5.B2I10_TCTH.4R5.B2	13476.12	TCTH.4R5.B2
BLMEI.04L6.B2I10_TCSG.4L6.B2	16505.55	TCSG.4L6.B2
BLMEI.04L6.B2I10_TCDQA.A4L6.B2	16512.49	TCDQA.A4L6.B2
BLMEI.07L7.B2I10_TCLA.A7L7.B2	19755.46	TCLA.A7L7.B2
BLMEI.06L7.B2I10_TCLA.D6L7.B2	19773.09	TCLA.D6L7.B2
BLMEI.06L7.B2I10_TCLA.C6L7.B2	19775.09	TCLA.C6L7.B2
BLMEI.06L7.B2I10_TCLA.B6L7.B2	19808.36	TCLA.B6L7.B2
BLMEI.06L7.B2I10_TCLA.A6L7.B2	19839.24	TCLA.A6L7.B2
BLMEI.06L7.B2I10_TCSG.6L7.B2	19846.3	TCSG.6L7.B2
BLMEI.05L7.B2I10_TCSG.E5L7.B2	19880.91	TCSG.E5L7.B2
BLMEI.05L7.B2I10_TCSG.D5L7.B2	19884.91	TCSG.D5L7.B2
BLMEI.05L7.B2I10_TCSG.B5L7.B2	19900.91	TCSG.B5L7.B2
BLMEI.04L7.B2I10_TCSG.A4L7.B2	19984.16	TCSG.A4L7.B2
BLMEI.04R7.B2I10_TCSG.A4R7.B2	20000.16	TCSG.A4R7.B2
BLMEI.04R7.B2I10_TCSG.B4R7.B2	20004.16	TCSG.B4R7.B2
BLMEI.04R7.B2I10_TCSG.D4R7.B2	20070.09	TCSG.D4R7.B2
BLMEI.05R7.B2I10_TCSG.A5R7.B2	20091.42	TCSG.A5R7.B2
BLMEI.05R7.B2I10_TCSG.B5R7.B2	20095.42	TCSG.B5R7.B2
BLMEI.06R7.B2I20_TCSG.A6R7.B2	20154.65	TCSG.A6R7.B2
BLMEI.06R7.B2I10_TCP.B6R7.B2	20194.14	TCP.B6R7.B2
BLMEI.06R7.B2I10_TCP.C6R7.B2	20196.14	TCP.C6R7.B2
BLMEI.06R7.B2I10_TCP.D6R7.B2	20198.14	TCP.D6R7.B2
BLMEI.06L8.B2I10_TCLIB.6L8.B2	23096.86	TCLIB.6L8.B2
BLMEI.04R8.B2E10_TCTVB.4R8	23387.93	TCTVB.4R8
BLMEI.04R8.B2E20_TDI.4R8.B2	23392.94	TDI.4R8
BLMEI.04R8.B2E10_TCTH.4R8.B2	23431.79	TCTH.4R8.B2
BLMEI.05L1.B2E10_TCL.5L1.B2	26473.15	TCL.5L1.B2

C. Alignment Measurements

Table C.1: Measurements from an alignment of the LHC B1 collimators (injection optics derived from version 6.503, $E = 450$ GeV). The alignment was performed on the 22.03.2012.

Name	β_x [m]	β_y [m]	σ_n [mm]	σ_m [mm]	Δx [mm]	$x^{L,set}$ [mm]	$x^{R,set}$ [mm]
TCSG.4R6.B1	518.86	174.68	1.950	1.793	0.110	12.663	-12.443
TCDQA.B4R6.B1	506.40	169.73	1.920	1.716	1.592	15.320	N/A
TCL.5R5.B1	144.38	132.93	1.030	1.039	-0.060	24.940	-25.060
TCTH.4L5.B1	160.46	79.47	1.080	1.105	-3.620	10.740	-17.980
TCLA.7R3.B1	66.33	96.17	0.696	0.757	0.015	7.590	-7.560
TCLA.6R3.B1	129.44	168.92	0.972	1.041	0.013	10.420	-10.395
TCLA.B5R3.B1	151.74	168.65	1.050	1.194	-0.440	11.500	-12.380
TCSG.B5R3.B1	45.59	312.50	0.639	0.762	-0.428	6.660	-7.515
TCSG.A5R3.B1	35.91	343.90	0.565	0.756	-0.448	6.585	-7.480
TCSG.4R3.B1	26.23	394.93	0.437	0.467	-1.168	3.175	-5.510
TCSG.5L3.B1	54.65	298.44	0.632	0.658	-0.410	5.705	-6.525
TCP.6L3.B1	131.68	144.66	0.980	1.103	0.413	9.240	-8.415
TCTH.4L2.B1	47.05	48.29	0.586	0.687	-1.013	7.920	-9.945
TCL.5R1.B1	144.81	132.37	1.030	0.993	0.308	25.310	-24.690
TCTH.4L1.B1	160.63	79.58	1.080	1.080	-0.255	13.780	-14.290
TCTH.4L8.B1	46.93	48.36	0.585	0.623	2.535	10.635	-5.565
TCLA.A7R7.B1	63.97	148.15	0.683	0.649	-0.525	5.970	-7.020
TCLA.D6R7.B1	65.05	157.80	0.689	0.625	-0.420	5.830	-6.670
TCLA.B6R7.B1	159.43	76.35	1.080	1.078	-0.345	10.435	-11.125
TCSG.6R7.B1	335.56	47.38	1.560	1.533	-0.190	10.085	-10.465
TCSG.B4L7.B1	139.84	131.04	1.010	1.026	0.873	7.750	-6.000
TCP.C6L7.B1	150.46	82.75	1.050	1.050	-0.098	5.875	-6.070
TCTVA.4L5.B1	157.98	79.64	0.762	0.813	-0.545	10.030	-11.120
TCLA.A5R3.B1	142.65	175.97	1.130	1.237	-0.458	11.910	-12.825
TCLIB.6R2.B1	261.19	37.34	0.522	0.588	0.575	4.575	-3.425
TCLIA.4R2	49.67	122.06	0.944	1.014	-6.830	0.065	-13.725
TCTVA.4L2.B1	48.29	46.49	0.582	0.631	1.970	10.175	-6.235
TDI.4L2	109.18	44.58	0.570	1.139	3.858	11.605	-3.890
TCTVA.4L1.B1	158.14	79.76	0.763	0.798	2.035	12.410	-8.340
TCTVB.4L8	128.17	52.45	0.619	0.680	-0.425	8.420	-9.270
TCLA.C6R7.B1	68.62	151.78	1.050	1.174	1.373	13.110	-10.365
TCLA.A6R7.B1	296.90	48.17	0.593	0.653	0.305	6.835	-6.225
TCSG.D4L7.B1	333.17	68.81	0.709	0.768	0.015	5.165	-5.135
TCP.D6L7.B1	158.80	78.26	0.756	0.756	0.235	4.540	-4.070
TCSG.E5R7.B1	241.24	136.20	1.150	1.104	-0.055	7.345	-7.455
TCSG.D5R7.B1	213.73	158.65	1.150	1.209	-0.155	7.945	-8.255
TCSG.B5R7.B1	121.76	267.74	1.140	1.259	0.315	8.750	-8.120
TCSG.A4R7.B1	118.35	152.28	0.997	1.058	0.848	7.935	-6.240
TCSG.A4L7.B1	128.75	141.34	0.993	1.011	0.820	7.595	-5.955
TCSG.A5L7.B1	186.10	145.83	1.110	1.084	-0.067	7.195	-7.330
TCSG.B5L7.B1	160.10	166.40	1.090	1.065	-0.388	6.750	-7.525
TCSG.A6L7.B1	39.84	226.81	0.910	0.919	-0.090	6.065	-6.245
TCP.B6L7.B1	142.40	87.47	0.885	0.885	-0.343	4.700	-5.385

Table C.2: Measurements from an alignment of the LHC B2 collimators (injection optics derived from version 6.503, $E = 450$ GeV). The alignment was performed on the 22.03.2012.

Name	β_x [m]	β_y [m]	σ_n [mm]	σ_m [mm]	Δx [mm]	$x^{L,set}$ [mm]	$x^{R,set}$ [mm]
TCTH.4R8.B2	46.96	48.35	0.585	0.650	-3.580	4.865	-12.025
TCL.5L1.B2	142.46	136.29	1.020	1.018	1.270	26.270	-23.730
TCSG.6L7.B2	336.01	47.37	1.570	1.463	-0.200	9.603	-10.003
TCTH.4R1.B2	160.00	79.45	1.080	1.121	-1.285	13.285	-15.855
TCTH.4R2.B2	47.10	48.32	0.586	0.608	-1.860	6.050	-9.770
TCLA.7L3.B2	65.97	98.22	0.694	0.928	-0.100	9.185	-9.385
TCLA.6L3.B2	129.56	168.89	0.972	1.132	-0.410	10.915	-11.735
TCLA.B5L3.B2	151.80	168.74	1.050	1.523	-1.170	14.065	-16.405
TCSG.B5L3.B2	45.57	312.66	0.633	0.896	-0.310	8.025	-8.645
TCSG.A5L3.B2	35.89	344.08	0.565	0.787	-0.400	6.920	-7.720
TCSG.4L3.B2	26.20	395.13	0.437	0.518	-0.280	4.540	5.100
TCSG.5R3.B2	54.68	298.33	0.632	0.737	-0.525	6.335	-7.385
TCP.6R3.B2	131.63	144.59	0.980	1.345	-0.155	10.605	-10.915
TCL.5L5.B2	142.37	135.73	1.020	1.299	-0.420	24.580	-25.420
TCTH.4R5.B2	160.57	79.58	1.080	1.049	1.140	14.780	-12.500
TCSG.4L6.B2	523.02	173.82	1.950	1.842	-0.185	12.710	-13.080
TCDQA.B4L6.B2	510.46	169.42	1.930	1.944	-1.010	14.540	N/A
TCLA.A7L7.B2	68.86	136.17	0.709	0.769	0.590	8.280	-7.100
TCLA.D6L7.B2	65.13	157.85	0.689	0.645	0.055	6.500	-6.390
TCLA.B6L7.B2	159.66	76.37	1.080	1.011	-0.045	10.065	-10.155
TCSG.B4R7.B2	151.47	121.34	1.050	0.999	-1.200	5.490	-7.890
TCP.C6R7.B2	150.36	82.75	1.050	1.050	0.360	6.330	-5.610
TCLIB.6L8.B2	158.69	78.26	0.756	0.415	-0.385	2.435	-3.205
TCLIA.4L8	49.51	122.01	0.944	0.985	0.000	6.700	-6.700
TCTVB.4R8	128.10	52.45	0.619	0.675	0.930	9.700	-7.840
TDI.4R8	108.75	44.62	0.571	1.144	2.275	10.055	-5.505
TCTVA.4R1.B2	157.53	79.63	0.762	0.824	1.875	12.590	-8.840
TCTVA.4R2.B2	48.29	46.49	0.582	0.596	2.460	10.210	-5.290
TCLA.A5L3.B2	142.70	176.06	1.130	1.171	0.350	12.060	-11.360
TCTVA.4R5.B2	158.10	79.76	0.763	0.809	1.060	11.585	-9.465
TCLA.C6L7.B2	68.70	151.83	1.050	1.077	0.730	11.505	-10.045
TCLA.A6L7.B2	297.30	48.16	0.593	0.646	0.290	6.750	-6.170
TCSG.D4R7.B2	333.01	68.84	0.709	0.762	-0.200	4.900	-5.300
TCP.D6R7.B2	158.69	78.26	0.756	0.756	0.730	5.035	-3.575
TCSG.E5L7.B2	241.53	136.15	1.150	1.093	-0.090	7.235	-7.415
TCSG.D5L7.B2	213.98	158.60	1.150	1.273	-0.233	8.295	-8.760
TCSG.B5L7.B2	121.88	267.65	1.140	1.228	0.385	8.610	-7.840
TCSG.A4L7.B2	99.51	175.98	0.988	1.156	-0.795	6.950	-8.540
TCSG.A4R7.B2	139.68	131.02	0.992	1.031	-0.890	6.020	-7.800
TCSG.A5R7.B2	186.05	145.87	1.110	1.305	0.085	8.830	-8.660
TCSG.B5R7.B2	160.07	166.45	1.090	1.197	0.050	8.070	-7.970
TCSG.A6R7.B2	39.88	226.85	0.908	1.085	0.050	7.315	-7.220
TCP.B6R7.B2	142.30	87.48	0.887	0.887	-0.360	4.695	-5.415

Table C.3: Measurements from an alignment of the LHC B1 collimators (collision optics derived from version 6.503, $E = 4$ TeV). The alignments were performed on the 29.03.2013 (IR3, IR6 and IR7) and the 30.03.2012 (TCTs and TCLs).

Name	β_x [m]	β_y [m]	σ_n [mm]	σ_m [mm]	Δx [mm]	$x^{L,set}$ [mm]	$x^{R,set}$ [mm]
TCSG.4R6.B1	518.85	174.68	0.653	0.717	0.125	4.760	-4.510
TCDQA.B4R6.B1	495.25	165.46	0.638	0.645	-0.800	4.045	N/A
TCL.5R5.B1	157.02	835.04	0.342	0.391	0.010	3.600	-3.580
TCTH.4L5.B1	1437.43	551.50	1.086	1.038	-4.565	5.210	-14.340
TCLA.7R3.B1	67.39	89.39	0.235	0.362	0.025	4.165	-4.115
TCLA.6R3.B1	129.44	168.71	0.326	0.436	0.000	5.735	-5.735
TCLA.B5R3.B1	151.62	168.69	0.353	0.573	0.000	6.210	-6.210
TCSG.B5R3.B1	45.54	312.68	0.193	0.405	0.000	3.345	-3.345
TCSG.A5R3.B1	35.87	344.11	0.172	0.341	0.000	2.955	-2.955
TCSG.4R3.B1	26.21	395.19	0.147	0.240	-1.143	1.145	-3.430
TCSG.5L3.B1	54.61	298.62	0.212	0.315	-0.383	2.920	-3.685
TCP.6L3.B1	131.52	144.70	0.329	0.518	0.335	4.280	-3.610
TCTH.4L2.B1	207.90	232.37	0.413	0.451	0.095	5.345	-4.575
TCL.5R1.B1	156.63	832.11	0.343	0.379	-0.345	3.240	-3.930
TCTH.4L1.B1	1437.43	551.50	1.086	1.035	0.630	10.405	-9.145
TCTH.4L8.B1	241.16	301.69	0.445	0.482	-0.103	5.235	-5.445
TCLA.A7R7.B1	64.63	146.46	0.230	0.268	-0.418	1.495	-2.330
TCLA.D6R7.B1	65.05	157.92	0.360	0.249	-0.225	1.695	-2.145
TCLA.B6R7.B1	159.51	76.39	0.362	0.403	-0.353	2.650	-3.355
TCSG.6R7.B1	335.77	47.36	0.525	0.518	-0.233	3.075	-3.540
TCSG.B4L7.B1	139.76	131.00	0.339	0.454	0.845	2.980	-1.290
TCP.C6L7.B1	150.53	82.76	0.352	0.351	-0.178	1.335	-1.690
TCTVA.4L5.B1	1443.12	582.27	0.691	0.720	0.818	7.040	-5.405
TCLA.A5R3.B1	142.53	176.01	0.380	0.475	-0.505	6.185	-7.195
TCTVA.4L2.B1	218.44	235.00	0.439	0.501	2.645	7.915	-2.625
TCTVA.4L1.B1	1443.12	582.27	0.691	0.725	2.763	8.985	-3.460
TCTVB.4L8	536.56	335.18	0.525	0.573	-2.993	3.300	-9.290
TCLA.C6R7.B1	68.62	151.89	0.353	0.439	1.443	4.375	-1.490
TCLA.A6R7.B1	297.08	48.15	0.199	0.247	0.328	1.980	-1.325
TCSG.D4L7.B1	332.95	68.86	0.238	0.365	-0.070	1.430	-1.570
TCP.D6L7.B1	158.87	78.26	0.253	0.253	0.240	1.330	-0.850
TCSG.E5R7.B1	241.41	136.12	0.385	0.360	0.020	2.445	-2.405
TCSG.D5R7.B1	213.89	158.55	0.385	0.397	-0.228	2.195	-2.650
TCSG.B5R7.B1	121.86	267.58	0.383	0.485	0.370	2.780	-2.040
TCSG.A4R7.B1	118.28	152.22	0.334	0.336	0.693	2.800	-1.415
TCSG.A4L7.B1	128.67	141.30	0.333	0.355	0.835	2.935	-1.265
TCSG.A5L7.B1	185.99	145.93	0.372	0.390	-0.240	2.105	-2.585
TCSG.B5L7.B1	160.02	166.52	0.365	0.366	-0.375	1.925	-2.675
TCSG.A6L7.B1	39.87	226.93	0.305	0.309	-0.078	1.845	-2.000
TCP.B6L7.B1	142.46	87.49	0.297	0.297	-0.320	0.955	-1.595

Table C.4: Measurements from an alignment of the LHC B2 collimators (collision optics derived from version 6.503, $E = 4$ TeV). The alignments were performed on the 29.03.2013 (IR3, IR6 and IR7) and the 30.03.2012 (TCTs and TCLs).

Name	β_x [m]	β_y [m]	σ_n [mm]	σ_m [mm]	Δx [mm]	$x^{L,set}$ [mm]	$x^{R,set}$ [mm]
TCTH.4R8.B2	241.16	301.69	0.445	0.471	-0.700	4.640	-6.040
TCL.5L1.B2	152.21	861.97	0.342	0.325	0.313	3.850	-3.220
TCSG.6L7.B2	335.77	47.36	0.525	0.456	-0.128	3.180	-3.435
TCTH.4R1.B2	1437.43	551.50	1.086	0.965	-0.570	9.205	-10.345
TCTH.4R2.B2	207.90	232.38	0.413	0.384	-0.430	4.635	-5.280
TCLA.7L3.B2	66.78	93.22	0.234	0.330	-0.128	3.995	-4.250
TCLA.6L3.B2	129.44	168.71	0.326	0.431	-0.388	5.350	-6.125
TCLA.B5L3.B2	151.62	168.69	0.353	0.498	-1.153	5.055	-7.360
TCSG.B5L3.B2	45.54	312.68	0.193	0.362	-0.370	2.940	-3.680
TCSG.A5L3.B2	35.87	344.11	0.172	0.403	-0.448	2.510	-3.405
TCSG.4L3.B2	26.21	395.20	0.147	0.214	-0.305	1.985	-2.595
TCSG.5R3.B2	54.60	298.62	0.212	0.354	-0.438	2.865	-3.740
TCP.6R3.B2	131.52	144.69	0.329	0.532	-0.090	3.855	-4.035
TCL.5L5.B2	151.79	859.17	0.343	0.324	0.028	3.560	-3.500
TCTH.4R5.B2	1437.43	551.50	1.086	0.959	1.928	11.705	-7.850
TCSG.4L6.B2	523.37	173.62	0.655	0.610	-0.188	4.465	-4.840
TCDQA.B4L6.B2	499.53	165.45	0.640	0.647	-0.184	4.680	N/A
TCLA.A7L7.B2	65.95	143.13	0.233	0.231	0.688	2.620	-1.245
TCLA.D6L7.B2	65.05	157.92	0.360	0.211	0.188	2.105	-1.730
TCLA.B6L7.B2	159.51	76.39	0.362	0.391	0.113	3.115	-2.890
TCSG.B4R7.B2	151.54	121.32	0.353	0.294	-1.058	1.165	-3.280
TCP.C6R7.B2	150.53	82.76	0.351	0.351	0.520	2.030	-0.990
TCTVB.4R8	536.56	335.18	0.525	0.571	-3.158	3.135	-9.450
TCTVA.4R1.B2	1443.11	582.27	0.691	0.725	2.295	8.520	-3.930
TCTVA.4R2.B2	218.44	235.00	0.439	0.933	1.655	6.925	-3.615
TCLA.A5L3.B2	142.53	176.02	0.380	0.402	0.293	6.985	-6.400
TCTVA.4R5.B2	1443.11	582.27	0.691	0.726	-0.375	5.850	-6.600
TCLA.C6L7.B2	68.62	151.89	0.353	0.388	0.805	3.735	-2.125
TCLA.A6L7.B1	297.08	48.15	0.199	0.238	0.338	1.990	-1.315
TCSG.D4R7.B2	332.96	68.86	0.238	0.265	-0.150	1.350	-1.650
TCP.D6R7.B2	158.87	78.26	0.253	0.253	0.770	1.860	-0.320
TCSG.E5L7.B2	241.41	136.12	0.385	0.374	0.035	2.460	-2.390
TCSG.D5L7.B2	213.89	158.55	0.385	0.401	-0.240	2.180	-2.660
TCSG.B5L7.B2	121.86	267.58	0.383	0.500	0.520	2.930	-1.890
TCSG.A4L7.B2	99.59	175.95	0.332	0.409	-0.760	1.330	-2.850
TCSG.A4R7.B2	139.76	131.00	0.333	0.387	-0.735	1.360	-2.830
TCSG.A5R7.B2	185.99	145.93	0.373	0.370	0.540	2.885	-1.805
TCSG.B5R7.B2	160.02	166.52	0.365	0.387	0.315	2.615	-1.985
TCSG.A6R7.B2	39.87	226.93	0.305	0.462	0.075	1.995	-1.845
TCP.B6R7.B2	142.46	87.49	0.297	0.297	-0.235	1.045	-1.515

D. Simulated BPM Non-Linearity Corrections

This section reports on simulations performed by A. Nosych, which serve as a background for the BPM non-linearity measurements. A collimator CAD model was used to study and characterize the BPM readouts through electromagnetic simulations in CST Particle Studio [125]. The sensitivity of collimator BPMs to beam displacements was analyzed by displacing the simulated beam in horizontal plane for a set of jaw gaps ranging from 2 to 60 mm. In particular, for each given jaw gap a set of beam offsets on horizontal axis was simulated, namely between [-50%, 50%] of the jaw half gap, that is $G/2$ (e.g. Fig. D.1). An original horizontal offset of the beam with respect to the jaw centre J_c is defined as X_{beam} at a corresponding step of ΔX:

$$X_{beam,n} = J_c + n \times \Delta X \tag{D.1}$$

where n is an iterator over each beam scan position. For simulation purposes, the collimator axis was aligned with the beam axis so that $J_c = 0$ and $X_{abs} = 0$. At each iteration, three values were recorded: the original beam position X_{beam}, the raw position X_{raw}, given by BPM electrodes (Eq. (3.4)), and the value of B which is provided by jaw positions J_L and J_R. All simulations were performed with parallel jaws, i.e. zero tilt, resulting in the same voltages on the upstream and downstream pick-ups on same jaw. This excluded separate treatment of upstream and downstream BPM pairs and they were considered to be identical. The plots in Fig. D.2 show the non-linear relationship between X_{beam} and X_{raw}, depending on the beam offset and jaw gap. A subset of the simulation results were successfully verified with circulating beam in the SPS ring [91].

In the perfect case, a linearized BPM reading should provide the original offset value with $X_{bpm} \approx X_{beam}$. In Eq. (3.4) it was shown that the calibration constant amounts to $k_x = B/4$ for infinitely small beam offsets. The BPM response can be then approximated to mm via:

$$X_{bpm} = B/4 \times X_{raw} \approx X_{beam} \tag{D.2}$$

and is referred to as the *linearized position* by the difference-over-sum method. Here, a *linearity factor* parameter L_f must be introduced, which is a non-linear conversion coefficient between the linearized and original beam positions:
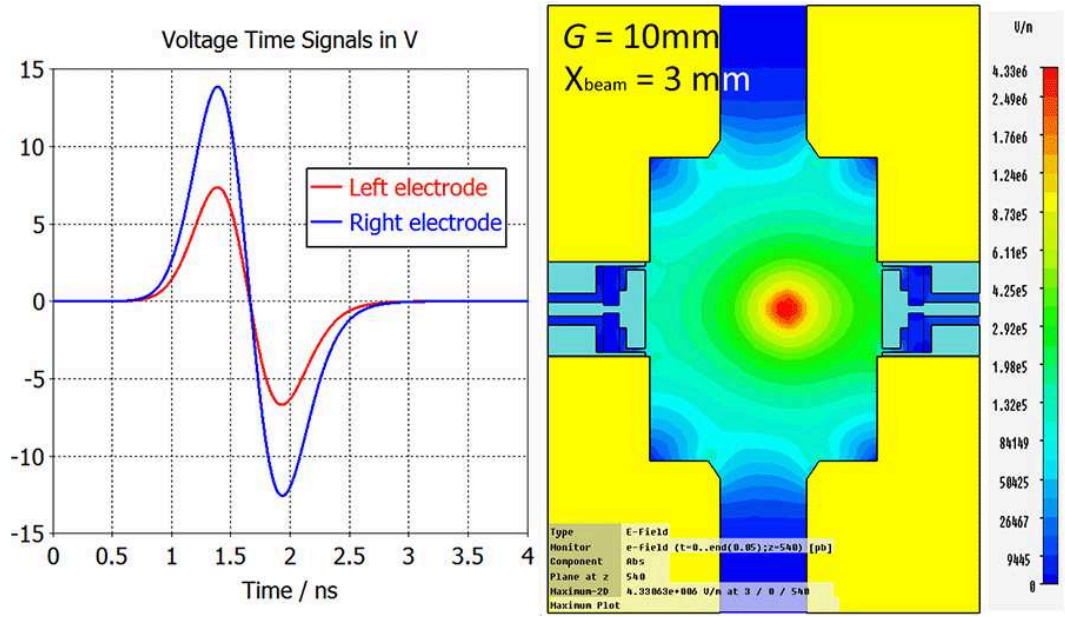
Figure D.1: Simulated BPM time signal (left) and snapshot of the E-field distribution of a single off-centred bunch (by 60% of $G/2$, $G = 10$mm) passing in a cross-section at the upstream BPM centre (right).
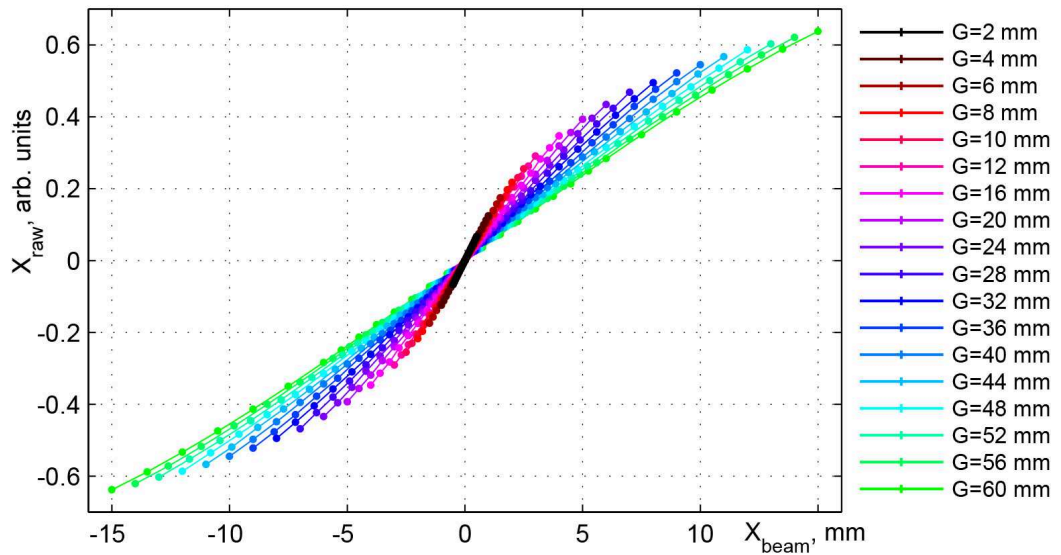
Figure D.2: Non-linear relationship between X_{beam} and X_{raw}, depending on the beam offset and jaw gap.
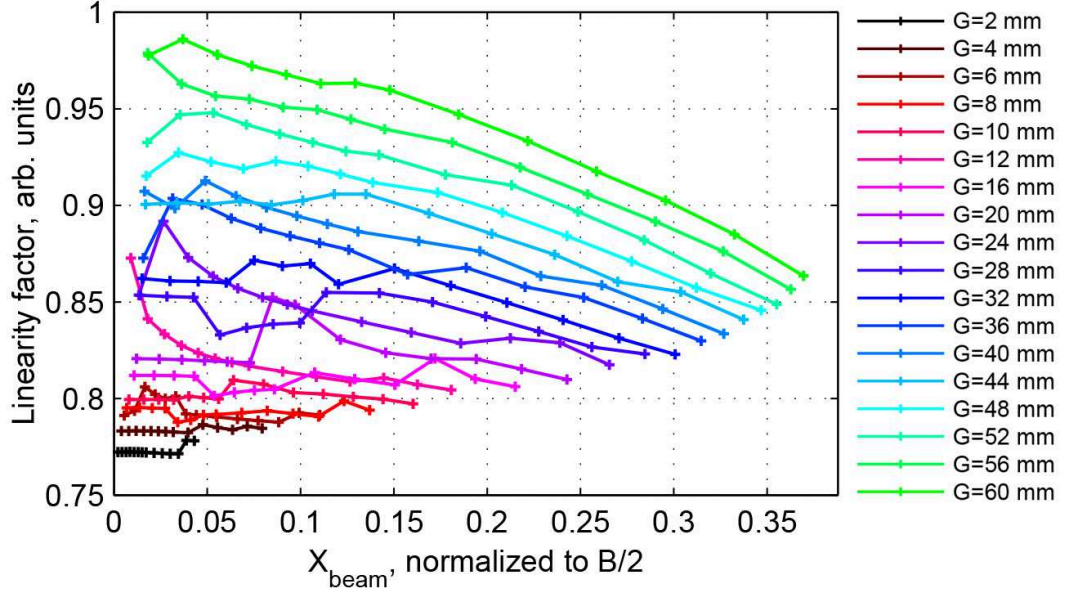
Figure D.3: Linearity factor as a function of the beam offset normalized to the BPM aperture.

$$L_f = \frac{X_{bpm}}{X_{beam}} \tag{D.3}$$

The values of the linearity factor, calculated during horizontal beam sweep simulations as in Fig. D.2, are shown in Fig. D.3. It is convenient to plot L_f against the beam offset X_{beam} normalized by $B/2$ so the aperture is always within [-1, 1] for all G. It can be seen that the L_f curve is non-linear for each set of beam positions at a corresponding jaw gap. The value of L_f increases with aperture, although even at the largest gap it changes by no more than 15% between the smallest and largest beam offset.

The noisy artifacts in the left part of each curve in Fig. D.3 reflect the default accuracy of the wakefield solver of CST Particle Studio (-30 dB) and the effects of automatic hexahedral mesh adaptation by the CST mesher at each sweep iteration. The maximum mesh count of the model altered between 2.2 and 3 million between iterative simulations of jaw gaps, while the sizes of mesh cell edges were in the range of 0.2 and 6 mm. Each simulation took under 40 minutes on a moderate desktop PC (3 GHz Dual Core, 8 GB RAM). It can be concluded that the BPM time response simulation of small beam offsets in small jaw gaps is extremely sensitive to the mesh cell size and the total mesh count of the CAD model.

The behavior of collimator BPM signals for jaw gaps other than the ones simulated in Fig. D.2 can be predicted through simulation. Based on values of simulated X_{raw} on a grid of X_{beam}, mapped for a set of jaw gaps, a fast and accurate algorithm which covers correction of non-linear BPM readings of feasible beam offsets within the full jaw motion range was developed.

A relationship between the calculated raw positions X_{raw}, original beam positions X_{beam} and BPM aperture B can be described using an invertible function: $X_{raw} = P(X_{beam}, B)$, so that:

$$X_{beam} = P^{-1}(X_{raw}, B) = Q(X_{raw}, B) \tag{D.4}$$

By fitting the surface Q with a 2D mn-degree polynomial (see Fig. D.4) with coefficients c_{pq}:

$$X_{beam} = \sum_{p,q=0}^{m,n} c_{pq} X_{raw}^p B^q = X_{bpm} \tag{D.5}$$

one can use it to convert raw position data X_{raw} at a given jaw gap back to original beam position X_{beam}, with an accuracy mainly defined by polynomial's power. Due to the smooth properties of the surface Q, the fitting scheme can be a general polynomial regression model in two dimensions. Already for $m = 5$ and $n = 2$ the r.m.s. error is 0.008 and goodness of fit $R^2 = 1$, so these powers can be considered to be optimal for the requirements. Excluding negligibly small fit coefficients, the final polynomial is:

$$X_{bpm} = c_{10} X_{raw} + c_{11} X_{raw} B + c_{30} X_{raw}^3 + c_{12} X_{raw} B^2$$
$$+ c_{31} X_{raw}^3 B + c_{50} X_{raw}^5 + c_{32} X_{raw}^3 B^2 \tag{D.6}$$

where c_{pq} are the fit coefficients, listed in Table D.1. This polynomial provides *corrected* BPM readings X_{bpm} and will be referred to as *Poly52*. The coefficients of *Poly52* are unique for a given collimator geometry and valid within jaw gap limits and beam offsets up to defined limits in horizontal plane.

It is convenient to express the correction accuracy of *Poly52* in μm within the BPM aperture B, rather than in between jaw surfaces G. Figure D.5 shows such
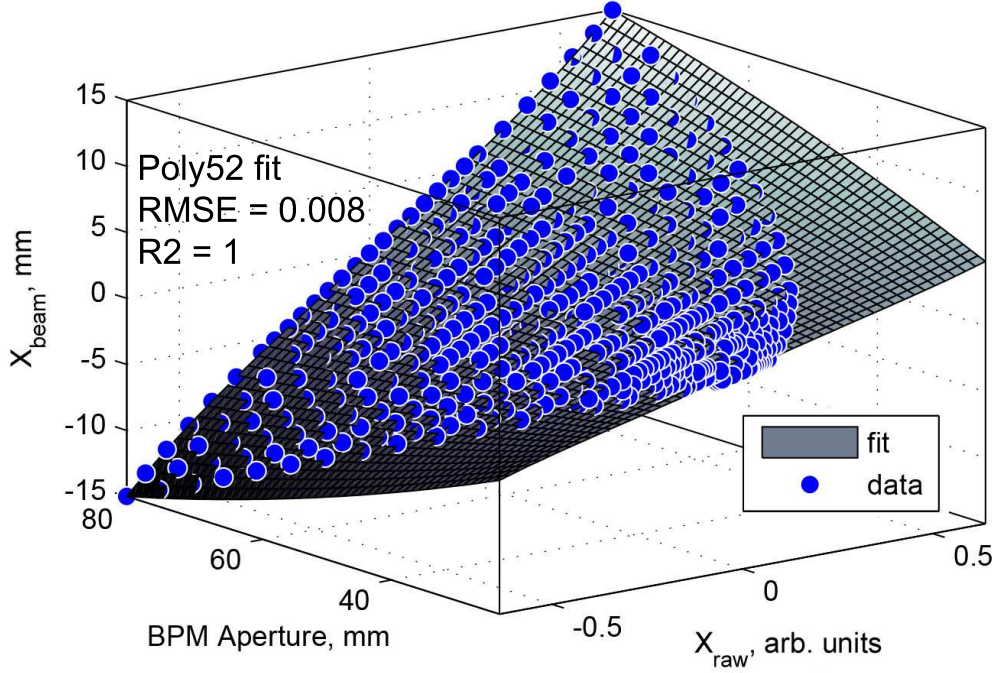
Figure D.4: The 2D polynomial fit (*Poly*52) used to correct the non-linear BPM readings for full jaw motion range.

Table D.1: Coefficients of the 2-D surface fit, used to obtain the corrected beam position for full jaw motion range and maximum beam offset of 50% G.

Coefficient	Value
c_{10}	0.03097
c_{11}	0.34601
c_{30}	-4.7501
c_{12}	-0.0011109
c_{31}	0.15941
c_{50}	4.3138
c_{32}	-0.00050142

an error map, where the overall error inside the considered limits is well below 50 μm, which is less than 0.1% of B. For example, at a 2 mm jaw gap and a 0.5 mm beam offset, the *Poly52* would estimate the beam position within 2 μm, while at a 30 mm jaw gap and a 1.5 mm beam offset, the position would be calculated within 20 μm.

The aligned horizontal collimator cannot identify a vertical beam displacement due to the fact that it is equipped with only horizontal electrodes. With a vertical beam offset, a gradual decrease of the left and right signals is expected. The BPM readout versus the vertical centre of the collimator could be calibrated by sweeping the coasting beam on the vertical Y-axis (looking into the observer in Fig. 3.5) with high resolution bumps, which is not feasible in reality.
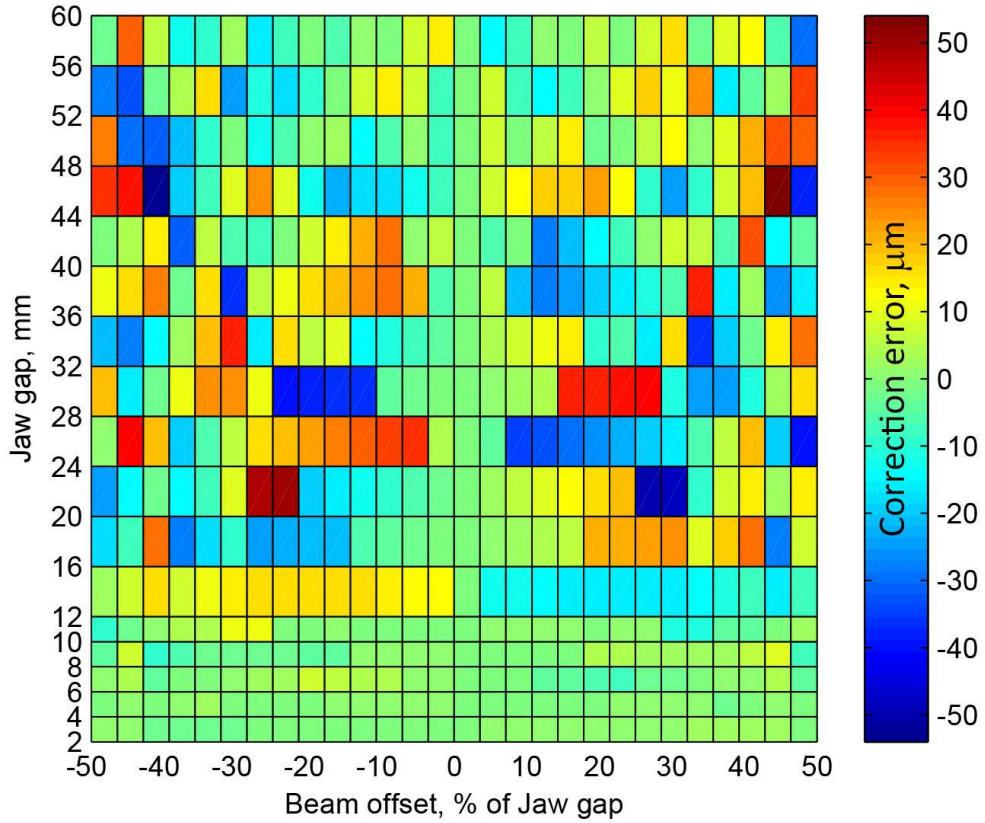
Figure D.5: Error map of corrected BPM readings with *Poly52* for full jaw motion range, where the overall error inside the considered limits is below 50 μm (less than 0.1% of BPM aperture).

In view of possible beam offsets in the orthogonal plane XY plane, *Poly52* was tested on a simulated 2D grid of beam offsets with small vertical (up to 2 mm), and rather large horizontal displacements, located inside and beyond the effective area of the polynomial, i.e. up to 80% of G. Fig. D.6a and Fig. D.6b compare the performance of a difference-over-sum linearization and of the *Poly*52 non-linearity correction. Here $G = 40$ mm and $k_x = 15.3$ for difference-over-sum method.

Figure D.7 shows correction errors by both methods for two rows of points, highlighted in Fig. D.6a and Fig. D.6b. The *Poly*52 shows overall a factor of 100 higher accuracy than the difference-over-sum linearization.
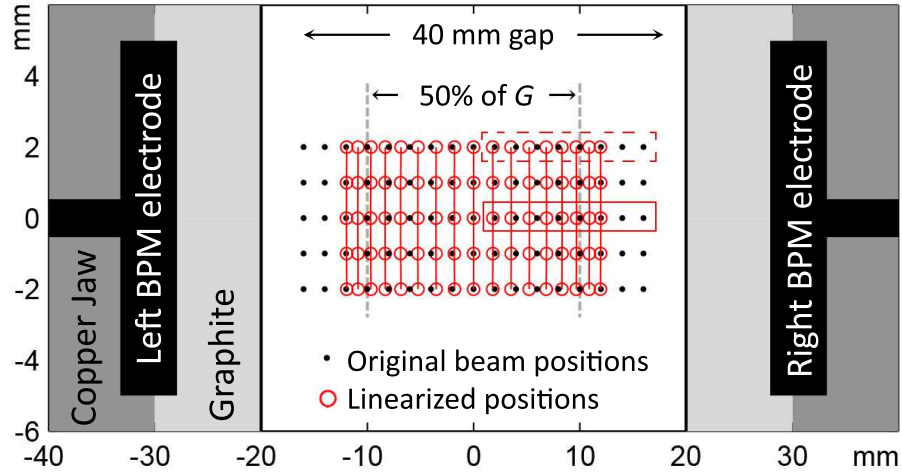
(a) Difference-over-sum linearization
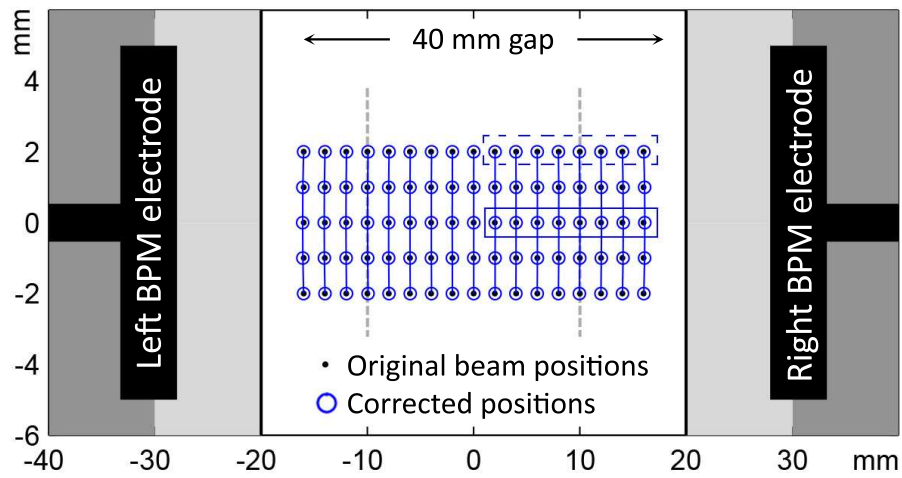
(b) *Poly*52 correction

Figure D.6: Cross-section schematics of the collimator depicting comparison of the performance of a difference-over-sum linearization (top) and of the *Poly*52 (bottom) correction methods for simulated beam sweeps in transverse plane.
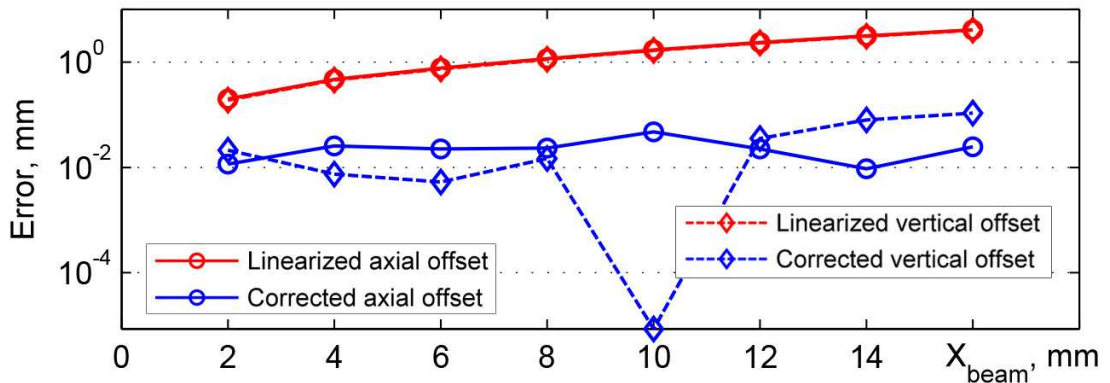
Figure D.7: Correction errors by difference-over-sum and *Poly*52 methods for two rows of points highlighted correspondingly in Fig. D.6a and Fig. D.6b.

E.   Static Model of Beam Scraping

The derivations of the fraction of particles lost and the resulting beam distribution are reproduced from [107] for clarity. If normalised coordinates x, x' are used, then the horizontal and vertical phase space distribution can be expressed as a two-dimensional Gaussian:

$$g_2(x, x') = \frac{1}{2\pi} e^{-\frac{x^2 + x'^2}{2}} \tag{E.1}$$

where g_2 is normalised to 1. The fraction of particles remaining after a single-sided cut at n_σ is then given by integrating over the tail of the Gaussian distribution up to n_σ.

$$F_{single}(n_\sigma) = \int_{-\infty}^{\infty} dx' \int_{-\infty}^{n_\sigma} g_2(x, x') dx = \frac{1}{2}[1 + \mathrm{erf}(n_\sigma)/\sqrt{2}] \tag{E.2}$$

For a double-sided cut at $\pm n_\sigma$:

$$F_{round}(n_\sigma) = \int_{-\infty}^{\infty} dx' \int_{-n_\sigma}^{n_\sigma} g_2(x, x') dx = \mathrm{erf}(n_\sigma)/\sqrt{2} \tag{E.3}$$

After multiple turns, a round cut is observed at $n_\sigma = \sqrt{x^2 + x'^2}$, as displayed in Fig. 7.4. The remaining particles are then distributed according to:

$$g_{round} = \int_{-\sqrt{n_\sigma^2 - x^2}}^{\sqrt{n_\sigma^2 - x^2}} g_2(x, x') dx' = \frac{e^{-x^2/2}}{\sqrt{2\pi}} \mathrm{erf}\left(\sqrt{\frac{n_\sigma^2 - x^2}{2}}\right) \tag{E.4}$$

The fraction of the remaining particles is then:

$$F_r(n_\sigma) = \int_{-n_\sigma}^{n_\sigma} g_{round}(x) dx \tag{E.5}$$

This integral can then be evaluated analytically in polar coordinates $x = r\cos\varphi, x' = r\sin\varphi, dxdx' = rdrd\varphi, 0 \le \varphi \le 2\pi$ and $0 \le r \le n_\sigma$. The fraction of particles left after scraping at n_σ over many turns (corresponding to a round cut in phase space) is:

$$F_r(n_\sigma) = \frac{1}{2\pi} \int_0^{n_\sigma} \int_0^{2\pi} re^{-r^2/2} d\varphi dr = \int_0^{n_\sigma} re^{-r^2/2} dr = [-e^{-r^2/2}]_0^{n_\sigma} = 1 - e^{-n_\sigma^2/2}$$

(E.6)

The fraction of particles lost after scraping, $F_{lost}(n_\sigma)$, can be expressed in terms of the collimator jaw position x and the beam centre x_0 as follows:

$$F_{lost}(n_\sigma) = e^{-n_\sigma^2/2} = e^{\frac{-\frac{1}{2}(x-x_0)^2}{\sigma_x^2}}$$

(E.7)

The distribution of the beam after a cut of n_σ in terms of the collimator jaw position x and the $1\,\sigma$ beam size in mm is then:

$$y = \frac{e^{\frac{-x^2}{2\sigma_x^2}}}{\sqrt{2\pi}} \text{erf}\left(\frac{\sqrt{n_\sigma^2 - \frac{x^2}{\sigma_x^2}}}{2}\right) \times N_0$$

(E.8)

where N_0 is the beam intensity.

References

[1] L. R. Evans, "The Large Hadron Collider," *New J. Phys.*, vol. 9, p. 335, 2007.

[2] A. Beuret *et al.*, "The LHC lead injector chain," in *Proceedings of EPAC'04*, Lucerne, Switzerland, 2004, pp. 1153–1155.

[3] L. R. Evans, "Beam physics at LHC," in *Proceedings of the 20th IEEE Particle Accelerator Conference*, Portland, USA, 2003, pp. 19–23.

[4] ATLAS collaboration website, available at http://www.atlas.ch/.

[5] CMS collaboration website, available at http://cms.web.cern.ch/.

[6] P. W. Higgs, "Broken symmetries and the masses of gauge bosons," *Phys. Rev. Lett.*, vol. 13, 1964.

[7] Observation of a new Higgs-like particle, CERN press release (04/07/2012), available at http://press.web.cern.ch/press-releases/2012/07/cern-experiments-observe-particle-consistent-long-sought-higgs-boson.

[8] Experiments at CERN, available at http://greybook.cern.ch/.

[9] ALICE collaboration website, available at http://aliceinfo.cern.ch/.

[10] LHCb collaboration website, available at http://lhcb.web.cern.ch/lhcb/.

[11] ALFA experiment website, available at http://atlas-project-lumi-fphys.web.cern.ch/atlas-project-lumi-fphys/ALFA/.

[12] TOTEM experiment website, available at http://totem.web.cern.ch/Totem/.

[13] M. Oriunno *et al.*, "The Roman pot for the LHC," in *Proceedings of EPAC'06*, Edinburgh, Scotland, 2006, pp. 562–564.

[14] LHC 2008 inauguration website, available at http://lhc2008.web.cern.ch/LHC2008/inauguration/lhcexpo.html.

[15] ATLAS experiment website, available at http://www.atlas.ch/photos/lhc.html.

[16] M. Lamont, "The LHC from commissioning to operation," in *Proceedings of IPAC'11*, San Sebastian, Spain, 2011, pp. 11–15.

[17] Report No. CERN-2004-003-V1, edited by O. S. Brüning, P. Collier, P. Lebrun, S. Myers, R. Ostojic, J. Poole, P. Proudlock, 2004.

[18] E. Metral, Longitudinal Beam Dynamics, JUAS 2011, Archamps, France.

[19] O. Brüning, "LHC challenges and upgrade options," *J. Physics*, vol. 110, p. 112002, 2008.

[20] LHC public outreach website, available at http://lhc-machine-outreach.web. cern.ch/lhc-machine-outreach/collisions.htm.

[21] A. Macpherson, "LHC availability and performance in 2012," in *Proceedings of the Fourth LHC Beam Operation Workshop*, Evian, France, 2012.

[22] J.-B. Jeanneret, D. Leroy, L. R. Oberli, and T. Trenkler, "Quench levels and transient beam losses in LHC magnets," CERN-LHC-Project-Report-44, 1996.

[23] R. W. Assmann *et al.*, "An improved collimation system for the LHC," in *Proceedings of the 9th European Particle Accelerator Conference*, Lucerne, Switzerland, 2004, pp. 536–538.

[24] R. W. Assmann *et al.*, "Requirements for the LHC collimation system," in *Proceedings of the 8th European Particle Accelerator Conference*, Paris, France, 2002, pp. 197–199.

[25] C. Bracco, CERN-THESIS-2009-031, 2009.

[26] M. Church, A. I. Drozhdin, A. Lega, N. P. Mokhov, and R. Reilly, "Tevatron run-II beam collimation system," in *Proceedings of PAC'99*, New York, USA, 1999, pp. 56–58.

[27] A. Drees, R. P. Filler, D. Gassner, G. McIntyre, and D. Trbojevic, "RHIC collimator performance," in *Proceedings of the 8th European Particle Accelerator Conference*, Paris, France, 2002, pp. 2673–2675.

[28] R. W. Assmann, B. Goddard, E. Vossenberg, and E. Weisse, LHC Project Note 293, 2002.

[29] R. W. Assmann, "Collimation for the LHC high intensity beams," in *Proceedings of HB2010*, Morschach, Switzerland, 2010, pp. 21–33.

[30] R. W. Assmann, "Operational experience with LHC collimation," in *Proceedings of PAC'09*, Vancouver, Canada, 2009, pp. 789–793.

[31] S. Redaelli, R. W. Assmann, R. Bruce, A. Rossi, and D. Wollmann, "Operational performance of the LHC collimation," in *Proceedings of HB2010*, Morschach, Switzerland, 2010, pp. 395–399.

[32] R. W. Assmann, 2007, beam losses and collimation at the LHC, seminar given at GSI, Darmstadt, Germany.

[33] J.-B. Jeanneret, "Optics of a two-stage collimation system," *Phys. Rev. ST. Accel. Beams*, vol. 12, 1998.

[34] G. Robert-Demolaize, CERN-THESIS-2006-069, 2007.

[35] D. Kaltchev, M. K. Craddock, R. V. Servranckx, and J.-B. Jeanneret, "Numerical optimization of collimator jaw orientations and locations in the lhc," in *Proceedings of PAC'97*, Vancouver, Canada, 1997, pp. 153–155.

[36] N. Mounet, CERN-THESIS-2012-055, 2012.

[37] K. Kostro, V. Baggiolini, F. Calderini, F. Chevrier, S. Jensen, R. Swoboda, and N. Trofimov, "Controls middleware - the new generation," in *Proceedings of EPAC'02*, Paris, France, 2002, pp. 2028–2030.

[38] A. Guerrero, J.-J. Gras, J.-L. Nougaret, M. Ludwig, M. Arruat, and S. Jackson, "CERN front-end software architecture for accelerator controls," in *Proceedings of ICALEPCS'03*, Gyeongju, Korea, 2003, pp. 342–344.

[39] A. Masi and R. Losito, "LHC collimators low level control system," *IEEE Trans. Nucl. Sci.*, vol. 55, no. 1, pp. 333–340, 2008.

[40] S. Redaelli, R. W. Assmann, M. Jonker, and M. Lamont, CERN-EDMS document LHC-TCT-ES-0001, 2007.

[41] S. Redaelli, R. W. Assmann, R. Losito, M. Donze, and A. Masi, "Lhc collimator controls for a safe lhc operation," in *Proceedings of ICALEPCS'11*, Grenoble, France, 2011, pp. 1104–1107.

[42] R. Bruce, R. W. Assmann, and S. Redaelli, "Principles for generation of time-dependent collimator settings during the LHC cycle," in *Proceedings of IPAC'11*, San Sebastian, Spain, 2011, pp. 3753–3755.

[43] R. Alemany-Fernandez, V. Baggiolini, R. Gorbonosov, D. Khasbulatov, M. Lamont, P. L. Roux, and C. Roderick, "The lhc sequencer," in *Proceedings of ICALEPCS'11*, Grenoble, France, 2011, pp. 300–303.

[44] G. Guaglio, CERN-THESIS-2006-012, 2006.

[45] K. Dahlerup, R. Denz, J.-L. Gomez-Costa, D. Hagedorn, P. Proudlock, F. Rodriguez-Mateos, R. Schmidt, and F. Sonnemann, "The protection system for the superconducting elements of the Large Hadron Collider at CERN," in *Proceedings of PAC'99*, New York, USA, 1999, pp. 3200–3202.

[46] E. B. Holzer, B. Dehning, E. Effinger, J. Emery, G. Ferioli, J. L. Gonzalez, E. Gschwendtner, G. Guaglio, M. Hodgson, D. Kramer, R. Leitner, L. Ponce, V. Prieto, M. Stockner, and C. Zamantzas, "Beam loss monitoring system for the LHC," in *Proceedings of the IEEE Nuclear Science Symposium Conference Record*, San Juan, Puerto Rico, 2005, pp. 1052–1056.

[47] M. Stockner, B. Dehning, C. Fabjan, E. B. Holzer, and D. Kramer, "Classification of the LHC BLM ionization chamber," in *Proceedings of DIPAC'07*, Venice, Italy, 2007, pp. 328–330.

[48] BLM Acquisition System - Running Sums, available at http://ab-div-bdi-bl-blm.web.cern.ch/ab-div-bdi-bl-blm/Acquisition_system/Data_acquisition_integration_durations_20100313.htm.

[49] B. Dehning, E. Effinger, J. Emery, G. Ferioli, G. Guaglio, and C. Zamantzas, "The LHC beam loss monitoring system's data acquisition card," in *Proceedings of LECC'06*, Valencia, Spain, 2006, pp. 108–112.

[50] C. Zamantzas, B. Dehning, C. Chery, E. Effinger, J. Emery, S. Grishin, C. F. Hajdu, E. B. Holzer, S. Jackson, C. Kurfuerst, A. Marsili, A. Nordt, M. Sapinski, R. Tissier, and G. G. Venturini, "The LHC beam loss monitoring system commissioning for 2010," in *Proceedings of the First 2010 Evian Workshop on LHC beam operation*, Evian, France, 2010, pp. 57–66.

[51] C. Zamantzas, CERN-THESIS-2006-037, 2006.

[52] C. Zamantzas, "LHC BLM system: hardware changes during LS1," in *In Proceedings of the Second LHC Machine Protection Workshop*, Annecy, France, 2013.

[53] O. R. Jones, "LHC beam instrumentation," in *Proceedings of PAC'07*, Albuquerque, New Mexico, USA, 2007, pp. 2630–2634.

[54] C. Bovet, J. P. Papis, H. Schmickler, and L. Vos, "LHC BPM design," in *Proceedings of DIPAC'97*, Frascati, Italy, 1997, pp. 64–69.

[55] J.-P. Koutchouk, "Measurement of the beam positions in the LHC main rings," LHC Project Document No. LHC-BPM-ES-0004, 2002.

[56] J. Wenninger and R. Steinhagen, "LHC orbit feedback control requirements," LHC Project Document No. LHC-DC-ES-0001, 2007.

[57] J. Wenninger, LHC requirements on orbit control and correction issues. Presented at the Orbit Feedback workshop, 06.10.2003.

[58] A. Dallocchio, A. Bertarelli, C. Boccard, F. Carra, M. Gasior, L. Gentini, and M. Timmins, "LHC collimators with embedded beam position monitors: a new advanced mechanical design," in *Proceedings of IPAC'11*, San Sebastian, Spain, 2011, pp. 1611–1613.

[59] A. Bertarelli, C. Boccard, A. Dallocchio, M. Gasior, L. Gentini, and A. Nosych, "Embedded collimator beam position monitors," in *Proceedings of DIPAC'11*, Hamburg, Germany, 2011, pp. 80–82.

[60] P. Piot, Fermilab Beams-doc-1894-v1, 2005.

[61] C. R. Carman and J.-L. Pellegrin, "The beam positions of the SPEAR storage ring," *Nucl. Instrum. Methods*, vol. 113, pp. 423–432, 1973.

[62] R. J. Steinhagen, CERN-THESIS-2007-058, 2007.

[63] R. W. Assmann, E. Holzer, J.-B. Jeanneret, V. Kain, S. Redaelli, G. Robert-Demolaize, and J. Wenninger, "Expected performance and beam-based optimization of the LHC collimation system," in *Proceedings of the 9th European Particle Accelerator Conference*, Lucerne, Switzerland, 2004, pp. 1825–1827.

[64] S. Redaelli, O. Aberle, R. W. Assmann, B. Dehning, C. Bracco, M. Jonker, A. Masi, R. Losito, M. Sapinski, T. Weiler, and C. Zamantzas, "Operational experience with a LHC collimator prototype in the CERN SPS," in *Proceedings of PAC'09*, Vancouver, Canada, 2009, pp. 2835–2837.

[65] D. Wollmann *et al.*, "First cleaning with LHC collimators," in *Proceedings of IPAC'10*, Kyoto, Japan, 2010, pp. 1237–1239.

[66] R. W. Assmann and D. Wollmann, "LHC collimation - too good or too bad?" in *Proceedings of the Chamonix 2011 Workshop on LHC Performance*, Chamonix, France, 2011.

[67] W. Höfle, R. W. Assmann, S. Redaelli, R. Schmidt, D. Valuch, D. Wollmann, and M. Zerlauth, "Controlled transverse blow-up of high energy proton beams for aperture measurements and loss maps," in *Proceedings of IPAC'12*, New Orleans, USA, 2012, pp. 4059–4061.

[68] Report No. FERMILAB-DESIGN-1984-01, 1984.

[69] N. Mokhov, J. Annala, R. Carrigan, M. Church, A. Drozhdin, T. Johnson, R. Reilly, V. Shiltsev, G. Stancari, D. Still, A. Valishev, X. L. Zhang, and V. Zvoda, "Tevatron beam halo collimation system: design, operational experience and new methods," *JINST*, vol. 6, no. 8, p. T08005, 2011.

[70] Report No. BNL 51932, 1986.

[71] Angelika Drees, private communication.

[72] Report No. DESY-HERA-81-10, 1981.

[73] M. Seidel, "The proton collimation system of HERA," DESY 94-103, 1994.

[74] R. Bruce, R. W. Assmann, and W. Herr, "Calculation method for safe beta-star," in *Proceedings of IPAC'11*, San Sebastian, Spain, 2011, pp. 1828–1830.

[75] G. Valentino, R. W. Assmann, S. Redaelli, N. Sammut, and D. Wollmann, "Semi-automatic beam-based alignment algorithm for the LHC collimation system," in *Proceedings of IPAC'11*, San Sebastian, Spain, 2011, pp. 3768–3770.

[76] G. Valentino, R. W. Assmann, R. Bruce, S. Redaelli, A. Rossi, N. Sammut, and D. Wollmann, "Semiautomatic beam-based LHC collimator alignment," *Phys. Rev. ST. Accel. Beams*, vol. 15, p. 051002, 2012.

[77] M. Deile, G. H. Antchev, R. B. Appleby, R. W. Assmann, I. Atanassov, V. Avati, J. Baechler, R. Bruce, M. Dupont, K. Eggert, B. Farnham, J. Kaspar, F. L. Rodriguez, J. Morant, H. Niewiadomski, X. Pons, E. Radermacher, S. Ravat, F. Ravotti, S. Redaelli, G. Ruggiero, H. Sabba, M. Sapinski, W. Snoeys, G. Valentino, and D. Wollmann, "The first 1 1/2 years of TOTEM roman pot operation at LHC," in *Proceedings of IPAC'11*, San Sebastian, Spain, 2011, pp. 502–504.

[78] G. Valentino, R. W. Assmann, R. Bruce, F. Burkart, M. Cauchi, D. Deboy, L. Lari, S. Redaelli, A. Rossi, and D. Wollmann, CERN-ATS-Note-2011-062, 2011.

[79] F. Burkart, R. W. Assmann, R. Bruce, M. Cauchi, D. Deboy, L. Lari, S. Redaelli, A. Rossi, D. Wollmann, and G. Valentino, "Halo scrapings with collimators in the LHC," in *Proceedings of IPAC'11*, San Sebastian, Spain, 2011, pp. 3756–3758.

[80] B. Boser, I. M. Guyon, and V. N. Vapnik, "A training algorithm for optimal margin classifiers," in *Proceedings of the 5th Annual ACM Workshop on Computational Learning Theory*, 1992, pp. 144–152.

[81] I. Steinwart and A. Christmann, *Support Vector Machines*. Springer-Verlag, 2008.

[82] F. Moisy, ezyfit, software available at http://www.fast.u-psud.fr/ezyfit/.

[83] G. Valentino, R. W. Assmann, R. Bruce, and N. Sammut, "Classification of LHC beam loss spikes using support vector machines," in *Proceedings of the IEEE 10th Jubilee International Symposium on Applied Machine Intelligence and Informatics*, Herl'any, Slovakia, 2012, pp. 355–358.

[84] C.-C. Chang and C.-J. Lin, "LIBSVM: A library for support vector machines," *ACM Transactions on Intelligent Systems and Technology*, vol. 2, pp. 27:1–27:27, 2011, software available at http://www.csie.ntu.edu.tw/~cjlin/libsvm.

[85] G. Valentino, R. W. Assmann, R. Bruce, and N. Sammut, "Automatic threshold selection for blm signals during lhc collimator alignment," in *Proceedings of the Sixth UKSim/AMSS European Symposium on Computer Modeling and Simulation (EMS)*, Valletta, Malta, 2012, pp. 210–213.

[86] G. J. Müller, BPM interpolation calculation. Presented at the Orbit feedback workshop, 10.02.2011.

[87] G. J. Müller, K. Fuchsberger, and S. Redaelli, "Aperture meter for the large hadron collider," in *Proceedings of ICALEPCS'11*, Grenoble, France, 2011, pp. 70–73.

[88] G. Valentino, R. W. Assmann, R. Bruce, G. J. Müller, S. Redaelli, B. Salvachua, and N. Sammut, "A tool based on the BPM-interpolated orbit for speeding up LHC collimator alignment," in *Proceedings of HB2012*, Beijing, China, 2012.

[89] G. Valentino, R. W. Assmann, R. Bruce, G. J. Müller, S. Redaelli, and B. Salvachua, CERN-ATS-Note-2012-046, 2012.

[90] D. Wollmann, O. Aberle, R. W. Assmann, A. Bertarelli, C. Boccard, R. Bruce, F. Burkart, M. Cauchi, A. Dallocchio, D. Deboy, M. Gasior, R. Jones, S. Redaelli, A. Rossi, and G. Valentino, "First beam results for a collimator with in-jaw beam position monitors," in *Proceedings of IPAC'11*, San Sebastian, Spain, 2011, pp. 3747–3749.

[91] D. Wollmann, O. Aberle, R. W. Assmann, A. Bertarelli, C. Boccard, R. Bruce, F. Burkart, M. Cauchi, A. Dallocchio, D. Deboy, M. Gasior, R. Jones, S. Redaelli, A. Rossi, and G. Valentino, "Experimental verification for a collimator with in-jaw beam position monitors," in *Proceedings of HB 2012*, Beijing, China, 2012.

[92] M. Gasior, J. Olexa, and R. J. Steinhagen, "Bpm electronics based on compensated diode detectors - results from development systems," in *Proceedings of BIW'12 Workshop*, Newport News, VA, USA, 2012.

[93] M. Gasior, "Calibration of a non-linear beam position monitor electronics by switching electrode signals," in *Proceedings of the International Beam Instrumentation Conference*, Oxford, United Kingdom, 2013.

[94] G. Valentino, R. W. Assmann, R. Bruce, and N. Sammut, "Development and beam tests of an automatic algorithm for alignment of LHC collimators with embedded BPMs," in *Proceedings of IPAC'13*, Shanghai, China, 2013.

[95] A. Dallocchio, Status of TCSP manufacturing. Presented at the LHC Collimation Working Group meeting, 24.06.2013.

[96] The Agile Manifesto, available at http://agilemanifesto.org/.

[97] G. Kruk, development process of accelerator controls software. Presented at ICALEPCS'05, 14.10.2005.

[98] Apache Ant, available at http://ant.apache.org/.

[99] V. Baggiolini, jAPC - the Java API for Parameter Control. Presented at ICALEPCS'05, 14.10.2005.

[100] M. Gourber-Pace, G. Kruk, and M. Misiowiec, "Status report of the measurement service for the CERN accelerator logging," in *Proceedings of ICALEPCS'09*, Kobe, Japan, 2009, pp. 325–327.

[101] M. Gasior, J. Olexa, and R. J. Steinhagen, "A high resolution diode-based orbit measurement system - prototype results from the LHC," in *Proceedings of DIPAC'11*, Hamburg, Germany, 2011, pp. 98–100.

[102] G. Valentino and E. Veyrunes, LHC Project Document No. LHC-OP-ES-0025, 2011.

[103] LHC Collimation Vistar, available at http://op-webtools.web.cern.ch/op-webtools/vistar/vistars.php?usr=LHCCOLLB1.

[104] B. Liskov and J. Guttag, *Program Development in Java*. Addison-Wesley, 2001.

[105] G. Valentino, R. W. Assmann, R. Bruce, S. Redaelli, N. Sammut, and D. Wollmann, "Automatic computer algorithms for beam-based setup of the LHC collimators," in *Proceedings of ICAP'12*, Rostock-Warnemunde, Germany, 2012, pp. 15–19.

[106] H. Wiedemann, *Particle Accelerator Physics.* Springer, 2007.

[107] H. Burkhardt and R. Schmidt, "Intensity and luminosity after beam scraping," Tech. Rep. CERN-AB-2004-032-ABP, July 2004.

[108] G. Valentino, R. W. Assmann, F. Burkart, S. Redaelli, A. Rossi, N. Sammut, and D. Wollmann, "Modeling and simulation of LHC beam-based collimator setup," in *Proceedings of IPAC'12*, New Orleans, USA, 2012, pp. 2059–2061.

[109] G. Stancari, "Diffusion model for the time evolution of particle loss rates in collimator scans: a method for measuring stochastic transverse beam dynamics in circular accelerators," FERMILAB-FN-0926-APC, arXiv:1108.5010, 2011.

[110] K. H. Mess and M. Seidel, "Collimators as diagnostic tools in the proton machine of hera," *Nucl. Instr. and Meth. in Phys. Res. A*, vol. 351, pp. 279–285, 1994.

[111] G. Valentino, R. W. Assmann, R. Bruce, F. Burkart, V. Previtali, S. Redaelli, B. Salvachua, G. Stancari, and A. Valishev, "Beam diffusion measurements using collimator scans in the LHC," *Phys. Rev. ST. Accel. Beams*, vol. 16, p. 021003, 2013.

[112] G. Valentino, R. W. Assmann, R. Bruce, F. Burkart, V. Previtali, S. Redaelli, B. Salvachua, G. Stancari, and A. Valishev, CERN-ATS-Note-2012-074, 2012.

[113] R. W. Assmann, J.-B. Jeanneret, and D. Kaltchev, "Status of robustness studies for the LHC collimation," in *Proceedings of APAC'01*, Beijing, China, 2001, pp. 204–208.

[114] I. Mierswa, M. Wurst, R. Klinkenberg, M. Scholz, and T. Euler, "Yale: rapid prototyping for complex data mining tasks," in *KDD '06: Proceedings of the 12th ACM SIGKDD international conference on Knowledge discovery and data mining*, L. Ungar, M. Craven, D. Gunopulos, and T. Eliassi-Rad, Eds. New York, NY, USA: ACM, August 2006, pp. 935–940. [Online]. Available: http://rapid-i.com/component/option,com_docman/task,doc_download/gid,25/Itemid,62/

[115] G. Valentino, R. W. Assmann, R. Bruce, F. Burkart, M. Cauchi, D. Deboy, S. Redaelli, A. Rossi, N. Sammut, and D. Wollmann, "Comparison of LHC collimation setups with manual and semi-automatic collimator alignment," in *Proceedings of IPAC'11*, San Sebastian, Spain, 2011, pp. 3771–3773.

[116] S. Redaelli, "Optimisation of the nominal cycle," in *Proceedings of the Chamonix 2011 Workshop on LHC Performance*, Chamonix, France, 2011, pp. 75–80.

[117] R. W. Assmann, 2010, talk on collimation in the Internal Machine Protection Review.

[118] R. Tomas, O. Brüning, M. Giovannozzi, P. Hagen, M. Lamont, F. Schmidt, and G. Vanbavinckhove, "CERN Large Hadron Collider optics model, measurements and corrections," *Phys. Rev. ST. Accel. Beams*, vol. 13, 2010.

[119] B. Salvachua, R. W. Assmann, R. Bruce, M. Cauchi, D. Deboy, L. Lari, A. Marsili, D. Mirarchi, E. Quaranta, S. Redaelli, A. Rossi, and G. Valentino, "Cleaning performance of the LHC collimation system up to 4 TeV," in *Proceedings of IPAC'13*, Shanghai, China, 2013.

[120] G. Valentino, proton-lead run: collimation commissioning. Presented at the LHC Collimation Working Group meeting, 28.01.2013.

[121] G. Valentino, R. W. Assmann, G. Bellodi, R. Bruce, F. Burkart, M. Cauchi, J. M. Jowett, L. Lari, S. Redaelli, A. Rossi, B. Salvachua, and D. Wollmann, "Multi-turn losses and cleaning in 2011 and 2012," in *Proceedings of the Third 2011 Evian Workshop on LHC beam operation*, Evian, France, 2011, pp. 111–116.

[122] G. Valentino, R. W. Assmann, R. Bruce, S. Redaelli, B. Salvachua, N. Sammut, and D. Wollmann, "Operational results with fast automatic beam-based LHC collimator alignment," *Xjenza*, 2013, in press.

[123] G. Valentino, R. W. Assmann, R. Bruce, G. J. Müller, S. Redaelli, A. Rossi, and N. Sammut, "Comparison of LHC collimator beam-based alignment centers to the BPM-interpolated orbit," in *Proceedings of IPAC'12*, New Orleans, USA, 2012, pp. 2062–2064.

[124] W. V. Delsolaro, "LHC operational efficiency in 2010," in *Proceedings of the Second LHC Beam Operation Workshop*, Evian, France, 2010, pp. 37–40.

[125] A. Nosych, C. Boccard, and M. Gasior, "Electromagnetic simulations of an embedded bpm in collimator jaws," in *Proceedings of DIPAC'11*, Hamburg, Germany, 2011, pp. 71–73.